UNIVERSITEIT VAN PRETORIA
UNIVERSITY OF PRETORIA
YUNIBESITHI YA PRETORIA

Petrography and geochemistry of the Holocene monogenetic Bayuda Volcanic Field, Sudan: Insights into the magma plumbing system

Faculty of Natural and Agricultural Sciences

University of Pretoria

Research project submitted in partial fulfilment of the requirements for the degree of:

MSc (Masters)

In

Geology

Francois Jacobus Petrus Lötter

Supervisor: Dr Nils Lenhardt

Co-Supervisors:

Prof. Lothar Viereck (Friedrich-Schiller-University Jena, Germany)

Dr Mohammed Altigani (Al Neelain University Khartoum, Sudan)

16 March 2020

DECLARATION OF ORIGINALITY

UNIVERSITY OF PRETORIA

Full names of student: Francois Jacobus Petrus Lötter

Topic of work: The Bayuda Monogenetic Volcanic Field

Declaration

1. I understand what plagiarism is and am aware of the University's policy in this regard.

2. I declare that this thesis is my own original work. Where other people's work has been used (either from a printed source, Internet or any other source), this has been properly acknowledged and referenced in accordance with departmental requirements.

3. I have not used work previously produced by another student or any other person to hand in as my own.

4. I have not allowed, and will not allow, anyone to copy my work with the intention of passing it off as his or her own work.

SIGNATURE

____

FJP Lötter

Abstract

The Bayuda monogenetic volcanic field (BMVF) is an active, understudied Holocene volcanic field located in the great bend of the Nile, Sudan. The BMVF's location provides an excellent opportunity to study monogenetic volcanism in an African context. Recent studies have shown that monogenetic volcanoes can have more intricate plumbing systems than initially thought. The project sets out to provide a general description and genesis of the BMVF emphasising the plumbing system. Petrography reveals olivine and clinopyroxene as the main phenocryst phases in a groundmass of predominantly plagioclase and subordinate pyroxene and olivine microcrysts. A significant amount of crystals display pronounced disequilibrium textures alongside sector and oscillatory zoning. Major and trace elements indicate that the BMVF is sodic-alkaline, resembling an OIB signature. Melting models that use partitioning coefficients of Zr, Hf and Nb in phenocrysts estimate 2-4% melting of a metasomatised garnet pyroxenite at a depth of ~2.8GPa as the source melt for the BMVF.

The isotopic signature suggests mixing of an enriched mantle component (HIMU) and a depleted mantle component (DMM). Textural evidence alongside K_D (Fe-Mg) of olivine indicate open system dynamics by revealing separate magma batches with differing times and depths of emplacement. Ni, Ca and Mn content of olivine, furthers the idea of open system dynamics by revealing processes of 1) 'failed eruptions', 2) magma mixing and 3) deep-seated fractionation. This project forms part of a growing number of studies that suggest complex plumbing system for monogenetic volcanic fields.

Keywords: African volcanism; Cenozoic volcanism; monogenetic volcanism; complex plumbing system; open system dynamics.

Acknowledgements

I would first like to thank my main supervisor, Dr Nils Lenhardt, for all the support, guidance and opportunities throughout this project. The project (and the "legendary, fictional Chapter 5") would have been dead in the water if it weren't for his excellent knowledge on volcanology and openness to ideas and debates. Thanks to Dr Mohammed Altegani for sending all samples and helpful guidance in understanding the overall geology of Sudan. I would also like to thank Prof Lothar Viereck for his in-depth contributions (and patience) and greatly furthering my understanding of the geochemical aspects of the project.

I would like to thank Prof Carstens Münker of the University of Cologne who graciously granted me access to their clean lab facilities and showed me the ropes of isotope geochemistry. A special thanks to Chris S. Marien for taking the time to help with all the chemistry, using the ICP-MS and showing me around Cologne. Alongside Chris, I would like to thank Sepp (Sebastian) and Erik for making my time in Cologne very enjoyable.

I owe gratitude to my University of Pretoria colleagues, Kyle Lusted, Nicholas Fraser and Salazzle, for all the shenanigans and high jinks. If it weren't for them, I probably would have finished a year earlier.

I would also like to thank my parents, Casper- and Sunette Lötter, for their financial and moral support, which without I would not have been able complete this project and pursue my dreams.

Lastly, I would like to thank Alice who supported me through it all.

'n Handvol gruis uit die Hantam -
My liewe, lekker Hantam-wyk!
'n Handvol gruis en gedroogde blare,
Waboom-blare, ghnarrabos-blare!
Arm was ek gister, en nou is ek ryk.

Arm in herinnering, arm in verbeelding,
Arm in onthou van die vroeër jare
Deurgebring in die Hantam-wyk.
'n Handvol gras en gedroogde blare
Maak my, wat arm was, koning-ryk -

Ryk in herinnering, ryk in verbeelding,
Ryk in onthou van die vroeër tyd
Toe die Hantam-wêreld al die wêreld
Vir my was in die vroeër tyd.
'n Handvol gruis en gedroogde blare
Vertel so veel van die wonderjare
In my liewe lekker Hantam-wyk -
Waboom-blare, ghnarrabos-blare -
Arm eergister en nou skatryk!

C. Louis Leipoldt

Table of Contents

List of Figures

List of Tables

1 Introduction

Monogenetic volcanic fields consist of volcanoes that are characterised by low eruption rates alongside a short lifespan (Nakamura, 1977). Generally, they are recognised by several volcanoes no larger than 1 km^3 with a single eruption time (Kereszturi and Németh, 2012). Monogenetic volcanoes, as the term suggests, exhibit a singular eruption period per conduit. If the eruption stops, the volcanism will not occur at the same conduit again. The cause of the volcanism might still be active, and volcanism and can occur in new conduits in the monogenetic volcano. The eruption lifespan of a monogenetic volcano is short, but a monogenetic volcanic field may have a longer lifespan than a polygenetic volcano (Németh, 2010). Scoria cones are the most prevalent volcano in monogenetic volcanic fields. Alongside scoria cones in monogenetic volcanic fields are volcanoes that are characterised by a predominance of phreatomagmatic eruptions, such as maars and tuff rings. Maars and tuff rings form when there is magma/water interaction during its formation (Walker, 1993). The majority of monogenetic volcanic fields continuously erupt the same magma leading to relatively to homogenous deposits (Brenna et al., 2011). The plumbing system of the monogenetic volcano, however, can significantly influence the form and composition of different eruptions of a single volcano (Brenna et al., 2011). The authors showed through geochemical analysis of the stratigraphic layers of several monogenetic volcanoes that the eruptions that differed by days also differed geochemically.

Nakamura (1977) stated that the conduits of a monogenetic volcano are necessarily dykes and that at shallow depths, the dykes could transform into cylindrical conduits. The formation of these dykes could be indicative of tectonic environments. Takada (1994a) furthers this notion by adding that magma filled cracks coalesce; they tend to form polygenetic volcanoes. When magma-filled cracks do not coalesce or experience small levels of coalescence monogenetic volcanoes, tend to form. The tendency of magma-filled cracks to coalesce is determined through differential stress and magma input rate. High magma input rate and small differential stress cause cracks to coalesce and therefore create polygenetic volcanoes. On the other hand, if the magma input rate is low and differential stress is high, monogenetic volcanoes tend to form. The localised stress field of polygenetic volcanoes, like stratovolcanoes and calderas induced by a shallow magma chamber, can override the regional stress field if the shallow magma chamber is large enough. The opposite is true for volcanoes lacking a large magma chamber (Al Shehri and Gudmundsson, 2018). The recent developments in monogenetic volcanism research caused the revaluation of several studies and ignited several more. The global push from volcanologists to grasp a better understanding of monogenetic volcanism has led to pinning down a new definition of what a monogenetic volcano is. This thesis will use the definition by Németh and Kereszturi (2015):

“A volcanic edifice with a small cumulative volume (typically ≤1 km3) that has been built up by one continuous, or many discontinuous, small eruptions occurred in a short timescale (typically ≤10 of years) and fed from one or multiple magma batches through a relatively simple, closely spaced feeder dyke (and sill) system with no well-developed magma chambers associated with.”

Africa and the Arabian peninsula contains some 26 major sites of volcanic activity, which formed during the Cenozoic (Thorpe and Smith, 1974). Figure 1.1 shows that southern Africa lacks large-scale Cenozoic volcanism. The only Cenozoic volcanism in Southern Africa is represented by small kimberlitic plugs in South Africa (Moore and Verwoerd, 1985, Janney et al., 2002) and phonolitic lavas, ignimbrites and eroded tholoids present in Namibia (Marsh, 1987). Although, Southern Africa experienced minor volcanism during the Cenozoic, it might change in the future. New evidence points at a mantle plume (called the Quathlamba mantle plume) that is responsible for the unusual elevation and heat flow in Southern Africa (Gilfillan et al., 2019). There is yet to be an extensive, volcanic expression of this mantle plume.

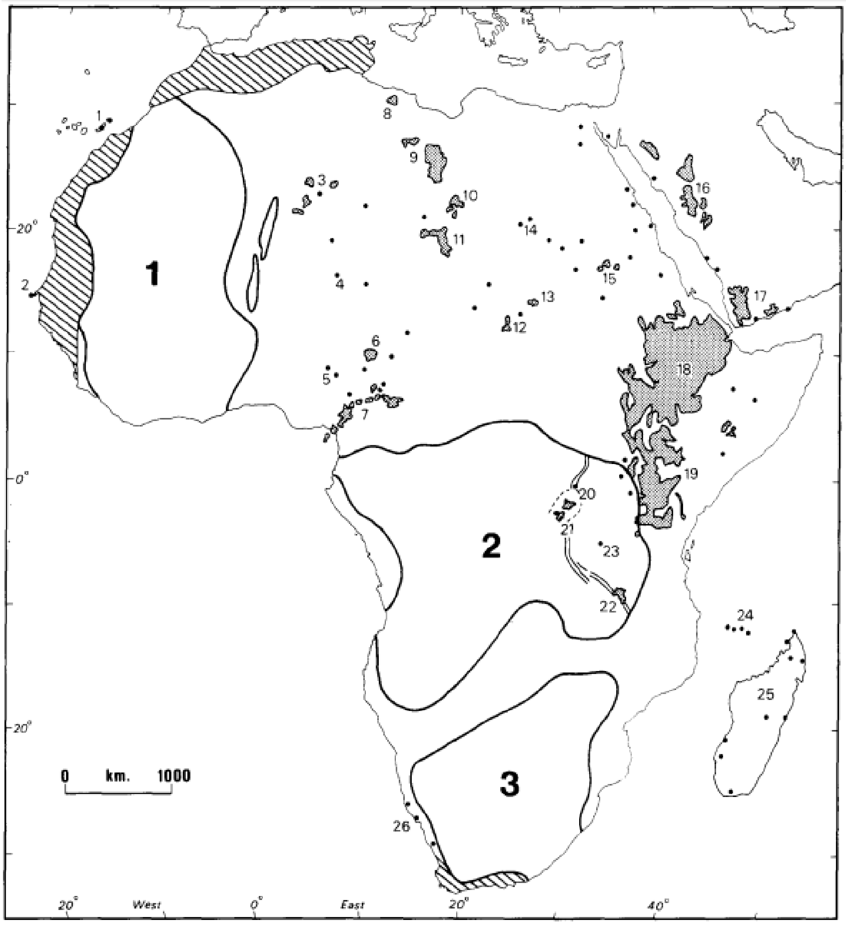

Figure 1.1. *:* Map of Africa showing A) the various stable cratons: 1) the Kaapvaal Craton 2) Congo Craton 3) West African Craton. B) The Cenozoic volcanoes of Africa. Distribution of volcanoes concentrated in Northern Africa. Volcanoes of importance: 12) The Jebel Marra Volcanic Complex, 13) The Meidob Volcanic Complex , 15) The Bayuda Monogenetic Volcanic Field and 16) The Harrat Rahat (Thorpe and Smith, 1974)

North Africa conspicuously hosts several volcanic regions that formed during the Cenozoic Era. These events relate to the 1) Alpine orogeny (Liegeois et al., 2005) 2) the Cameroon Volcanic Line (Fitton, 1987, Nkouathio et al., 2002) 3) the African rift system (Rogers et al., 2000) 4) the Red Sea rift system(Camp and Roobol, 1989, Féraud et al., 1991) and 5) crustal swells in the Precambrian basements (Franz et al., 1994) . Alternatively, Ebinger and Sleep (1998) argues that the elevated Cenozoic volcanic activity is the resultant of a large, single plume in Ethiopia and that the magma travels through a series of fault systems to form volcanism across Northern Africa.

So far, the large polygenetic volcanoes of Northern Africa have been the major focus point of studies on Cenozoic Volcanism in Africa. Africa's monogenetic volcanoes have been basking in the shadow of their larger counterparts. Monogenetic volcanism in Africa is often restricted to the edifices of polygenetic volcanoes and seldom occur in the form of volcanic fields. This is often the case, as monogenetic volcanoes can occurs as a type of offshoot from main conduits in polygenetic volcanoes(Carn, 2000, Németh and Kereszturi, 2015) where the monogenetic volcano's conduit is directly controlled by the larger, polygenetic volcano's conduit. Few Cenozoic monogenetic fields exist in Africa, namely the Tombel Graben monogenetic volcanic field in western Cameroon (Nkouathio et al., 2002), the Lake Natron-Engaruka monogenetic volcanic field in Tanzania (Dawson, 2008, Mattsson and Tripoli, 2011) and the Bayuda Monogenetic Volcanic Field (BMVF) in the Sudan (Almond et al., 1969, Almond, 1974, Almond et al., 1984, Lenhardt et al., 2018).

With the renewed interest in monogenetic volcanism, a project surrounding a monogenetic field in Africa will prove useful as it can give further insights into monogenetic volcanism as well as further insight into the increased volcanic activity during the Cenozoic Era in North Africa. This project will focus on the Bayuda Monogenetic Volcanic Field (BMVF) of the Sudan. Sudan hosts more than one volcanic province, alongside the BMVF there is the Meidob hills and the Jebel Marra volcanic fields of the Darfur dome, but consist of polygenetic and monogenetic volcanoes. The proximity of the Darfur dome could be a fundamental factor in the formation of the BMVF making it pertinent that the Darfur dome be investigated alongside the BMVF. The BMVF is still a relatively under-studied volcanic field, lacking extensive geochemical analysis, definitive age dating, and a formational model. The study area had a research hiatus of 30 years with the most recent publication being that of Lenhardt et al. (2018). The purpose of this project is to provide a comprehensive look at the genesis and the evolution of the magma beneath the BVMF, making the project the first of its kind.

Aims and Objectives

This project will: 1) Determine a magmatic plumbing system of the BVMF, - 2) determine the mantle source of BMVF and any parallels in geochemistry between the BMVF and selected Cenozoic volcanoes of Africa and the Arabian peninsula, and - 3) compare the volcanism occurring on the Saharan metacraton to the volcanism happening on other metacratons in the world.

2 Geological Background

2.1 Geology of North East Africa

2.1.1 The assemblage of the North African and Arabian crust

The supercontinent Gondwana was formed during the Neoproterozoic through the closing of the Mozambique ocean and the amalgamation of the west and east Gondwana continents (Fitzsimons, 2000, Meert and Lieberman, 2008). Modern-day Africa formed the central part of the amalgamation event. The amalgamation event is known as the Pan-African Event or the Pan-African Orogeny (Gass, 1977, Kröner et al., 1987, Abdelsalam et al., 2003). West Gondwana contained the majority of the stable cratons that Africa consists of today, namely: the Kalahari Craton, the Congo Craton and the West African Craton. Figure 1.1 shows the distribution of these cratons. North East Africa conspicuously lacks a stable craton. Studies have shown that outcrops of the east African crust in Egypt and Libya present older ages than that of the Pan-African event (Stern et al., 1994, Küster and Liégeois, 2001). This section of the African crust has been described as the Central Saharan Ghost Craton or the Saharan metacraton. A metacraton (or Ghost craton) is described by Abdelsalam et al. (2002) as a craton that experienced remobilisation or partial delamination, but maintained its rheological, geochronological and isotopic properties. The Saharan metacraton consists of poorly outcropping Precambrian gneisses and migmatites, alongside Neoproterozoic ophiolites, juvenile volcanic arcs, and Neoproterozoic granites that intruded the metamorphosed rocks from 750-550 Ma (Abdelsalam et al., 2002, Küster et al., 2008)

The sub-continental lithospheric mantle (SCLM) of the Saharan metacraton is only typical of a craton for depths up to 100 km, seismic readings deeper than 100km show that it lacks a cratonic signature for the SCLM (Abdelsalam et al., 2011). The mantle structure of the Saharan metacraton might have been the result of partial crustal delamination, i.e. during the Pan African event sections of the cratonic root may have become too heavy and eventually separated from the metacraton. When compared to other, stable cratons of Africa (Figure 1.1) the apparent differences become clear. The cratons have similar shear wave velocity variation signatures up to a 100km, but lose any similarities at greater depths. The Saharan metacraton is thinnest at its centre at ~20 degrees latitude (Figure 2.1). Partial crustal delamination is also observed in the North China Craton where the eastern section of the North China Craton experienced crustal delamination while the western section kept its cratonic signature (Zhu et al., 2011, Zhu et al., 2012). The Saharan metacraton is Africa's only example of a craton that experienced partial crustal delamination.

The north-trending Keraf-Kebus-Sekerr suture or Keraf-suture marks the eastern boundary of the Saharan metacraton. The Keraf- suture formed through the collision of the Arabian Nubian Shield and the Saharan metacraton (Suliman and Bailo, 2000). Furthermore, the Saharan metacraton is bounded by the Tuareg shield to the west, the Congo craton to the south, (Henry et al., 2009) and the Arabian Nubian-Shield (ANS) to the east.

The ANS formed due the accretion of several back-arc basins and volcanic arcs that collided during the Pan African Orogeny, which marks the end of a Wilson cycle (Kröner and Stern, 2005). The different terranes of the ANS are separated by North to East striking sutures that predominantly contain ophiolites and tectonite mélange with talc and serpentine matrix (Abdelsalam and Stern, 1996, Ali and Rahman, 2011). The formation of the ANS occurred in a three-phase process: 1) formation of the volcanic arcs 950-900 Ma, -2) closing of the Mozambique Ocean causing the accretion of the volcanic arcs ~ 640 Ma, and 3) post-collisional extension and continued volcanism and sedimentation (Kröner, 1985, Johnson and Woldehaimanot, 2003, Stoeser and Frost, 2006, Abdelsalam, 2010). The ANS orogeny occurred in the northern section of the Pan-African event (Abdelsalam and Stern, 1996).

The ANS forms the crust of North East Africa and the west of Arabia. The Nubian shield forms the north eastern most African crust while the Arabian shield forms the western Arabia crust. The ophiolite bearing suture zones act as an indicator of the tectonic activity of the Neoproterozoic and as proof for the Wilson cycle (Kröner and Stern, 2005). The ANS experienced 500 Myr of stability (Blanchette et al., 2018) until a rifting event that led to the opening of the Red Sea bisected the ANS by ~25 Ma (Stern and Johnson, 2010).

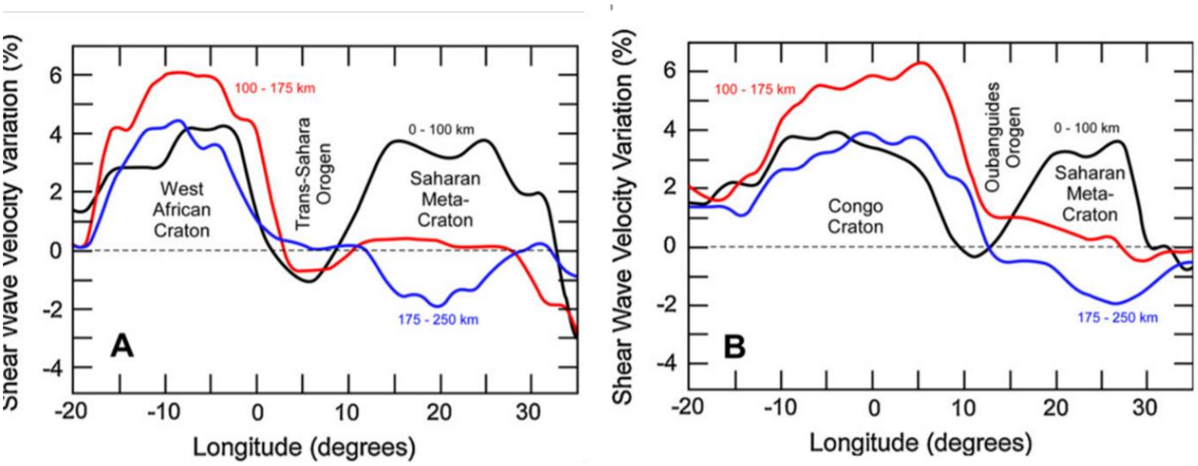

Figure 2.1. The graphs compare the SCLM signatures of the A) West African Craton and the B) Congo craton to the SCLM signature of the Saharan Meta-Craton. The Saharan Meta-Craton clearly shows similar Shear Wave Velocity variations up to a 100km than the other African cratons. The disparities between the Saharan Meta-craton and the other African cratons are apparent with Shear Wave Velocity Variation at depths greater than 100km (Abdelsalam et al., 2011)

The Afar triple junction is a three-way spreading centre at the southern tip of the Red Sea, off the coast of Yemen and Ethiopia, which is believed to be induced by the Afar plume (Baker et al., 1998, Furman et al., 2006). It is the intersection of three rifts: the Gulf of Aden, the African rift valley, and the Red Sea rift system (Furman et al., 2006). The Afar plume associated volcanism has been active since 40 Ma with initial small-scale volcanism followed by extensive flood basalts at 30 Ma in Yemen, Eritrea and Ethiopia (Baker et al., 1996, Hofmann et al., 1997, George et al., 1998).The rifting induced by the Afar plume uplifted parts of the ANS and broke the shield into two sections, the Arabian Shield and the Nubian Shield (Kröner and Stern, 2005)

The Red Sea rift is an active divergent plate boundary within the Red Sea that stretches from the Bitlis suture in Turkey to the Afar triple junction (Davison et al., 1994). The Red Sea consists of a spreading centre with 5-6 Ma aged oceanic crust located inside young sedimentary basin (Izzeldin, 1987, Davison et al., 1994). The rifting initially started during the Late Oligocene epoch and is still ongoing, spreading at a rate of 16-10 mm per year (Chu and Gordon, 1998). No consensus has been reached on the formation of the Red Sea rift as concise time constraints for the initial volcanism, doming and rifting has not yet been determined (Drury et al., 1994). A general accepted formational model is that the Red Sea rift system is not an active or a passive rift model as basaltic and rhyolitic volcanism predates doming at 31-29 Ma. The rifting occurs at ancient sutures of the ANS. However, regional stresses are too weak to induce continental breakup. The driving force behind the rifting is thought to be the Afar plume that weakened the lithosphere (Davison et al., 1994, Kenea et al., 2001).

The Arabian shield consists of eight different terranes that are separated by five ophiolite containing suture zones (Stoeser and Frost, 2006). The Arabian shield is the amalgamation of the Hijaz-, Jeddah-, Asir-, Afif-, Midyan-, Sinai-, Haiil- and Hulayfah terranes (Kröner and Stern, 2005, Bierlein et al., 2016). The Nubian Shield consist of the Nafka-, Haya-, Gebeit-, Gabgaba-, Halfa- and Eastern Desert-terranes. It was speculated whether the Bayuda terrane is part of the ANS or the Sahara metacraton due to the metamorphic nature of the Bayuda terrane (Abdelsalam et al., 2003). The Bayuda terrane has a higher degree of metamorphism than the other lithologies of the Sahara metacraton. It was initially thought that the Bayuda terrane was accreted on the Sahara metacraton along with the other terranes of the ANS. The implication would then be that the Keraf suture is not the boundary between the ANS and the Saharan metacraton. The Bayuda terrane could, therefore, be part of the Nubian Shield. The difference in metamorphic grades between the Bayuda terrane and the Sahara metacraton was attributed to collisional and post-collisional horizontal movements (Küster and Liégeois, 2001). Although unclear, it is generally accepted that the Keraf-suture zone is the boundary between the ANS and the Sahara metacraton (Küster et al., 2008, Ali et al., 2014)

2.1.2 The Bayuda desert basement

The Bayuda desert lies in and around the Great Bend of the Nile in the Sudan. The Bayuda desert basement is made up of three terranes: The Bayuda terrane, the Halfa terrane and the Gabgaba terrane (Lenhardt et al., 2018). The Bayuda terrane forms the largest section of the desert and is bounded by the Gabgaba terrane in the east and the Halfa terrane in the north (Abdelsalam et al., 2003, Lenhardt et al., 2018). The Keraf suture separates the Gabgaba terrane from the Bayuda terrane, and the Atmur-Delgo terrane separates the Halfa terrane from the Bayuda terrane (Abdelsalam et al., 2003). The Keraf-suture separates the pre-Proterozoic Sahara metacraton from the Neoproterozoic ANS. However, in the southern part of the desert, is a small section of Neoproterozoic, unmetamorphosed volcano sedimentary rocks can be found. The outcrop of Neoproterozoic material lies on the western side of the Keraf suture, however, recently ophiolitic sags have been found west of the suture zone. The phenomenon has been interpreted as a part of the ANS that was thrusted westward, over the Keraf-suture and, into the Saharan metacraton (Abdelsalam and Stern, 1996, Küster and Liégeois, 2001, Abdelsalam et al., 2003).

The Bayuda desert predominately consists of medium-grade gneisses and high-grade migmatites with volcanoclastic sediments separated by occasional ophiolites (Barth and Meinhold, 1979). The Bayuda desert can be divided into two sections: the first section containing migmatised granitic gneisses alongside amphibolites. The second section contain medium grade felsic gneisses, marble, schists, quartzites and metavolcano-sedimentary lithologies (Küster and Liégeois, 2001). In recent field trips it has been revealed that Barth and Meinhold (1979) may have misclassified the sheared granites of the Abu Arik Formation as gneisses (M.Altegani, personal communications, 28 November 2019). The intrusion of A-type granites is linked with crustal thickening of the northern section of the Sahara metacraton (Abdelsalam et al., 2003).

Alkaline ring complexes are prevalent throughout Sudan. Approximately 22 alkaline ring complexes are hosted within the Bayuda desert basement (Vail, 1985). The ring complexes formed during the Cretaceous-Tertiary alongside the A-type granite plutons, where the younger ring complexes overlap with the older ring complexes. Early phases of the ring complexes were volcanic with sequences of trachytic lava flows and ignimbrites outcropping in collapsed calderas(Vail, 1985). Felsic ring dykes preserve the structures of the collapsed calderas. The plutonic phases of the ring complexes are highly alkaline consisting of alkali granite and alkali syenite (Vail, 1985). These ring dykes are compositionally similar to a collection of dykes striking E-W in the desert. The dyke swarms and ring dykes, alongside the A-type granitic plutons, are younger than the gneissic basement and are referred to as the young granites (Almond et al., 1969).

2.2 Cenozoic Volcanism in Africa and Arabia

2.2.1 The Bayuda Monogenetic volcanic field

The Bayuda desert hosts the remnants of Cretaceous volcanic activity; one of these volcanic features is the Bayuda Monogenetic Volcanic Field (BMVF) described by Almond (1984) as the "Main Field". The BMVF erupted through and onto the Bayuda terrane. The volcanic field consists of 70 small monogenetic volcanoes, predominantly scoria cones, with some showing flank collapses. Alongside scoria cones, maars and tuff rings are also prevalent in the BMVF (Lenhardt et al., 2018). The main volcanic field is NW striking and appears to be structurally controlled by either the rifting of the Red Sea or the Young Granite ring dykes in the Bayuda desert.

The BMVF consist of a younger, well-preserved group of volcanoes and a group volcanoes that get progressively older and more eroded towards the outer rim of the Bayuda desert (Almond et al., 1984). The older volcanic fields in the Bayuda desert have been K-Ar age dated at around late Cretaceous-Pleistocene (70 Ma-1.7 Ma) (Barth and Meinhold, 1979, Almond et al., 1984). Observations on weathering of the scoria cones has led to the speculation the BMVF is late Pleistocene-recent in age (Almond, 1974). However, the apparent erosion of some of the volcanic edifices is ascribed to be deformation that occurred during the formation of the volcanoes rather than weathering at a later stage (Almond, 1974). The preservation of the cones is attributed to the recent formation of the volcanic field and arid weather of the Bayuda desert. One eruption of the BMVF has been determined through ^{14}C dating of a baked piece of mammalian dung preserved on one of the volcano's lava flows. The baked mammalian dung indicates the most recent eruption was 1102 ± 48 years ago (Almond et al., 1984).

Maar volcanoes and tuff rings are both formed through phreatomagmatic eruptions, an eruption type that can only occur in the presence of water. When magma rises through the crust it may react with ground- or shallow water, leading to violent eruptions and forming maar volcanoes and/or tuff rings (Waters and Fisher, 1971). The presence of both maar volcanoes and tuff rings indicate that the groundwater was abundant at some point in the Bayuda desert. The recent age of the volcanism and the signs of increased water coincides with the Bîrbet recession. The Bîrbet recession was a period of deluge where the Nile River experienced extreme down cutting called the "wild floods". Evidence for increased discharge in the late Pleistocene/early Holocene~1200 BP can be found in archaeological, faunal and floral studies (Paulissen and Vermeersch, 1987, Nicoll, 2004).

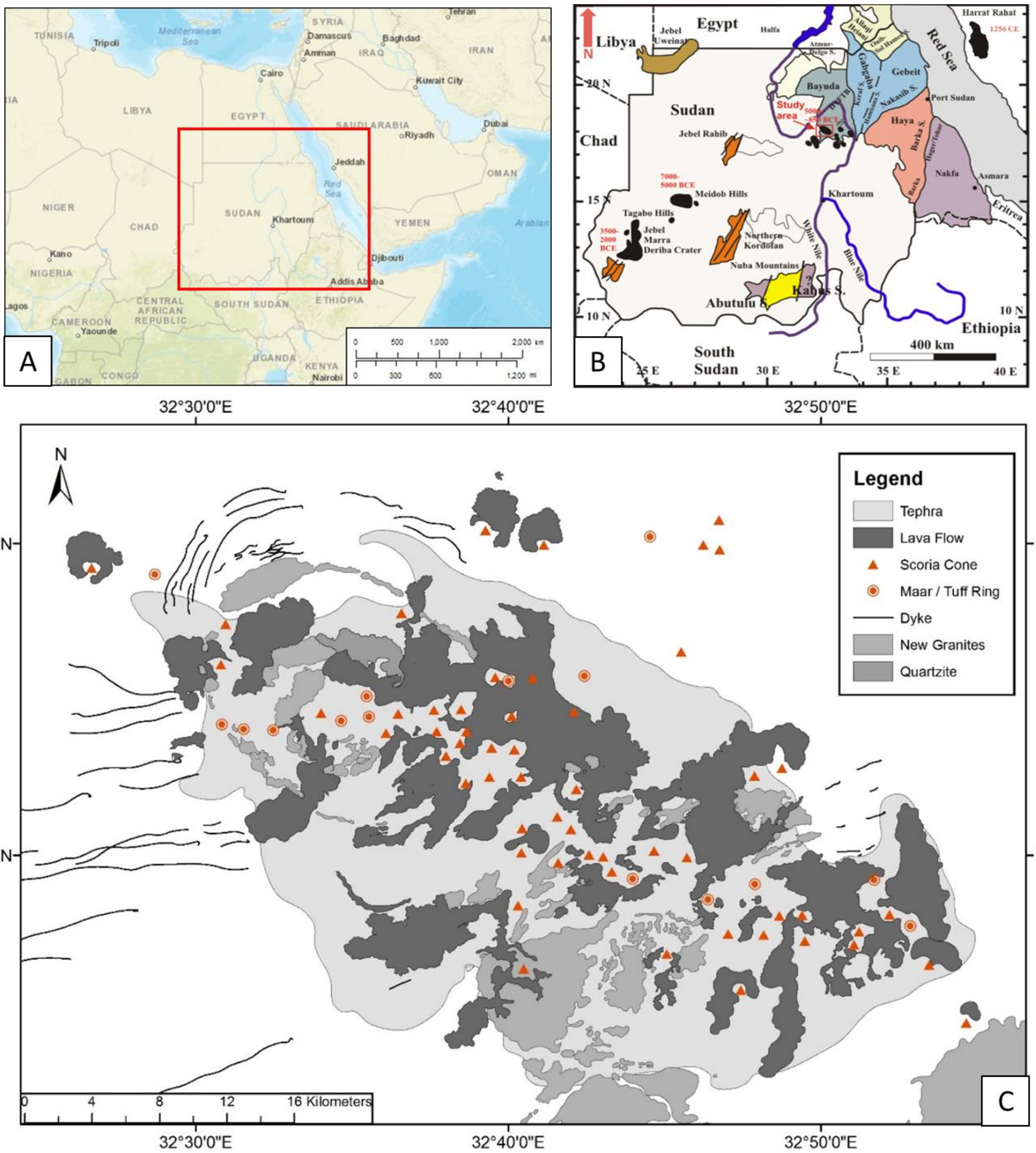

Figure 2.2 : A) Topographical map of Africa. Red box indicates study area B) Tectonic diagram of North Africa showing 1) the terranes of the Nubian shield 2) selected volcanic regions of North Africa and Arabia showing Cenozoic eruption dates. Study area indicates the BMVF. Modified after (Lenhardt et al., 2018) C) A simplified geological map of the BMVF showing the distribution of volcanoes and volcano type throughout the BMVF. Modified from Almond et al. (1969)

The BMVF is a predominately mafic volcanic field, with compositions ranging from melabasinites, basanites and nepheline hawa iite (Almond, 1974, Almond et al., 1984). All of the lavas are silica under saturated. Most lavas have a porphyritic texture with some lavas showing trachytic texture.

In almost all cases, olivine is the most abundant phenocryst (Almond, 1974, Almond et al., 1984). The trachytic lavas differ from the basalt by containing a groundmass of plagioclase microlites showing some orientation (Almond, 1974). The lavas of the BMVF are vesicular and predominantly empty; the few amygdales present are carbonates, chabazites and natrolites (Almond et al., 1984). The lavas host several xenocrysts and are divided into two groups: the granulites group consist of quartz and feldspar xenoliths that are derived from the granitic/gneissic basement while the ultra-mafic group is made up of mantel-derived, magnesium-rich olivine xenocrysts and large spinel-lherzolite xenoliths (Almond et al., 1984).

2.2.2 The Darfur Volcanic complex

The Darfur Volcanic complex is a Cenozoic volcanic complex located in the western part of Sudan. The Darfur Volcanic complex lies on top of the Darfur dome, a topographic swell in the Saharan metacraton (Abdelsalam et al., 2011). The Darfur dome is found at the western side of Sudan induced by gravity anomaly believed to be a mantle plume (Paulick and Franz, 1997, Franz et al., 1999). The Darfur dome forms at a possible triple junction in central Africa with the Abu Gabra rift and the Ngaoundere lineament forming the limbs of the proposed triple junction (Davidson and Wilson, 1989). The dome started to swell in the late Cretaceous, but related volcanism only started later during the Cenozoic. Three main volcanic features define the Darfur dome (Figure 2.2B) in Sudan namely: the Jebel Marra Volcano (JMV), the Tagabo Hills and the Meidob Volcanic Field (MVF) (Franz et al., 1997).

The JMV formed in the Miocene at 16-10 Ma alongside the Tagabo Hills to the north east of the JMV. The eruption of a major, 5 km wide caldera marked the peak of volcanic activity for the JMV (Davidson and Wilson, 1989). A charcoal piece found within tephra deposits of the calderas was carbon dated 3.5 ka (Francis et al., 1973). After the caldera eruption, the JMV has since been in a dormant state (Philibert et al., 2010). The JMV is a composite volcano that, stratigraphically, has a younger and an older series. The lavas that are older than 2 Ma are considered part of the old series while lavas younger than 2 Ma are part of the young series. The old series consist of pyroclastic material and is separated from the younger series by an unconformity marking an eruptional hiatus. The younger series consists of lavas of trachytic, alkali basaltic and rare phonolitic compositions. The magmatic source of the younger series is similar to that of the older series (Davidson and Wilson, 1989).

The MVF formed in the middle Miocene to ca. 5ka and lies north-west of the JMV at the NE border of the Darfur Dome. Basanitic lava flows were produced here from 7-1 Ma while the more trachytic lava started to erupt between 1 Ma - 0.5 ka, forming mesa and scoria cones (Franz et al., 1997, Paulick and Franz, 1997). The central section of the MVF consist of the trachytic lavas, mesa lava flows and maars while the outer edges of the volcanic field consist of the more basaltic lava flows and scoria cones (Franz et al., 1997). The MVF erupted on a >100 m layer of Cretaceous sandstone, not directly on the Sahara ghost craton like the JMV (Franz et al., 1997).

Finally, the Tagabo Hills are a small volcanic feature lodged between the JMV and the MVF. Despite being related to the Darfur dome, no studies have been performed on the Tagabo Hills to date.

2.2.3 The Harrat Rahat

The Harrat Rahat forms part of the harrats (Arabian for volcanic country) found on the Western plate of Arabia. The Harrat Rahat is a monogenetic volcanic field (Murcia et al., 2015) that erupted through the Arabian shield, the eastern part of the Precambrian ANS(Camp and Roobol, 1989) The harrats, although Cenozoic, show no direct magmatic relationship with the continental rifting that later formed the Red Sea (Camp and Roobol, 1989). In addition , they are also not parallel to the NW-trending Red Sea. Instead, they are north-trending, differing from the Red Sea by 25°. Therefore, the harrats are thought have formed in relationship to the Afar plume through the initial uplift and rifting during the Miocene (Almond, 1986).

The Harrat Rahat is the biggest of the harrats, with a surface area of 19,830 km^2 containing 644 scoria cones, 36 basaltic shield volcanoes and 24 benmoreite-trachytic domes (Camp and Roobol, 1989). The Harrat Rahat extruded in the late Miocene and experienced three distinct eruption events. These three events are divided into three chrono-stratigraphies: 1) the Shawahit (10 Ma -2.5 Ma), 2) the Hamah (2.5 Ma-1.7 Ma) and 3) the Madinah (1.7 Ma-recent) (Camp and Roobol, 1989, Murcia et al., 2014). Compositionally, the Harrat Rahat follows a calc-alkaline trend where the oldest eruption products are almost exclusively basaltic while the younger products are characterised by more evolved material (Camp and Roobol, 1989). The volcanic landforms differ in each chrono-stratigraphy, coinciding with the eruption material. Only the youngest deposits display, signs for phreatomagmatic eruptions (Murcia et al., 2014).

3 Materials and Methods

Sample collection was mostly restricted to the western side of the BMVF as it is the most accessible; however, some samples were collected deeper in the main field. See Appendix 1 for the complete list of the samples and their corresponding coordinates. Selected samples of the BMVF underwent isotopic and microprobe analysis. Eighteen samples were analysed by means of X-ray diffraction (XRD). All 52 samples were geochemically analysed by means of X-ray fluorescence (XRF) and ICP-MS. The volcanic samples will be the focus of the project.

The areas where the volcanic material was collected is depicted in Figure 3.1, where several lava flows and volcanoes are indicated. Nine lava flows were sampled on the western flank of the BMVF as well as the edifices of five maar volcanoes, one tuff ring and one scoria cone.

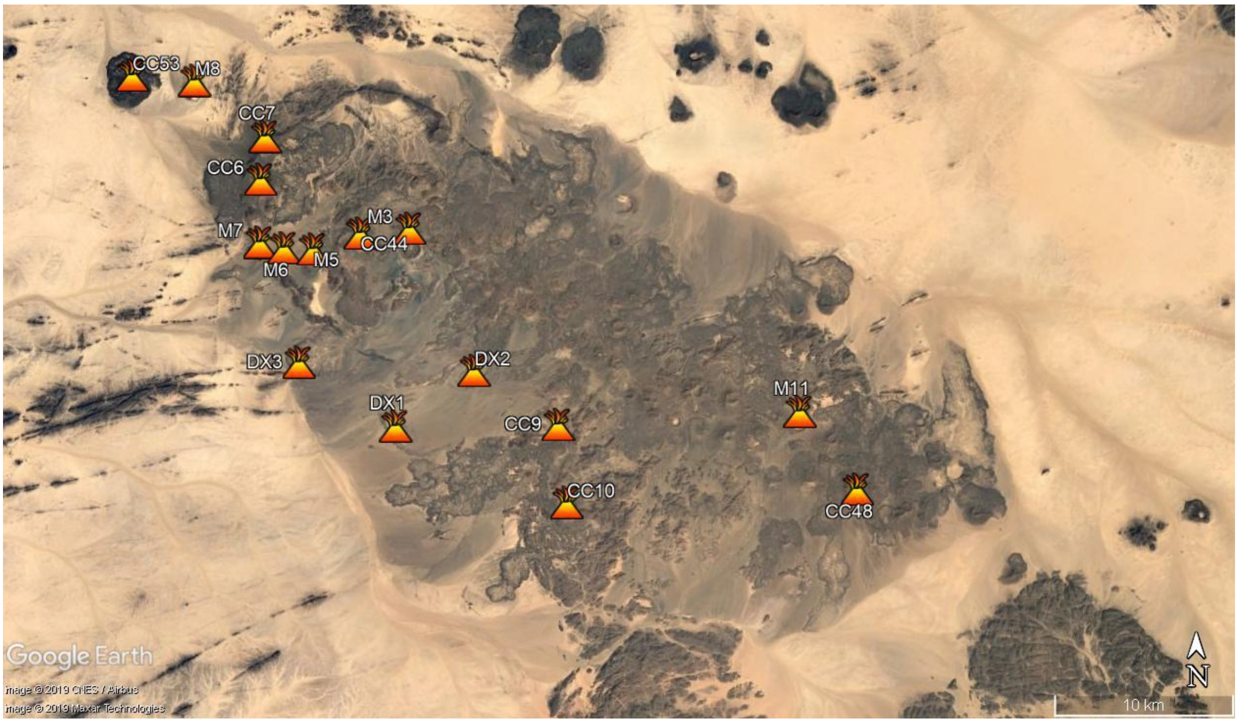

Figure 3.1: Google Earth Image of the sampling sites in the BMVF. Coloured sections indicate the different lava flows that were sampled and points indicate different volcano edifices sampled: CC48: Bayt al Nur, M11: unnamed tuff ring, M3: Hosh Alzalam, M5: unnamed maar volcano, M6: unnamed maar volcano, M7: Jebel Mazrub and M8: Jebel Heibesh

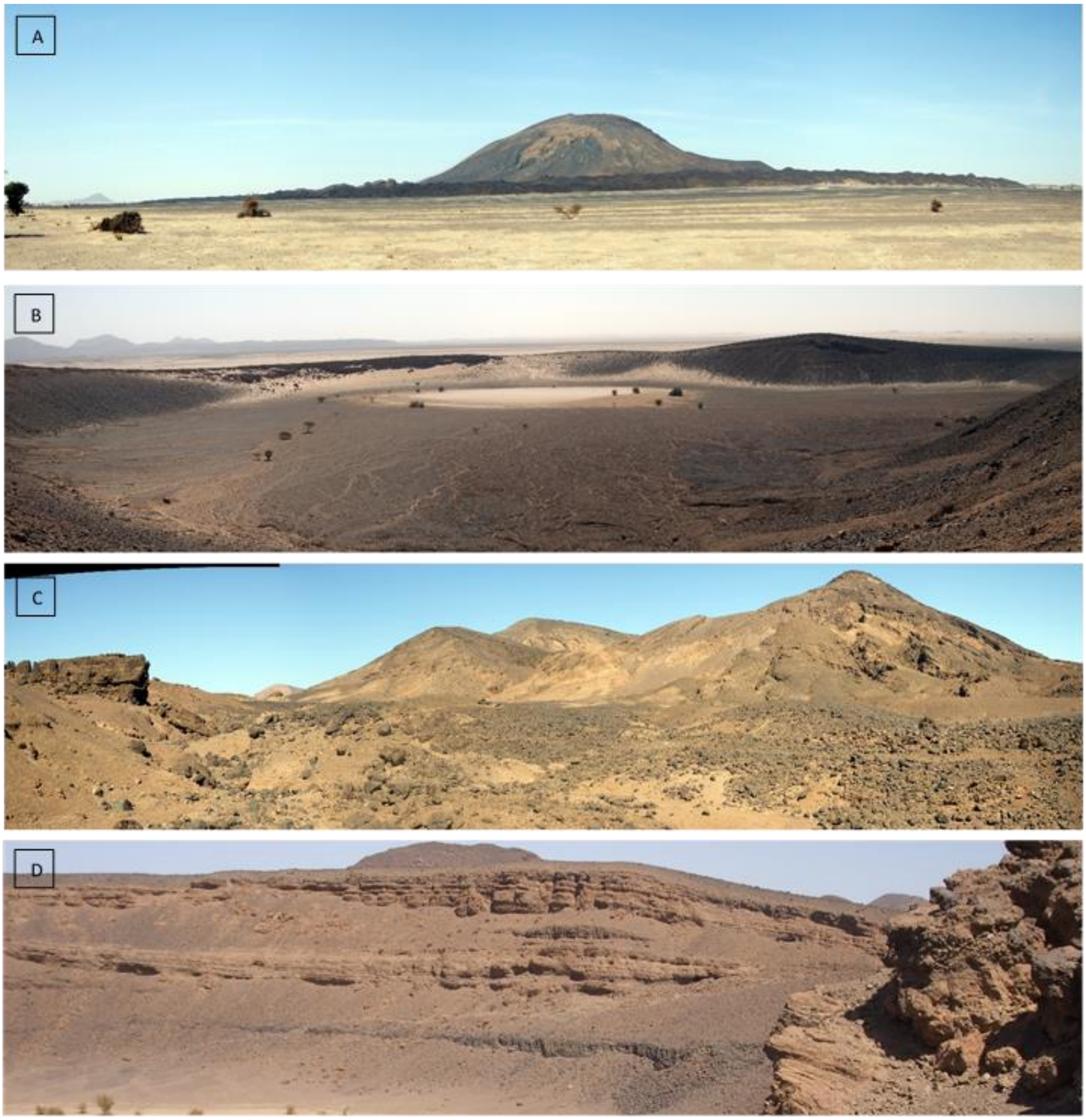

Figure 3.2: Photographs of the volcanoes A) M8: Jebel Heibesh B)M7: Jebel Mazrub C) CC48:Bayt al Nur D) M11: unnamed tuff ring (Lenhardt et al., 2018)

3.1 Thin Sections

45 samples from lava flows, baked sediments, a lava bomb, four dykes, and one basement rock were sent to the University of Witwatersrand for the production of thin sections. The samples were cut down further into smaller suitable sizes for thin sections. The blocks were coarsely ground by silicon carbide (grit powder) on an automated grinder. The blocks were then finely ground on a sheet of glass with fine silicon carbide. The pores in the block were filled by saturating the sample in Araldite epoxy. The epoxy saturated blocks were mounted on glass and compressed until the glass was firmly attached to the sample. The samples were then cut away from the glass and ground by hand to the ideal 0.3 mm thickness of the end product. The University of Witwatersrand produced several thin sections thinner than the ideal thickness of 30 µm leading to minerals displaying a lower order of birefringence than the thin sections that were 30 µm thick.

3.2 X-ray Florescence (XRF)

52 samples of the BMVF rocks underwent XRF analyses. The larger samples were crushed into ~1 cm chips before milling. The chips and -3φ tephra were milled to >75 microns in a tungsten-carbide milling pot. Quartz sand was used to clean the milling pot after the milling of each sample. Loss on Ignition was determined by placing 10 g of the milled sample into a crucible and baking the samples at 100°C and 1000°C, drying and baking the sample, respectively. A stable glass bead was made by fusing 1 g of the milled sample with 6 g of Lithiumtetraborate ($Li_2B_4O_7$) flux at 1050°C.

Surface trace element analyses preparation used roughly 30 g of milled sample mixed with 10 drops of Polyvinyl acetate (PVA) binder. The mixture was then compressed into a metal cup at 10 tons. Analyses of both trace element and XRF used the Thermo Fischer ARL Perform 'X Sequential XRF instrument with OXSAS software.

3.3 X-ray Diffraction (XRD)

18 samples from five lava flows, eight scoria samples, three dyke samples, one basement sample and one sample of the Sahara dust underwent XRD analyses. The XRD analyses used the same milled samples that the XRF analyses used; however; the samples were further milled to roughly < 15 microns.

A spoonful of the milled sample was placed into the sample holder. Using a razor and a metal rod, the samples were pressed into the holder. The samples were analysed using a PANalytical Aeris powder diffractometer with a PIXcel detector and fixed divergence- and receiving slits with Fe filtered Co-Kα radiation(λ=1.789Å). The phases were identified using X'Pert Highscore plus software. The relative phase amounts (weight%) were estimated using the Rietveld method by means of the X'Pert Highscore plus software.

3.4 Inductively Coupled Plasma Mass Spectrometry (ICP-MS)

49 milled samples were sent to the University of Cape Town and the University of Witwatersrand for ICP-MS analysis. 50g of each milled sample was dissolved in a 4:1 ratio of HF/HNO3. The mixture was sealed and placed on a hotplate for 48 hours. The solution was evaporated until incipient dryness was achieved with added 2ml of concentrated HCl. The dried-out samples were taken up in a 5% HNO3 solution containing 10 ppb Re, Rh, In and Bi, used as internal standards. The samples were then tested using an Xseries2 Thermo Fischer machine with Argon as the carrier gas at 10ms dwell time. The calibration curves were determined by using artificial, multi-element standards.

3.5 Electron Microprobe Analyser (EMPA)

9 samples from 8 volcanoes were selected for electron microprobe analysis. Each selected sample was coated in carbon prior to measurement. Analysis was performed on a CAMECA SX 100 electron microprobe at the University of Johannesburg. An acceleration voltage of 20kV, a current of 20nA was used for quantitative spot analysis. Point measurements were set to 200 sec measure time. The elements Na, Mg, Si, K, Ca, Ti, Fe, Mn, Cr, Ni and Al was measured.

3.6 Isotopes

Isotope analysis was performed on selected samples of the BMVF, 10 samples were selected for Hf, Nd and Sr analysis and 6 samples were selected for Pb analysis due to limited sample material. The samples that were selected for Hf, Nd and Sr analysis were fresh basanites and a trachybasalt were free of secondary alteration, amygdales and xenoliths. All 10 samples were milled in an agate milling pot to avoid W contamination. The samples were leached of any carbonates and zeolites with 6N HCL. A solution of concentrated HF and HNO3 were used to dissolve the samples and contain all newly formed fluoride phases in solution. A concentrated HNO3 was used to remove all fluorides in solution. Ln Spec chemistry was used to separate the various isotope cuts. Six ~200g samples made up out of 2-4mm chips free of alteration, amygdales and xenoliths were handpicked and analysed for Pb isotopes. The sample chips were cleaned in an ultrasonic bath to get rid of any residual dust and particles. The Pb samples underwent two leaching steps of 3N HCl and 6HCl, respectively. After the leaching, the samples were placed in a 1:1 ratio of Hf and HNO3 solution on a hotplate at 120^{o}C overnight to be digested. HNO3 was added three times and allowed to dry out. Following Mainz chemistry, 2ml of 0.5N HBr was added to the samples and placed on a hotplate at 60^{o}C overnight. The samples were pipetted onto the columns, and the Pb isotopes were collected using chromatography. The measurement was done through isotope dilution on the Thermo-Finnigan Neptune MC-ICP-MS at the University of Cologne, Germany.

3.7 Maps and Images

Google Earth Pro and ArcMap 10 was used to collect satellite imagery and to create topographic maps respectively. A simplified geological map (Figure 2.2 C) of the BMVF was created on ArcGIS. The polygons of the geological map were hand drawn using satellite imagery and an incomplete orthophoto from Almond (1969) was used as reference material. A Wacom pen and tab were used to ensure polygons were accurately drawn. Polygons were geo-referenced to the WGS84 coordinate system. All geochemical graphs were plotted using GCDkit version 5 (El Chupacabra) and Microsoft Excel. Graphs created on GCDkit were then converted into vector files by overlaying polygons and lines in CorelDRAW (2019).

3.8 Dataset used for comparison

Geochemical comparison data for the selected Cenozoic volcanoes of North Africa and the Arabian Peninsula. All literature sources needed whole rock chemistry, trace element chemistry and Nd, Sr and Pb isotope chemistry to be considered for a relevant comparison to the BMVF.

- Meidob hills (Franz et al., 1999)
- Jebel Marra (Davidson and Wilson, 1989)
- Harrat Rahat (Moufti et al., 2012)

4 Results

4.1 Petrography of the BMVF

The 16 sampled (Figure 3.1) volcanoes are individually described by means of texture, phenocrysts, groundmass and vesicles distribution. Overall, the volcanic rocks of the BMVF are predominantly vesicular mafic lava flows and tephra deposits. The lavas display seriate textures with varying degrees of trachytic textures. Phenocrysts make up 30% of the lavas consisting of olivine, clinopyroxene and rarely brown-green spinel. Plagioclase, reaction rim baring quartz and the rare orthopyroxene are present as xenocrysts. In most cases, the clinopyroxene and olivine phenocrysts are the dominant phases in the samples analysed. All phenocrysts phases are present as anhedral, subhedral and euhedral crystals often cracked with various forms of zoning and resorption textures. Olivine and clinopyroxene phenocrysts show fracturing and undulose extinction indicating signs of strain. The groundmass of the lava flows predominantly consist of plagioclase laths and microcrysts of olivine, clinopyroxene, nepheline, brown spinel and interstitial magnetite with varying degrees of alignment. Sparsely distributed, magnetite rimmed, brown and rare green spinels are present throughout the BMVF as both phenocrysts and microcrysts. The microcrysts are usually fragments of the larger phenocryst. Spinel inclusions are common in olivine and clinopyroxene.

4.1.1 Volcano CC6

The sampled material is a mafic lava flow originating from volcano CC6 belongs to a lava flow. The sample displays a seriate and strong, localised trachytic texture. The phenocryst phase makes up 30% of the lava flow, the vesicles make up 5%, and the groundmass makes up to 65% of the lava flow. The phenocryst phases consist of olivine and clinopyroxene. Olivine phenocrysts are subhedral-euhedral ranging in size from 0.34-2.78mm, making up 15% of the phenocryst phase. Some olivines show embayment textures and minor fractures (Figure 4.1D). The clinopyroxene phenocrysts are subhedral-euhedral, ranging in size from 0.31-2.21mm, making up 15% of the phenocryst phase. The clinopyroxene phenocrysts host large, brown and smaller, green spinel inclusions (Figure 4.1F). The groundmass of the lava flow consists of aligned microcrysts of elongated tabular plagioclase, olivine, clinopyroxene, and interstitial magnetite. Magnetite crystals have a bimodal size distribution of ~10µm and ~40µm making up 10% of the lava flow. Some vesicles and cracks in phenocrysts partially filled by secondary carbonates (Figure 4.1E). Vesicles shapes range from rounded to elongate. They may be parallel to the flow direction. Generally, vesicles range in size from 0.09-2.88mm making up 10% of the lava flow.

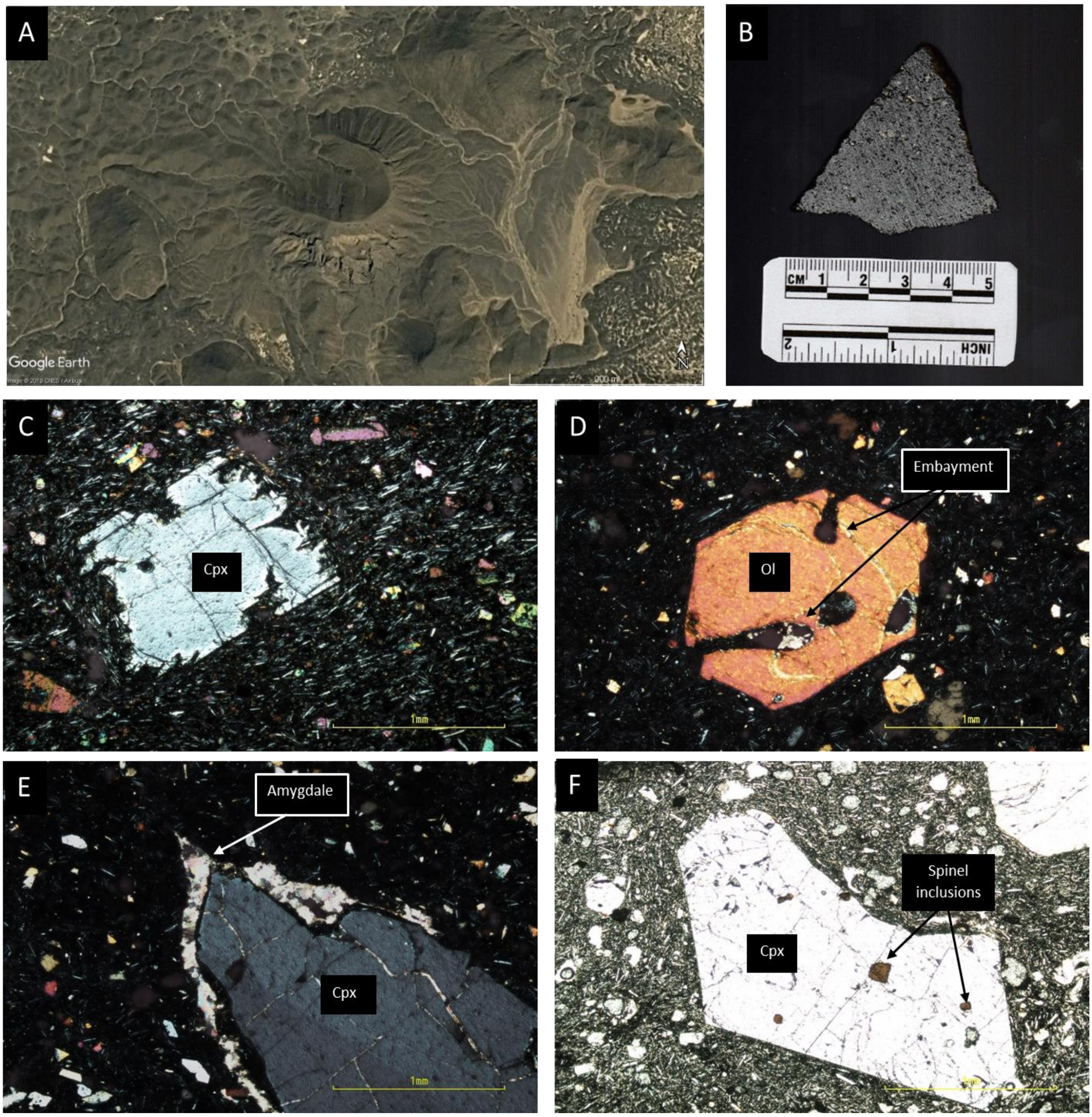

Figure 4.1: *A)* Satellite image of Volcano CC6. B) Sample B24 displaying porphyritic texture and phenocrysts of clinopyroxene. C) Micrograph displaying the seriate texture of the lava flow and a clinopyroxene with embayment textures. XPL (5x) D) Micrograph of an olivine with pronounced embayment textures. E) Clinopyroxene phenocryst surrounded by an amygdale. XPL (5x). F) Micrograph of brown spinel inclusions within a clinopyroxene phenocryst. PPL (10x).

4.1.2 Volcano CC7

The samples from volcano CC7 are sampled from a vesicular, mafic lava flow (Figure 4.2). The lava flow displays a seriate texture. The phenocryst phase makes up 25% of the lava flow, while vesicles amount to 20% of the lava flow, interstitial magnetite makes up 5% of the lava flow, and the groundmass makes up the remaining 50%. The phenocryst phase consists out of clinopyroxene and olivine. The clinopyroxene phenocrysts are anhedral-euhedral displaying embayment textures, undulose extinction, sector zoning and often contains fractures. The clinopyroxene crystals range in size from 0.33-1.79mm making up 20% of the lava flow. The olivine phenocryst phase is characterised by anhedral-subhedral shapes with minor embayment structures. Olivine phenocryst ranges in size from 0.56-0.64mm making up 5% of the lava flow. The groundmass of the samples consists of tabular plagioclase, clinopyroxene, magnetite and brown spinel microcrysts. Magnetite has a bimodal size distribution of ~10µm and ~33µm making up 5% of the lava flow. Sparsely distributed magnetite-rimmed spinel ranging in size from 53-92micrometer make up 1% of the lava flow. The vesicles are elongated but do not show preferential alignment and appear to be randomly distributed. The vesicles range in size from 0.08-5mm making up 20% of the lava flow.

4.1.3 Volcano CC9

The lava flow that erupted from volcano CC9 is vesicular, mafic, with a seriate texture, and minor localised trachytic texture (Figure 4.3). The phenocryst phase makes up 35% of the lava flow, the vesicles make up 10 % of the lava flow, and the groundmass makes up the remaining 55% of the lava flow. The phenocrysts phase is exclusively made up of clinopyroxene. The clinopyroxene phenocrysts are anhedral-euhedral displaying skeletal growth, sector zoning and embayment textures (Figure 4.3C). Clinopyroxene phenocrysts range in size from 0.34-0.7mm making up 15% lava flow. The groundmass is glassy with microcrysts of tabular plagioclase, clinopyroxenes, magnetite and magnetite rimed brown spinel. The magnetite crystals have a bimodal size distribution of ~10µm and ~30µm and makes up 2% of the lava flow. Magnetite rimmed spinels are a subordinate phase and have subhedral crystal habit. The magnetite rimmed spinels range in size from 39-215.81µm making up <1% of the lava flow. The spinels that occur as inclusions, do not possess the pronounced magnetite rim of the brown spinels in the groundmass. The vesicles are rounded and elongated with some alignment of flow. Some vesicles display secondary carbonate infilling. The size of the vesicles range from 0.1-0.5mm making up 10% of the lava flow.

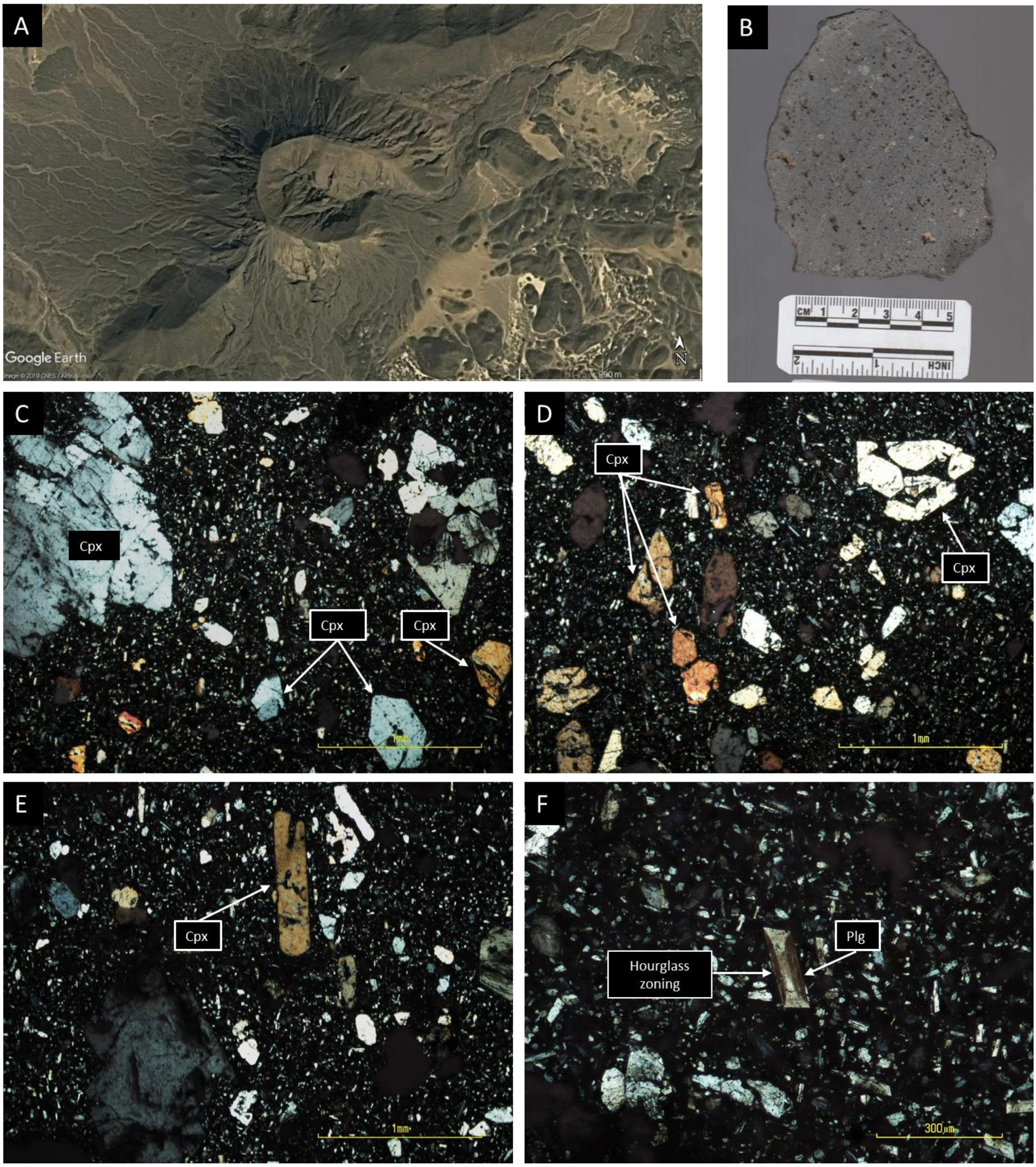

Figure 4.2: A) Satellite image of volcano CC7. B) Sample B is a vesicular basanite showing a porphyritic texture with clinopyroxene phenocrysts visible. C) Photomicrograph displaying several clinopyroxene microcrysts and a large clinopyroxene phenocryst. D) Clinopyroxene phenocryst and microcrysts. XPL (4x) magnification. E) Tabular clinopyroxene phenocrysts hosted in a glassy matrix. XPL (4x) magnification. F) Plagioclase displaying hourglass zoning. XPL (10x) magnification.

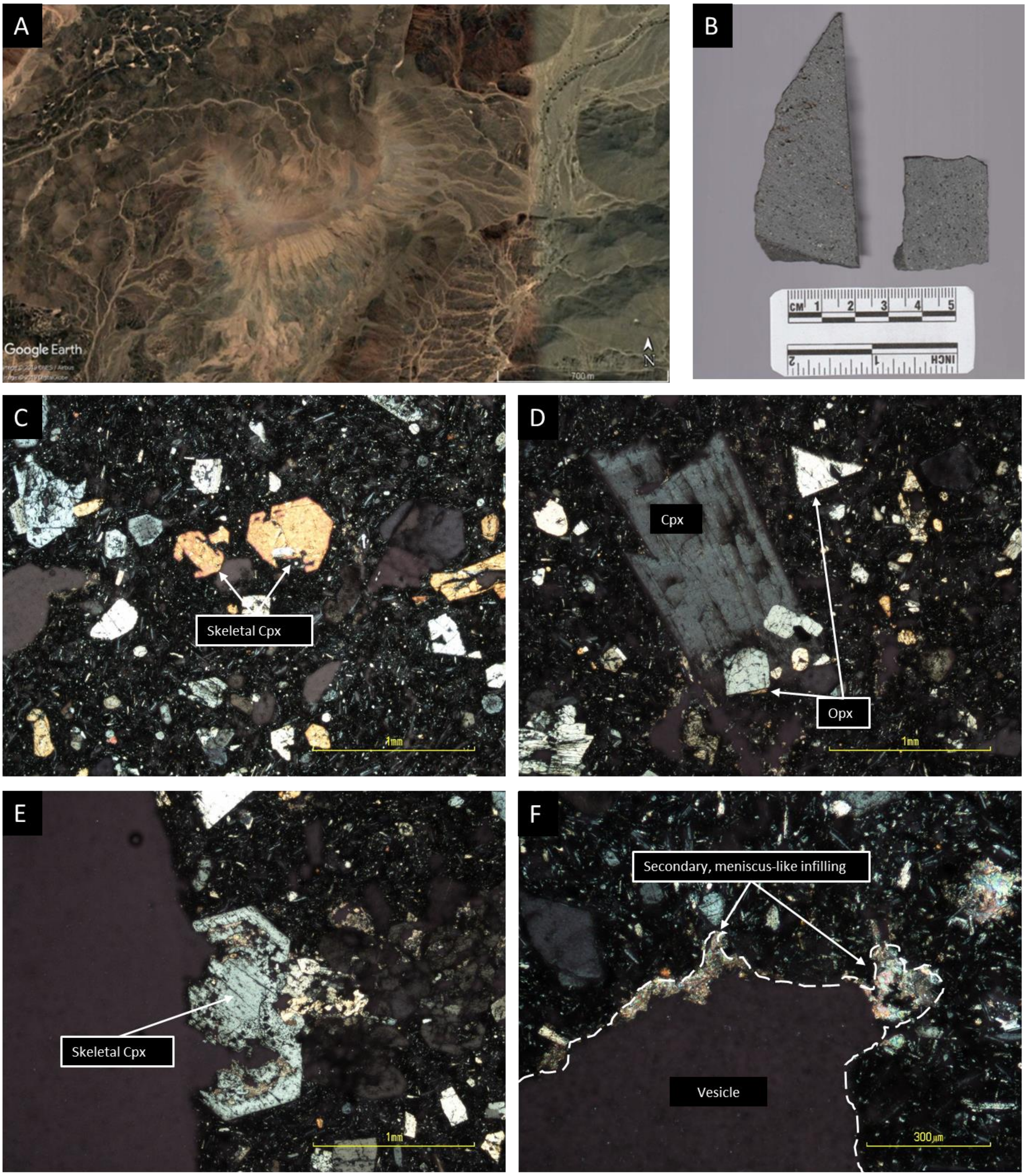

Figure 4.3: A) Satellite image of Volcano CC9. B) Photograph of the lava flow. The lava flow is a vesicular basanite with a porphyritic texture with minor amount of clinopyroxene phenocrysts. C) Photomicrograph showing the skeletal growth of clinopyroxene microcrysts. XPL (4x) magnification. D) Clinopyroxene oikocrysts with clinopyroxene chadacrysts. XPL (4x) magnification. E) Skeletal growth of clinopyroxene with secondary infilling of zeolites. XPL (4x) magnification. F) Vesicle displaying minor secondary infilling. XPL (10x) magnification

4.1.4 Volcano CC10

A vesicular mafic lava flow that erupted from volcano CC10 displaying a seriate texture with localised trachytic texture (Figure 4.4). The phenocryst phase makes up 30% of the lava flow, the vesicles make up 10%, and the groundmass makes up the remaining 60% of the lava flow. The phenocryst phase consists of olivine and clinopyroxene. Olivine phenocrysts are anhedral-subhedral often displaying elongated growth aligned with flow and high amounts of fracturing. The olivine phenocrysts range in size from 0.32-2.34mm, making up 15% of the lava flow. The clinopyroxene phenocrysts are anhedral-euhedral displaying skeletal growth (Figure 4.4E), sector zoning and sieve textures (Figure 4.4D. In several samples clinopyroxene appear as oikocrysts (Figure 4.4C). The clinopyroxene phenocryst range in size from 0.31-3.31mm making up 15% of the lava flow. The groundmass consists of sporadically aligned microcrysts of tabular plagioclase alongside olivine and clinopyroxene microcrysts. Magnetite crystals display bimodal size distribution of ~20µm and ~55µm making up 5% of the lava flow. The shape of the vesicles range between rounded and amorphous and often clustered around phenocrysts lacking flow alignment. The vesicles range in size from 0.05-0.67mm making up 10% of the lava flow.

4.1.5 Volcano CC44

The sample from volcano CC44 originates from a mafic lava flow that predominantly displays a seriate texture. Localised, a trachytic texture can be seen as well (Figure 4.5). The phenocrysts make up 25% of the rock, xenocrysts make up 2% of the rock while vesicles make up 15% of the lava flow, and the groundmass makes up the remaining 53% of the lava flow. The phenocryst phase exclusively consists of clinopyroxene and the accessory phenocrysts phase consist of plagioclase and minor garnet. The clinopyroxene phenocrysts are anhedral-subhedral displaying pronounced sieve textures (Figure 4.5E), minor skeletal growth and embayment textures. The clinopyroxenes range in size from 0.32-1.17mm making up 25% of the lava flow. Plagioclase xenocrysts are anhedral and moderately weathered displaying weak albite twinning. Plagioclase xenocrysts range in size from 0.34-0.52mm making up 2% of the lava flow. A single 0.27mm, brown subhedral spinel present. The lava flow contains two crystals with a vermicular texture, a garnet and a clinopyroxene crystal. The garnet displays a kelyphite reaction rim (Figure 4.5F) and the clinopyroxene displays intergrowths of unknown minerals. The lava flow also contains several plagioclase xenoliths (Figure 4.5C) ranging in size from 0.46-1.78mm and making up <1% of the lava flow. The xenoliths consist of interlocking crystals of coarse plagioclase and large magnetite crystals. The groundmass consists of microcrysts of tabular plagioclase, clinopyroxene, and magnetite. Magnetite crystals range in size from (3.5-33µm) and make up 2% of the lava flow. Vesicles are amoeboid-shaped and moderately aligned with the flow. The vesicles range in size from 0.002-0.43mm making up 20% of the lava flow.

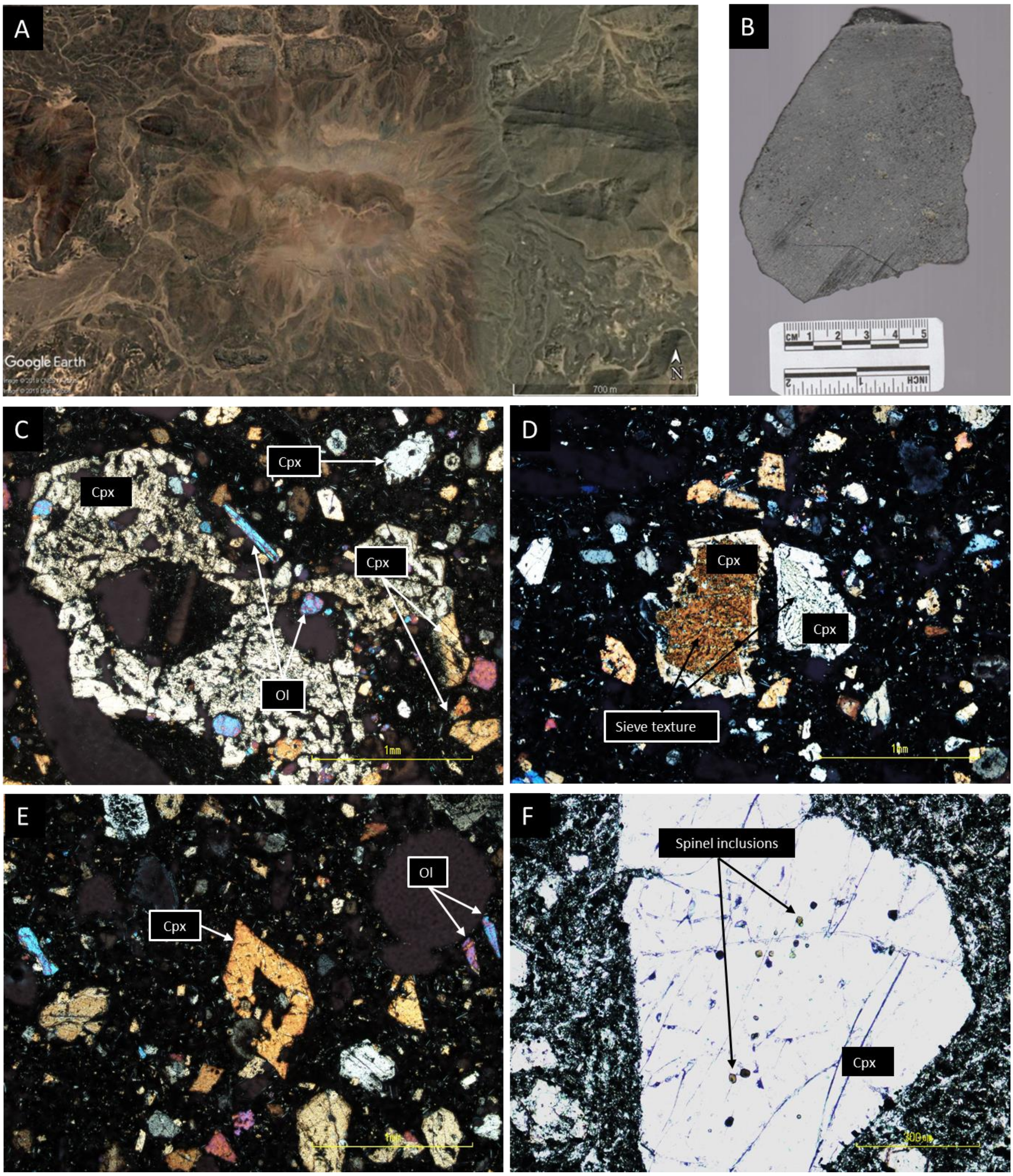

Figure 4.4: A) Satellite image of Volcano CC10. B) Sample B is a vesicular basanite displaying a porphyritic texture and several phenocrysts of clinopyroxene and olivine. C) Large clinopyroxene oikocryst with olivine and pyroxene chadacrysts. XPL (4x) magnification. D) Clinopyroxene phenocrysts displaying distinct sieve textures. XPL (4x) magnification. E) Skeletal growth of a subhedral clinopyroxene with a large central embayment and tabular olivine microcrysts. XPL (4x) magnification. F) Large subhedral clinopyroxene phenocryst with several green spinel inclusions. PPL (10x) magnification.

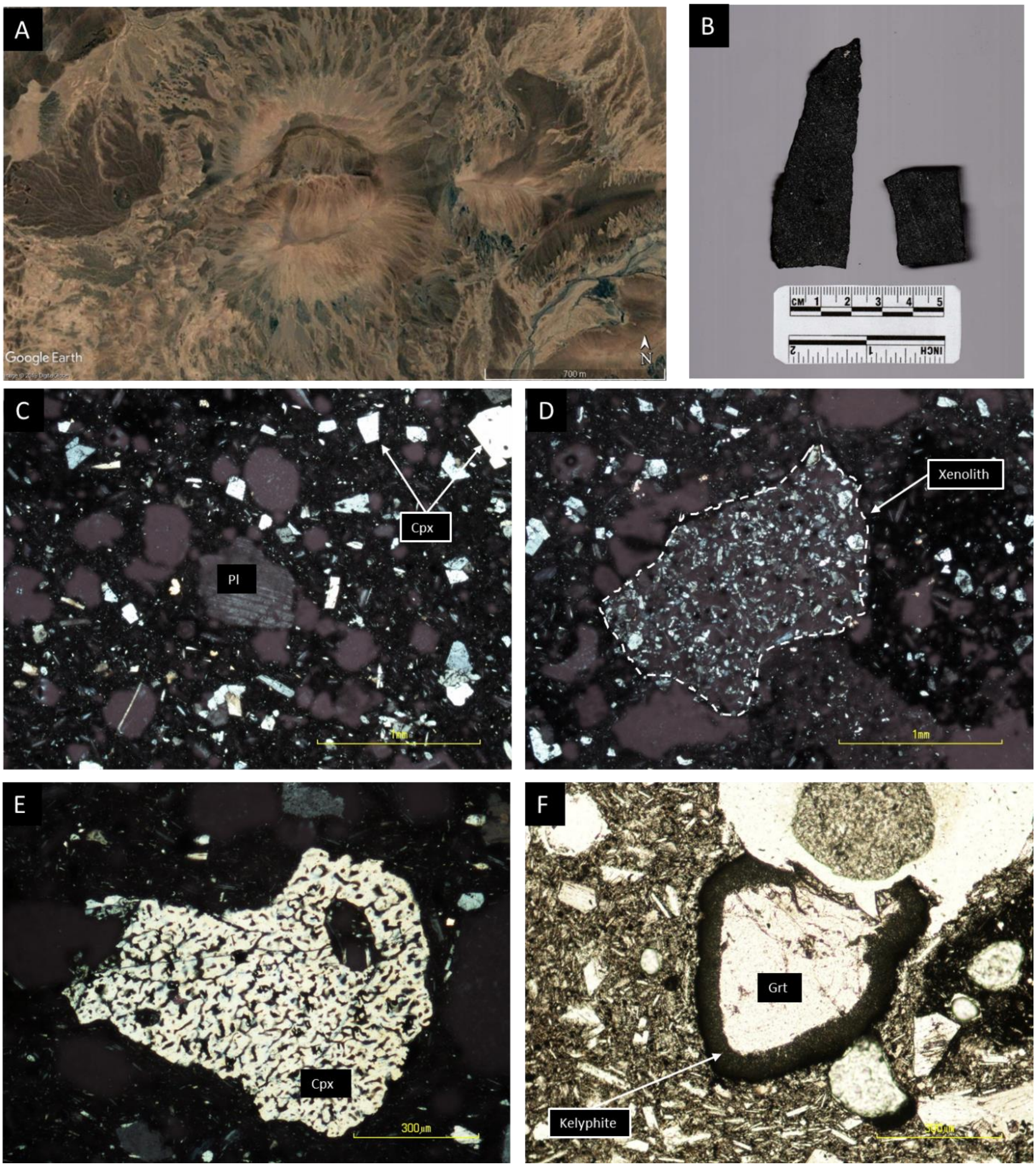

***Figure 4.5**:* A) Satellite image of Volcano CC44. B) Sample B is highly vesicular displaying a porphyritic texture with clinopyroxene phenocrysts and minor amygdales. C) Photomicrograph displaying a large population of vesicles and a plagioclase microcryst. XPL (4x) magnification. D) A xenolith, demarcated by the dashed line, with a notably more crystalline appearance. XPL (4x) magnification. E) Clinopyroxene phenocryst with a coarse sieve texture. XPL (10x) magnification. F) A garnet xenocryst with a kelyphite reaction rim. XPL (10x) magnification.

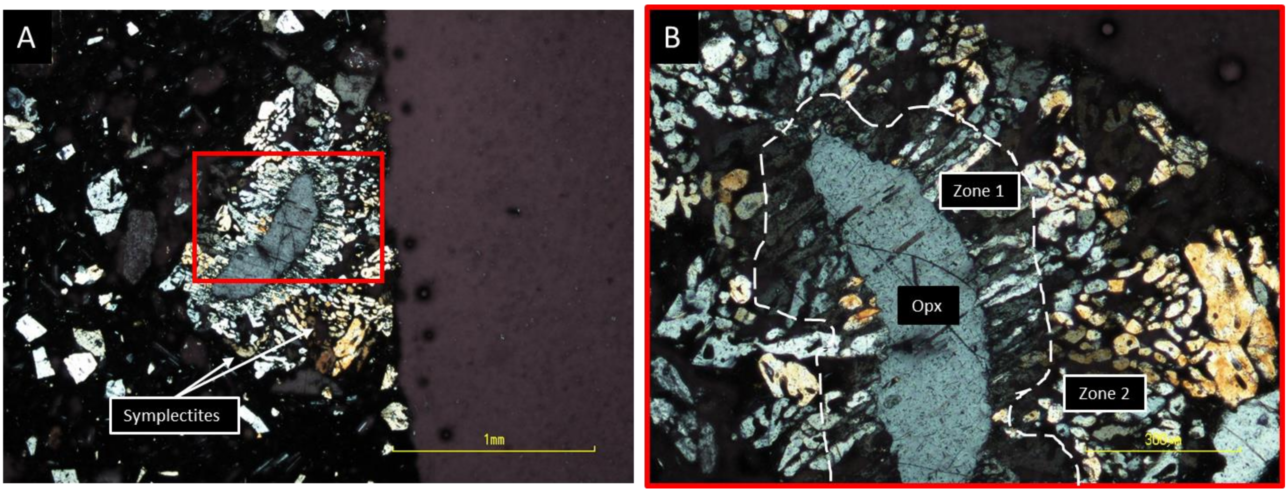

Figure 4.6 A) Micrograph of an orthopyroxene xenocryst surrounded by symplectites hosted in Volcano CC44. XPL (4x) magnification. B) The red rectangle in in Figure 4.6A was observed in a higher magnification to produce Figure 4.6B. Figure 4.6B shows that there are two zones of Symplectites. Zone 1: consists of closely packed linear intergrowths. Zone 2 consist of large globular intergrowths. XPL (10x) magnification.

4.1.6 Volcano CC48

The samples of volcano CC48 belong to a vesicular mafic lava flow displaying a seriate and trachytic textures (Figure 4.7). The phenocryst phase makes up 35% of the lava flow, the vesicles make up 15% of the lava flow, and the groundmass makes up the remaining 50% of the lava flow. The phenocryst phase consists out of olivine, clinopyroxene and brown spinel. Minor orthopyroxene and plagioclase xenocrysts make up a negligible portion of the rock. The olivine phenocrysts are anhedral-euhedral and show small embayment textures (Figure 4.7E). The olivine phenocrysts range in size from 0.44-3.1mm and make up 5% of the lava flow. Clinopyroxene phenocrysts have anhedral-subhedral crystal habit with opaque inclusions and often-displaying sieve textures (Figure 4.7E). Clinopyroxene phenocrysts range in size from 0.32-5.1mm making up 15% of the lava flow. The orthopyroxene phenocrysts are anhedral with minor embayment textures. A single,1.1mm grain of a clinopyroxene rimmed orthopyroxene visible within the lava flow (Figure 4.7C) forms part of the lava flow. The groundmass consists of tabular plagioclase and microcrysts of clinopyroxene, olivine and magnetite. Magnetite crystals have a bimodal size distribution of ~15µm and ~25µm making up 3% of the lava flow. The vesicles have a rounded-elongated shape and show strong alignment with the flow direction of the groundmass. Some of the vesicles have minor secondary infilling of secondary carbonate minerals. The vesicles range in size from 0.05-2.23mm and make up 15% of the lava flow.

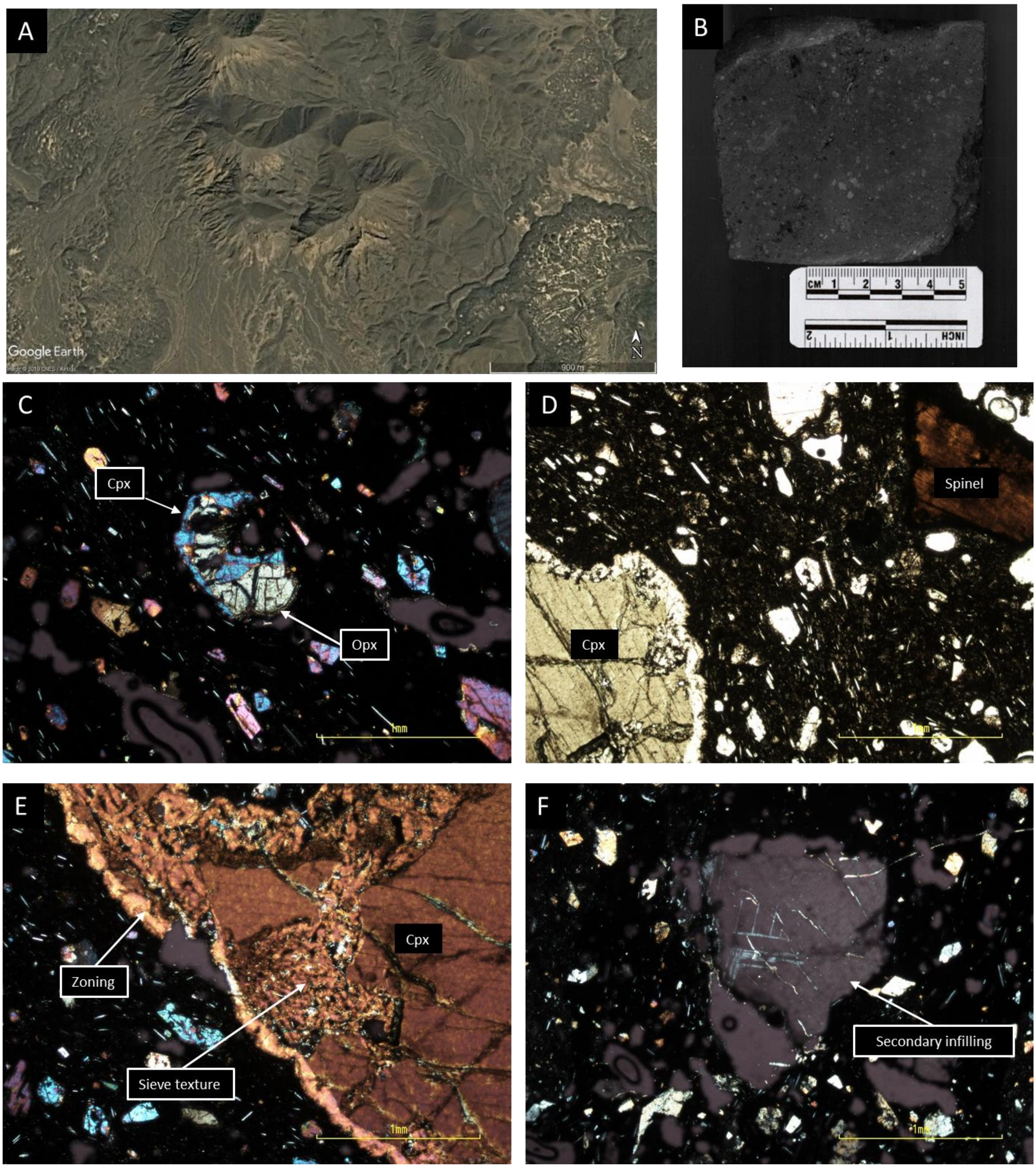

Figure 4.7: A) Satellite image of Volcano CC48. B) Sample II-2 is a vesicular basanite with a porphyritic texture displaying phenocrysts of clinopyroxene and olivine. C) Clinopyroxene and orthopyroxene intergrowth. XPL (4x) magnification. D) Large green clinopyroxene and magnetite rimmed, brown spinel phenocryst. PPL (4x) magnification. E) Large clinopyroxene phenocrysts displaying a coarse sieve texture as well as zoning. XPL (4x) magnification. F) A vesicle with secondary infilling. XPL (4x) magnification

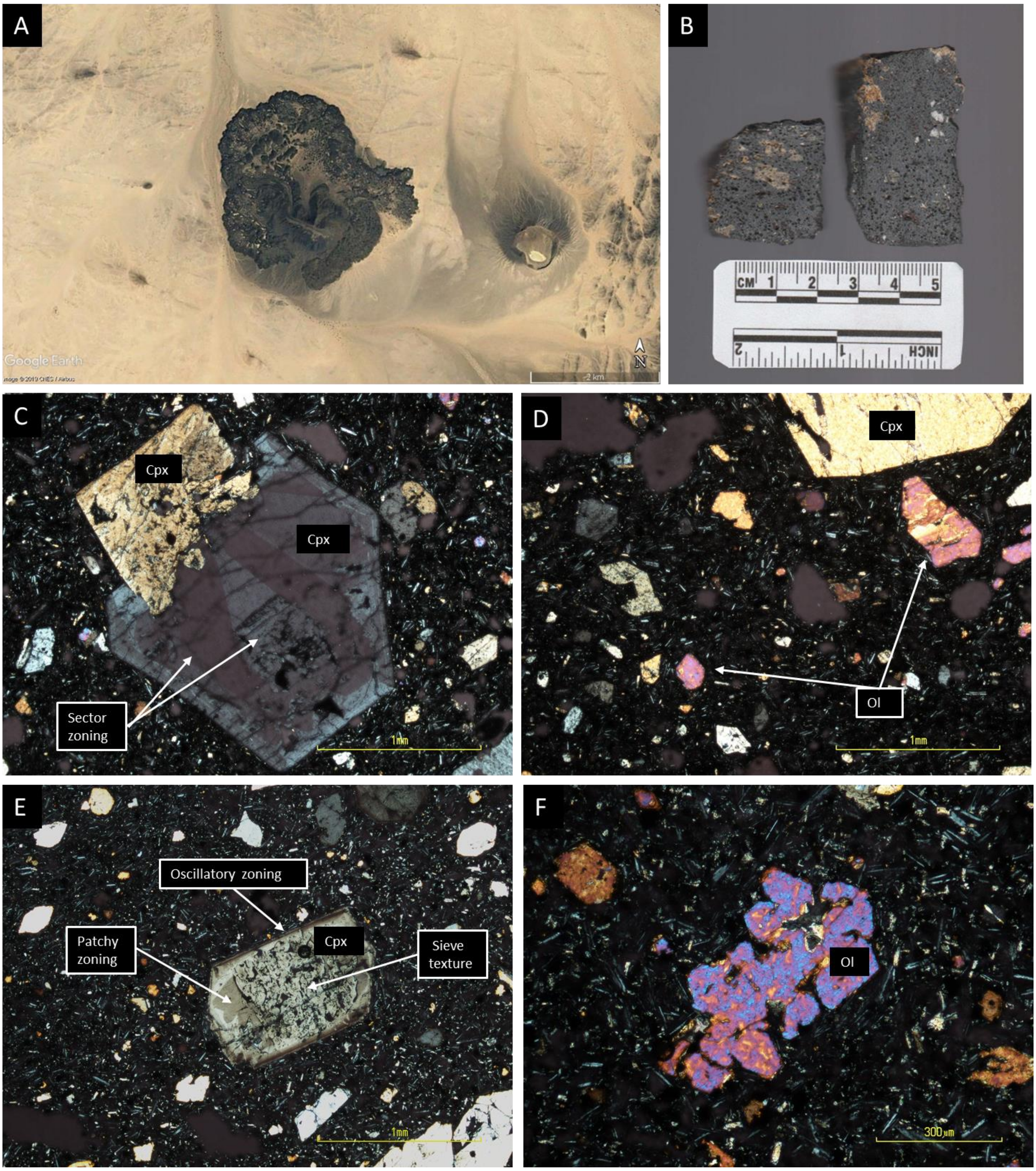

***Figure 4.8**: A) Satellite image of Volcano CC53. B) Sample B25 is a moderately vesicular basanite displaying a porphyritic texture with clinopyroxene phenocrysts and minor amygdales. Weathering mottles are also visible on the Sample B25. C) Large phenocryst of intergrown clinopyroxene and clinopyroxene anomalous birefringence. XPL (4x) magnification. D) A large clinopyroxene phenocrysts with minor embayments and several minor olivine microcrysts. XPL (4x) magnification. E) Clinopyroxene phenocryst displaying a sieve texture, sector zoning as well as oscillatory zoning. XPL (4x) magnification. F) Skeletal growth of an olivine microlite. XPL (10x) magnification.

4.1.7 Volcano CC53

A vesicular mafic lava flow that erupted from volcano CC53 displaying a seriate and minor trachytic texture (Figure 4.8). The phenocrysts phase makes up 35% of the lava flow, the vesicles make up 20% of the lava flow, and the groundmass makes up the remaining 45%. The phenocryst phase consists out of olivine and clinopyroxene. The olivine phenocrysts are anhedral-subhedral, displaying skeletal growth (Figure 4.8F) and embayment textures. The olivine phenocrysts range in size from 0.36-1.68mm making up 15% of the lava flow. Clinopyroxene phenocrysts are anhedral-euhedral displaying sieve textures and intricate zoning patterns (Figures 4.8C and E). The clinopyroxene phenocrysts range in size from 0.32-2.13 mm making up 20%. Only one 0.36 mm plagioclase xenocryst was observed forms part of the mineral assemblage. The groundmass consists out of tabular plagioclase and microcrysts of clinopyroxene, olivine, magnetite and spinel. Magnetite has a bimodal size distribution of 17µm and 30µm making up 5% of the lava flow. The brown spinels rimmed by magnetite range in size from 0.10-0.31mm making up <1% of the lava flow. The vesicles of volcano CC53 have an elongated shape and is aligned with the flow of the lava. Some vesicles are partially filled by a secondary infilling of goethite. Vesicles range in size from 0.06-2.29 mm making up 20% of the lava flow.

4.1.8 Lava flow: DX1

A vesicular mafic lava flow DX1, originating from an unknown volcano displaying a seriate and localised trachytic texture (Figure 4.9). The phenocrysts phase makes up 30% of the lava flow, the vesicles make up 3% of the lava flow, and the groundmass makes up the remaining 67% of the lava flow. The phenocryst phase consists out of olivine, clinopyroxene, and subordinate brown spinels. The olivine phenocrysts are anhedral-euhedral with minor embayment structures. Olivine phenocryst range in size from 0.39mm-3.2mm, making up 15% of the lava flow. Clinopyroxene phenocrysts are subhedral-euhedral displaying skeletal growth, oscillatory zoning, sieve textures (Figure 4.9D) and minor embayment textures. Clinopyroxenes range in size from 0.31-4.9 mm making up 15% of the lava flow. Spinel crystals are anhedral-subhedral and are rimmed by magnetite. The spinels range in size from 0.06-0.34 mm making up 1% of the lava flow. The groundmass consists out of weakly aligned microcrysts of tabular plagioclase, olivine, clinopyroxene, magnetite and spinel. Magnetite has a bimodal size distribution of ~15µm and ~25µm and makes up 5% of the lava flow. Sections of needle like growth are visible throughout the thin section (Figure 4.10). Needles range in size from ~15µm to ~43µm. The needles most likely represent hopper olivines. The vesicles of the lava flow are amorphous and show no preferred alignment. The vesicles range in size from 0.04-0.061 mm making up 3% of the lava flow.

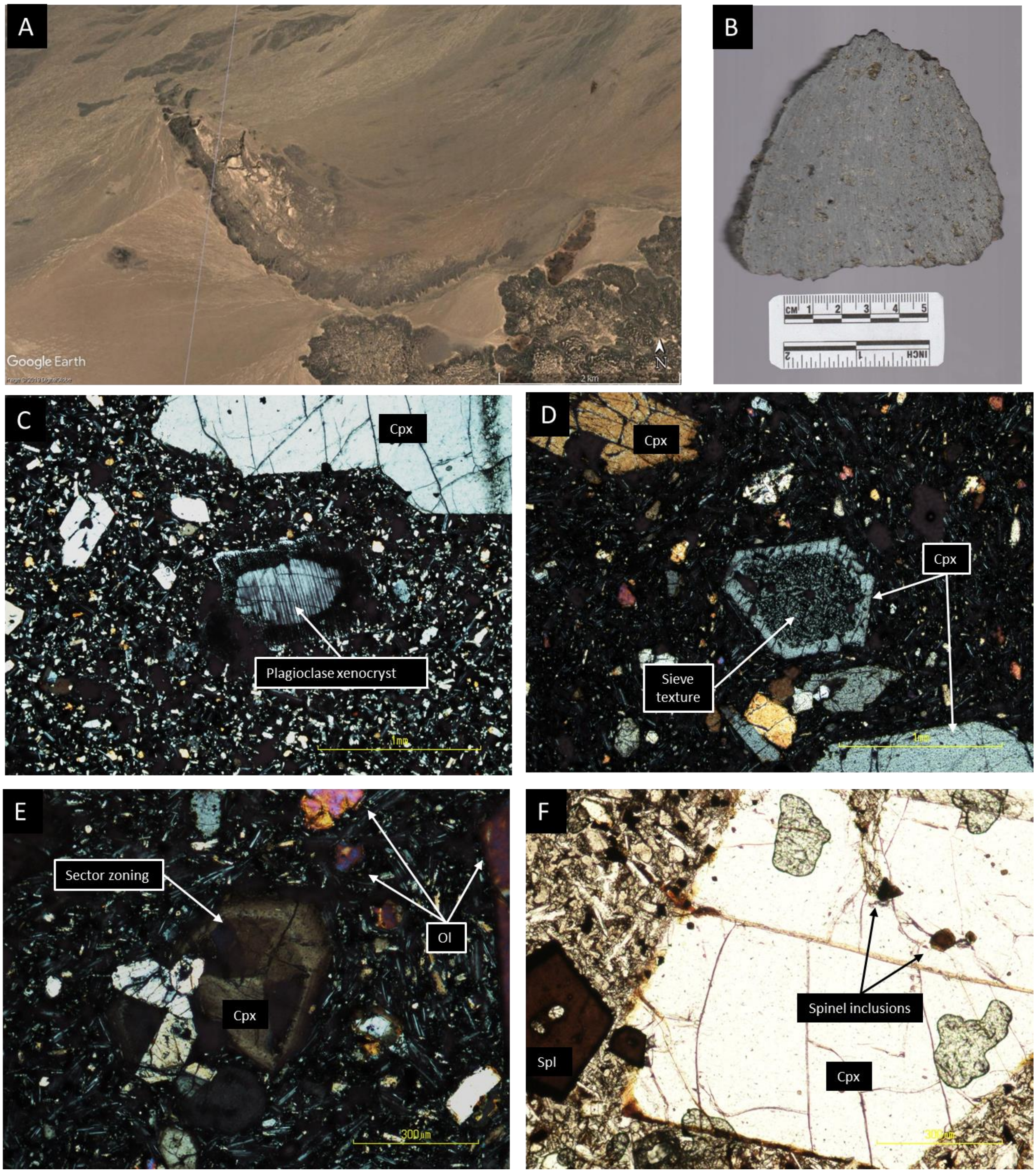

Figure 4.9: Satellite image of unknown lava flow DX1. B) Sample B10 has a porphyritic texture with minor vesicles and large clinopyroxene and olivine phenocrysts. C) Plagioclase xenocryst with albite twinning and a reaction rim. XPL (4x) magnification. D) Clinopyroxene phenocrysts that displays a pronounced sieve texture alongside microlites of clinopyroxene and nepheline. XPL (4x). E) Clinopyroxene microlite with sector zoning alongside olivine microlites. XPL (10x) magnification. F) Spinel phenocrysts rimmed with magnetite alongside clinopyroxene phenocryst with spinel inclusions.

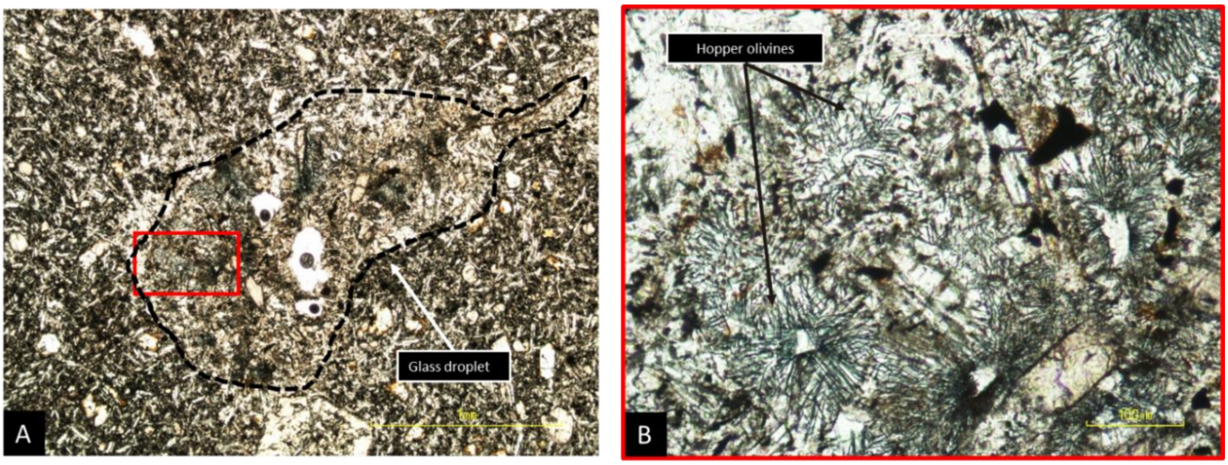

Figure 4.10: A) A micrograph of a glass droplet enveloped in a lava flow. PPL (4x) magnification. B) close up of the indicated red area in Figure 4.10A. The photomicrograph displays the needle-like growth of the hopper olivines

4.1.9 Lava flow: DX2

Material from lava flow DX1 are mafic and vesicular that displays a seriate and localised trachytic texture (Figure 4.11). The phenocryst phase makes up 35% of the lava flow, the vesicles make up 5% of the lava flow, the groundmass makes up the remaining 60% of the lava flow. The phenocryst phase consists out of olivine and clinopyroxene. The olivine phenocrysts are subhedral-euhedral and highly fractured (Figure 4.11D) with occasional spinel inclusions. The olivine phenocrysts range in size from 0.32-4.8mm, making up 20% of the lava flow. Clinopyroxenes are subhedral-euhedral, highly fractured (Figure 4.11D) displaying sieve textures (Figure 4.11F) and melt inclusions. Clinopyroxene phenocrysts range in size from 0.34-4.5 mm making up 15% of the lava flow. The groundmass phase consists of microcrysts of tabular plagioclase, olivine, clinopyroxene, magnetite and brown spinel displaying moderate flow alignment. The magnetite crystals have a bimodal size distribution of ~15 µm and ~25 µm. The brown spinels are anhedral-subhedral and rimmed by magnetite (Figure 4.11E). Brown spinel crystals range in size from 0.1-0.4 mm making up <1% of the lava flow. The vesicles of the lava flow have an amorphous-rounded shape and display no alignment with the groundmass. The vesicles range in size from 0.02– 0.42 mm and make up 5% of the lava flow.

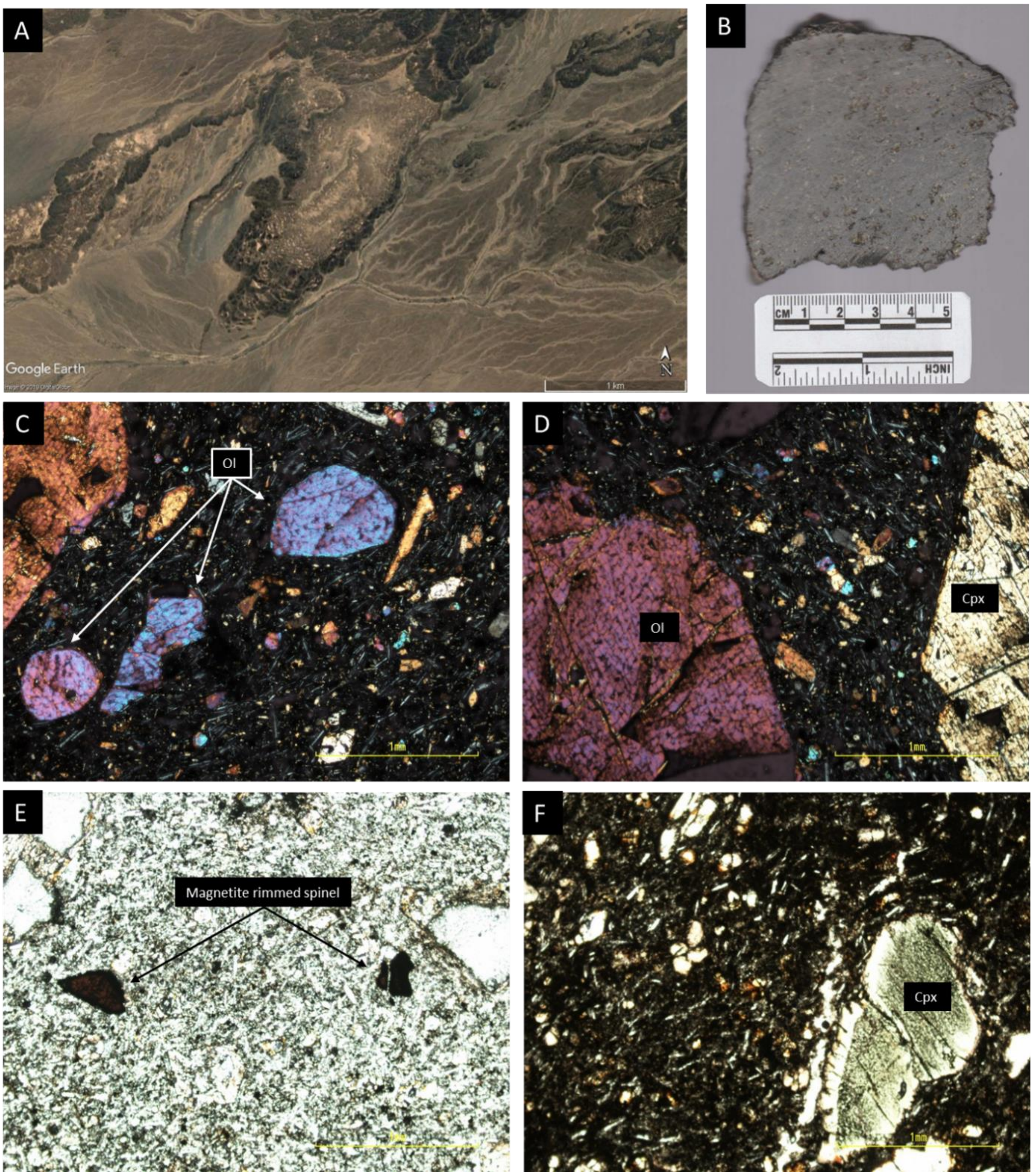

Figure 4.11: A) Satellite image of the unknown lava flow DX2. B) Sample B09 is a moderately vesicular basanite displaying a porphyritic texture with olivine and clinopyroxene phenocrysts. C) A tabular and rounded olivine phenocryst displaying flow alignment. XPL (x4) magnification. D) Highly fractured olivine and clinopyroxene phenocryst. XPL (x4) magnification. E) Brown spinel microcryst with a magnetite rim PPL (4x) magnification. F) Green clinopyroxene displaying a pronounced sieve texture. PPL (4x) magnification.

4.1.10 Lava flow: DX3

The vesicular mafic lava flow DX3, that originated from an unknown volcano, displays a seriate texture (Figure 4.12). The phenocrysts phase makes up 35% of the lava flow, the vesicles make up 5% of the lava flow, and the groundmass makes up the remaining 62% of the lava flow. The phenocrysts phase consists out of clinopyroxene and olivine. All phenocrysts display brown weathering rim (Figure 4.12D). Clinopyroxene phenocrysts are anhedral-subhedral with embayment textures and spinel inclusions. Clinopyroxene phenocrysts range in size from 0.3-4.1mm, making up 25% of the lava flow. The olivine phenocrysts are subhedral-euhedral displaying skeletal growth and embayment texture (Figure 4.12F). Olivines phenocrysts range in size from 2.5 mm-0.5 mm making up 10% of the lava flow. The groundmass of the lava flow consists out of microcrysts of tabular plagioclase, clinopyroxene, olivine and magnetite. Magnetite has a bimodal size distribution of 10 and 30 making up 2% of the lava flow. Spinels are subhedral and often present as inclusions in the larger phenocrysts. The spinels range in size from 0.1-0.2 mm making up 1% of the lava flow. Vesicles are amorphous to round with no alignment to flow. The vesicles range in size from 10-100 μm making up 5% of the lava flow.

4.1.11 Volcano M3

The vesicular mafic lava flow sampled from Volcano M3 displays a seriate texture. A moderate trachytic texture can also be seen (Figure 4.13). The phenocrysts make up 30 % of the rock, the vesicles make up 10 %, and the groundmass makes up 60 % of the rock. The phenocrysts exclusively consist of clinopyroxenes, often as a glomerocryst. Clinopyroxene phenocrysts are anhedral-euhedral and highly fractured fragments. Clinopyroxene phenocrysts range in size from in size from 0.3-0.71 mm, making up 30% of the lava flow. The groundmass is glassy and consists out of microcrysts of tabular plagioclase, clinopyroxene and magnetite. Magnetite displays bimodal size distribution of 10 μm and 35 μm making up 3% of the lava flow. The vesicles are amorphous ranging in size from 0.04-0.17mm making up 10% of the lava flow.

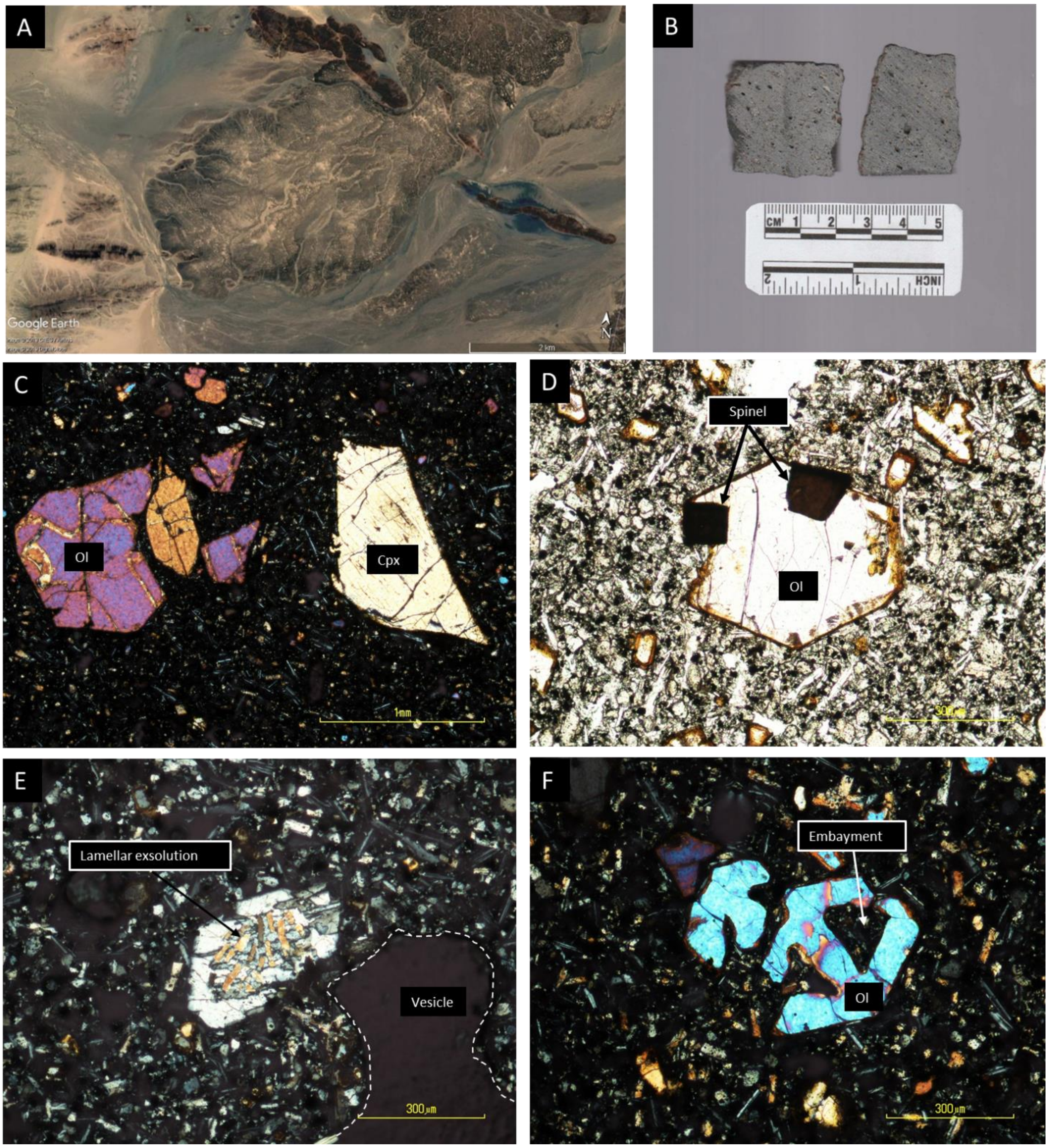

Figure 4.12: A) Satellite image of unknown lava flow: DX3. B) Sample B11 is a vesicular basanite displaying a porphyritic texture with minor phenocrysts of clinopyroxene visible. C) Phenocrysts of olivine and clinopyroxene alongside microcrysts of olivine and clinopyroxene. XPL (4x) magnification. D) A microlite of a euhedral olivine with brown spinel inclusions and a secondary weathering rim. PPL (10x) magnification. E) Grain displaying exsolution. XPL (10x) magnification. F) A skeletal olivine microlite with prominent embayments. XPL (10x) magnification.

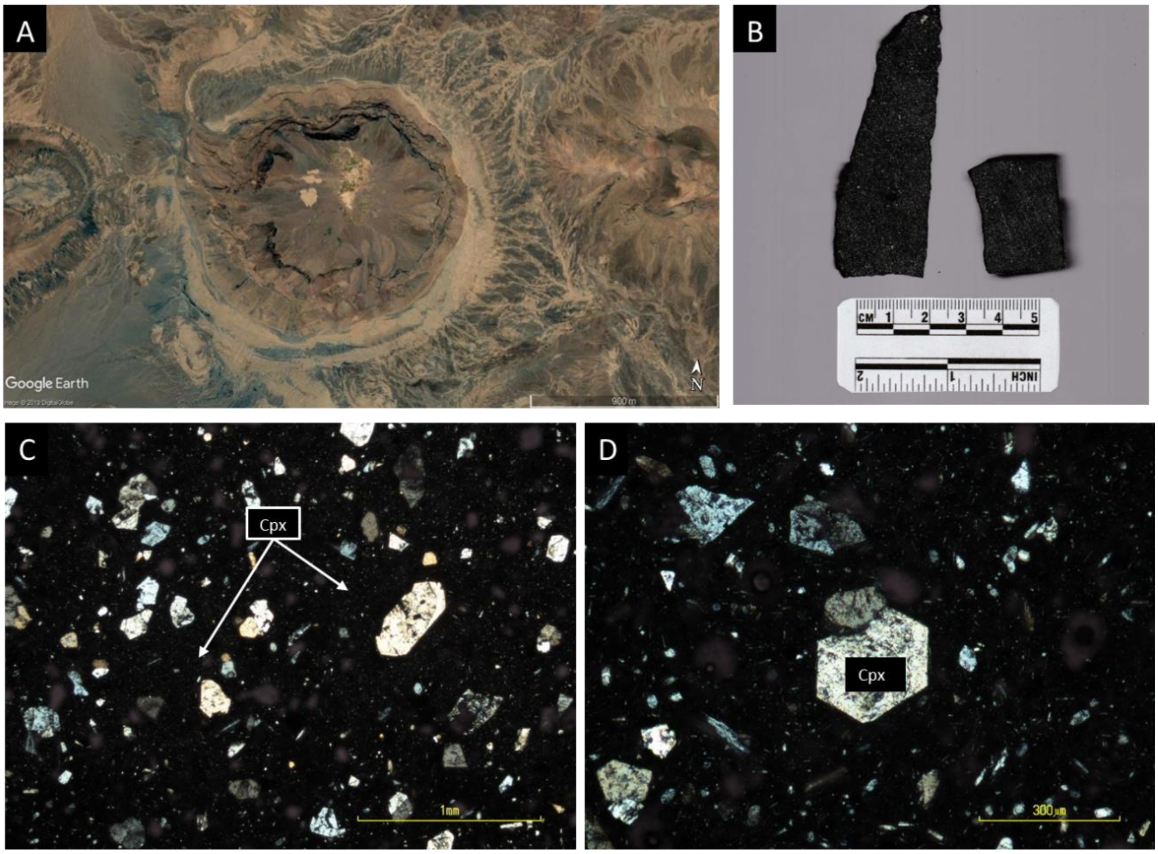

***Figure 4.13**:* A) satellite image of Volcano M3. B) Sample: B13 is a highly vesicular rock with minor amygdales. C) Minor subhedral microlites of clinopyroxene. XPL (4x) magnification (D) Euhedral clinopyroxene microcryst. XPL (10x) magnification.

4.1.12 Volcano M5

The sampled material is vesicular mafic lava flow that from erupted from volcano M5, and displays a seriate and trachytic textures (Figure 4.14). The phenocrysts phase makes up 35% of the lava flow, xenocrysts make up 1% of the lava flow, the vesicles make up 15% of the lava flow, and the groundmass makes up the remaining 49% of the lava flow. The phenocrysts phase consists out of clinopyroxene, olivine and minor brown spinel. Several glomerocryst present as clusters of phenocryst constituents (Figure 4.14D). Clinopyroxene phenocrysts are subhedral-euhedral displaying minor skeletal growth embayment textures (Figure 4.14C). Clinopyroxene phenocrysts range in size from 0.32-5.9 mm, making up 30% of the lava flow. Olivine phenocrysts are anhedral-euhedral where the anhedral olivines are fragments of euhedral olivines. Olivine phenocrysts range in size from 0.34-0.78mm making up 5% of the lava flow. Plagioclase phenocrysts are anhedral and moderately weathered. Plagioclase xenocrysts range in size from 0.43-0.64 mm making up 1% of the lava flow. A single 0.35 mm rounded, green, magnetite rimmed spinel is one of two green spinel phenocrysts found during this study. The groundmass consists of tabular plagioclase and microcrysts of clinopyroxene, olivine, spinel and interstitial magnetite. Magnetite ranges in size from ~10 µm to ~40 µm making up 2% of the lava flow. Groundmass magnetite rimmed spinels are predominantly brown displaying anhedral-euhedral crystal habits. Spinel crystals as inclusions in the larger phenocrysts are not rimmed by magnetite (Figure 4.14F). Brown spinels range in size from 34 µm-94 µm making up 2% of the groundmass. The vesicles range from amorphous-rounded in shape displaying minor alignment with the lava flow. Vesicles are in some cases partially filled by secondary carbonates. Vesicles range in size from 0.08-1.22 mm making up 15% of the lava flow.

4.1.13 Volcano M6

A vesicular mafic lava flow originating from the volcano M6 displays a seriate texture and minor localised trachytic texture (Figure 4.15). The phenocrysts phase makes up 40 % of the lava flow, the vesicles make up 10% of the lava flow, and the groundmass makes up the remaining 50% of the lava flow. The phenocryst phase consists out of olivine, clinopyroxene and brown spinel. Olivine phenocrysts are subhedral-euhedral displaying fractures and minor embayment textures (Figure 4.15D). The olivine phenocrysts range in size from 0.37-2.66 mm, making up 15% of the lava flow. The clinopyroxene phenocrysts are subhedral-euhedral displaying sector and oscillatory zoning alongside pronounced embayed textures and fracturing (Figure 4.15E). Clinopyroxene phenocrysts range in size from 0.33-3.9mm making up 25% of the lava flow. A singular anhedral green spinel 0.88 mm forms part of the phenocryst phase and is one of only 2 green spinel phenocrysts found in this study (Figure 14.5C). The groundmass is often glassy and shows flow alignment (Figure 15.E and F). The groundmass consists out of microcrysts of tabular plagioclase, olivine, clinopyroxene, interstitial magnetite and minor spinel. Magnetite has a modal size distribution of ~15µm making up 2% of the lava flow. Brown subhedral-euhedral spinels range in size from 56-230µm making up <1% of the lava flow. The vesicle shapes are predominantly amorphous and often clustered around phenocrysts (Figure 4.15 D). the vesicles range in size from 0.06-0.64 mm making up 10% of the lava flow.

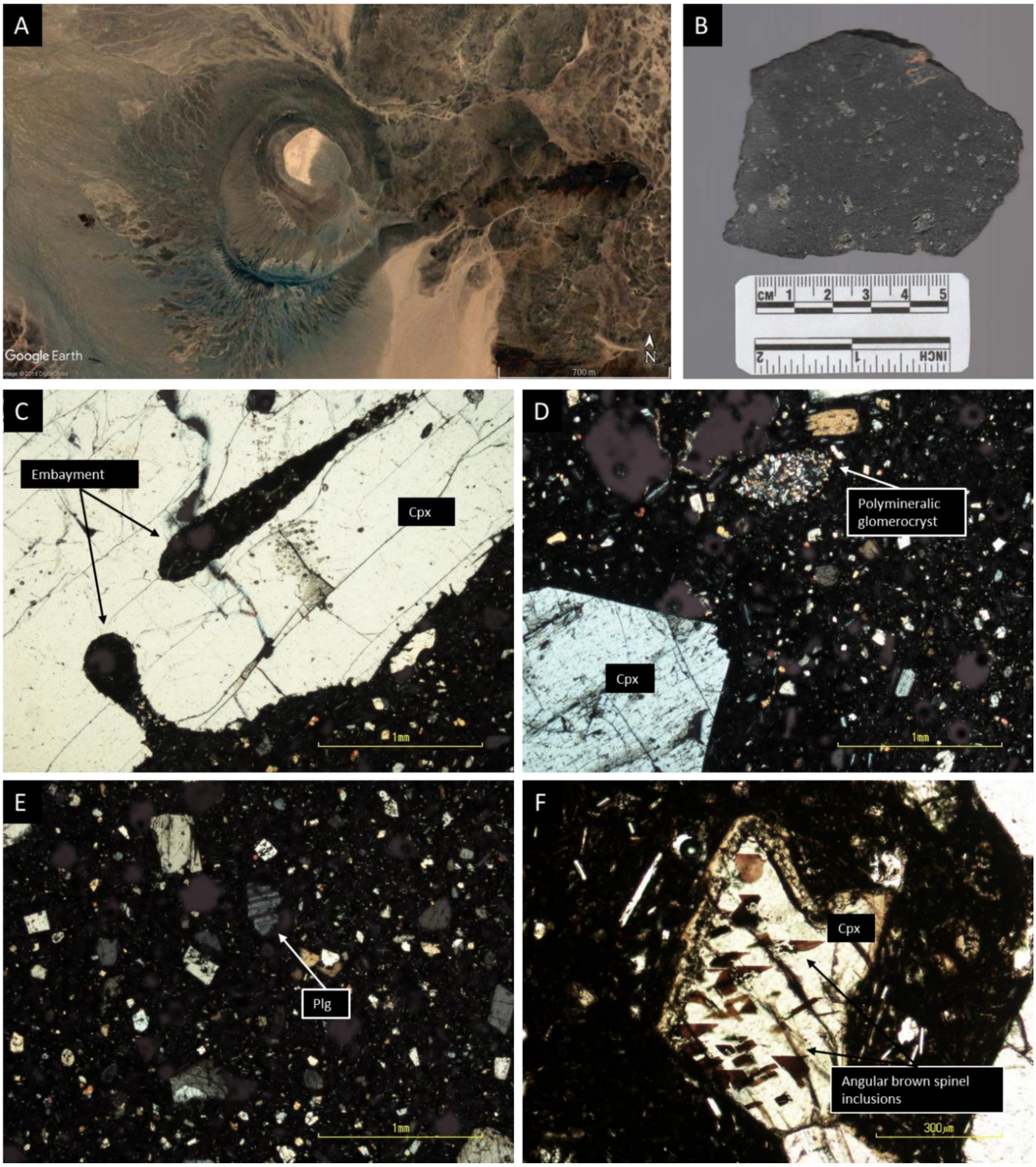

Figure 4.14: A) Satellite image of Volcano M5. B) Sample B21 is a basanite with minor vesicles and a porphyritic texture. The phenocrysts consist of large clinopyroxenes and olivines. C) A large clinopyroxene with large embayments. XPL (4x) magnification. D) A large clinopyroxene phenocryst with a glomerocryst consisting of several minerals. XPL (4x) magnification. E) A collection of microcryst, with the plagioclase microcryst being the most prominent. XPL (4x) magnification. F) A clinopyroxene phenocryst with several, angular brown spinel inclusions. PPL (10x) magnification.

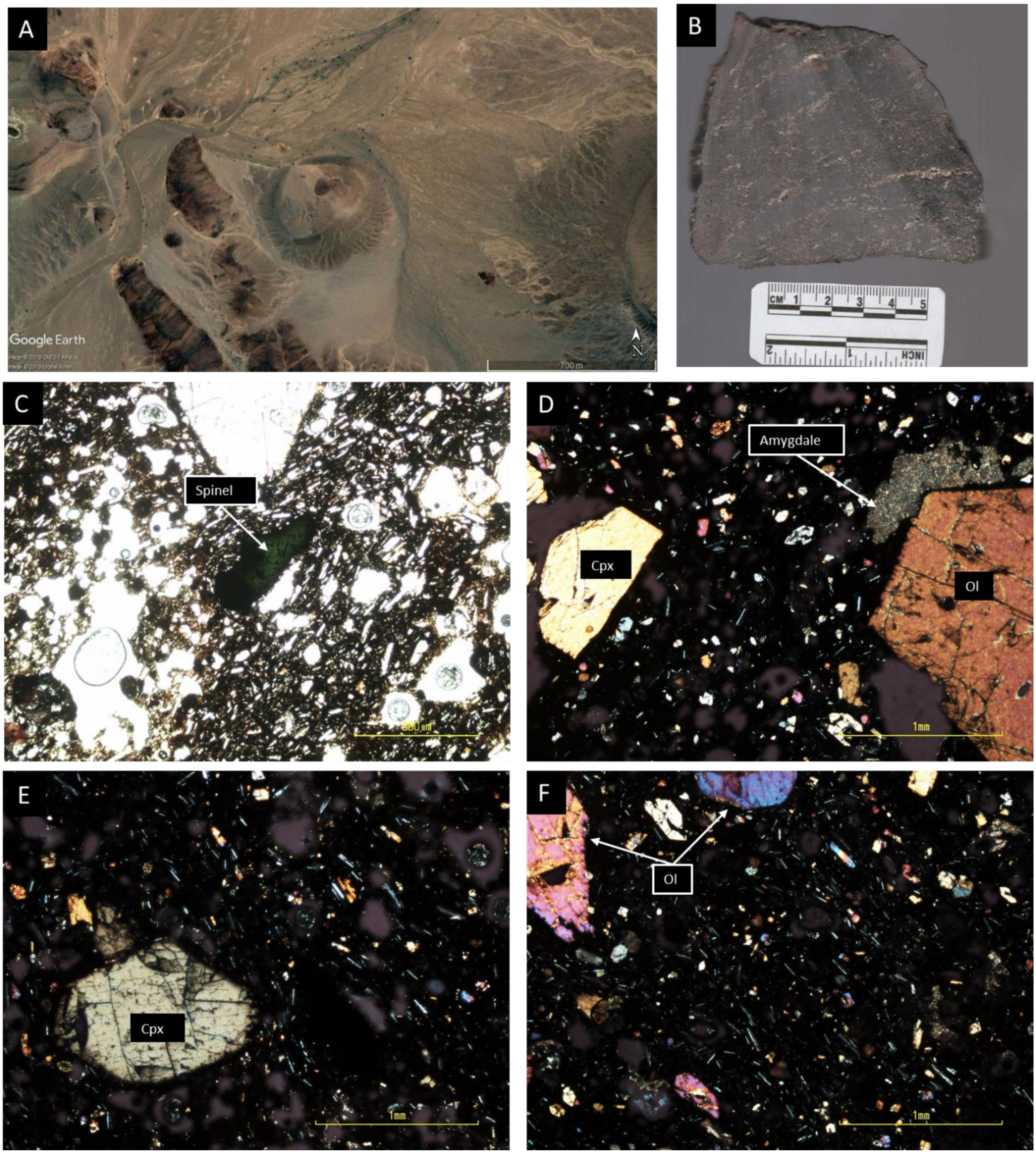

***Figure 4.15**: A) Satellite image of Volcano M6. B) Sample B18 is a moderately vesicular basanite displaying a porphyritic texture with clinopyroxene phenocrysts. The sample also show weathering bands through its interior. C) A rare elongate green spinel. PPL (10x) magnification. D) Olivine and clinopyroxene phenocrysts with an amygdale folded around the olivine grain. XPL (4x) magnification. E) A subhedral clinopyroxene phenocryst inside a flow aligned matrix. XPL (4x) magnification. F) Olivine microcryst in a flow aligned matrix. XPL (4x) magnification.*

4.1.14 Volcano M7

The sampled material sampled from volcano M7 is vesicular mafic lava flow displaying a seriate texture and minor localised trachytic textures (Figure 4.16). The phenocrysts phase makes up 25% of the lava flow, the vesicles make up 10% of the lava flow, and the groundmass makes up the remaining 65% of the lava flow. The phenocrysts phase consists out of clinopyroxene and olivine. A brown weathering rim is around the majority of phenocrysts (Figure 4.16F). Several plagioclase xenocrysts are hosted within the rock. The clinopyroxene phenocrysts are anhedral-euhedral and highly fractured displaying embayed textures (Figure 4.16D). Clinopyroxene phenocrysts range in size from 0.34-2.73 mm making up 15% of the lava flow. Olivine phenocrysts are subhedral-euhedral and fractured with minor embayment textures. Olivine's range in size from 0.36-1.84 mm making up 10% of the lava flow. Plagioclase crystals are predominantly part of the groundmass or as minor anhedral xenocrysts. The Plagioclase xenocryst phase ranges in size from 0.44-1.83 mm making up <1% of the lava flow. The groundmass consists of tabular plagioclase and microcrysts of clinopyroxene, olivine and interstitial magnetite. Samples: 10-1A, 10-1B and B15 displays a more prominent trachytic texture than samples B16 and B17. Magnetite rimmed spinel ranging in size from 39.5-161.1 µm making up <1% of the lava flow. Magnetite displays a bimodal size distribution of ~10 µm and ~30µm making up 3 % of the lava flow. Vesicles shapes are amorphous-rounded and partially filled with secondary carbonates. Vesicles range in size from 0.06-0.18 mm with the exception of one large amygdale 2.57 mm (Figure 4.16E) making up 10% of the lava flow.

4.1.15 Volcano M8

The sampled vesicular mafic lava flow from volcano M8 has a seriate and minor trachytic texture (Figure 4.17). The phenocryst phase makes out 35% of the lava flow, the vesicles make up 20% of the lava flow, and the groundmass makes up the remaining 45 % of the lava flow. The phenocryst phase consists of olivine and clinopyroxene. Olivine phenocrysts are anhedral-subhedral displaying skeletal growth and embayment textures (Figure 4.17C). Olivine phenocrysts range in size from 0.32-0.86 mm, making up 15% of the lava flow. Clinopyroxene phenocrysts have subhedral-euhedral crystal habit displaying sector zoning, embayment textures (Figure 4.17C) and fracturing (Figure 4.17D). The clinopyroxene phenocryst sizes range from 0.32-0.78 mm making up 20% of the lava flow. The groundmass is glassy with minor microcrysts of tabular plagioclase, clinopyroxene, olivine and magnetite rimmed brown spinel (Figure 4.17F). Vesicles are amoeboid-shaped to rounded with elongation in direction of flow. Vesicles range in size from 0.05-2.75 mm making up 20% of the lava flow.

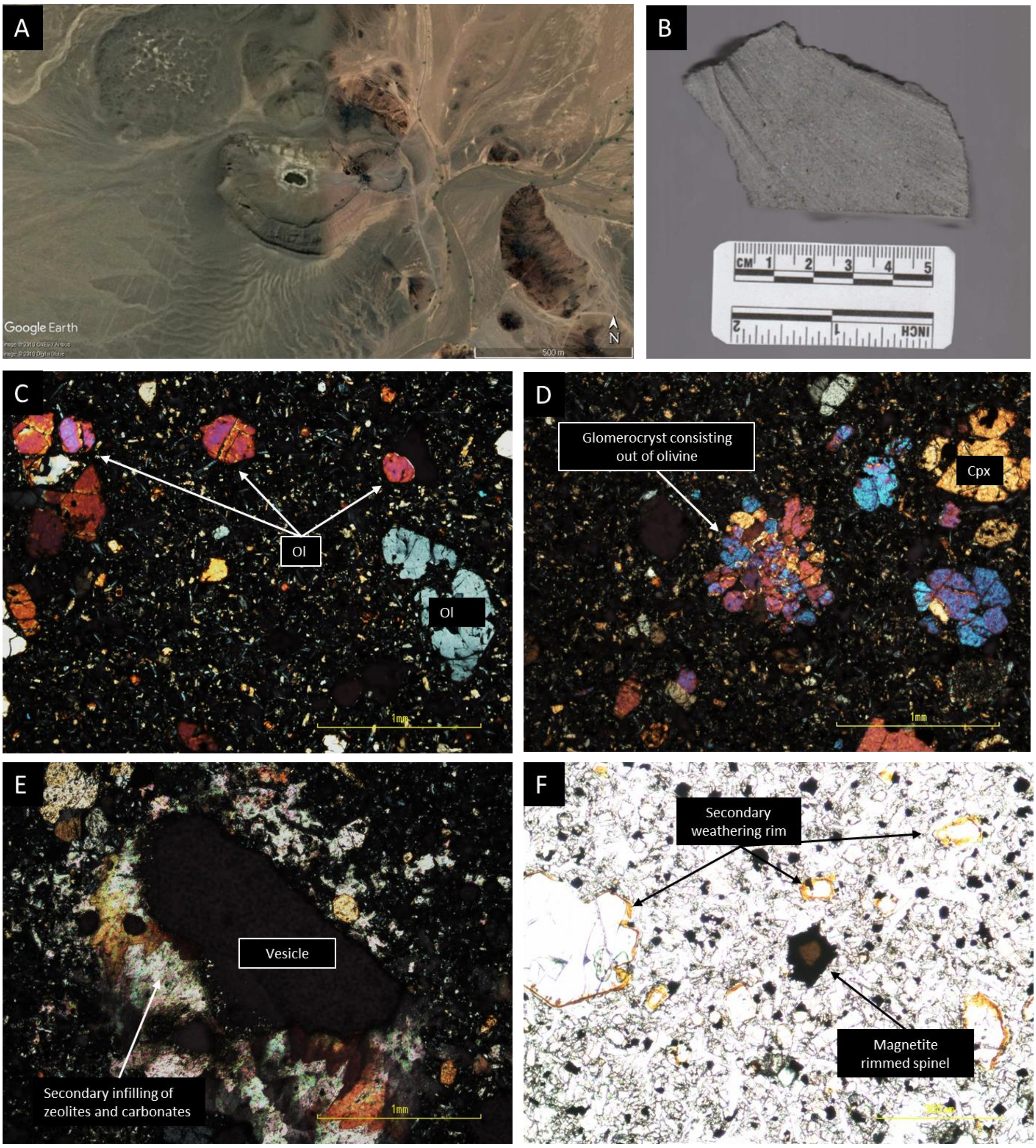

Figure 4.16: A) Satellite image of Volcano M7. B) Sample B16 is a vesicular basanite that has a porphyritic texture with small phenocryst of clinopyroxene. Bands on the sample are marks from the saw when it was cut. C) Several rounded olivine microcrysts and an anhedral nepheline with an embayment. XPL (4x) magnification. D) A glomerocryst consisting out of many olivine microlites alongside smaller glomerocryst and a clinopyroxene phenocryst. XPL (4x) magnification. E) A singular, large vesicle that is partially filled by secondary minerals. XPL (4x) magnification. F) A euhedral, magnetite rimmed brown spinel microlite in a groundmass rich in magnetite. Several crystals have a secondary weathering rim. PPL (10x) magnification.

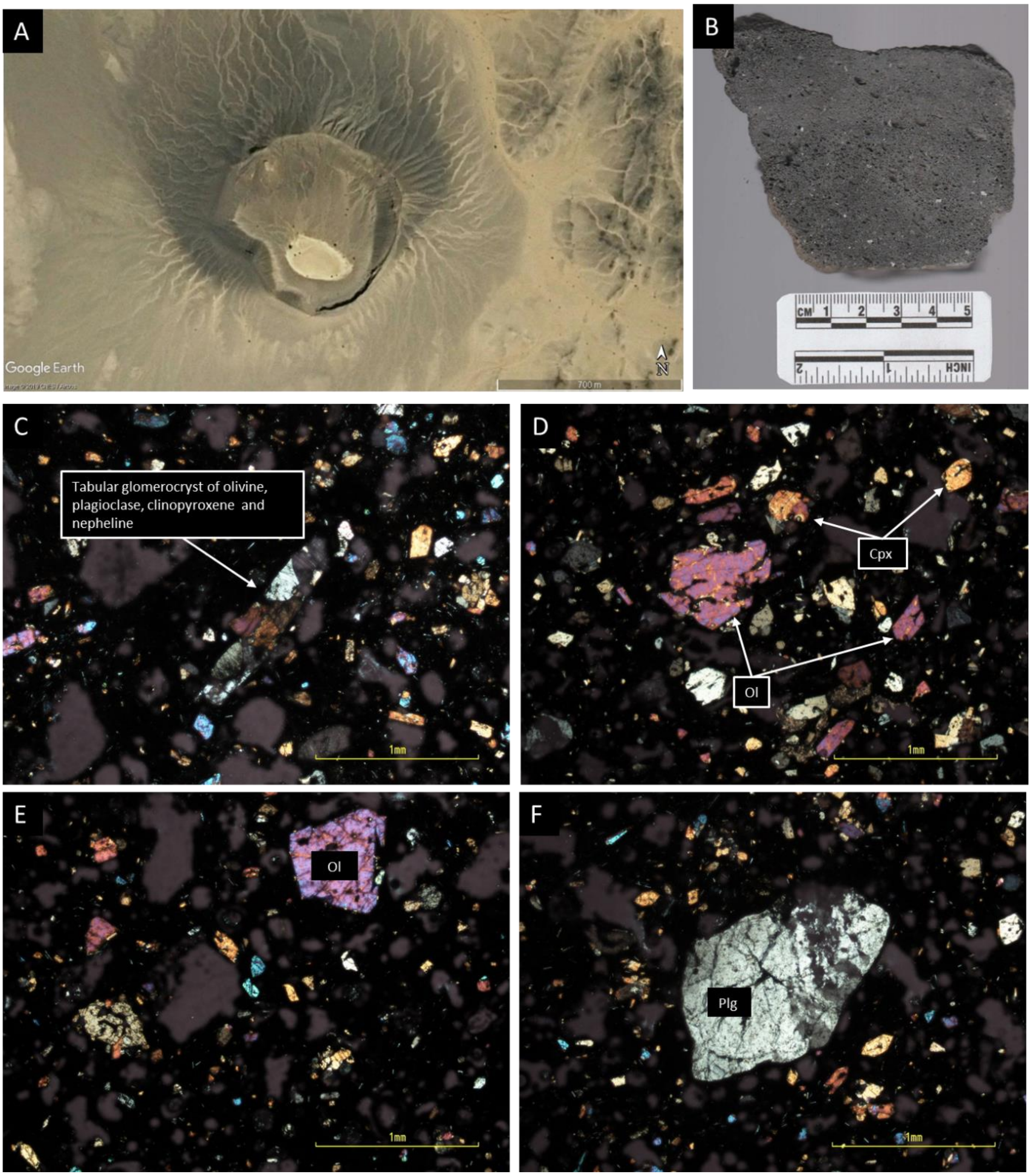

***Figure 4.17**:* A) Satellite image of Volcano M8. B) Sample V07 is a moderately vesicular basanite that has a porphyritic texture with phenocrysts of olivine, clinopyroxene and plagioclase with additional amygdales. C) A tabular glomerocryst consisting out of several mineral phases. XPL (4x) magnification. D) Skeletal microcryst of olivine alongside microcrysts of clinopyroxene. XPL (4x) magnification. E) A vesicular portion of the lava flow with small, fractured microcrysts of olivine and clinopyroxene. XPL (4x) magnification. F) A plagioclase phenocryst displaying dark banding across one portion of the phenocrysts. XPL (4x) magnification.

4.1.16 Volcano M11

The erupted material sampled at volcano M11 is a vesicular mafic lava flow, displaying a seriate and strong trachytic texture (Figure 4.18). The phenocryst phase makes up 30% of the lava flow, the vesicles make up 5% of the lava flow, and the groundmass makes up the remaining 65% of the lava flow. The phenocrysts phase consists out of clinopyroxene, olivine and plagioclase. All phenocryst shows a rim of brown weathered material. Clinopyroxene phenocrysts are anhedral-subhedral displaying oscillatory zoning and sieve textures. The clinopyroxene phenocryst range in size from 0.30-1.94mm, making up 20% of the lava flow. Olivine phenocrysts are anhedral-subhedral with minor embayment textures and spinel inclusions. The olivine phenocryst range in size from 0.32-0.49mm making up 10% of the lava flow. Plagioclase is represented by tabular phenocrysts and microcrysts that forms the majority of the groundmass. The plagioclases consist of aligned large tabular crystals ranging in size from 0.11-0.60 mm. In addition, minor microcrysts of olivine, clinopyroxenes and interstitial magnetite also forms part of the groundmass. Magnetite displays a bimodal size distribution of 20 μm and 40 μm making up 5% of the lava flow. The vesicles are rounded and aligned with the flow of the lava. Vesicles range in size from 0.03–0.7 mm making up 5% of the lava flow.

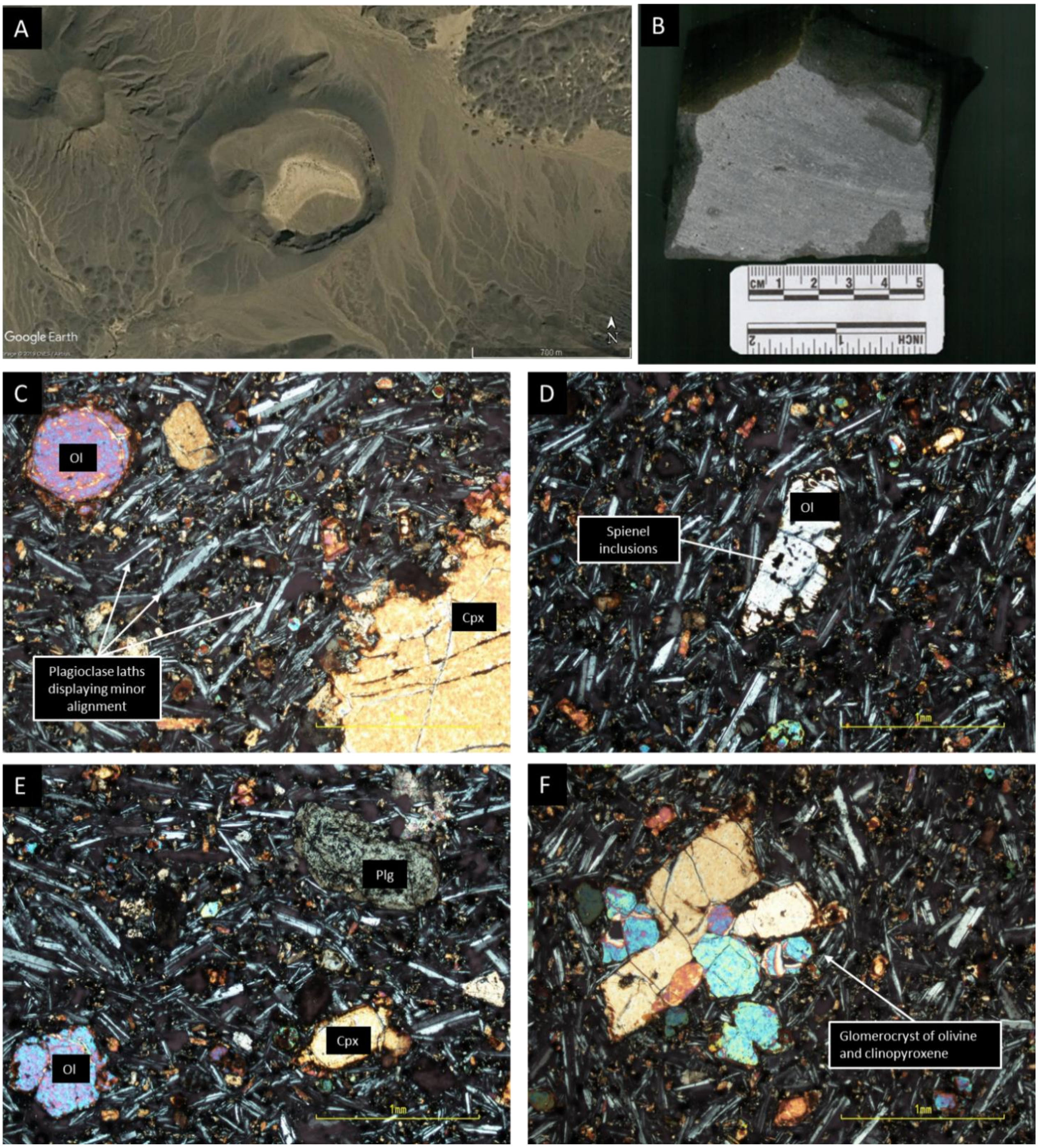

Figure 4.18: Satellite image of Volcano M11 B) Sample V-1 is a sparsely vesicular trachy-basalt with a porphyritic texture with minor phenocrysts of olivine and clinopyroxene. C) Micrograph showing a large clinopyroxene phenocryst and a rounded olivine phenocryst in a matrix of large plagioclase laths. The laths show minor alignment. D) An elongate olivine phenocryst with magnetite inclusions. XPL (4x) magnification. E) Phenocrysts of olivine and clinopyroxene in a coarse plagioclase matrix. All phenocryst phases display brown weathering rim. XPL (4x) magnification. F) A large glomerocryst consisting out of olivine and clinopyroxene. XPL (4x) magnification

4.2 Whole rock geochemistry of the BMVF

4.2.1 Major element geochemistry

The XRF analysis indicates that the volcanoes share similar concentrations of major elements. The volcanic rocks of the BMVF are SiO_2 undersaturated and ranges in SiO_2 content from 40.78 to 54.00 wt% (average=44 wt% SiO_2). The MgO content of the BMVF ranges from 6.18 to 14.92 wt% (average=10 wt% MgO), and Fe_2O_3 ranges in content from 9.96-15.26 wt% (average=12 wt% Fe_2O_3). TiO_2 ranges in content from 1.78-3.00 wt% (average= 2 wt% TiO_2). The calculated Mg# ranges in content from Mg#53- Mg#72 (average=Mg#62) and the total alkali's (K_2O+Na_2O) ranges in content from 1.79-6.66 wt% (average= 5 wt%).

The major element weight percentages are used in selected classification diagrams to define the type of rocks that are found throughout the BMVF. The TAS diagram (Le Bas et al., 1986) (Figure 4.19A) shows that the rocks of the BMVF are predominantly basanitic/tephritic with several rocks plotting in the more evolved section as basalt, trachy-basalt and basaltic andesite. Generally, the rocks are spread over the ultrabasic and basic zone with the majority of the rocks plotting in the ultrabasic field. Samples from CC7 are the most silica poor. In contrast, the rocks from volcanoes CC48, M8 and M11 exhibits more evolved, SiO_2-rich rocks of the BMVF. The AFM diagram (Figure 4.19B) modelled after Irvine and Baragar (1971) indicates that all the samples of the BMVF are calc-alkaline, plotting close to and on the boundary of the calc-alkaline and tholeiitic fields. The AFM diagram further shows that there is decrease in MgO wt% together with an increase in Fe_2O_3 wt% while A (K_2O + Na_2O) remains relatively constant.

The rocks of the BVMF are considered unaltered, having experienced no weathering or large-scale alteration due to the field's young age and arid environment. The Chemical Index of Alteration (CIA) devised by Nesbitt and Young, (1982) is a method of quantifying the amount of weathering a rock has been subjected to. The CIA value is a measurement of plagioclase weathering and breaking down into a clay mineral. Values close to 50 indicates a low amount of weathering while values close to 100 are considered highly weathered. The data in Appendix A shows CIA values of the BMVF range from 43.88-61.68 (average=53.98%), in conjunction with low LOI values, indicates that the samples are not highly weathered.

Binary plots of the major oxides of the BMVF are not plotted as conventional Harker diagrams, due to the ultrabasic/basic nature of the BMVF rocks. Using SiO_2 wt% on the abscissa will not clearly illustrate the magma evolution as the majority of the BMVF rocks are SiO_2 undersaturated. Instead, using MgO as abscissa will be best suited for the BMVF as the MgO displays a more substantial variation in concentration with ultrabasic/basic rocks than SiO_2 (Figure 4.20).

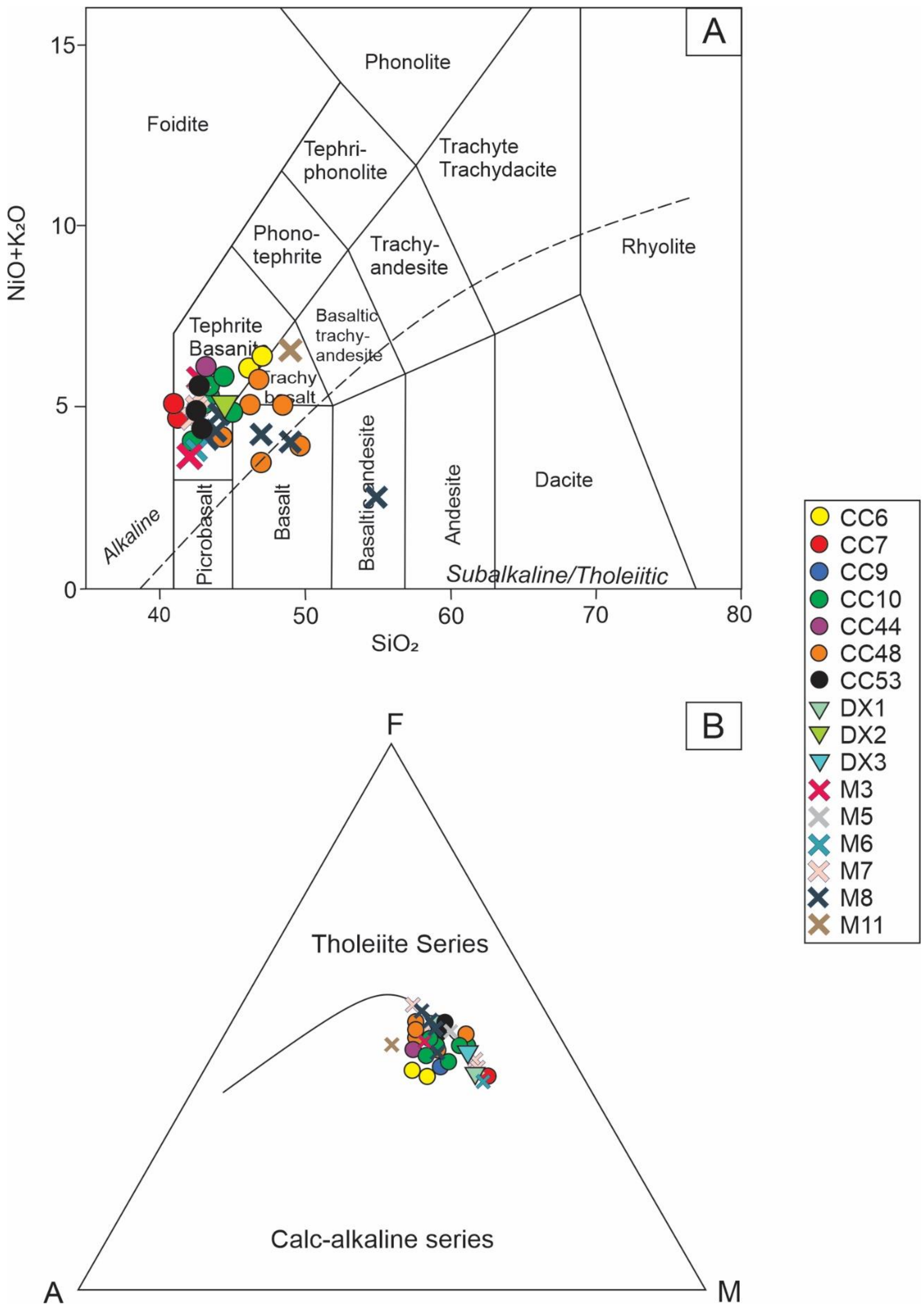
A
15
10
5
0
NiO+K₂O
40
50
60
70
80
SiO₂
Phonolite
Foidite
Tephri-
phonolite
Trachyte
Trachydacite
Phono-
tephrite
Trachy-
andesite
Rhyolite
Tephrite
Basanite
Basaltic
trachy-
andesite
Trachy
basalt
Picrobasalt
Basalt
Basaltic andesite
Andesite
Dacite
Alkaline
Subalkaline/Tholeiitic
B
F
Tholeiite Series
Calc-alkaline series
A
M
CC6
CC7
CC9
CC10
CC44
CC48
CC53
DX1
DX2
DX3
M3
M5
M6
M7
M8
M11

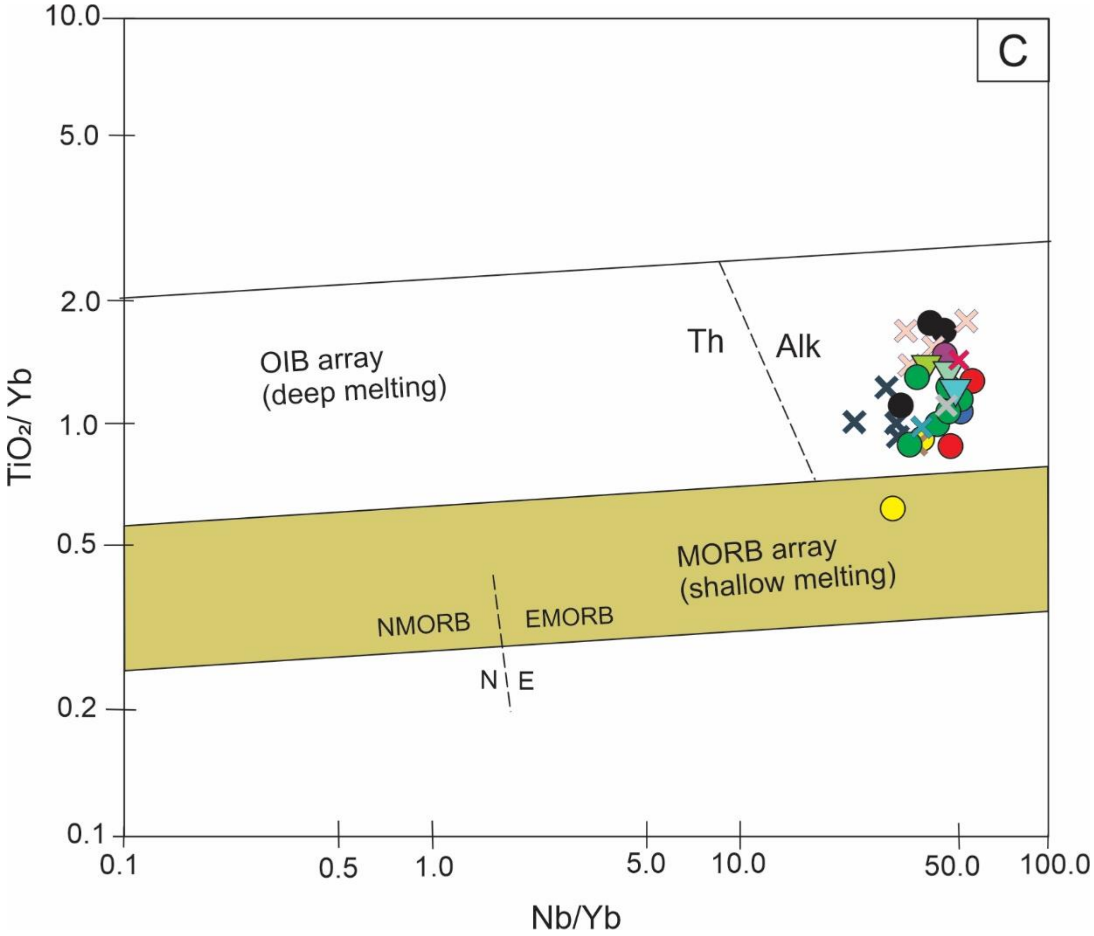

Figure 4.19. A) TAS diagram (BAS et al., 1986) B) AFM diagram (Irvine and Baragar, 1971) shows that the samples of the BMVF plots on predominantly on the calc-alkaline side of the trend. C) Nb/Yb-TiO2/ Yb diagram after Pearce (2008) demonstrating that the majority of the data plots within the alkaline OIB field.

The Binary plots of the BMVF were plotted with MgO wt% plotted against SiO_2 wt%, Al_2O_3 wt%, Fe_2O_3 wt%, CaO wt%, K_2O wt%, Na2O wt%, P_2O_5 wt% and TiO_2 wt% (Figure 4.20). The MgO vs SiO_2 binary scatter plot (Figure 4.20A) displays, two distinct groups. The first group is characterised by relatively constant SiO_2 values (values never vary more than ~2% as magma evolves) while MgO content increases. The second group displays a stronger negative relationship between SiO_2 and MgO, with a moderate increase in SiO_2 as MgO decreases. The MgO vs Al_2O_3 binary scatter plot (Figure 4.20B) shows a clear negative trend, that shows a decrease in MgO while Al_2O_3 increases. This is the case for all samples except 3 samples from volcano CC6 that only display a minor decrease in the 6-8 wt% MgO range. The MgO vs Fe_2O_3 binary scatter plot (Figure 4.20C) -displays two trends, a positive and a negative trend. The plot initially displays a positive trend up to ~11 wt% MgO where the Fe contents change into a negative trend with two Fe_2O_3 rich outliers from Volcano M7. The MgO wt% vs CaO binary scatter plot (Figure 4.20D) displays a positive trend. A decrease in MgO wt% leads to a decrease in CaO. The MgO vs K_2O binary scatter plot displays various slopes as MgO decreases. The plot initially shows a positive slope that changes into a negative slope at ~12wt% MgO and flattens out at ~1.5 wt% K_2O. The MgO vs Na_2O binary plot (Figure 4.20F) displays a prong-like scatter plot, consisting of two converging limbs with positive slopes. The two limbs have differing slopes that converge at ~10 wt% of MgO. The MgO vs TiO_2 scatter plot (Figure 4.20G) shows a similar pronged appearance as the MgO vs Na_2O binary scatter plot. The scatter plots initially display a negative slope that changes into a positive slope at ~10 wt% MgO. Finally, the MgO vs P_2O_5 plot (Figure 4.20H) shows no clear correlation between P_2O_5 and decreasing MgO.

The geotectonic classification diagrams are used in conjunction with composition classification diagrams to provide information on the definition the sampled rocks. The Nb/Yb-TiO2/Yb graph after Pearce (2008) confirms that the rocks resemble an OIB type composition with the rocks plotting in the OIB (deep melting) field (Figure. 4.19) The only exception is a sample from volcano CC6 that plots in the MORB (shallow melting) field. Generally, the rocks of the BMVF plot on the alkaline side of the OIB (deep melting) field correlating with the plots of the AFM diagram.

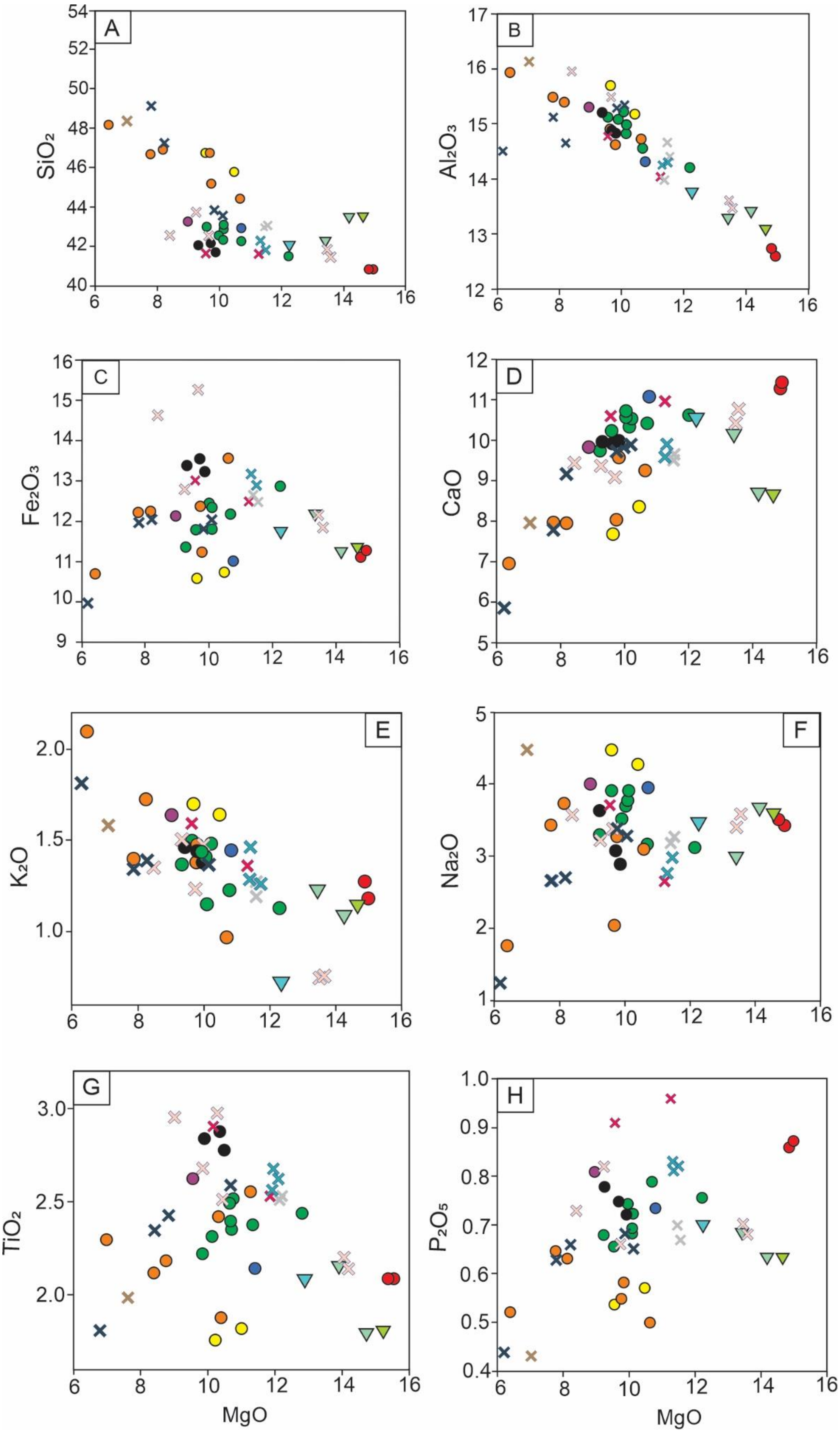

***Figure 4.20**: Multiple scatter plots using MgO as the abscissa: MgO vs A) SiO_2, B) Al_2O_3, C) Fe_2O_3, D) CaO, E) K_2O, F) Na_2O, G) TiO_2, H) P_2O_5.*

4.2.2 Trace Elements

The Nb/Y-Zr/Ti plot after Pearce (1998) (Figure 4.21A) classifies the rocks by using immobile trace elements as the parameters, reducing the effects of weathering or alteration. The classification graph plots the majority of the rocks in the foidite field close to the alkali basalt field border. A moderate amount of rocks plot on the border of the foidite and alkali basalt field and a minor amount of rocks plot in the alkali basalt field. The samples of volcano M8 as well as one sample each of volcanoes CC48 and CC53 plot within the alkali basalt field. This classification diagram correlates with the TAS diagram classification. The La/Yb – Nb/La diagrams after Hollocher et al. (2012) (Figure 4.21B) plots all the samples (with minor spread) within the Ocean Islands field.

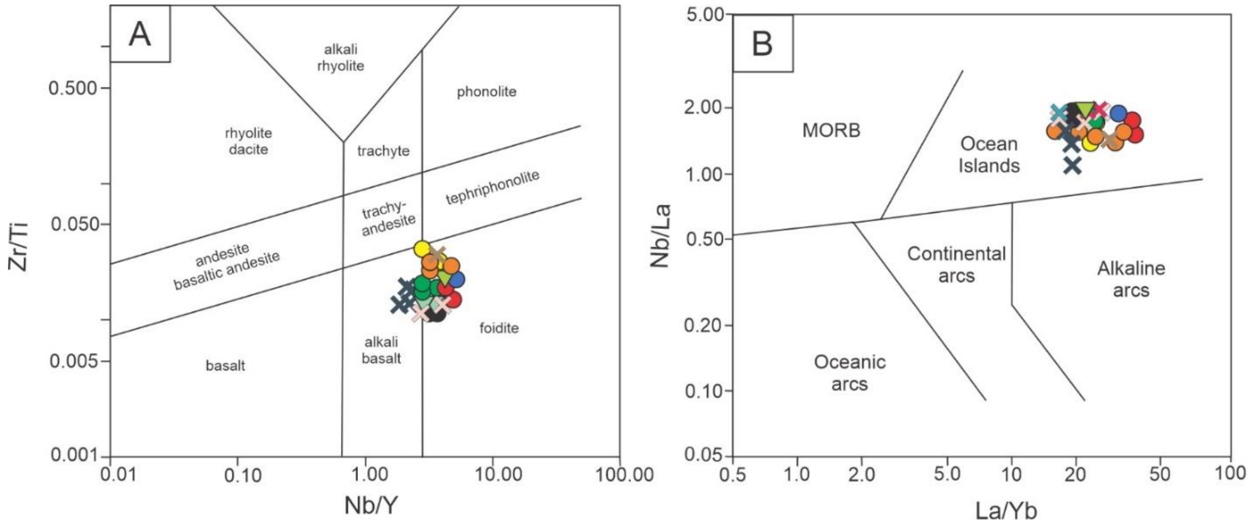

***Figure 4.21**:* A) A Nb/Y-Zr/Ti plot (Pearce,1996) used to classify rock type indicates the plots lies between the foidite and alkali basalt field. B) A La/Yb-Nb/La (Hollocher et al. 2012) is a tectonic setting classification diagram showing that all the samples of the BMVF plots within the Ocean Island field.

Figure 4.22A is a La vs La/K*1000 diagram that indicates whether there is an amphibole/phlogopite phase present in the magmatic source. Amphibole and phlogopite are useful phases in alkaline rocks as the phases can give further insight into the depth of melting and whether the mantle has experienced a metasomatic enrichment event (Furman and Graham, 1999). The binary plot (Figure 4.22A) makes use of La and K as both are compatible with phlogopite and amphibole. An increase in K and La would indicate the presence of either phlogopite or amphibolite.

It should be noted that La and K are both affected by fractional crystallisation due to both being incompatible under anhydrous conditions (Le et al., 2019). The samples of the BMVF display a clear positive trend when plotted on the La vs K diagram (Fig 4.22A).

Ba/Rb vs Rb/Sr plot (after Furman and Graham, 1991) shows whether there has been a phlogopite or an amphibolite phase in the magmatic source (Figure 4.22B). The diagram is typically used for ultrapotassic rocks, but allowances are made for other alkaline extrusive rocks. The amphibole and phlogopite phases are the product of metasomatism that tends to occur in the mantle. Phlogopite has higher partition coefficients for Ba and Rb while amphibole has higher partition coefficients for Sr (LaTourrette et al., 1995, Furman and Graham, 1999, Le et al., 2019). The phlogopite field is defined by a Rb/Sr ratio higher than 0.1 and a Ba/Rb ratio lower than 20. The amphibole field is defined by Ba/Rb higher than 20 and a Rb/Sr ratio lower than 0.1. The Primitive Mantle (PM) (Sun and McDonough, 1989) places in between the two metasomatism fields. The majority of the BMVF lava flows plot in between the two phases overlapping mostly with the PM field. Several samples of volcanoes M7 and, -CC10, and a sample from lava flow DX3 plots within the amphibole field. In addition, one sample from volcano M8 plots within the phlogopite field.

The trace element data of the BMVF are plotted on selected fractionation diagrams that indicate the magmatic evolution of the BMVF Figure (Figure 23A) displays a clear positive trend between Ni and Cr. Pearce and Norry (1979) used the abundances of the HFS elements Zr, Nb, Ti and Y to determine crystallisation patterns. The Zr vs Nb binary plot (Figure 4.24B) displays an overall positive trend. The La vs La/Yb plot (Figure 23C) displays a larger grouping with samples displaying a positive slope of La/Yb values, attributing to an heterogenous source or that partial melting was a more significant differentiation factor than fractional crystallisation. The Zr vs Nb binary plot (Figure 23B) displays an overall positive trend which suggests the crystallisation of olivine, clinopyroxenes, feldspars and magnetite Pearce and Norry (1979). Zr vs Sr (Figure 23D) exhibits an increase in Sr as the system evolves suggesting that large scale plagioclase crystallisation did not occur.

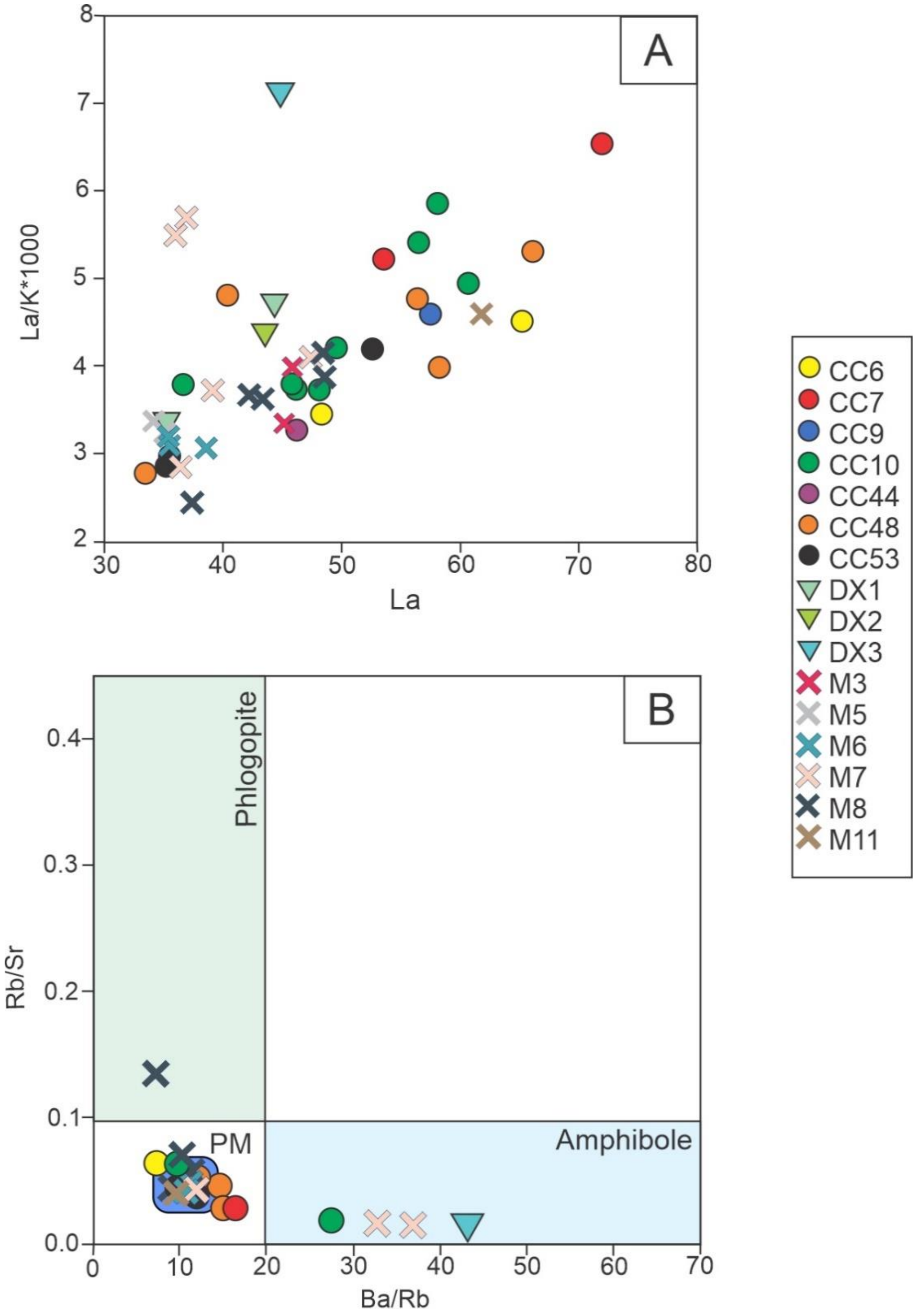

Figure 4.22: A) The La vs La/K*1000 diagram demonstrates a positive trend with three outliers from Volcano M7 and Lava flow: DX3, plotting above the main trend. B) A Ba/Rb vs Rb/Sr diagram after (Furman and Graham, 1999) shows that the data is grouped in and around the PM field with outliers in the Amphibole field and a singular outlier in the phlogopite.

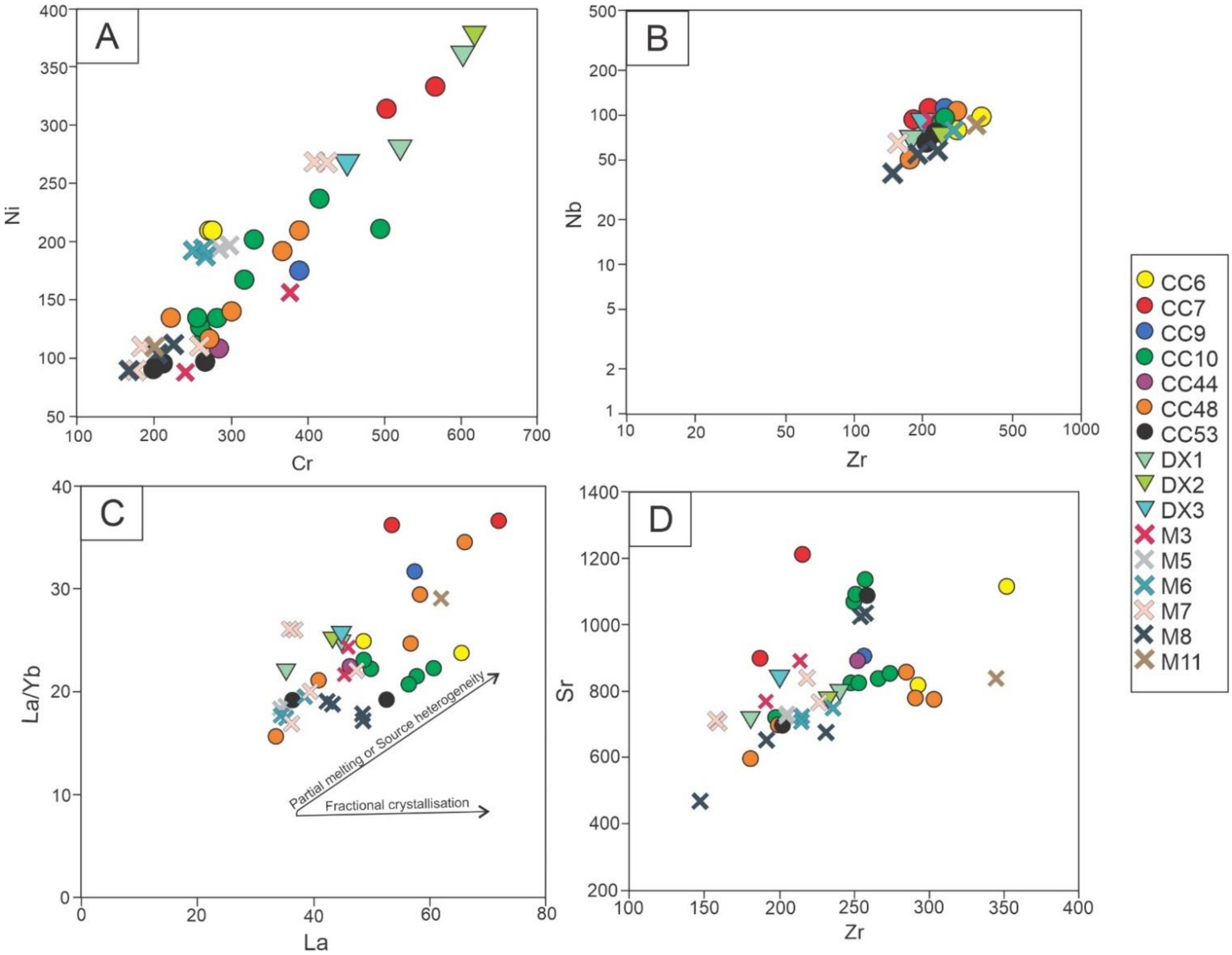

Figure 4.23: A) Cr vs Ni plot demonstrating a positive trend B) Zr vs Nb C) La vs La/Yb D) Zr vs Sr. Fig 2.23 A,B,C and D demonstrates a positive trend.

Spider plots

The volcanic rocks of the BMVF were plotted on several multi-element diagrams to illustrate any differences the lava flows might have in terms of trace element concentrations. Figure 4.24 plots the BMVF lava flows on a Primitive Mantle normalised spider plot (Sun and McDonough, 1989). The spider plot also contains the two plots of an Ocean Island Basalt (OIB) and Normal Mid Oceanic Ridge Basalts (NMORB) (Sun and McDonough, 1989). The trace element abundances of the BMVF matches the trace element abundances of OIB. The BMVF shows a more enriched version of the OIB. The spider plot has a minor positive trend from Cs-Nb, where it changes into a pronounced negative trend from La-Lu. The HSF elements have the closest similarities in concentration while the LIL elements display the most variation in concentration between the different volcanoes. The spider plot displays a pronounced drop in K for all the volcanoes of the BMVF. Pb has the highest variation in concentration ranging from ~8-105ppm. Similar to Pb, Rb displays one of the largest concentration differences with values ranging from >10-100 ppm, (volcano M7 has the lowest Rb value).

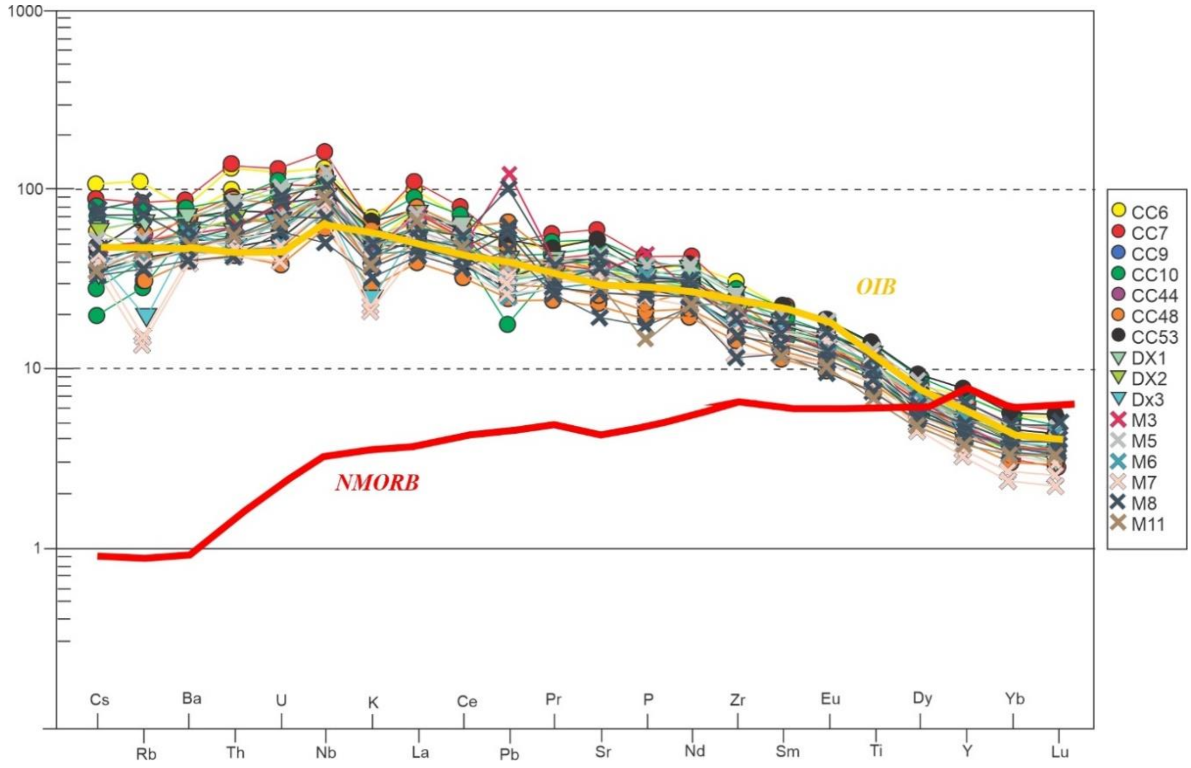

Figure 4.24: Primitive Mantle normalised (Sun and McDonough, 1989) spider plot of the BMVF. The orange line indicates the typical OIB trace element signature when normalised to Primitive mantle. The red line indicates the typical NMORB trace element signature when normalised to Primitive Mantle. OIB and NMORB compositions from Sun and McDonough (1989).

The NMORB normalised spider plot (Sun and McDonough, 1989) (Figure 4.25) has a strong negative trend displaying high abundances of LIL elements and low abundances of HREE compared to NMORB. The graph does little to illustrate the trace element abundances more clearly than the primitive mantle normalised spider plot. The substantial concentration differences between a typical NMORB and the BMVF are too big to see the trace element relationships.

A more suited spider plot for the BMVF is the OIB normalised (Sun and McDonough, 1989) spider plot (Figure 4.26). Due to the similarities in trace element abundances, any differences in concentration is illustrated clearer in the OIB-normalised spider plot than the Primitive mantle and NMORB normalised graphs. The OIB spider plot better illustrates the differences in Cs and Rb content. There is a clear divide between samples with Cs and Rb displaying a positive trend. The first group exhibits Cs and Rb content <1ppm and the second group displays samples with a positive trend >1ppm. The Rb contents do not show large variation except for 3 samples from volcano M3 and M7. A sample from CC10 also displays a lower value than the rest of the BMVF. Similar to the PM normalised plot, there is an overall drop in K for all the volcanoes with samples from volcano M3 and M7 having the lowest values of ~0.5. The OIB normalised plot displays a large variation in Pb values where samples from volcanoes M3 and M8 display the highest Pb values of`~3ppm while CC10 displays the lowest Pb value of 0.4ppm. A sample from CC6 displays a negative Ti anomaly There is also a noticeable split at the HFS elements Dy, volcanoes CC6, CC10, CC53 and M8 show a more HFS element enriched signature. The remaining volcanoes of the BMVF display a rather depleted nature.

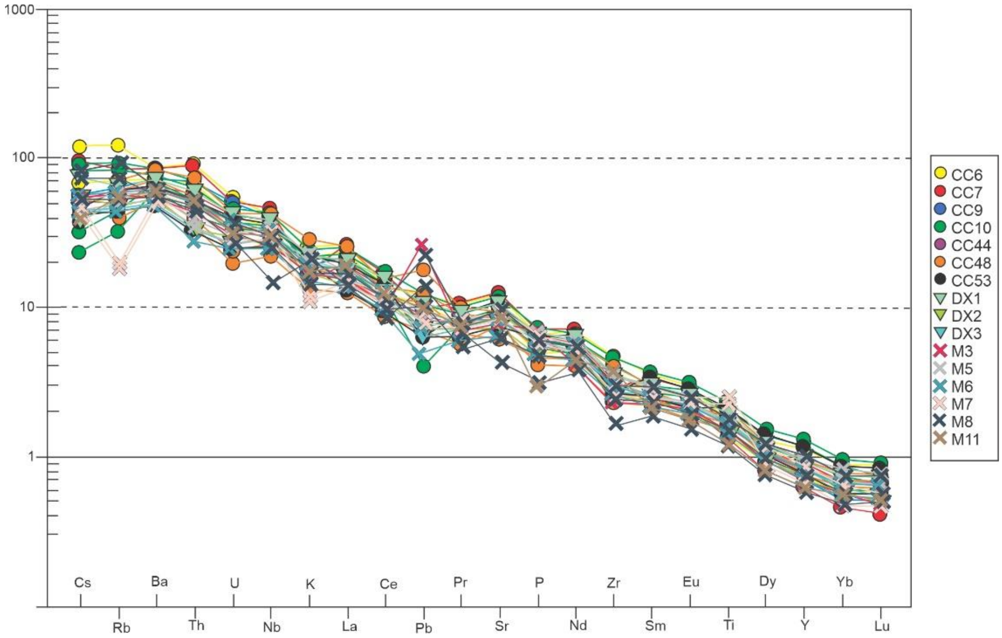

Figure 4.25: A NMORB normalise spider plot (Sun and McDonough, 1989). Trace element abundances are far higher than that of a typical NMORB.

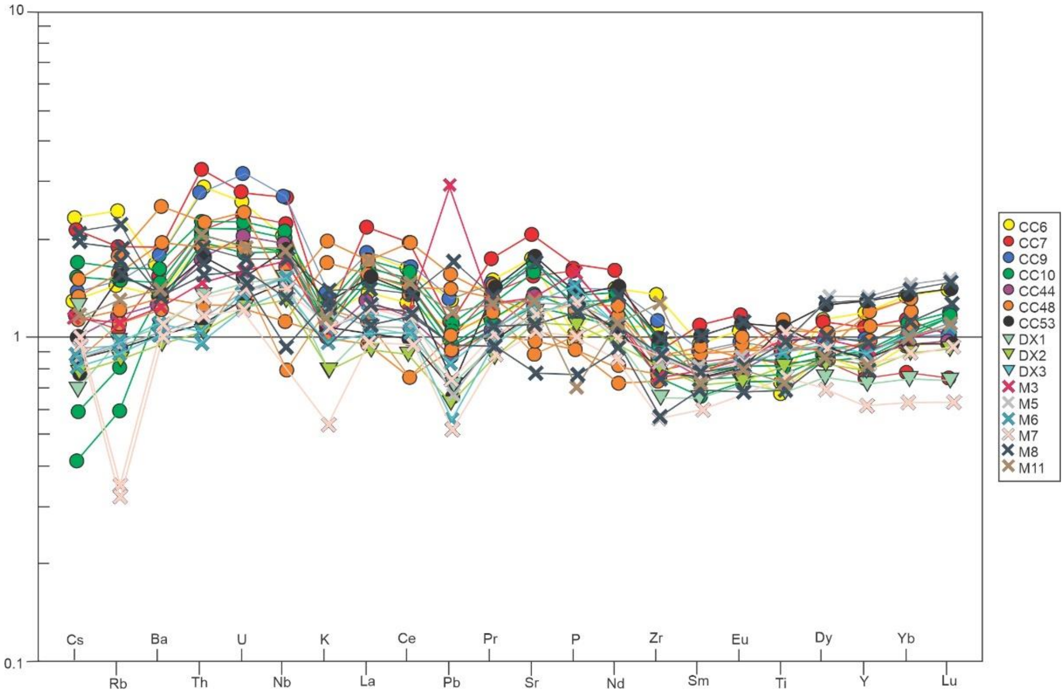

Figure 4.26: An OIB normalised spider plot (Sun and McDonough, 1989) of the BMVF. The trace element abundances of the BMVF are exaggerated due to the scale of the plot.

To further illustrate the differing trace element concentrations, the samples of the BMVF were plotted as a function of rock type, rather than the erupted volcano. Plotting the samples by rock type could potentially indicate whether the compositional maturity of the rock has any influence on trace elements. Figure 4.27 is an OIB normalised (Sun and McDonough, 1989) spider plot that displays the rock type plots set on the shaded area which represents the area of the entire OIB spider plot. Figure 4.27A represents the basaltic compositions; the plots fall well within the shaded area, displaying no extreme values. The basaltic rocks do show variation amongst themselves, with notable differences between Th, U, Nb an Pb. Figure 4.27B displays the only basaltic-andesite sample; the plot forms both the upper and the lower limits for many trace elements of the graph. The basaltic andesite sample has the highest values for Ba and Pb, while it has the lowest values for Pr, Sr, P, Nd, Zr, Sm, Eu and Ti. Figure 4.27C displays the basanitic rocks of the BMVF, making up the majority of the lava flows. The basanites display substantial changes in concentration with the majority of the trace elements. Notable differences include Rb, Th and Pb. Figure 4.27D represents the last composition of the BMVF, the trachy-basalt rocks. The plots fall within the grey area with some variation between the two trachy-basalt rocks.

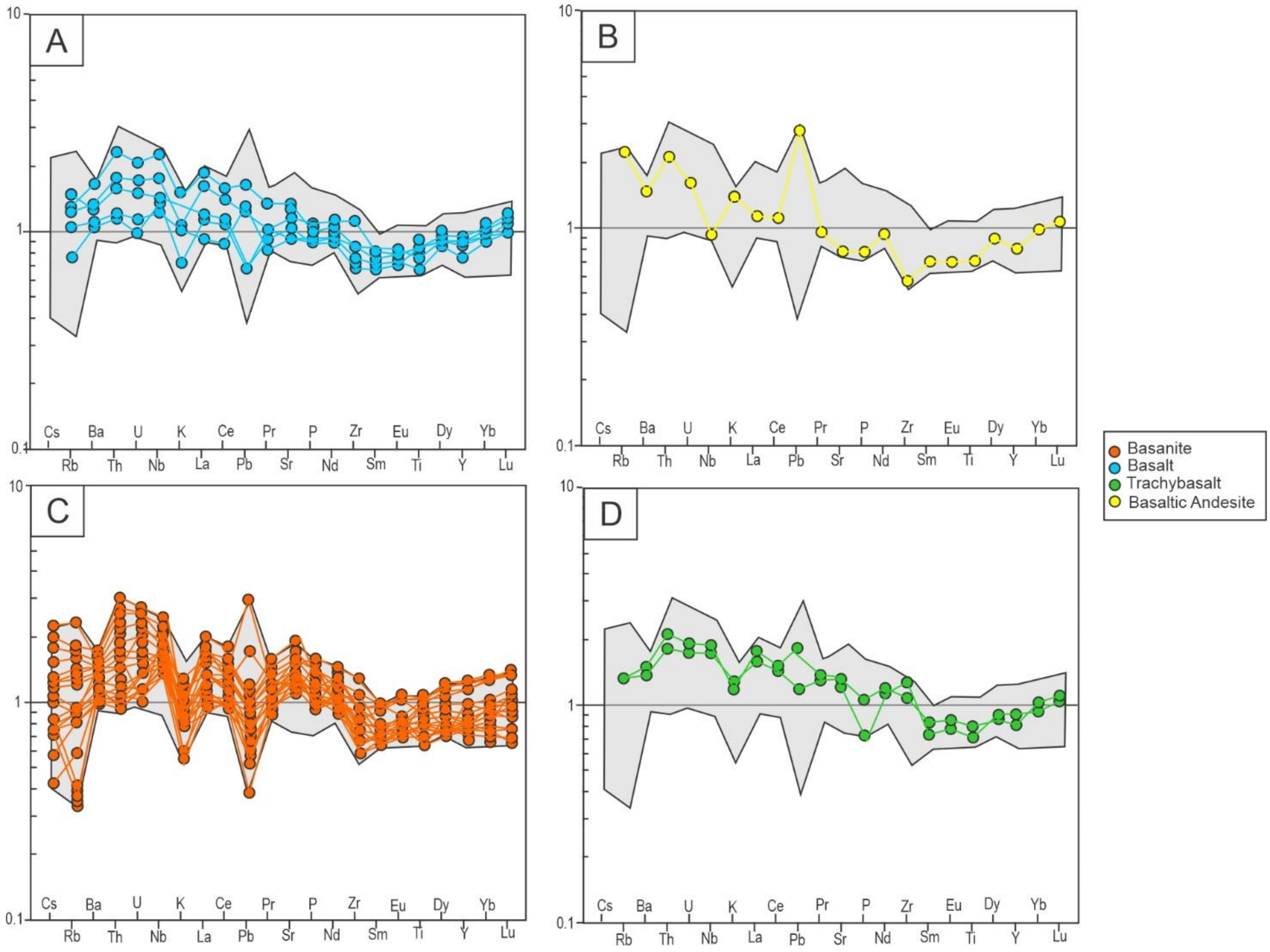

Figure 4.27: OIB normalised spider plots divided by rock type. A) basalt, B) basaltic-andesite C) basanite D) trachy-basalt. The basanites display the largest variation in trace element abundance.

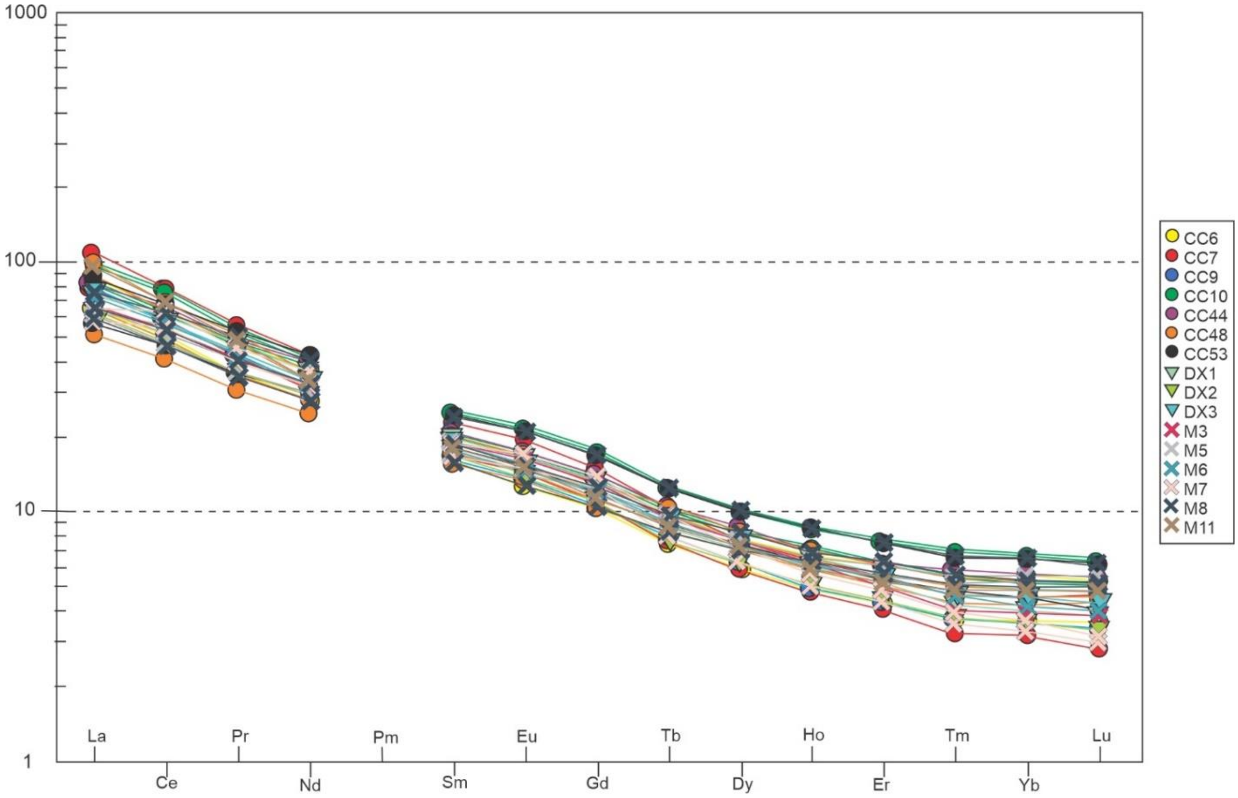

Figure 4.28: Primitive Mantle normalised REE diagram with the omission of Pm. LREE abundances display the most variety between the samples of the BMVF. The HREE abundances are the most similar.

The Primitive Mantle normalised REE (Sun and McDonough, 1989) diagram (Figure 4.28) has a negative trend, displaying high LREE abundances and depleted HREE abundances. The samples all show similar abundances with all the samples plotting with parallel slopes. The samples of the BMVF are generally enriched compared to the Primitive Mantle where the LREE concentrations of the BMVF have up to 100 times the concentration of the Primitive Mantle. The HREE concentrations of the BMVF are also enriched (up to 10 times the concentration of the Primitive Mantle), but to a lesser extent than LREE. The BMVF REE’s were also plotted with the focus on rock type (Figure 4.29) The basaltic-andesite sample has relatively depleted LREE abundances but has an average HREE abundance. The basanites make up the majority of the field. The two trachyte-basalt samples display average LREE and HREE abundances relative to the other lithologies.

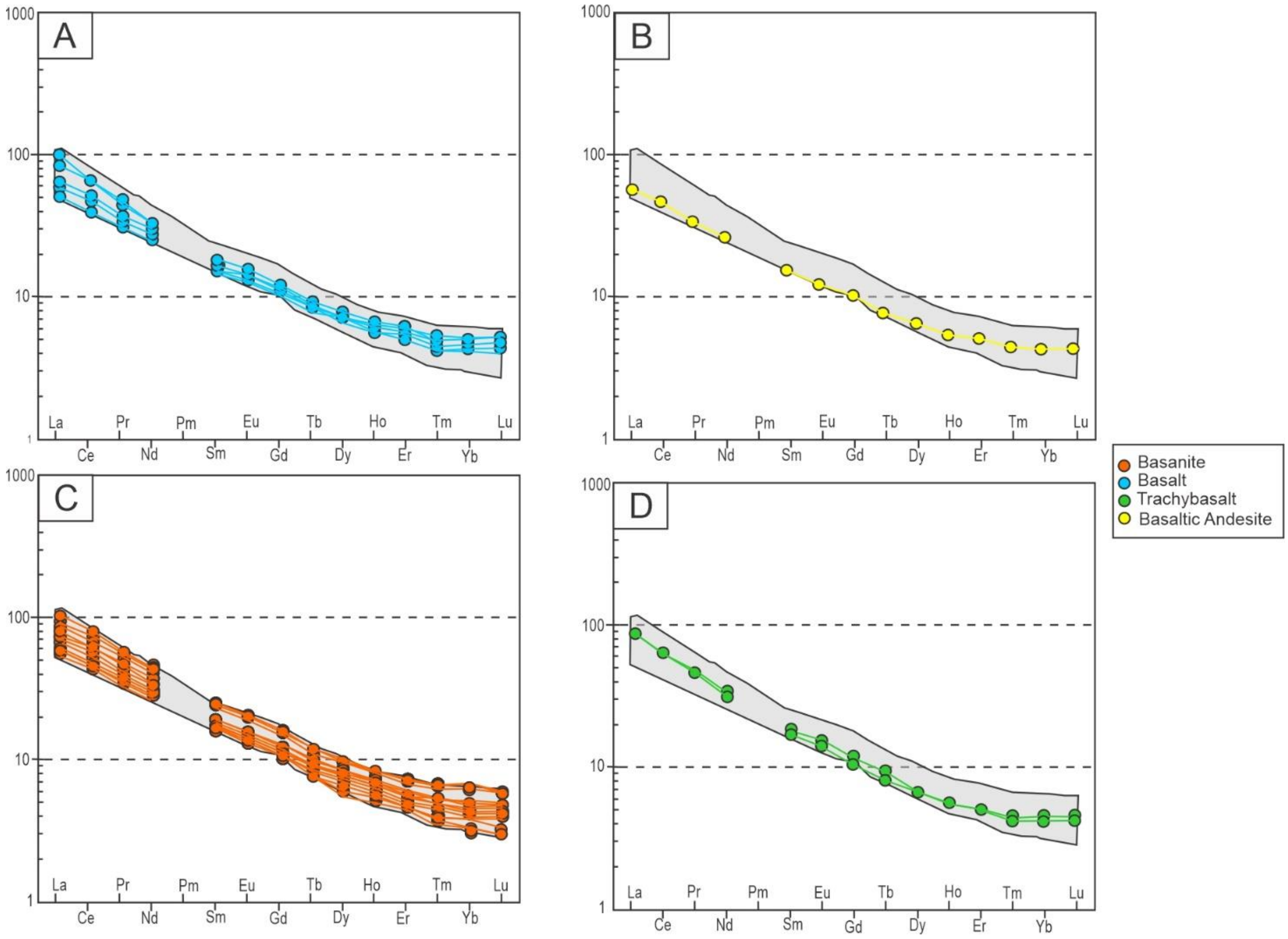

Figure 4.29: Primary Mantle normalised REE divided by rock type. A) basalt, B) basaltic-andesite C) basanite D) trachy-basalt. The basanites display the largest variation in trace element abundance.

4.2.3 Isotopes

The Sr, Nd, Hf and Pd isotopes of the BMVF do not show large variation in composition. The ^{87}Sr/^{86}Sr ranges from 0.703097-0.703347 (average=703182) and ^{143}Nd/^{144}Nd ranges from 0.512869-0.512995 (average = 5,196854). The ^{176}Hf/^{177}Hf ranges from 0.283017-0.283006 (average=0.283017) and ^{206}Pb/^{204}Pb ranges from 19,45095-19,89533 (average=19,79244) , ^{207}Pb/^{204}Pb ranges from 15,63934-15,67705 (average=15,65247) and Pb^{208}Pb/^{204}Pb ranges from 39.3066 – 39.6777 (average=39,5748).The Sr and Nd isotopes of the BMVF resembles the isotopic compositions of Continental basalts, the Ocean Islands and the MORB isotopic signatures (Figure 4.30A). The Pb isotope classification diagrams (Figure 4.30 B and C) plot the BMVF within the "Oceanic Islands" field as well as in the "Marine Sediment" field. The Pb classification diagrams indicate an outlier in the dataset. The outlier of the data plots within the "marine sediment/upper crust" field in the ^{206}Pb/^{204}Pb vs ^{207}Pb/^{204}Pb diagram field and likely represents crustal contamination.

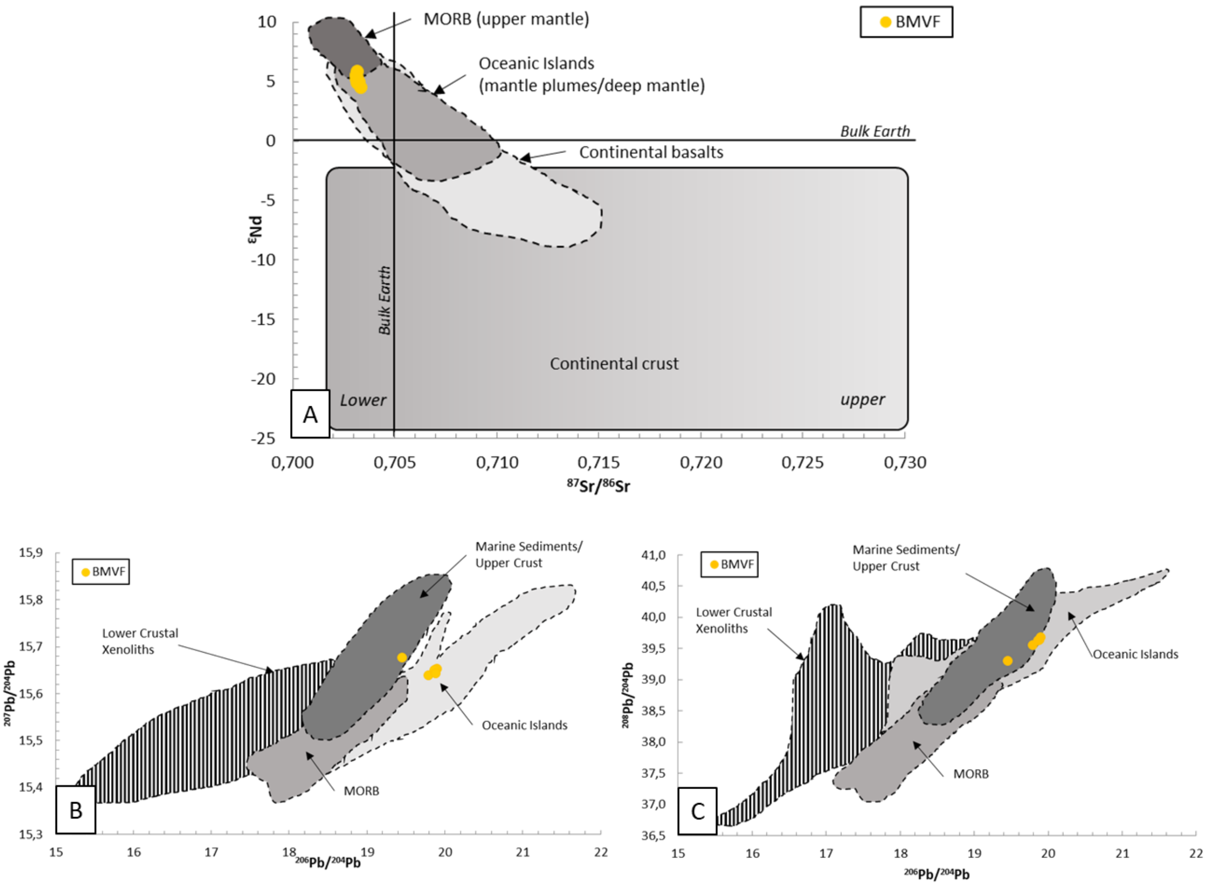

Figure 4.30: A) ^{87}Sr/^{86}Sr vs ε_{Nd} diagram with the fields: MORB, Oceanic Islands, Continental basalts and continental crust. The BMVF plots within the Continental Basalts field, the OCEANIC ISLAND field and part of the MORB field. B) ^{206}Pb/^{204}Pb vs ^{207}Pb/^{204}Pb diagram C) ^{206}Pb/^{204}Pb vs ^{208}Pb/^{204}Pb diagram. Tectonic setting fields (Zindler and Hart, 1986).

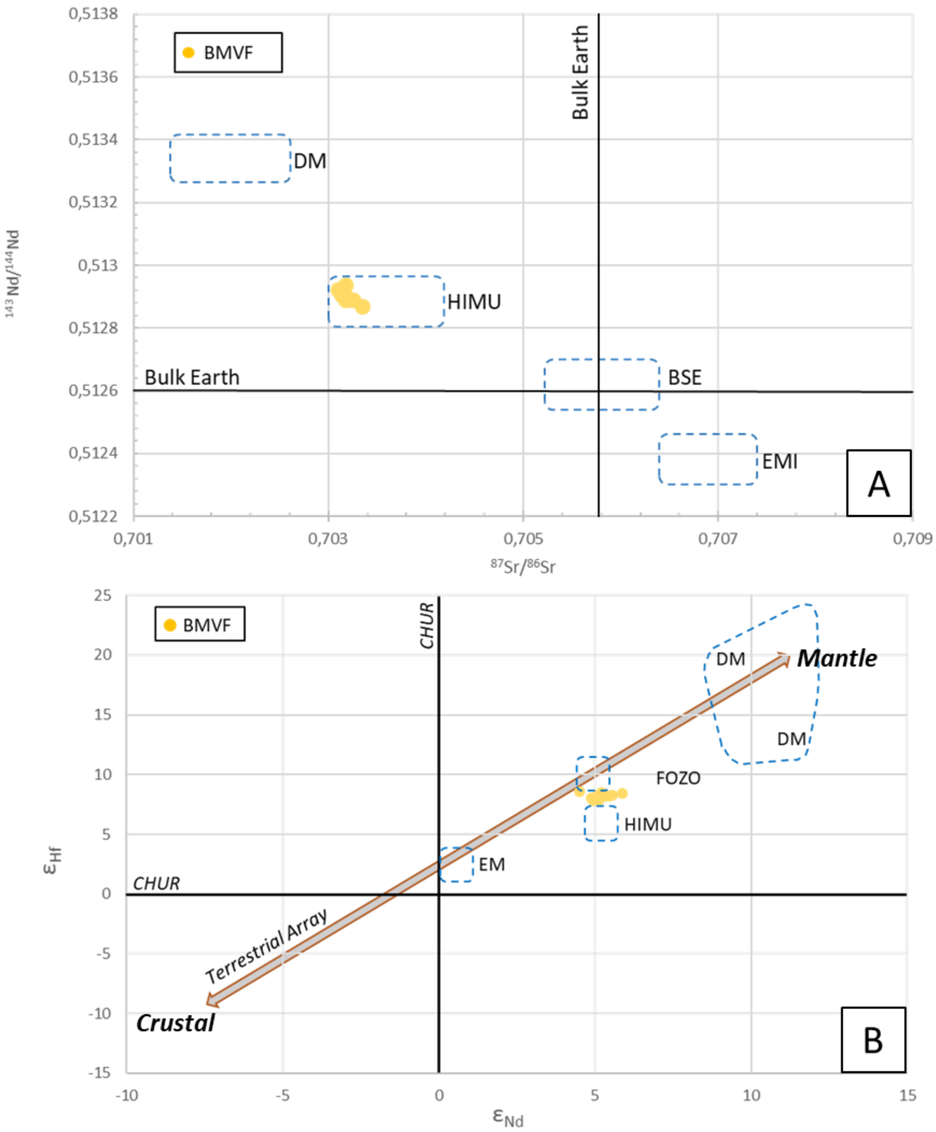

Figure 4.31: Mantle reservoir end-members: EM I, EM II, HIMU and DM (Zindler and Hart, 1986) classification diagrams A) ^{87}Sr/^{86}Sr vs ^{143}Nd/^{144}Nd diagram indicating that the BMVF plots within the HIMU mantle reservoir field. B) ε_{Nd} vs ε_{Hf} diagram displaying the BMVF plotting between the FOZO (Hart 1992) and the HIMU field. Terrestrial array line represents Hf-Nd ratios from 0-3.5Ga of crustal and mantle sample (Vervoort et al., 1999).

The BMVF displays a distinct HIMU isotopic signature in terms of ^{87}Sr/^{86}Sr and ^{143}Nd/^{144}Nd. All of the samples fall within the HIMU mantle endmember field (Figure 4.31A). The Sr and Nd isotopic compositions show little variation and contains no outliers. Figure 4.31B indicates that the BMF plots between the HIMU and FOZO with samples on the border of both of the respective mantle endmember component fields. The samples of the BMVF plots close to the Terrestrial array line resembling the mantle-like Hf-Nd isotopic ratios rather than the crustal Hf-Nd ratios.

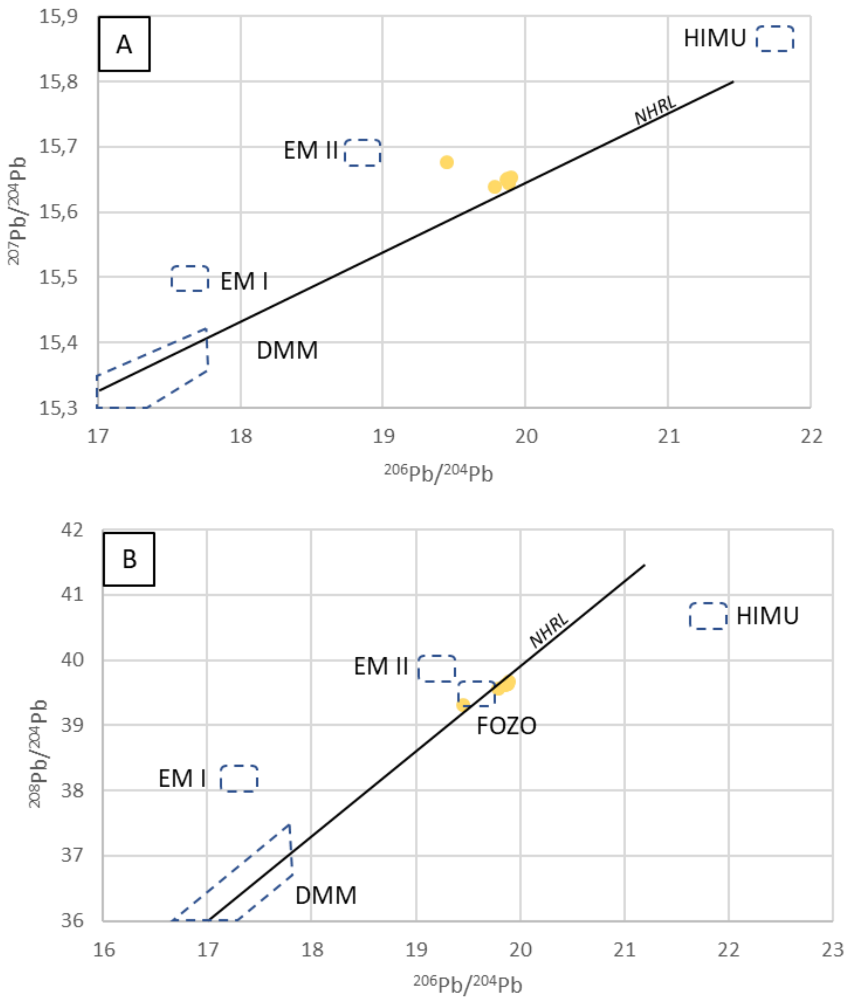

Figure 4.32: Pb-isotope classification diagrams with mantle endmember fields. A) $^{206}Pb/^{204}Pb$ vs $^{207}Pb/^{204}Pb$ diagram with the mantle endmembers: EM I, EM II and HIMU B) $^{206}Pb/^{204}Pb$ vs $^{208}Pb/^{204}Pb$ diagram with the mantle endmembers: DMM, EMI, EM II, FOZO and HIMU. See Figure 4.31 caption for mantle endmember references. The Northern Hemisphere Reference Line (NHRL) (Zindler and Hart, 1986).

The Pb-isotope classification diagrams (Figure 4.32) plots the samples of the BMVF closer to the EM II (Figures 4.32A and B) and FOZO (Figure 4.32A) mantle endmembers. The samples have a limited range in Pb isotopic compositions except for one outlier that is visible in Figure A and B. The same outlier is visible in Figure 4.31 B and C. The samples plot along the NHRL mixing lines in both Pb diagrams.

4.3 Single mineral chemistry

4.3.1 Olivine

A total of 70 olivines (consisting of phenocrysts and microcrysts), from 7 volcanoes and 1 lava flow were examined by electron microprobe (EMP) to give insight into the plumbing system of the BMVF. A two-point analysis was performed on each olivine crystal. The first point analysis was taken at the core of the crystal while the second point analysis was taken towards the edge of the mineral, avoiding accidental groundmass measurements.

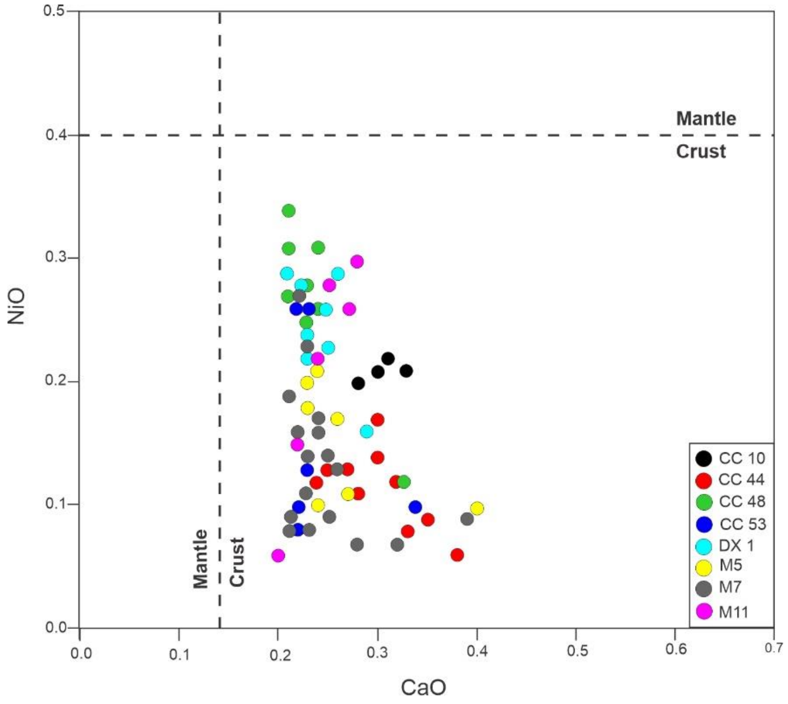

Figure 4.33. Olivine classification diagram indicating the typical Ni and Ca compositions of olivines that crystallised in the crust and olivines that crystallised in the mantle. The CaO mantle crust boundary was determined by Simkin and Smith (1970) and the NiO mantle/crust boundary value was determined by Sato (1977).

Using selected trace elements, the origin of the olivines can be determined. Specifically, Ca is helpful in determining at what depth (i.e. mantle or crustal) the olivines crystallised. Ca is readily partitioned into olivine at lower pressures, but less so at higher pressures (Simkin and Smith, 1970). A high Ca content in olivines suggest crystallisation at the lower pressure conditions of the crust and a low Ca content would suggest the higher-pressure conditions of the mantle. The olivine cores of the BMVF have CaO >0.2 wt% exhibiting a crustal origin (Figure 4.33). Ni content is equally useful. Ni content in olivines are dependant the composition of the parental rock as well as temperature. The $D_{Ni}^{Ol/melt}$ is negatively related to temperature, so olivines crystallising at high temperatures will have higher Ni content than olivines forming a lower temperature (Sato, 1977). The NiO content of all the measured BMVF olivines ids NiO < 0.40 wt% which, like the Ca content, indicates a crustal origin.

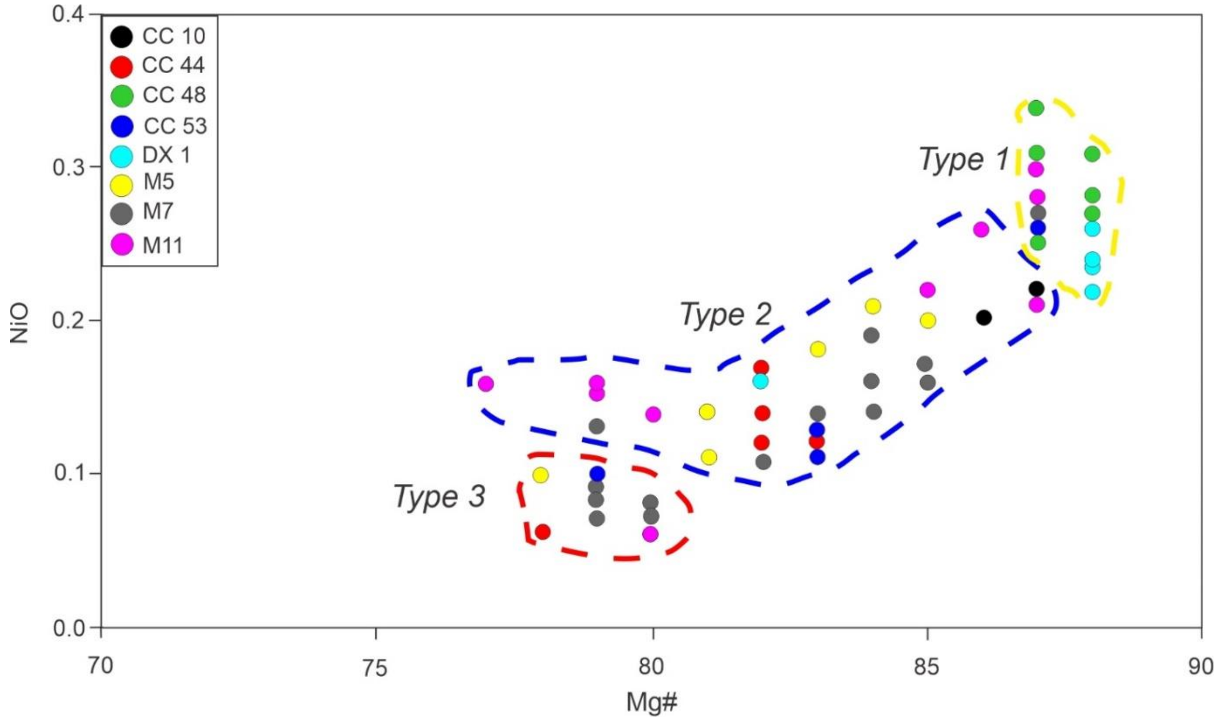

Figure 4.34: A) Mg# and NiO contents of the olivine cores found within the BMVF. The graph exhibits three olivines types when classified by varying Ni and Mg# content.

Olivine types

Classifying olivines by means of core composition allows for greater insight into the changing environments the olivines crystallised in. Mg# and Ni content in olivines is a method of differentiating and illustrating olivines that crystallised under different conditions (Abratis et al., 2015, Ray et al., 2016). Figure 4.34 show that the olivines of the BMVF can broadly be separated into 3 groups. The group of olivines with constant Mg# and varying NiO contents represents the type 1 olivines. The olivines that have varying Mg# and varying NiO contents represents type 2 olivines. Type 3 olivines are represented by the olivine cores with relatively constant NiO contents with varying Mg#. Adding to core compositions, the olivines exhibit different zoning patterns and mantles. The mantles and zoning patterns reveal the changing conditions of the olivine, after initial crystallisation.

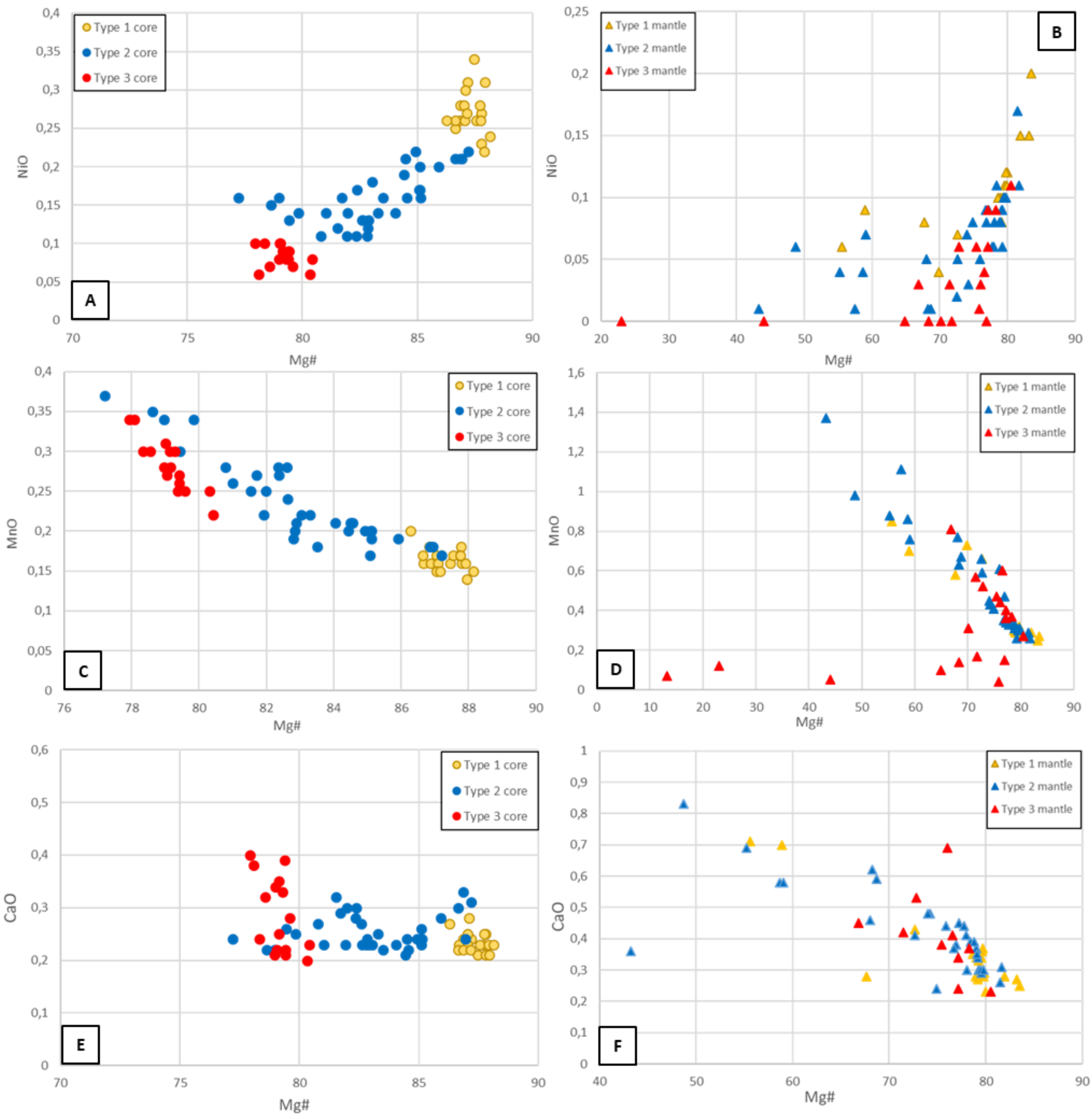

Figure 4.35. Composition scatterplots displaying the different olivine types and core and mantle compositions. A) Mg# vs NiO of olivine cores B) Mg# vs NiO of olivine growth mantles. C) Mg# vs MnO of olivine cores D) Mg# vs MnO of olivine growth mantles E) Mg# vs CaO cores of olivine F) Mg# vs CaO of olivine growth mantles.

Type 1 olivines crystals have euhedral and subhedral habits displaying predominantly step zone profiles with pronounced embayments that often contain groundmass. BSE imagery exhibits type 1 olivines having a euhedral core, with occasional spinel inclusions, and a defined mantle around the euhedral core (Appendix E and Figure 4.37). Mineral 2 of sample B10 does not show the defined step zoning characteristic of type 1 olivines (Figure 4.37). Type 1 olivines have a magnesium-rich cores (Fo_{86-88}) displaying little variation. The cores have the highest Ni contents olivines, ranging from 0.23 – 0.34 wt% (Figure 3.35A). The mantles of type 1 olivines have Ni compositions that range from 0,04-0,2 wt%. The Mn of the type 1 olivine cores exhibit little variation with a Mn composition of 0.14-0.20 wt% (Figure 3.35C). Mn content within the mantle exhibits two clusters: the first cluster ranges from 0.27-0.32 wt% and the second cluster ranges from 0.58-0.85 wt% (Figure 3.35D). The cores have the lowest Ca content of the olivine types, with core compositions varying from 0.21-0.28 wt% (Figure 3.35E). The mantles show variation in Ca compositions ranging from 0.25-1.46 wt%. Type 1 olivines are found in volcanoes CC44, CC48, DX1, M7 and M11 (Figure 4.36).

Type 2 olivines are subhedral and anhedral crystals that exhibits step zoning, gradational step zoning, gradational zoning and clinopyroxene reaction rims (Figure 3.37). Type 2 olivines have the most variation in core compositions of the olivine types. The Ni contents of the of the olivine cores display a positive trend with Mg#, exhibiting that a decrease in Mg# leads to a decrease in Ni content. Towards the lower Mg# core values, olivines from volcano M11 display a progressive Ni enrichment (Figures 3.34 and 3.35A). Type 2 olivine core Ni contents exhibits a large variation (0.11-0.22 wt%) that is mirrored in the mantle Ni contents (0.01-0.17 wt%). The Mn contents of both the core and the mantles exhibit a negative relationship, indicating that as Mg# decreases Mn content increases. The core Ca content of the crystals display an initial positive relationship with Mg# causing Ca to decrease to 0.21 wt%, but turns into a negative relationship at Mg# 84 where Ca contents increase to 0.33 wt%. The relationship turns back into positive relationship at Mg#82. The Ca content in the mantles do not reflect the altering relationships seen in the core compositions, mantles exhibit a positive relationship between Ca and Mg # with Ca mantle compositions ranging from 0.3-0.83 wt%. Type 2 olivines are found in volcanoes CC10, CC44, CC53, DX1, M5, M7 and M11 (Figure 4.36).

Type 3 olivines have subhedral and anhedral crystal habits exhibiting gradational zoning as well as several olivine crystals with a clinopyroxene rim. The type 3 olivines are characterised by having both low Mg# (Mg# 78-80) and low Ni content (0.06-0.1 wt%) cores (Figure 3.35A). The mantles of the type 3 olivines have similar compositions to that of the other olivine types (0-0.11 wt% NiO), but several mantles sections of type 3 olivines have no Ni in their composition. The cores are Mn rich (0.05-0.81 wt%) and share similar values to some of the type 2 olivines. Mn mantle compositions are low, with some sharing similar compositions to both type 1 and 2 olivines. A group of mantle compositions do not form part of the negative trend between Mg# and MnO (Figure 3.35D), but displays a pronounced depletion of MnO with a decrease in Mg#. The core compositions have the highest Ca contents of the olivine types (0.20-0.40 wt%). Ca contents of type 3 olivine rims exhibit the same negative relationship with Mg# similar to the other olivine types. A group of 9 type 3 olivine mantle compositions are highly enriched in Ca and were not included in Figure 4.35F due to their Ca content being 2 orders of magnitude larger than the other olivine types (4.74-22.73 wt%) which can be seen in Appendix E,these measurements are interpreted as measurement errors. Type 3 olivines can be found in volcanoes CC44, CC53, M5, M7 and M11 (Figure 4.36).

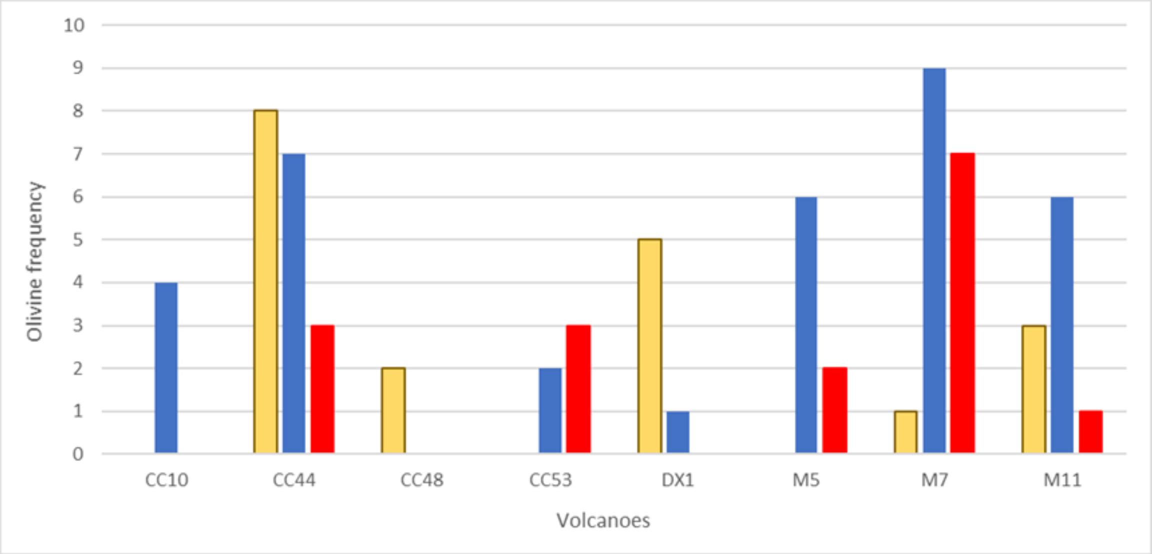

Figure 4.36: Bar graph displaying the distribution of olivine types throughout the volcanoes and lava flow analysed.

Zoning type	***Type 1 Olivines***	***Type 2 Olivines***	***Type 3 Olivines***
Step zoning	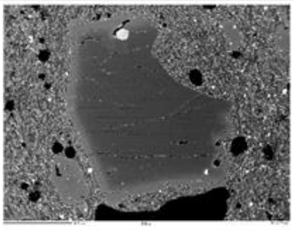	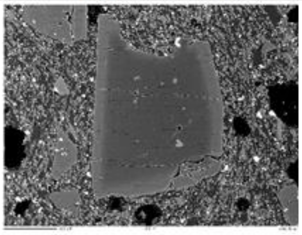	Not applicable
Gradational Step Zoning	Not applicable	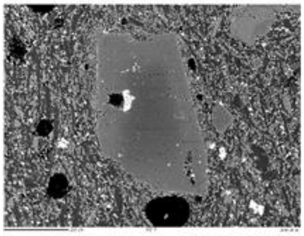	Not applicable
Gradational Zoning	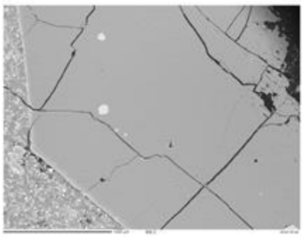	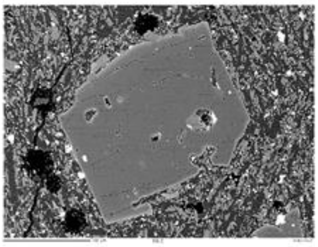	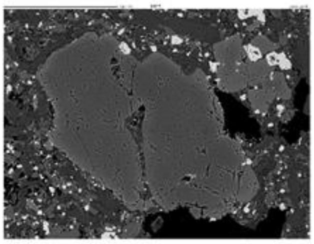
Clinopyroxene Rim	Not applicable	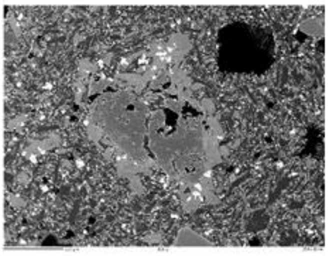	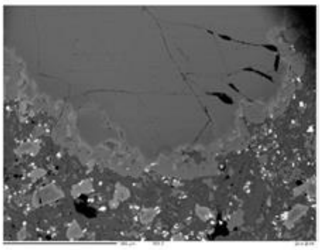

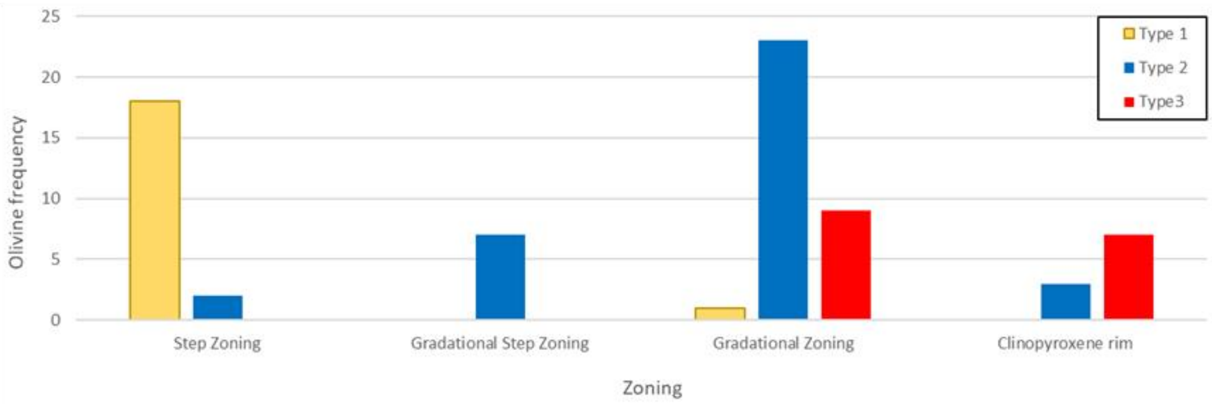

Figure 4.37. Zoning types of the olivine types and the zoning type distribution throughout the different olivine types.

4.3.2 Clinopyroxenes

A two-point analysis was performed on 14 clinopyroxenes cores and 22 clinopyroxenes rims of the BMVF, the first point analysis was performed in the core of the pyroxene and the second point analysis was performed on the mantle of the pyroxene. Microprobe analyses show that the majority of clinopyroxene cores measured belong to the Ca/Mg rich endmember, diopside (Figure 4.38A). The diopside cores of the clinopyroxene show minor variation in Fe content. A single crystal from volcano DX1 plots within the hedenbergite field.

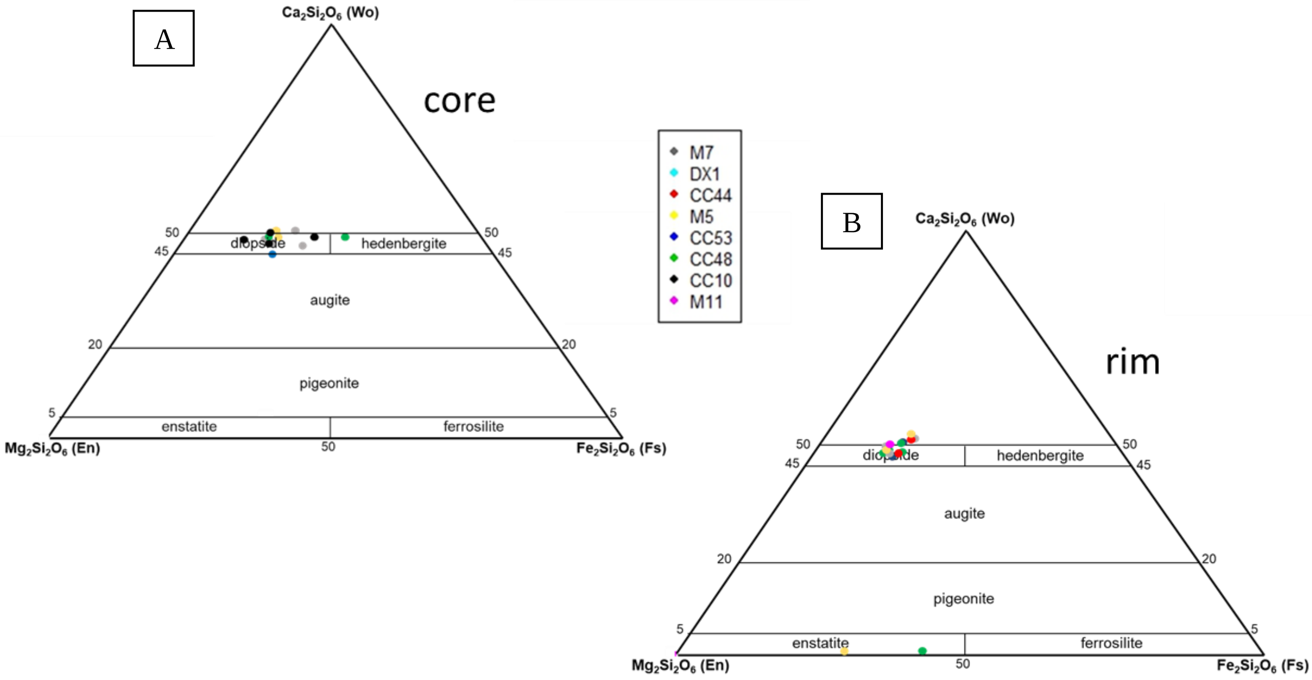

Figure 4.38: Pyroxene ternary classification diagram, plotting the composition of the a) pyroxenes cores and the b) pyroxene rims.

The clinopyroxene mantle point analyses include the clinopyroxene rims found on the type 1 olivine (Figure 4.38B). Rim compositions are similar, if not closer grouped, than the compositions of the clinopyroxene cores. The clinopyroxene rims plot within the diopside field, with some, Ca-rich samples plotting just outside the diopside field (Figure 4.35B). Two rim compositions from volcanoes CC48 and M5 plot within the Mg-rich, enstatite field. The classification diagram was plotted with the PX-NOM spreadsheet of Sturm (2002) using the pyroxene nomenclature of Morimoto (1988).

Pyroxene traverses

Several point analyses were performed in sequence to produce a line scan on 2 clinopyroxenes from volcano CC10 (Figure 4.39).

Neither of the clinopyroxenes are in equilibrium with the host rock at any point from core to rim, but show very different zoning patterns. Clinopyroxene 3 (Figure 4.39A) shows minor oscillating Mg# of Mg#75-78 from point 1-12. At point analysis 13 the Mg# gradually declines towards ~Mg#70 at point 15. There is a minor increase in Mg# from point 15 to point 16. The change in Mg# is illustrated by the almost mirrored Mg and Fe compositions of the clinopyroxene. The Ca content of Clinopyroxene 3 gradually increases to point analysis 14. After point analysis 14 the Ca content notably increases. Clinopyroxene 4 (Figure 4.39B) has a large light core with two distinct outer rims. The lighter core of clinopyroxene 4 is represented by point analyses 1-3. The second section that shows zoning is notably darker than any other section of the mineral and is represented by point analyses 4 and 5. The lighter rim is represented by point analysis 6 and 7. Clinopyroxene core values remain constant at ~Mg#60 until they transition into the dark zoned section, and the Mg# starts to increase to Mg#77 at point analysis 5. Point 5 marks the highest Mg# of the mineral. After point 5 the line scan transitions into the lighter rim and the Mg# decreases to ~Mg#70 at point 7. Like Clinopyroxene 3, the Fe and Mg compositions of Clinopyroxene 4 represent the interplay between Fe and Mg. The Ca composition of Clinopyroxene 4 remains constant (wt%) for the interior of the crystal, but exhibits an increase of Ca content after point 3 in the mantle, “dark zone”, display a pronounced increase (wt%). Towards the rim of Clinopyroxene 4, the Ca content decreases slightly at point 6, only to increase again towards point 7.

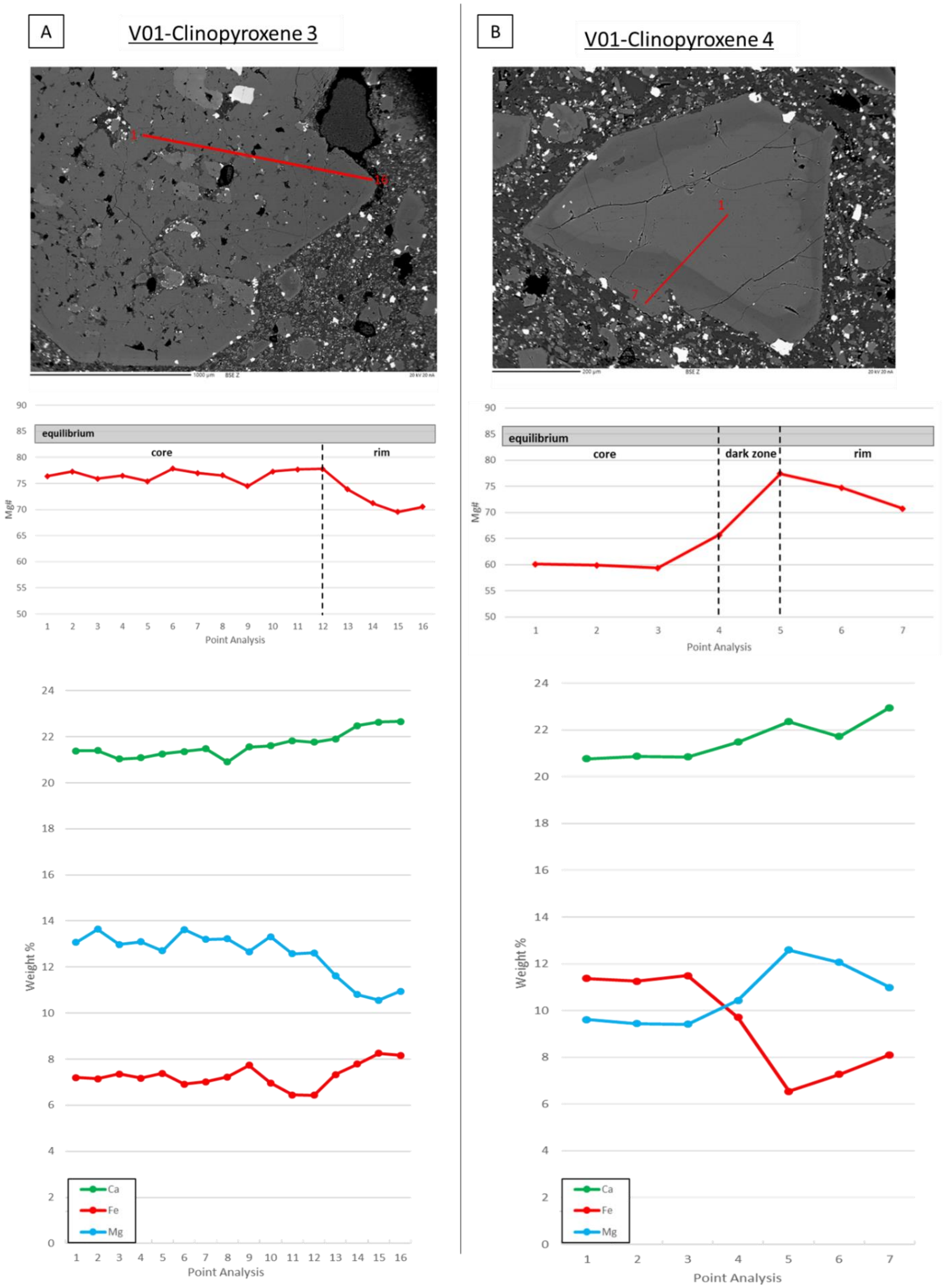

Figure 4.39: Two clinopyroxene traverses from volcano CC10. A) A large pyroxene displaying a sieve texture with spinel inclusions. The pyroxene exhibits constant Mg# values for the majority of the measurements until it reaches the rim of the mineral. B) A subhedral clinopyroxene crystal displaying pronounced sector zoning. The clinopyroxene Ca, Fe and Mg composition changes after "Point analysis 3". Neither clinopyroxene 3 or 4 is in equilibrium with the melt at any point. The grey field represents the whole rock Mg# equilibrium values based on K_D method (see text) of sample V01.

4.3.3 Plagioclase

The plagioclases of the BMVF are predominately microcrysts, making up the majority of the microcrysts in the groundmass phase. The several larger phenocrysts of plagioclase are usually xenocrysts from the surrounding country rock. Microprobe analysis of 11 plagioclase crystal laths show that the majority of the plagioclases are Ca rich with An content ranging from An_{54-92}. The plagioclases from volcano M11 have the lowest An% and plot within the labradorite field (Figure 4.40). The plagioclases from volcano M5 plots between the border of bytownite and labradorite. In addition, the plagioclases from volcano CC53 are the most Ca-rich of the measured plagioclases. One of the crystals plots in the bytownite field and two are close to being pure anorthite with An_{92}.

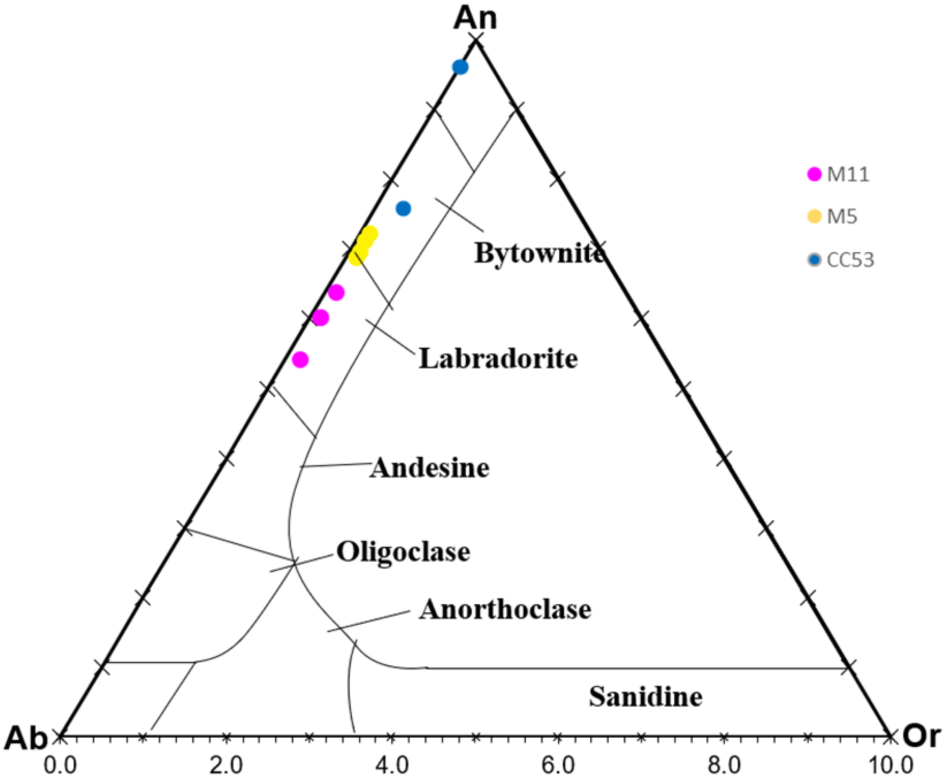

Figure 4.40: Felspar classification ternary diagram plotting the feldspar compositions of Volcanoes: M11, M5 and CC53. The classification diagram indicates the plagioclases of the BMVF are Ca rich plagioclases.

4.4 Thermobarometry

Olivine thermometry

Olivine thermometry is useful in demining the temperature at which the magma was stalled, and subsequent olivine crystallisation occurred in the crust. To produce useable temperatures from the thermometer, only olivines in equilibrium with the melt can be analysed. Olivines are considered to be in equilibrium with the melt if they have K_D (Fe-Mg) $^{cpx\text{-}liq}$ value of 0.30 ±0.03 (or ±1σ) (Roeder and Emslie, 1970). The test for olivines equilibrium can be graphically depicted by using the diagrams in Rhodes et al. (1979). Figures 4.41 A and B are the graphical depictions of olivine equilibrium values. Using diagrams to determine olivine equilibrium, as opposed to comparing K_D values only, allows for further interpretation of olivines that are not in equilibrium. The equilibrium test of the olivines (Figure 4.41A and B) makes it possible to classify them as a) autocrysts i.e. olivines that formed in and are in equilibrium with their host magma, b) antecrysts i.e. olivines that are not in equilibrium with their host melt and that were derived from other magmas or c) xenocrysts, olivines from a different lithology that were entrained in the melt (Coote et al., 2019). In Figure 4.38 olivines that plot within the "in equilibrium field" or on the +1σ/-1σ line are considered to be in equilibrium. Both Figures 4.41A and B show the small portion of olivines in equilibrium; only 27% of the measured olivines are in equilibrium with their host melt. When the olivines are plotted per volcano they are hosted in (Figure 4.41A) the relationship is unclear as it seems a small portion of each volcano's olivines are in equilibrium. When olivines are plotted as their classified types (Figure 4.41B) it becomes apparent that the majority of the olivines that are in equilibrium are type 2 olivines. Other olivine types that are in equilibrium are two type 3 olivines, two type 1 olivines (obscured by an olivine from volcano CC48).

The liquid-olivine thermometer devised by Beattie (1983) was used to calculate the temperatures of the olivines in equilibrium (Figures 4.41 C and D). The Beattie (1983) thermometer is highly accurate for temperatures calculated below 1650°C, having a Standard Error of Estimate (SEE) of only ± 10K. It should be noted that the Beattie (1983) thermometer overestimates temperatures when dealing with a hydrous melt (Beattie, 1993, Putirka, 2008). The calculations were based on the assumption that the BMVF rocks were produced from anhydrous melts. Figure 4.41A and B display the calculated temperatures as a function of the relevant volcano and as a function of olivine type, respectively. The temperatures calculated for the olivines in equilibrium range from 1215-1373°C. Figure 4.35C displays the different temperatures of each volcano, the lava flow: DX1 has the highest temperature while volcano M11 exhibits the lowest temperatures. The whole rock composition of volcano M11 is also more siliceous than the other host melts. When the olivines are plotted as olivine types, the type 2 olivines have the most significant spread of olivine temperatures ranging from 1243-

1310 °C. A pair of type 2 and type 3 olivine temperatures are the calculated temperatures of olivines that are both hosted in volcano M11. They have identical temperatures of 1215 °C. Olivines from volcanoes CC10, CC44, CC53 and M7 indicate similar crystallisation temperatures of 1244-1273°C. The spreadsheet provided by Putirka (2008) was used for all calculations.

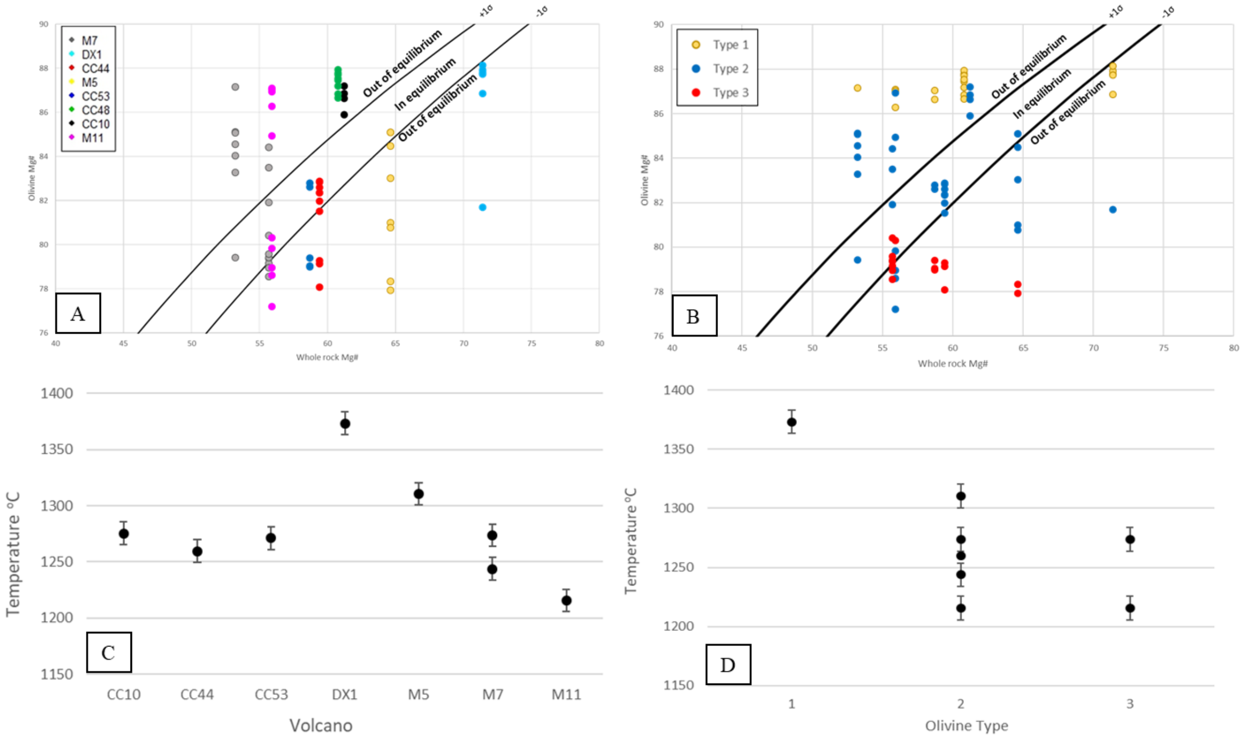

Figure 4.41: Equilibrium tests plotting #Mg of whole rock against Mg# of olivines (Rhodes et al., 1979). A) Olivines plotted as a function of the host volcano B) Olivines plotted as function of type. Calculated temperatures (°C) of olivines in equilibrium based on Beattie (1993) are plotted as a function of the C) host volcano and D) the olivine type. SEE = ±10K.

Clinopyroxene thermobarometry

Clinopyroxenes are extremely useful for determining the plumbing system of volcanoes as there are clinopyroxene and clinopyroxene-liquid thermobarometers that can determine temperatures and pressures of clinopyroxenes that crystallised in equilibrium with a chosen liquid (Putirka et al., 1996, Putirka et al., 2003, Putirka, 2008, Neave and Putirka, 2017). The whole rock composition was selected as the liquid in the calculations. The calculations were performed using the spreadsheet provided by Putirka (2008).

Thermobarometry can only provide accurate results if the clinopyroxenes are in equilibrium with the whole rock they are hosted in. The equilibrium test of clinopyroxene works similar to that of the olivine equilibrium test; if the measured clinopyroxene has K_D (Fe-Mg) $^{cpx\text{-}liq}$ of 0.27±0.03, it is considered to be in equilibrium. Calculating equilibrium values relying only on Fe-Mg exchange coefficients would ignore the effects of Ca-Na and Na-Al exchange coefficients in clinopyroxene and possibly produce erroneous equilibrium values (Putirka, 2008). Rhodes et al. (1979) and Putirka (1999a, 2005b, 2008) determined that when Ca-Na and Na-Al exchange coefficients are taken into account, the equilibrium values remain similar to when they are not included. To simplify the calculations, only the K_D(Fe-Mg) $^{cpx\text{-}liq}$ was used to determine equilibrium. Figure 4.42A is a graphical depiction of clinopyroxene cores in equilibrium. Of the 14 clinopyroxene cores that were measured, only one clinopyroxene from volcano CC10 falls within the equilibrium field. The rims of the clinopyroxenes do not have a single measurement that is in equilibrium. Figure 4.42B, showing the one clinopyroxene from volcano CC10 that formed in equilibrium, disequilibriated with the melt as the crystal grew. The overall trend in the core to rim composition is a decrease in Mg# as the system becomes more Fe rich.

The clinopyroxene hosted in volcano CC10 alongside a clinopyroxene, which is almost in equilibrium, hosted in volcano M5 was used to calculate pressure and temperature (Figure 4.42C).The barometer used to calculate pressure devised by Neave and Putirka (2017) has a SEE=1.4kbar and Equation 33 in Putirka (2008) was used to calculate the temperature having a SEE=±14 ^{o}C. The temperatures of the volcano CC10 clinopyroxene and the volcano M5 clinopyroxene are 1112 ^{o}C and 1095 ^{o}C, respectively. The two clinopyroxenes differ by 17 ^{o}C, which is just outside the SEE=±14 ^{o}C of the thermometer. The pressures of the CC10 and M5 clinopyroxenes are 775.6 MPa and 843.6 MPa respectively. The difference between the two clinopyroxenes is 68 MPa, which falls well within the barometer’s SEE=1.4kbar(140MPa). Nevertheless, the small amount of clinopyroxenes cores in equilibrium makes determining usable pressure and temperature values for the entire system improbable.

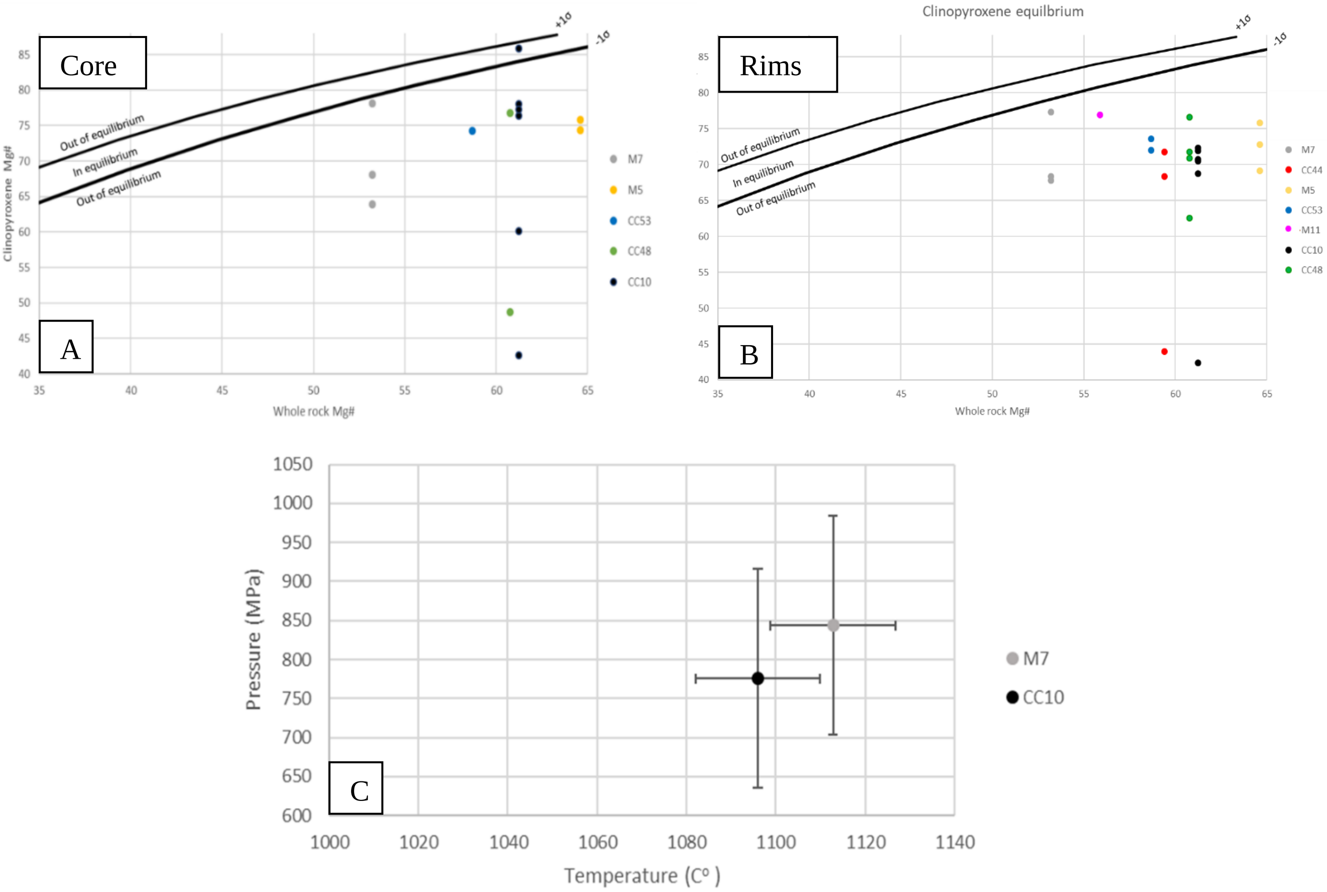

Figure 4.42: Equilibrium test comparing Mg# of the whole rock and the Mg# of a clinopyroxene: A) equilibrium test of the clinopyroxene cores B) equilibrium test of the clinopyroxene rims (Rhodes et al., 1979).

Plagioclase thermobarometry

Plagioclase is useful in determining the plumbing system constraints of a volcano as it can also be used to calculate pressure and temperatures. Plagioclase barometers are not accurate enough to be stand-alone pressure indicators; barometers based on plagioclase can only be used in conjunction with pressures calculated through more reliable barometers (Putirka, 2008). Only plagioclase with equilibrium in the melt can be used for the calculations. The whole rock composition is taken as the melt composition. Plagioclase with a $K_D(Ab\text{-}An)^{plg\text{-}liq} = 0.28 \pm 0.11$ are considered in equilibrium for temperatures >1050 °C. Of the 11 measured plagioclase laths, 9 crystals have a $K_D(Ab\text{-}An)^{plg\text{-}liq} = 0.25 \pm 0.05$, while 2 plagioclase laths from volcano CC53 have a $K_D(Ab\text{-}An)^{plg\text{-}liq} = 0.03$ and are considered to be out of equilibrium with the melt. The two plagioclases that are out of equilibrium are the An_{92} plagioclases. The disjointed nature of their composition compared to the other, plagioclases in equilibrium, could indicate that the An_{92} plagioclases are xenoliths. Equation 23 of Putirka (2008) was used as the plagioclase thermometer. Plagioclase thermometry of the BMVF produced temperatures of 1165 °C ± 20°C. Equation 25a from Putirka (2008) was used as the barometer. Plagioclase barometry produced pressures of 850MPa ±200MPa. Volcano CC53 produced the plagioclase with the highest temperature and pressure, volcano M11 produced the plagioclase with the lowest temperature and pressure. The pressure temperature graph (Figure 4.43) showcases an interesting trend observed in plagioclases from volcanoes M11 and M5. The temperatures of the plagioclases increase as pressure decreases. The changes in temperature are minor compared to the large changes in pressure and can be attributed to the SEE and the selected x-axis scale.

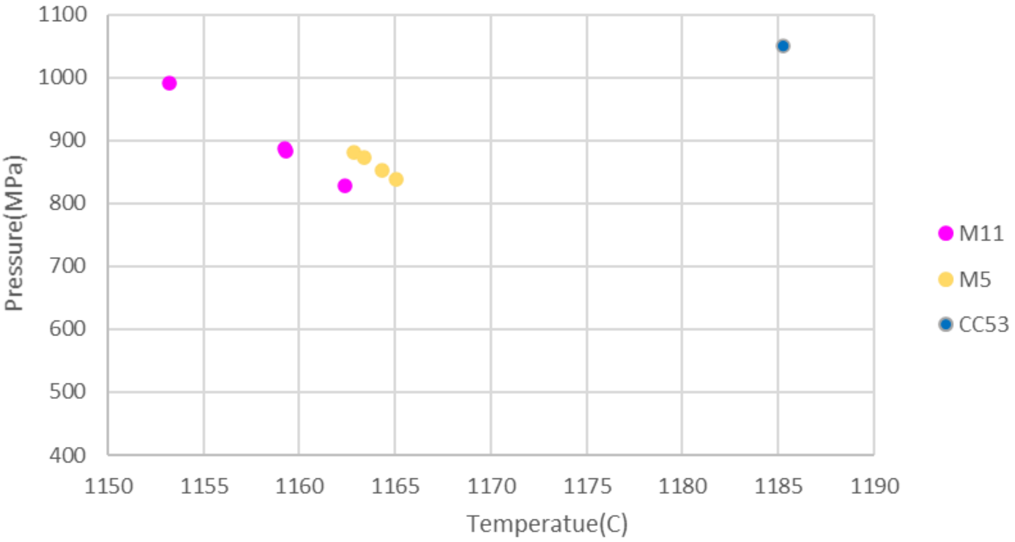

Figure 4.43: Pressure-temperature plot of the plagioclase laths from volcanoes M11, M5 and CC53. The temperatures of the plagioclases found in volcano M11 and M5 remain relatively constant with large changes in pressure. The single plagioclase measured from volcano CC53 has the highest pressure and temperature of the measured plagioclases.

5 Discussion

5.1 Petrogenesis of the BMVF

The BMVF consists of compositionally primitive lava flows and tephra deposits. The SiO_2 undersaturated rocks are prevalent throughout the entire BMVF (Figure 4.19A). The rock compositions range from basanite, basalt, trachybasalt, and basaltic andesite coinciding with the observations of Almond (1974) and, Almond et al. (1984) where the authors additionally reported small occurrences of phonolite. The BMVF is classified as an alkali basaltic volcanic field due to the high alkali (K_2O/Na_2O) content (Figure 4.19A and B) and trace element classification diagrams Nb/Yb vs TiO_2/Yb (Figure 4.19C) and Nb/Y vs Zr/Ti (Figure 4.21). Alkali basalts can simply be classified as sodic or potassic alkali basalts depending on their Na or K contents respectively (Farmer, 2014). The BMVF is considered a sodic-alkali basalt field due to the high Na (~2-4 wt%) (Figure 4.20F) content alongside high TiO2 wt% (~1.7- 3 wt%) (Figure 4.20G) content which is characteristic of sodic alkali basalts throughout the world (Farmer, 2014). Alkali basalts occurring in small scale intraplate volcanism are either derived from later eruptions of a tapped magma chamber or magma that was tapped directly from the mantle (Smith et al., 2008). The melt that usually produces mafic, sodic alkali basalts is typically the product of small-scale melting (<1%) through either plume related activity or passive upwelling of the mantle (Fitton and Dunlop, 1985).

The primary phenocrysts assemblage is made up of olivine, clinopyroxene and minor spinel. Alongside the phenocryst phase is a subordinate xenocryst group consisting of plagioclase, garnet and minor orthopyroxene. The phenocryst phases remain constant throughout the volcanoes studied. The groundmass consists of plagioclase laths, microcrysts of the larger phenocrysts, and magnetite. XRD analysis (Appendix B) indicates that nepheline phases are present in the BMVF. However, no visible nepheline was found during microscopic analysis. Similarly, in the paper by Almond et al. (1984) the authors only found normative nepheline but no visible phase of nepheline when analysed with a petrographic microscope. The nepheline, therefore, can be assumed to form part of the groundmass as a small microcryst phase.

The sequence of crystallisation is determined through the textural evidence (Figures 1-18) major element plots (Figures 4.20A-H), trace element plots (Figures 23) and thermometry. Textural evidence shows that clinopyroxene overgrows olivine (Figure 4.4C), indicating that olivine crystallised before clinopyroxene. Spinel inclusions in the major phenocrysts phases suggest that are they are intratelluric, phenocrysts that represent the earliest form of crystallisation (Hoshide and Obata, 2014). The phenocrysts without spinel inclusions generally represent later stages of crystallisation with magma recharge (Cox et al., 1979). The small crystals sizes of the groundmass imply that they crystallised last, when the magma was quenched. Therefore, the plagioclase, and magnetite crystals were among the last crystals to form. In most cases spinel is rimmed by magnetite (Figure 4.9F, Figure 4.11E, 4.16F), indicating magnetite formed after the spinel. However, care should be taken with crystal size as subordinate phases like apatite and chromite form small crystals despite of cooling rate (Cox et al., 1979).

The textural evidence exhibits fractionation sequence of:

Spinel + olivine + clinopyroxene + plagioclase + magnetite

The overall sequence is derived from petrographical thin sections of several volcanoes and cannot accurately represent the fractionation sequence occurring at a single volcano.

Whole rock and trace element geochemistry can aid petrographical estimations of the crystallisation sequence. The overall decline in SiO_2 as MgO increases represents the crystallisation of olivine (Figure 4.20A). The Fe_2O_3 vs MgO (Figure 4.20C) shows an initial enrichment phase followed by a depletion stage. This is typical for mafic melts as Mg gets incorporated into olivine initially, but this in turn causes the Mg composition of the melt to decrease. Fe^{2+} is the second most suitable ion for the M2 spot in olivine and is subsequently removed from the melt to crystallise Fe rich olivine, Iron-rich phases such as magnetite also formed. The overall decline in CaO (Figure 4.20D) indicates the crystallisation of the calcium-rich clinopyroxene, diopside and the calcium-rich plagioclases. The two-pronged trend observed in the K_2O vs MgO (Figure 4.20E) diagrams is most likely the transition from calcic plagioclases fractionation to sodic plagioclases fractionating at ~10 wt% MgO. The Ni vs Cr (Figure 4.23A) also indicates an early onset of olivine crystallisation. As Ni is compatible with olivine, the overall decline in Ni indicates Ni is removed from the melt as it is partitioned into olivine. The Ni vs Cr diagram also shows the crystallisation of clinopyroxene from the melt. Cr is compatible in clinopyroxene. The positive trend in Cr indicates a partitioning of Cr into the clinopyroxene and the subsequent removal of Cr from the melt. An increase in Sr as the magma evolves suggest that spinel is initially the preferred aluminous phase (Brenna et al., 2011)(Figure 23D). The depletion of Cr, Ni and V alongside the enrichment of Sr as the magma evolves indicate the crystallisation of olivine, clinopyroxene and spinel e.g. (Brenna et al., 2011). When relying on whole rock and trace element chemistry to determine the crystallisation sequence, it roughly resembles the textural evidence crystallisation sequences. The implied crystallisation sequence of the BMVF based on whole rock geochemistry is the following:

olivine + clinopyroxene + magnetite (±nepheline) + plagioclase

In a system that is cooling down, the minerals with the highest crystallisation temperatures correspond to ones that formed first. When crystallisation temperatures of olivine, clinopyroxene and plagioclase are compared with the crystallisation sequences discussed above, the olivine temperatures coincide with olivine forming first. Olivine has the highest crystallisation temperatures of the measured minerals (1373°C) (Figures 4.35A and B). Clinopyroxene thermometry indicates that measured clinopyroxenes forms at lower temperatures (1110°C) than the measured plagioclases (1165°C). Therefore, the implied crystallisation sequence of the BMVF based on olivine, clinopyroxene and plagioclase is as follows:

olivine + clinopyroxene

Thermometry with limited minerals cannot be used to much effect to determine the crystallisation sequence. Although the thermometry estimates agree with the petrography and geochemistry crystallisation sequences, the small amount of measured minerals cannot represent the entire field.

The crystallisation sequence of the BVMF is based on textural evidence, whole rock and trace element chemistry:

Spinel + olivine + clinopyroxene + magnetite + plagioclase

The assemblage can only be deduced when the plagioclase, orthopyroxene and garnet xenocrysts are excluded from the sequence.

Source of the Melt

The limited range of radiogenic isotopic compositions of the BMVF indicates the simplicity of its mantle source. The BMVF $^{87}Sr/^{86}Sr$ and $^{143}Nd/^{144}Nd$ isotopic signatures resembles the HIMU mantle endmember (Figure 4.31A). Nevertheless, the defined HIMU signature is not seen in the other radiogenic isotopes. The offset is interpreted as the presence of a secondary, depleted mantle component. In addition to a HIMU mantle source, the BMVF has a DMM mantle endmember that mixed with the HIMU mantle endmember component to produce the signature of the BMVF. The mixing of HIMU (enriched) and DMM (depleted) mantle components is a common mixing trend of Cenozoic volcanoes e.g. (Sims et al., 2008, Moufti et al., 2012). The mixing of these reservoirs imply that the melts were sourced from the asthenosphere (Fitton et al., 1997, Moufti et al., 2012). Therefore, the isotopic signature of the BMVF is the product of mixing a HIMU and DMM mantle endmember components.

The source lithology of the BMVF has to reflect the sodic alkali basalt composition and the mineral assemblages of the lavas of BMVF.

Radiogenic isotope diagrams $^{87}Sr/^{86}Sr$ vs ε_{Nd} (Figure 4.30A), $^{206}Pb/^{204}Pb$ vs $^{207}Pb/^{204}Pb$ (Figure 4.30B), trace element diagram plots Nb/Yb vs TiO2/Yb (Figure 4.24D), La/Yb vs Nb/La (Figure 4.21B) and the REE spider plot (Figure 4.24) indicate that the lithologies of the BMVF resemble elemental compositions of OIB. OIB island trace element signatures are expected for small scale alkali basalts (Farmer, 2014). REE's are useful in determining characteristics of the source rock as well as the degree of melting. Due to LREE being highly incompatible in solid phases, they tend to be concentrated in the melt. REE are incompatible in solid phases. REE reflects the amount of partial melting that occurs at the source rock, are highly incompatible. As the melt fraction increases, their concentration decreases as more elements are incorporated into the melt. The high content of LREE of the BMVF lithologies (Figure 4.24) indicates low partial melting from the source material that the magmas are derived from. The REE plots of the different volcanoes are parallel to one another, but with varying concentrations of REE suggesting a single source lithology with different degrees of melt producing the volcanic lithologies. The REE diagrams display a strong negative trend in HREE, representing a depletion in HREE (Figure 4.24). The depletion of HREE indicates garnet in its source rock as garnet is a repository for HREE (e.g. Brenna et al. 2011). Garnet xenocrysts are also found in samples of the BMVF (Figure 4.5F), with a reaction rim of kelyphite indicating that they are out of equilibrium with the host melt. Garnet is not stable throughout the entire mantle. At pressures lower than 2.5 GPa, the stability field favours the spinel phase from 2.5 - 1.5 GPa (Walter, 1998). The presence of garnet in the source provides a limiting source depth of at least 2.5 GPa (Walter, 1998). The Ba/Rb vs Rb/Sr diagram (Figure 4.22B) indicates that a few melts were derived from a source lithology containing amphibole and sample I-6 of volcano M8 indicates that a melt was derived from a source with phlogopite. Amphibole in the source lithology coincides with the observations made by Lucassen et al. (2010) of mantle xenoliths of the BMVF.

Trace element modelling can estimate the percentage of melt and/or fractionation from a selected source rock to produce the magmas of the BMVF. Salters and Longhi (1999) calculated the partitioning coefficients of trace elements in rock assemblages consisting out of olivine, clinopyroxene, orthopyroxene, garnet, and spinel. The partitioning coefficients were calculated at specific pressures, enabling a trace element melt model to estimate the depth of the melt generation. The 2.8 GPa and 2.4 GPa calculated Zr, Hf and Nb partitioning coefficients of Salters and Longhi (1991) were used for the trace element melting model of the BMVF. However, Salters and Longhi (1991) did not calculate all of the selected trace element partition coefficients used in the model. The partitioning coefficients for clinopyroxene at 2.4 GPa were calculated by Brenna et al. (2011), the olivine coefficients (at all pressures) were calculated by Fujimaki et al. (1983), and spinel partitioning coefficients at 2.5GPa were calculated by Elkins et al. (2008). The selected trace element coefficients and melting model is based on the model used by Brenna et al. (2011). Primary mantle compositions estimated by Sun and McDonough,

(1989) ; and Palme and O'Neill, (2003), and a mantle xenolith source rock averaged from 6 mantle xenoliths from the BMVF (Lucassen et al., 2011) were used as the source rock lithologies. The model uses Nb/Zr and Zr/Hf to determine the source rock, the depth of melting, the melt% and the occurrence of fraction. The melting model program PETROMODELERv4 (Ersoy, 2013) was used to produce the melting curves (Figure 5.1) using the partitioning coefficients from Table 2.

Table 1. Partitioning coefficients of Zr, Nb and Hf for selected minerals at calculated pressures. Olivine partitioning coefficients remains constant over an array of pressures. Partitioning coefficients of clinopyroxene, orthopyroxene and garnet are the averaged values of KD of samples from Salters and Longhi (1999). See text for olivine,spinel and 2.4 GPa clinopyroxene references.

Phenocryst phase:	*Garnet*	*Clinopyroxene*	*Orthopyroxene*	*Garnet*	*Clinopyroxene*	*Orthopyroxene*	*Olivine*	*Spinel*
Pressure	2.4 GPa	2.4 GPa	2.4 GPa	2.8 GPa	2.8 GPa	2.8 GPa	-	2.5 GPa
K_D (Zr)	0,656	0,051	0,019	0,555	0,038	0,22	0	0,0081
K_D (Nb)	0,01	0,01	0,0033	0,0179	0,0073	0,001	0,011	0,006
K_D (Hf)	0,68	0,085	0,0328	0,588	0,06	0,588	0,011	0,003

The melting curves of the BMVF indicate that the mantle xenoliths found in the lava flows of the BMVF were most likely the source lithology for the melt produced (Figure 5.1C). The xenolith source lithology composition is very similar to a garnet pyroxenite (Lucassen et al., 2011) and Primary Mantle of both Sun and McDonough (1989) and Palme and O'Neill (2004) but has a lower Zr/Hf ratio. The Zr/Hf ratio is sensitive to fractionation, when fractionation occurs in a system; the Zr/Hf ratio decreases (Brenna et al., 2011). The Nb/Zr and Zr/Hf ratios of the mantle xenoliths are slightly higher than the ratios of the primary mantle sources and could indicate that the mantle xenoliths of the BMVF were derived from Primary Mantle like source lithologies at pressures between 2.4 GPa and 2.8GPa. The majority of the BMVF compositional ratios plot in the proximity the 2.8 GPa melting curve by using the mantle xenolith composition as a source rock (Figure 5.1C). The magma derived from the source lithology indicates 1- 4% melting when following the 2.8GPa fractional melting curve and 1- 4% when following the 2.8GPa batch melting curve. The plots of the BMVF has vertical and horizontal variation, which indicates the magma differentiation is a product of partial melting and fractionation respectively. The variation in Zr/Hf could also indicate the metasomatic enrichment of the mantle source (Brenna et al., 2011). The Ba/Rb vs Rb/Sr diagram (Figure 4.22B) indicates the presence of minor amphibole and phlogopite that formed during metasomatism in the mantle. The OIB normalised spider plot (Figure 4.26) displays a negative trend for CS and Rb suggesting that they were incorporated in a phlogopite phase

(LaTourrette et al., 1995). This suggests that melt might have experienced a minor mantle metasomatic enrichment event e.g. (Le et al., 2019). The two outlier samples may suggest a different source or extreme fractionation. However, this is not likely. The two samples, II-4 and II-5, are both scoria samples from volcano CC48. The most likely explanation for their distinctive Zr/Hf signature is improper cleaning and removal of dust during sample preparation.

The melting models are not an exact representation of the melting, but merely an estimate. It can be inferred that a source rock resembles a garnet-bearing lithology with a composition similar to that of the Primary Mantle that possibly experienced minor metasomatism. The source rock of the BMVF is most likely the mantle xenoliths described by Lucassen et al., (2011) as a garnet pyroxenite. Nevertheless, the large concentration of olivines in the final mineral assemblage also point to garnet peridotite as possible source rock. The source rock experienced a combination of 1-4% fractional melting as well as minor fractionation at a later stage to produce the primitive melts of the BMVF.

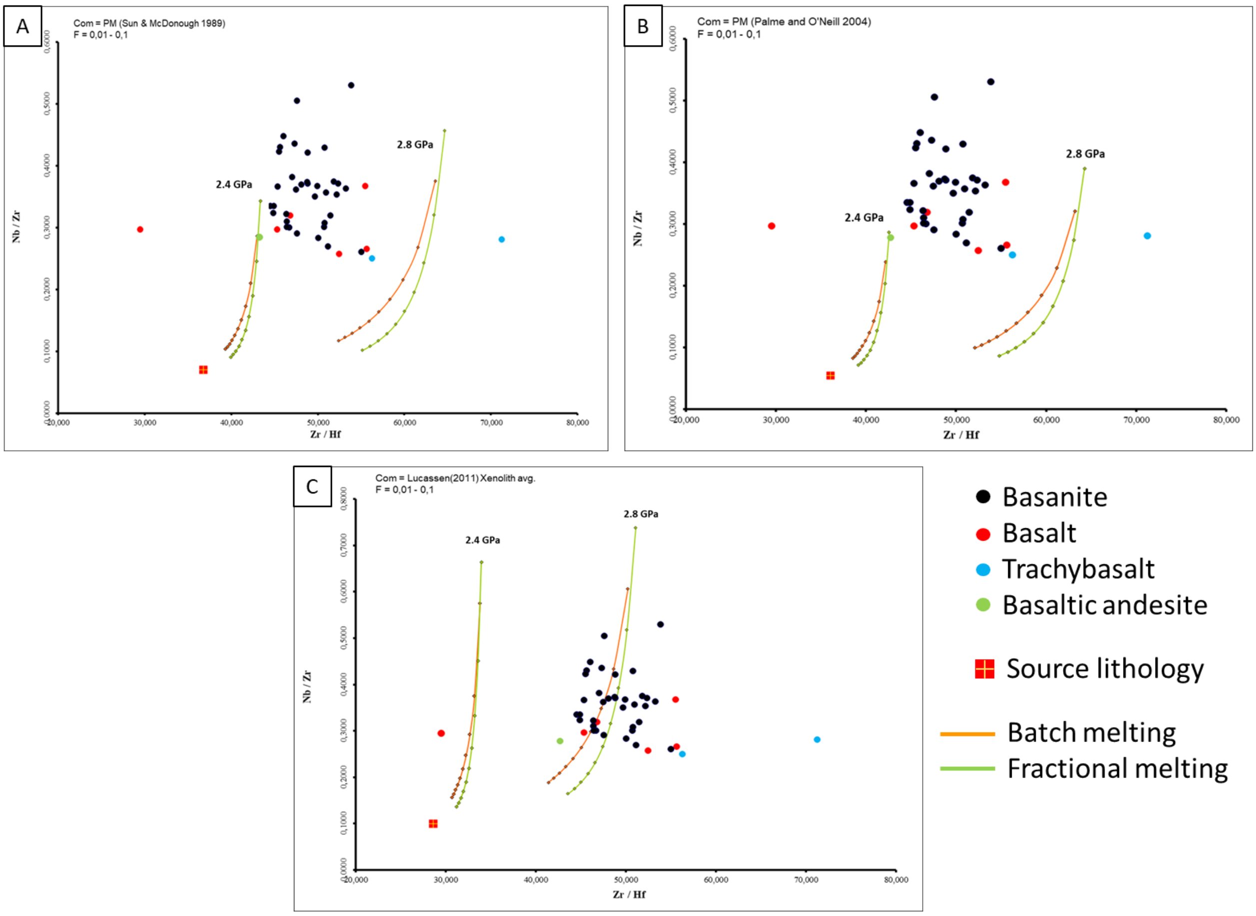

Figure 5.1. Melting curves representing the melt genesis of the BMVF plotted as a function of rock type. The different melt curves are modelled with the different source lithologies A) Primary Mantle (Sun and McDonough, 1989), B) Primary Mantle (Palme and O'Neill, 2003) and C) The mantle xenoliths of the BMVF(Lucassen et al., 2011). The melting curves were calculated at pressures 2.4GPa and 2.8GP using batch melting and fractional melting models. Melting curves start at 1% melting with increments of 1%.

Magma mixing

Numerically modelling magma mixing of a monogenetic field is not practical. Zoning in minerals is a simple method in evaluating magma differentiation. Differently zoned sections of a mineral reflect the changing magma composition and conditions that they are formed in. This change in zoning can also indicate magma mixing. Reverse zoning in minerals typically indicates magma mixing.

The clinopyroxene traverses from volcano CC10 (Figures 4.39A and B) exhibit the effects of magma mixing. Clinopyroxene 4 from volcano CC10 (Figure 4.39B) displays reverse zoning, which is the simplest indication for magma mixing. Minor aspects of the secondary magma's composition can be determined by analysing the mantles of the clinopyroxene 4. In addition to being more primitive in general, the increase in Ca content in the dark mantle suggests that the second magma is more enriched in Ca. The increase in Mg# from core to rim in Clinopyroxene 4 is interpreted as a secondary, primitive magma (high Mg#) mixing with an initial, more evolved magma (lower Mg#) that Clinopyroxene 4 formed in. Clinopyroxene 3 does not exhibit the reverse zoning pattern seen in clinopyroxene 4 and therefore crystallised under different conditions. The core Mg# of clinopyroxene 3 resembles the rim Mg# of clinopyroxene 4, indicating that clinopyroxene 3 crystallised after the suggested mixing event.

Trace element ratios that are not sensitive to fractionation can be used as a method of detecting magma mixing. If there is any variation in a selected incompatible trace element ratio, the differences can be attributed to magma mixing as fractionation would not have an effect on the trace element ratio. Figure 5.2 uses the Rb/Nb ratios to indicate magma mixing (Ngwa et al., 2019). Any variation in Rb/Nb ratio is attributed to two different sources. The diagram shows two distinct groups and an outlier when classified by Rb/Nb ratio. The outlier could represent a third batch of magma, but more samples would be need to prove this hypothesis. The two distinct magma batches alongside the reverse zoning in clinopyroxene 4 are interpreted as magma mixing occurring at volcano CC10. Although magma mixing played a part in volcano CC10's formation, it cannot indicate that magma mixing is a defining characteristic of the BMVF. An in-depth look at the plumbing system can determine the roll of magma mixing in the BMVF.

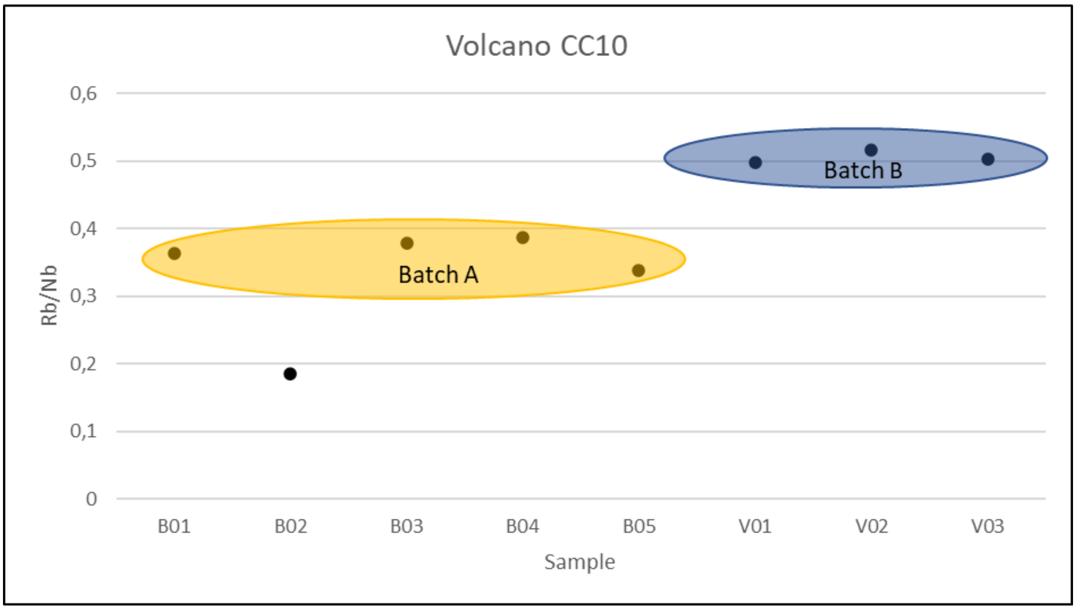

Figure 5.2. Rb/Nb ratios of volcano CC10. The ratios of volcano CC10 are divided into two groups of similar Rb/Nb ratios.

The Plumbing System

The plumbing system of a volcano refers to the network of subsurface magma filled dykes, chambers and conduits that interconnect and lead to the surface volcanic structure (Smith and Németh, 2017). The plumbing system of a monogenetic volcano can be relatively simple due to its singular eruptive nature and primitive compositions (Németh and Kereszturi, 2015, Smith and Németh, 2017). As more monogenetic volcano plumbing systems are studied it is becoming apparent they can be more intricate than expected (Németh et al., 2003, Németh and Kereszturi, 2015, Murcia et al., 2019, Coote et al., 2019). The implied plumbing system of the BMVF is mainly based on the olivine types (Figure 4.35) due to their ubiquity in the BMVF. Olivines are useful in determining plumbing systems, as they tend to crystallise first, they represent the earliest conditions of the melt. In this way they give insight into the early stages of the volcanic field's formation. Knowing whether olivines are autocrysts, antecrysts or xenocrysts can help determining magma differentiation and any other open system dynamics. The olivine types (Figure 4.35) in conjunction with equilibrium tests, thermobarometry, geochemistry and textural evidence alongside the analysed clinopyroxene and plagioclase are used to determine the suggested plumbing model of the BMVF.

The majority of the eruptions of the BMVF were basanitic, indicating the magma was directly tapped from the mantle and brought to surface with little to no differentiation. However, the occurrence of more evolved compositions like trachybasalt reported in this project and phonolite compositions reported in (Almond, 1974, Almond et al., 1984) indicates that magma was not only directly tapped from the mantle and erupted after a short travel time. Magma stagnation in the crust had to occur for the more evolved compositions like trachybasalt and phonolite to form. Barometry can indicate at what pressure, and by extension, what depth crystallisation occurred. The only reliable pressures calculated are the two clinopyroxenes in equilibrium (Figures 4.42A and C). Both clinopyroxenes crystallised at ~810MPa. If the continental crustal density is assumed to be 2.8 x10^3 kg/m^3 e.g. (Coote et al., 2019), the calculated pressures of the clinopyroxene indicate crystallisation between 30-33.3km. The crystallisation depth of the measured clinopyroxene is roughly the same as the MOHO boundary indicated by Lucassen et al. (2011) (36km depth). This crystallisation depth of the clinopyroxene crystal is the only indication of a stable, reliable crystallisation depth. Plagioclase barometry, as mentioned above, is not reliable and cannot be applied to the plumbing model.

When using the K_D equilibrium test for olivines (Figure 4.41A and B) and clinopyroxenes (Figure 4.42A and B) it is possible to estimate the Mg# of the magmas that form part of the BMVF plumbing system. The calculated olivine K_D (Fe-Mg) equilibrium values (Figure 5.3) indicate the olivines crystallised in magmas with Mg#50-67 (average= Mg#59). The calculated clinopyroxene K_D (Fe-Mg) core (Figure 4.41) equilibrium estimates indicate the clinopyroxenes crystallised in magmas with Mg#19-62 (average = Mg#41). The K_D (Fe-Mg) estimated Mg# of the magma the olivines crystallised in and generally correspond with the Mg# of the erupted material (Appendix A). However, the K_D (Fe-Mg) estimated Mg# of the magmas the clinopyroxenes crystallised do not correlate with the Mg# of the erupted material (Figure 4.42). The clinopyroxenes therefore crystallised in a more evolved melt (a magma of a lower Mg#) than the olivines. The low Mg# of the melt when clinopyroxene started to crystallise represents a melt that has experienced some fractionation. The olivines and clinopyroxenes most likely formed in the same magma batch, but as olivine crystallised out, the melt became more evolved. The clinopyroxene K_D estimates represent the evolved magma. The change in melt Mg# from olivines to clinopyroxene confirms clinopyroxene formed after olivine. The observed olivines and their subsequent types can further be applied to elucidate the open source dynamics occurring at the BMVF.

Typically, large, euhedral, Mg-rich olivines with spinel inclusions are interpreted as mantle xenoliths (Ray et al., 2016, Brenna et al., 2018). Despite several olivines of the BMVF displaying these characteristics, none of the olivines of the BMVF are mantle derived. Figure 4.33 indicates that the olivines are too Ca rich and Ni poor to be considered as mantle derived olivines. None of the measured olivines are xenocrysts are all therefore autocrysts in the magmatic system. The olivines will therefore be termed as phenocrysts and microphenocrysts based on their core compositions.

Ni contents in olivines are dependant the composition of the parental rock as well as temperature. The $D_{Ni}^{Ol/melt}$is negatively related to temperature So olivines crystallising at high temperatures will have higher Ni contents than olivines forming a lower temperatures (Li and Ripley, 2010). The compatible nature of Ni in olivine at high temperatures allows for classification in terms of olivine crystallisation sequence. In addition, Mg is preferred when olivine initially crystallises but as pressure decreases, Fe becomes the preferred over Mg. When Ni and Mg# number is combined, a holistic olivine crystallisation sequence can be determined. The olivine types of Figure 4.35 illustrate the grouping of olivines by Ni and Mg# content.

If olivine Ni and Mg contents decreases with a drop in temperature and pressure, the olivine with the highest Ni and Mg contents would represent the first olivines that formed and the olivines with the lowest Ni and Mg contents would represent the last olivines to form. Type 1 olivines represent the first phase of olivine crystallisation as it has the highest Mg and Ni contents.

The second phase of olivine crystallisation was during magma ascension. The compositions of these olivines are marked by varying compositions of both Mg and Ni. Initial depletion of Ni is source related, but as temperature drops Ni becomes less compatible in olivine (Simkin and Smith, 1970, Sato, 1977). As temperature and pressure decreases during magma ascension the partitioning of Fe becomes preferred over Mg, leading to a sequence of olivines that display a gradual decrease in Ni and Mg mirroring the gradational rise of the magma. Type 2 olivines represent the olivines that crystallised during ascension.

The third phase of olivine crystallisation was at low pressure and temperature that typically occurs at the surface/subsurface. At shallow depth Ni partitioning into olivine has reached its lowest and partitioning into the olivine will remain constant throughout this phase of crystallisation. Fe is still preferred in olivine over Mg leading to a decrease in Mg#. Surface/subsurface olivine crystallisation is represented by type 3 olivines. In addition, the high Ca content of the majority of type 3 olivines further indicate crystallisation at shallow depths (Simkin and Smith, 1970)

Magma Mg# estimates derived from the K_D(Fe-Mg) of olivines indicate that the different olivine groups crystallised in magmas with different Mg#. The Mg# of the magmas decreases from the crystallisation of type 1 olivines (average= Mg#67) through to the crystallisation of type 3 olivines (average= Mg#53). The declining trend seen in Figure 5.3 confirms the olivines represent different phases of olivine crystallisation in an evolving system.

The olivine cores therefore act as a gauge of analysing the plumbing systems at different phases. This could especially be useful in detecting magma differentiation through fractionation and possible magma mixing.

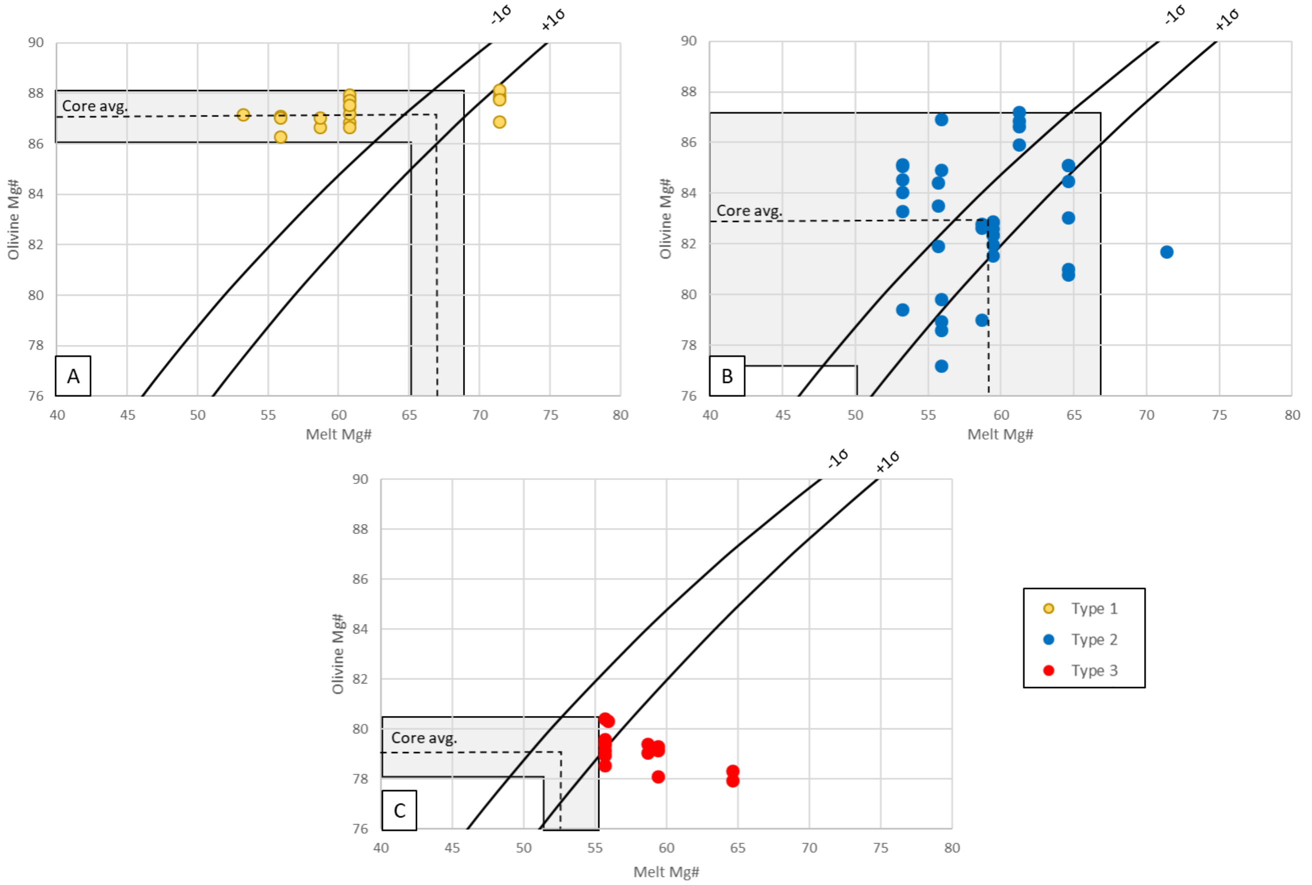

Figure 5.3. The estimated Mg# of magmas based on the K_D equilibrium test vs. core Mg# of olivines were used to estimate the corresponding magma they formed in. The dashed line represents the melt Mg# derived from the average olivine Mg# composition. The grey field represents the entire range of Mg# melt estimates.

Type 1 olivines crystallised in melts with Mg# 65-69 (average=Mg#67). At this phase of crystallisation, the melt has not been differentiated to a large degree. The homogeneity of type 1 olivine compositions indicates a stable crystallisation environment. The high Ni and Mg contents suggest deep crystallisation, indicating that the type 1 olivines crystallised at the base of the plumbing system, before any major differentiation. Due to the euhedral crystal habit and large size of many of the olivines, type 1 olivines most likely formed in a magma chamber beneath the BMVF. The proposed magma chamber also started to crystallise minor clinopyroxenes, until a recharge event dislodged the phenocrysts assemblage and forced the olivines to ascend.

The type 2 olivines indicates that the ascension phase of crystallisation is where the majority of magma differentiation occurred. Type 2 olivines crystallised in a melt with Mg#50-67 (average=Mg#59). The changing environment is not only reflected in the composition but in the array of different zoning types of type 2 olivines (Figure 4.37, Appendix E). The most primitive type 2 olivines form part of olivines that are most enriched in Ca. Type 1 olivines with similar Mg# does not reflect the high Ca content. The first group of Ca-enriched olivines indicate the initial phase ascension, where Ca increases as it becomes preferred in the crystal lattice at lower pressures and lower temperatures (Simkin and Smith, 1970, O'Reilly et al., 1997, De Hoog et al., 2010). The second group of high Ca-rich type 2 olivines are interpreted as the product a mixing event that occurred during the ascent phase. The Ca rich olivines are thought to be derived from the secondary, Ca rich, magma that formed the dark mantle on Clinopyroxene 4 of volcano CC10 (Figure 4.39 B). The two slopes indicating Ca depletion in Figure 4.35D are interpreted as Ca-rich phase that starts to crystallise. In many cases plagioclase formation would suggest a Ca depletion in the system (Abratis et al., 2015) but the rocks of the BMVF lacks a plagioclase phenocryst phase. The Ca depletion is interpreted as Ca-rich clinopyroxene that starts to crystallise in the system at 2 different phases. As the magma is ascending, the first phase of clinopyroxenes crystallise at deeper levels than the second phase of crystallisation. Interestingly, the Ca content of the type 2 olivines never decreases below 0.2 wt%. The overall enrichment of Ca in the system during the ascension indicates that type 2 olivines and clinopyroxene phenocryst assemblages crystallised before any major plagioclase fractionation.

Type 3 olivines consist of subhedral, micro-phenocrysts (Appendix E) that form part of the groundmass. The last phase of olivine crystallisation was marked by small, rapid change in olivine composition (Figures 35 B, D and F). The pronounced increase in Ca content of type 3 olivines indicate rapid decrease in both temperature and pressure. Alongside an increase in Ca content, the olivines display an enrichment of Fe which also indicates crystallisation at lower temperatures and pressures. Type 3 olivines, like type 1 and type 2 olivines, never have Ca compositions < 0.20 wt%. It can therefore be assumed that the olivines crystallised before the large-scale fractionation of the plagioclase and the other phases of the groundmass.

Olivine Mantle Environments

The mantles around olivine core types typically document the crystallisation environment after the initial core crystallisation. The zoning types and mantle compositions of the olivines can give indication of ascent rate and late stage crystallisation environments. These environments may overlap olivine core crystallisation environments; however, they may also represent certain crystallisation environments that did not experience a distinct olivine fractionation event that could be represented by the olivine types above. The BMVF exhibit 4 mantle crystallisation environments (A, B, C and D) illustrated in Figure 5.4.

Environment A represents the most distinguishable mantle around olivine cores. Olivine cores that ended up in environment A, display clinopyroxene dissolution/reaction textures around the olivine core. The clinopyroxene rims are represented by having little to no Ni in its composition (Figure 5.4A), the growth mantles with the low, constant MnO content (Figure 5.4B) and the growth mantles highly enriched in Ca (Appendix D). Reaction rims form due to a crystal being considerably out of equilibrium with its host melt e.g. when a olivine is introduced to a silicic melt (Tsuchiyama, 1986). Pyroxene rims can form on olivine due to dissolution of olivines induced by the effects of magma ascent or magma mixing events where an olivine is introduced to a silicic melt (Tsuchiyama, 1986).

The olivines with a clinopyroxene rim consist predominantly of the type 3 olivines. According to Wogelius and Walther (1992), the dissolution rate of olivine is increased with a higher Fe composition. Type 3 olivines are the most Fe rich of the olivine types and would therefore have a higher rate of dissolution. The proximity of type 3 olivines formation to the surface indicates that the clinopyroxene rims could be step-cooling induced dissolution textures created by being brought to the surface (Tsuchiyama, 1986, McCanta et al., 2007). Alternatively, the reaction rims could be the product of magma mixing occurring at shallow depths. The large amount of type 3 olivines with a clinopyroxene rim indicate that the rims are most likely the product of dissolution at surface conditions.

Environment B mantles are exclusively found on the olivines erupted in the trachybasalt sample of volcano M11. The growth mantles of environment B have notably lower Mg# (Mg#43-67) than the majority of the other olivines rims (Mg#66-83) (Figure 5.4A) but share similar Ni content as the majority of the other olivine rims. Also, the growth mantles that formed in Environment B have notably higher Mn content compared to the mantles of the other mantle environments. The composition of the mantles indicate that crystallisation environment B is more evolved than any of the crystallisation environments within the BMVF. The trachybasalt is more evolved than the majority of the basanites found within the BMVF. Therefore, environment B would reflect the more evolved nature of the magma.

Environment C represents a small fraction of the mantle formation zones. This type of mantle is exclusively found around a select few type 1 olivine cores. The mantles of environment C is the most primitive of the growth types displaying a similar NiO (0.1-0.2 wt%), MgO (80-84 wt%) and MnO (0.25-0.29 wt%) compositions as the type 2 cores (Figures 5.4 A and B). Environment C is interpreted as representing the same environment type 2 olivine cores crystallised in. The limited type 1 olivine cores that gained a mantle in environment C indicates that very few olivines were hosted in environment C for an adequate time to gain a mantle representing type 2 core olivine compositions.

Environment D is found on the majority of the olivines. The low Mg#, low Ni high Mn compositions of the rims indicate a late phase formation. Environment D displays a significant overlap with the type 3 olivine compositions at Mg#80 for Ni Mn (Figure 5.4 A and B). The initial stages of environment D represents type 3 olivine’s crystallisation environment, but the later stages of environment D is a continuation of the shallow crystallisation environment, that is not expressed as an olivine type. Environment D therefore represents the last phase of crystal growth of the BMVF.

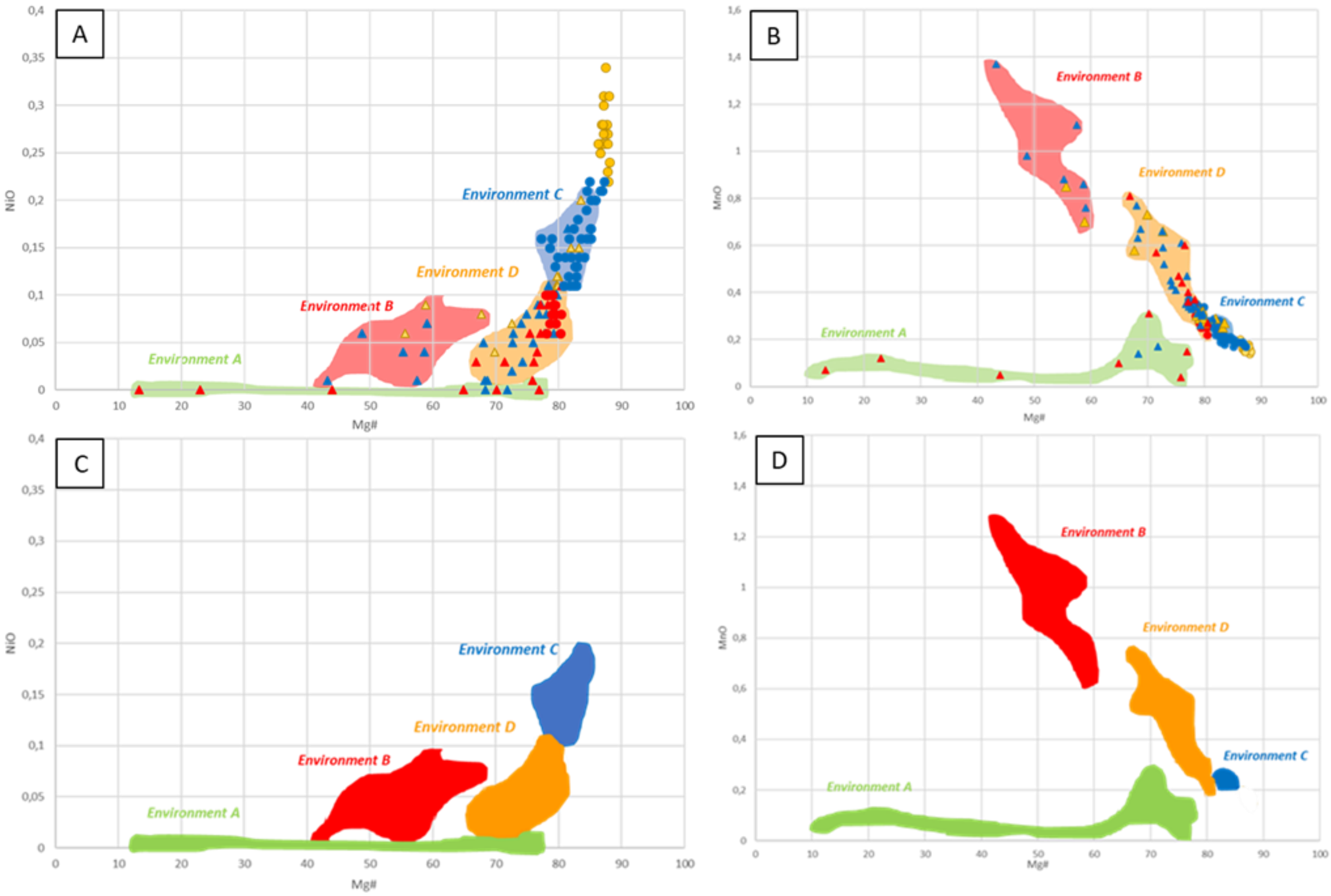

Figure 5.4. The suggested crystallisation environments of the growth mantles found on the different olivine types.

An Integrated Plumbing Model

The proposed integrated plumbing system model incorporates the olivine types and mantle crystallisation conditions with the whole rock chemistry, K_D (Fe-Mg) equilibriums, thermobarometry and petrography to provide the most probable plumbing systems of the BMVF (Figure 5.5). The proposed model is as follows:

The partial melting of garnet pyroxenite in the garnet stability field of the mantle, that experienced minor metasomatism, lead to the emplacement of ephemeral magma chambers within the crust, most notably, a deep seated-magma chamber ~36km beneath the BMVF. Minor fractional crystallisation in the deep-seated magma chamber formed the euhedral, cumulate phenocryst phases with spinel inclusions. The spinel inclusions that are present in many phenocryst phases indicate that crystallisation of the phenocrysts occurred predominantly in the spinel stability field of the mantle.

In typical polygenetic volcanoes, zoned magma chambers are commonplace occurrence, e.g. (Watanabe et al., 2006, Ngwa et al., 2019). A single, large magma chamber that typically undergoes fractionation is usually expressed in the compositions of the erupted material. The BMVF exhibits compositions ranging from basanite-trachybasalts reported in this thesis and evolved phonolites (Almond, 1974, Almond et al., 1984). However, due to the nature of monogenetic volcanism defined by a single eruption, a large compositionally zoned magma chamber with numerous eruptions are unlikely to form at a monogenic volcano. Németh et al. (2003) suggest that compositional variation in monogenetic volcanoes can be explained by means of small magma emplacement of varying spatial and temporal characteristics within the crust. Several studies follow the same reasoning e.g. (Brenna et al., 2018, Coote et al., 2019, Murcia et al., 2019). The proposed model of the BMVF is based on this interpretation.

The range in compositions present in the BMVF suggests the presence of stratified, ephemeral magma chambers that exhibit different depths and times of emplacement within the plumbing system. Spatially, the emplacement of a magma chamber typically occurs at density differences in the earth's interior, such as at the MOHO or the upper crust/lower crust boundary(UC/LC) (Watanabe et al., 1999). Clinopyroxene barometry indicates crystallisation occurring at the MOHO boundary which suggests the presence of a pocket of magma that was stalled at this depth. A trachybasalt hosted type 2 olivine has the lowest crystallisation temperature (1215^{o}C) of the olivines in equilibrium. Type 2 olivines generally have crystallisation temperatures of ~1265^{o}C. Therefore, the low crystallisation temperature of the trachybasalt-hosted type 2 olivine indicates cooler, and possibly shallower crystallisation conditions. The trachybasalt magma pocket is most likely emplaced at the UC/LC boundary.

The trachybasalt and more evolved compositions of the BMVF are the product of fractionation of primitive magmas hosted in the crust as failed eruptions. The magmatism did not lead to volcanism as the stress regimes were not favourable for eruptions. A recharge event with a basanitic composition emplaced new batches of primitive magma in the crust. The recharge event emplaced the chamber at the MOHO boundary where type 1 olivines and Ca-rich clinopyroxenes formed. With continued magma feeding into the system, the type 1 olivines and initial clinopyroxenes were dislodged from the chamber and forced towards the surface. During the ascent, the type 2 olivines started to crystallise inside the magma that experienced pressure and temperature changes. During the ascent phase, selected type 1 olivines gained a mantle that is represented by similar compositions (Environment C). At least two magma mixing events are expressed in the BMVF during the ascension phase. The first magma mixing event is of a Ca-rich magma with a more evolved magma exhibited in the Ca-enriched type 2 olivines and volcano CC10's reversely zoned Clinopyroxene 4. Secondly, during the magmatic recharge of the BMVF the ascending magmas interacted with the stalled, evolved magmas.

The primitive, ascending magma interacting with the failed eruptions is expressed in trachybasalt sample V-1 where there are two distinct populations of olivine: a group of olivines that formed in a magma of Mg#50-54 and a group of olivines that formed in a Mg# 63-66 (Figure). The olivines that crystallised in the lower Mg#50-54 magma, formed at same depths in the crust as the type 2 olivines, but interestingly display lower core Mg# at similar Ni contents as the other type 2 olivines (Figures 4.41 A). The lower olivine core Mg# suggests the type 2 olivines formed in a more evolved melt than the other type 2 olivines (with a similar Ni content). The olivines of volcano M11 that crystallised in a Mg#63-66 are all type 1 olivines. The type 1 olivines were dislodged from the magma chamber and during ascension interacted with the trachybasalt gaining a mantle with compositions representing environment B (Figures 5.4 A and B).

The recharge event injected dense magma into the system which forced the evolved, less dense magma to the surface leading to eruptions. In this scenario, the evolved magma eruptions would be expressed as maars, and tuff rings due to initial volcanism having more interaction with the groundwater, causing phreatomagmatic eruptions (Németh et al., 2003). This hypothesis is strengthened by volcano M11 being a maar volcano (Figures 2.2 and 3.1) and exhibits both compositional and textural evidence of being a trachybasalt. A caveat to this model is that the majority of the maars and tuff rings in this study has primitive compositions (Figure 4.19A). It can be argued that some of the ascending, primitive magma did not interact with pockets of failed eruptions and formed part of the first eruptions that were phreatomagmatic. Similar observations were made by Lenhardt et al. (2018).

As the magma from the recharge event continued to ascend, at shallow/surface pressures the final phase of olivine crystallisation occurred, creating type 3 olivines. After olivine crystallisation, clinopyroxene, plagioclase laths, Fe-oxides and the nepheline soon followed and crystallised forming the groundmass. During the eruption and cooling of the erupted material, the olivines gained the last mantle that formed in the BMVF. As the magma reached the surface, the step wise cooling of the system from ascent to eruption (Environment A) caused selected olivines to undergo partial-dissolution and gain a clinopyroxene rim.

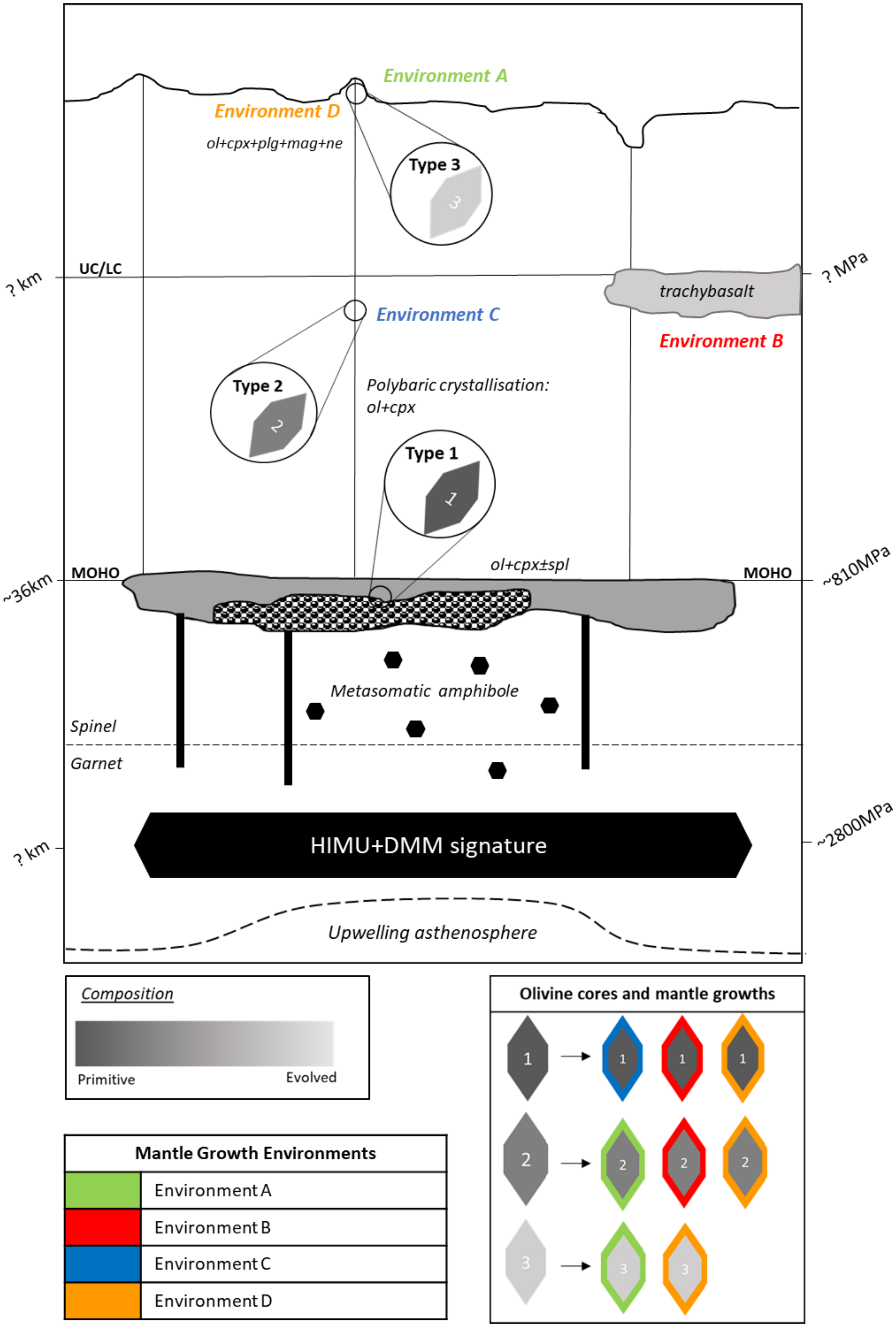

Figure 5.5. Suggested plumbing system of the BMVF. The plumbing model explains the mantle source of the BMVF, the genetic origin of the olivine types as well as the mantle environments. Depth and pressure of MOHO based stable clinopyroxene pressures alongside MOHO depth estimated by Lucassen et al. (2011) (see text). ol=olivine, cpx=clinopyroxene, spl=spinel, plg=plagioclase, ne=nepheline and mag=magnetite. Diagram not to scale.

5.2 The BMVF in a regional context

The Cenozoic volcanism in north Africa and the Arabian Peninsula is comparable to the BMVF as all these areas exhibit similar compositions and eruption times (Almond, 1986). The volcanism on the west coast of the Arabian Peninsula was formed due to the opening of the Red Sea and the volcanism of the Darfur dome is thought to be formed by a plume (as discussed in the Geological Background, Chapter 2). The proximity of both the Darfur dome and the Red Sea rift to the BMVF could both have influenced the formation of the BMVF. The centre of the Darfur dome lies approximately 850km south-east of the BMVF and the Red Sea rift approximately 620km to the west. It is unclear if either of these geological features played a role in the formation of the BMVF.

The NW striking nature of the BMVF implies that the NW-striking Red Sea rift played some part in its formation, or at least, acted as a structural control during the BMVF formation. Submarine basalts collected from the Red Sea rift indicate that the Red Sea rift has a depleted mantle signature, resembling N-type MORB (Volker et al., 1993). The BMVF does have a depleted mantle source component in its mantle signature, but the this is accompanied by an enriched mantle source resembling typical plume signatures. The Darfur dome is most likely the origin of the enriched signature. It is therefore pertinent that the BMVF be compared to volcanoes that were derived from the Darfur dome and the Red Sea rift respectively. If either the Red Sea rift or the Darfur dome played a part in the formation the BMVF, similarities in mantle sources would be indicative of a shared formational event between the BVMF, the Darfur dome and the Red Sea rift (Figure 5.6).

Of the compared volcanoes, the BMVF is closest related to the volcanoes of the Darfur dome (Figure 5.6), although the volcanoes of the Darfur dome indicate they are the product of several mantle sources and possible crustal contamination (Figures 5.6A, B, C and D). The similarity in isotopic signatures indicates that BMVF shares a similar, enriched mantle source that is also found in the volcanoes of the Darfur dome. The BMVF and the Darfur dome volcanoes all indicate the input of an enriched source while the Harrat Rahat’s mantle signature indicates that it resembles a more depleted source (Figures 5.6B and D). This depleted mantle source signature can be attributed to the Red Sea rift that possess a Depleted Mantle signature (Volker et al., 1993, Haase et al., 2000, Ligi et al., 2018). The BMVF has an enriched and a depleted component in its isotopic signature. This signature is most likely the mixing between the signature of the suggested plume of the Darfur dome and the Red Sea rift system.

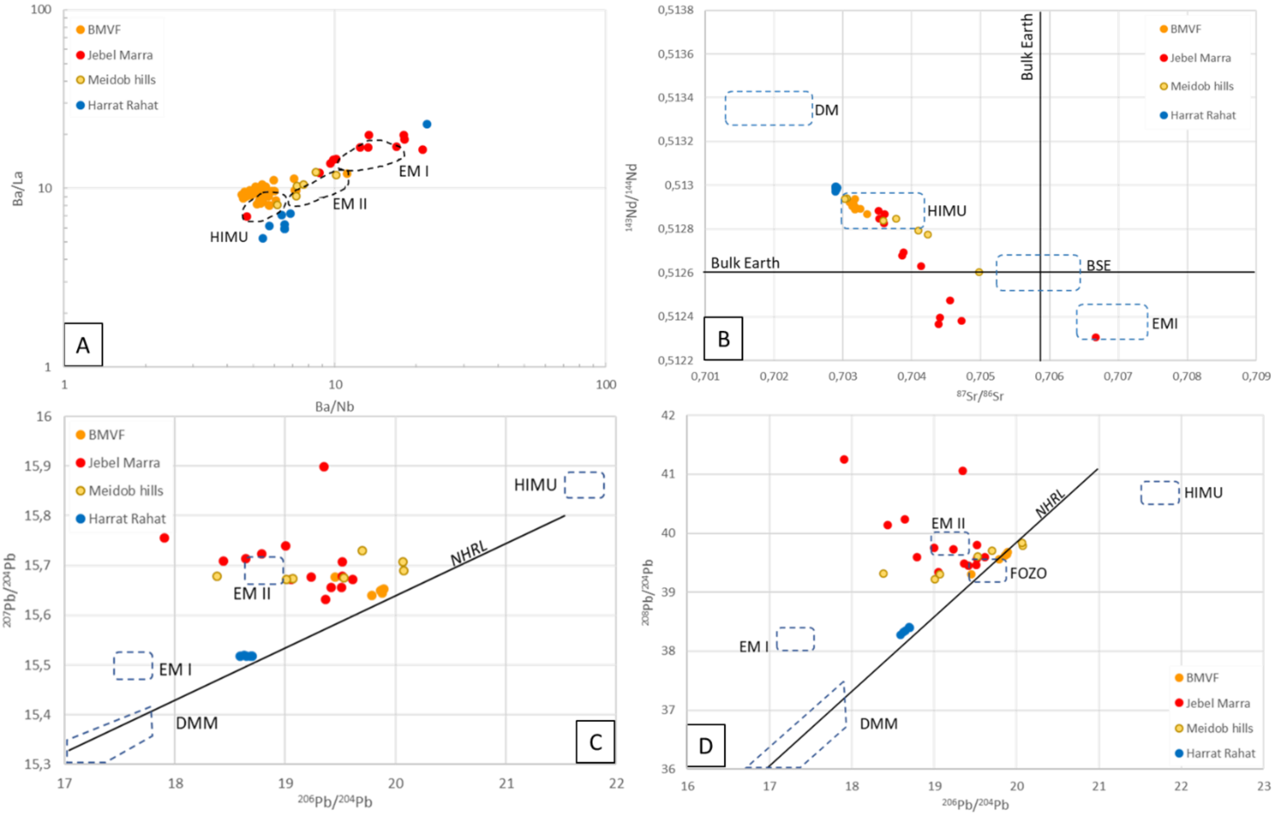

Figure 5.6. Mantle reservoir diagrams of the selected Cenozoic volcanoes of the Arabian Peninsula and North Africa. A) Ba/Nb vs Ba/La diagram with HIMU, EM I and EM II mantle endmembers (Weaver, 1991).B) ^{87}Sr/^{86}Sr vs ^{143}Nd/^{144}Nd diagram C) ^{206}Pb/^{204}Pb vs ^{207}Pb/^{204}Pb diagram D) ^{206}Pb/^{204}Pb vs ^{208}Pb/^{204}Pb. See Figure 4.31 and 4.32 captions for isotopic mantle endmember references.

5.3 Volcanism on a Metacraton

The BMVF and the volcanoes of the Darfur dome are situated on the partially delaminated Saharan metacraton. A partially delaminated craton could influence the composition of the erupted material of the BMVF, Jebel Marra and the Meidob hills. The thickness of the lithosphere limits the upwelling of the asthenosphere, which in turn dictates the amount of melting and initial crystallisation (Zhang et al., 2016). The influence is most notable in the trace element concentrations, where the relative enrichment of HREE indicates that the melt formed in the spinel stability zone. The opposite is true for melts sourced in the garnet stability zone (Ellam, 1992). Figure 5.7A indicates that the BMVF and the volcanoes of the Darfur have differing mantle reservoirs, but source lithology could still indicate differing lithosphere.

The Cenozoic volcanoes of the Songliaos basin, located on the North China Metacraton, in North-East China, illustrates the effects of lithospheric thickness on magma compositions (Zhang et al., 2016). The volcanoes erupted through varying lithospheric thicknesses of the North China Metacraton and showed that the volcanoes that erupted thorough thicker lithosphere displayed higher La/Sm and Sm/Yb ratios than the volcanoes that erupted through the thinner crust. Figure 5.7 display the Sm/Yb and La/Sm ratios of BMVF and the volcanoes of the Darfur Dome. When the ratios are plotted as a function of longitude, it may show the prominent thickness differences on the Metacraton. If the selected trace element ratios of the volcanoes are compared to the lithospheric density map (Figure 5.7A) of Liégeois et al. (2013), the Sm/Yb and the La/Sm (Figures 5.7 B and C) ratios correspond with the measured crustal thickness. The lower ratios of Jebel Marra correspond to a formation on a thinner part of the crust than the Meidob Hills and the BMVF.

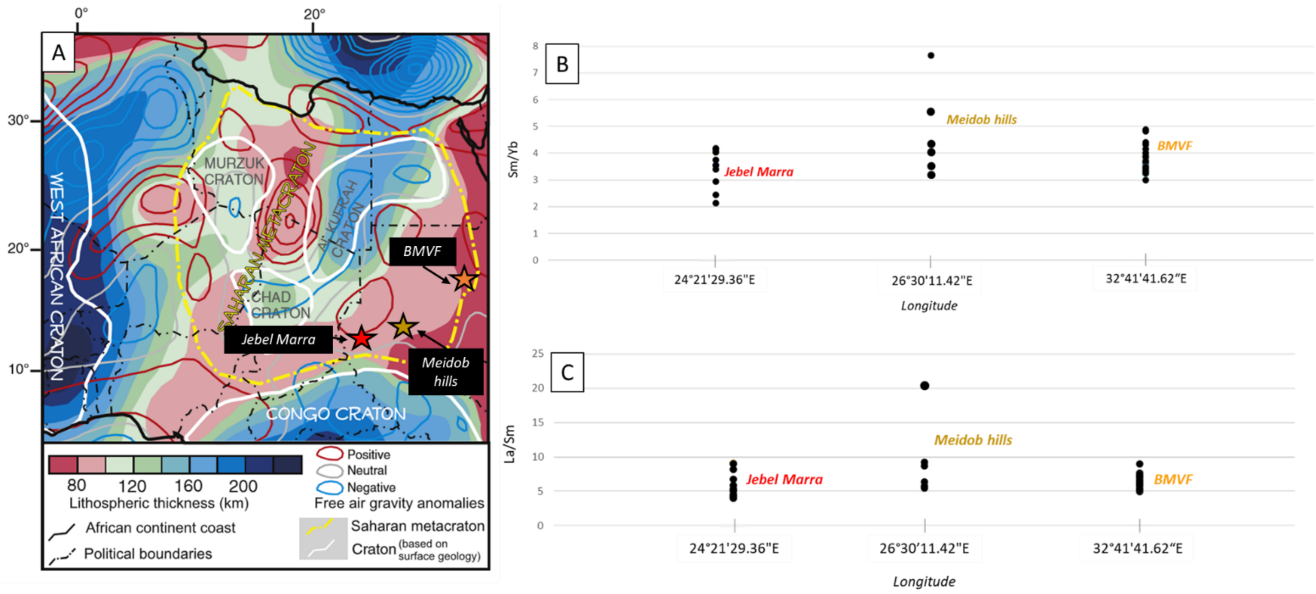

Figure 5.7. A) Lithospheric density map of North East Africa depicting the Saharan Metacraton and the edges of the Congo-and West African Craton (Liégeois et al., 2013). B) Sm/Yb ratios of the of the selected volcanoes of the Sahara Metacraton C) La/Sm ratios of the of the selected volcanoes of the Sahara Metacraton.

6 Conclusion

Petrographic and geochemical analysis of the BMVF classify the erupted material as predominantly basanites alongside subordinate evolved material such as basalt, trachyte and phonolite. Major- and trace element analysis indicates that the BMVF is a sodic-alkaline volcanic field, resembling a typical OIB signature. The BMVF isotopic signature suggests the mixing of an enriched mantle component (HIMU) and a depleted mantle components (DMM). The enriched and depleted mantle reservoirs can be attributed to the proximity of the Darfur dome and the Red Sea rift respectively. Although the Red Sea rift is closer to the BMVF, the BMVF shares more similarity to the volcanoes of the Darfur dome. HREE contents and melt modelling indicate that the source rock of the BMVF is garnet rich and is most likely a garnet peridotite due to the high amount of olivines in the phenocryst phase. Selected trace element ratios suggest minor amphibole mineralisation indicating metasomatism of the mantle source. Melting models that use partitioning coefficients of HFSE in selected minerals estimate 2-4% melting of the metasomatised garnet pyroxenite at a depth of ~2.8GPa as the source melt for the BMVF.

Lava compositions and K_D (Fe-Mg) of olivines exhibit the presence of ephemeral magma pockets emplaced at different density boundaries, at different times in the crust. Clinopyroxene barometry indicates the presence of a magma pocket at ~810MPa (~36km), roughly the same depth as the MOHO. The stalled, primitive magma pockets fractionated the majority of the crystal cargo that later mixed and erupted with more evolved lavas emplaced at the upper crust/lower crust boundary. Olivine types of the BMVF acted as a gauge of measuring crystallisation conditions within the crust as the magma was transported to the surface. Ni, Mn and Ca compositions in olivine cores reveal processes of 1) magma storage at the base of the plumbing system, 2) fractionation and 3) at least two mixing events. Olivine mantle and rim compositions reveal the presence of crystallisation environments, not indicated by the olivine types. Olivine mantle environments reveal 1) clinopyroxene rim formation, 2) the evolved nature of the trachybasalt and 3) different olivine types that were co-hosted in the same environment. thermometry indicates a significant number of olivines crystallised at ~1265 ^{o}C, but outlier temperatures of 1373^{o}C and 1215^{o}C are also present

The open system dynamics of the BMVF hint at an intricate plumbing system that is defined by stalled magmas that were emplaced during ‘failed eruptions’, magma mixing and fractionation of a phenocryst assemblage. The open system dynamics and the suggested plumbing system of the BMFV of agrees with the growing number of studies that determined complex plumbing systems of monogenetic volcanoes and volcanic fields are more commonplace than initially thought.

The way forward

The indication of an intricate plumbing system that feeds the BMVF system calls for further, in-depth projects that emphasise hazard assessment, as the BMVF is still considered active. Age dating and estimating crystallisation depths for a larger population of phenocrysts would give further insight into the plumbing system. The lack of clinopyroxenes viable for thermobarometry in this thesis and the limitations of plagioclase barometers calls for further investigations into alternative barometers. The classification of olivine hosted spinel could further map the sequence of phenocryst crystallisation within the plumbing system.

7 References

ABDELSALAM, M. G. 2010. Quantifying 3D post-accretionary tectonic strain in the Arabian–Nubian shield: superimposition of the Oko shear zone on the Nakasib suture, Red Sea Hills, Sudan. *Journal of African Earth Sciences,* 56**,** 167-178.

ABDELSALAM, M. G., ABDEL-RAHMAN, E.-S. M., EL-FAKI, E.-F. M., AL-HUR, B., EL-BASHIER, F.-R. M., STERN, R. J. & THURMOND, A. K. 2003. Neoproterozoic deformation in the northeastern part of the Saharan Metacraton, northern Sudan. *Precambrian Research,* 123**,** 203-221.

ABDELSALAM, M. G., GAO, S. S. & LIÉGEOIS, J.-P. 2011. Upper mantle structure of the Saharan Metacraton. *Journal of African Earth Sciences,* 60**,** 328-336.

ABDELSALAM, M. G., LIÉGEOIS, J.-P. & STERN, R. J. 2002. The saharan metacraton. *Journal of African Earth Sciences,* 34**,** 119-136.

ABDELSALAM, M. G. & STERN, R. J. 1996. Sutures and shear zones in the Arabian-Nubian Shield. *Journal of African Earth Sciences,* 23**,** 289-310.

ABRATIS, M., VIERECK, L., PFÄNDER, J. A. & HENTSCHEL, R. 2015. Geochemical composition, petrography and 40 Ar/39 Ar age of the Heldburg phonolite: implications on magma mixing and mingling. *International Journal of Earth Sciences,* 104**,** 2033-2055.

AL SHEHRI, A. & GUDMUNDSSON, A. 2018. Modelling of surface stresses and fracturing during dyke emplacement: Application to the 2009 episode at Harrat Lunayyir, Saudi Arabia. *Journal of Volcanology and Geothermal Research,* 356**,** 278-303.

ALI, E., ABDELRAHMAN, E. & GUANG, W. 2014. Southeast Bayuda volcano-sedimentary sequences (Kurmut terrane, Sudan): juvenile island arc series within the mega-shear zone marking the eastern boundary of the Saharan Metacraton. *Arabian Journal of Geosciences,* 7**,** 447-456.

ALI, E. & RAHMAN, E. A. 2011. New ophiolite occurrences in Sudan and constraint on the western boundary of the Nubian Shield: Petrographical and geochemical evidence. *Journal of African Earth Sciences,* 59**,** 101-110.

ALMOND, D. 1986. The relation of Mesozoic-Cainozoic volcanism to tectonics in the Afro-Arabian dome. *Journal of Volcanology and Geothermal Research,* 28**,** 225-246.

ALMOND, D. C. 1974. The composition of basaltic lavas from Bayuda, Sudan and their place in the cainozoic volcanic history of north-east Africa. *Bulletin Volcanologique,* 38**,** 345-360.

ALMOND, D. C., AHMED, F. & KHALIL, B. E. 1969. An excursion to the Bayuda volcanic field of Northern Sudan. *Bulletin Volcanologique,* 33**,** 549-565.

ALMOND, D. C., KHEIR, O. M. & POOLE, S. 1984. Alkaline basalt volcanism in northeastern Sudan: a comparison of the Bayuda and Gedaref areas. *Journal of African Earth Sciences (1983),* 2**,** 233-245.

BAKER, J., CHAZOT, G., MENZIES, M. & THIRLWALL, M. 1998. Metasomatism of the shallow mantle beneath Yemen by the Afar plume—implications for mantle plumes, flood volcanism, and intraplate volcanism. *Geology,* 26**,** 431-434.

BAKER, J., THIRLWALL, M. & MENZIES, M. 1996. Sr・ Nd・ Pb isotopic and trace element evidence for crustal contamination of plume-derived flood basalts: Oligocene flood volcanism in western Yemen. *Geochimica et Cosmochimica Acta,* 60**,** 2559-2581.

BARTH, H. & MEINHOLD, K. 1979. Mineral prospecting in the Bayuda Desert. *Unpublished Technical Report of the Sudanese–German Exploration Project, Vol. A. BGR, Hannover*.

BAS, M. J. L., MAITRE, R. W. L., STRECKEISEN, A., ZANETTIN, B. & ROCKS, I. S. O. T. S. O. I. 1986. A Chemical Classification of Volcanic Rocks Based on the Total Alkali-Silica Diagram. *Journal of Petrology,* 27**,** 745-750.

BEATTIE, P. 1993. Olivine-melt and orthopyroxene-melt equilibria. *Contributions to Mineralogy and Petrology,* 115**,** 103-111.

BIERLEIN, F., REYNOLDS, N., ARNE, D., BARGMANN, C., MCKEAG, S., BULLEN, W., AL-ATHBAH, H., MCKNIGHT, S. & MAAS, R. 2016. Petrogenesis of a Neoproterozoic magmatic arc hosting porphyry Cu-Au mineralization at Jebel Ohier in the Gebeit Terrane, NE Sudan. *Ore Geology Reviews,* 79**,** 133-154.

BLANCHETTE, A. R., KLEMPERER, S. L., MOONEY, W. D. & ZAHRAN, H. M. 2018. Two-stage Red Sea rifting inferred from mantle earthquakes in Neoproterozoic lithosphere. *Earth and Planetary Science Letters,* 497**,** 92-101.

BRENNA, M., CRONIN, S. J., NEMETH, K., SMITH, I. E. & SOHN, Y. K. 2011. The influence of magma plumbing complexity on monogenetic eruptions, Jeju Island, Korea. *Terra Nova,* 23**,** 70-75.

BRENNA, M., CRONIN, S. J., SMITH, I. E. M., TOLLAN, P. M. E., SCOTT, J. M., PRIOR, D. J., BAMBERY, K. & UKSTINS, I. A. 2018. Olivine xenocryst diffusion reveals rapid monogenetic basaltic magma ascent following complex storage at Pupuke Maar, Auckland Volcanic Field, New Zealand. *Earth and Planetary Science Letters,* 499**,** 13-22.

CAMP, V. E. & ROOBOL, M. J. 1989. The Arabian continental alkali basalt province: Part I. Evolution of Harrat Rahat, Kingdom of Saudi Arabia. *GSA Bulletin,* 101**,** 71-95.

CARN, S. A. 2000. The Lamongan volcanic field, East Java, Indonesia: physical volcanology, historic activity and hazards. *Journal of Volcanology and Geothermal Research,* 95**,** 81-108.

CHU, D. & GORDON, R. G. 1998. Current plate motions across the Red Sea. *Geophysical Journal International,* 135**,** 313-328.

COOTE, A., SHANE, P. & FU, B. 2019. Olivine phenocryst origins and mantle magma sources for monogenetic basalt volcanoes in northern New Zealand from textural, geochemical and δ18O isotope data. *Lithos*.

COX, K., BELL, J. & PANKHURST, R. 1979. Petrographic aspects of volcanic rocks. *The Interpretation of Igneous Rocks.* Springer.

DAVIDSON, J. P. & WILSON, I. R. 1989. Evolution of an alkali basalt—trachyte suite from Jebel Marra volcano, Sudan, through assimilation and fractional crystallization. *Earth and Planetary Science Letters,* 95**,** 141-160.

DAVISON, I., AL-KADASI, M., AL-KHIRBASH, S., AL-SUBBARY, A. K., BAKER, J., BLAKEY, S., BOSENCE, D., DART, C., HEATON, R. & MCCLAY, K. 1994. Geological evolution of the southeastern Red Sea Rift margin, Republic of Yemen. *Geological Society of America Bulletin,* 106**,** 1474-1493.

DAWSON, J. B. The Gregory rift valley and Neogene-recent volcanoes of northern Tanzania. 2008. Geological Society of London.

DE HOOG, J. C., GALL, L. & CORNELL, D. H. 2010. Trace-element geochemistry of mantle olivine and application to mantle petrogenesis and geothermobarometry. *Chemical Geology,* 270**,** 196-215.

DRURY, S., KELLEY, S., BERHE, S., COLLIER, R. & ABRAHA, M. 1994. Structures related to Red Sea evolution in northern Eritrea. *Tectonics,* 13**,** 1371-1380.

EBINGER, C. J. & SLEEP, N. 1998. Cenozoic magmatism throughout east Africa resulting from impact of a single plume. *Nature,* 395**,** 788.

ELKINS, L., GAETANI, G. & SIMS, K. 2008. Partitioning of U and Th during garnet pyroxenite partial melting: Constraints on the source of alkaline ocean island basalts. *Earth and Planetary Science Letters,* 265**,** 270-286.

ELLAM, R. 1992. Lithospheric thickness as a control on basalt geochemistry. *Geology,* 20**,** 153-156.

ERSOY, E. Y. 2013. PETROMODELER (Petrological Modeler): a Microsoft® Excel© spreadsheet program for modelling melting, mixing, crystallization and assimilation processes in magmatic systems. *Turkish Journal of Earth Sciences,* 22**,** 115-125.

FARMER, G. L. 2014. 4.3 - Continental Basaltic Rocks. *In:* HOLLAND, H. D. & TUREKIAN, K. K. (eds.) *Treatise on Geochemistry (Second Edition).* Oxford: Elsevier.

FÉRAUD, G., ZUMBO, V., SEBAI, A. & BERTRAND, H. 1991. 40AR/39AR age and duration of tholeiitic magmatism related to the early opening of the Red Sea rift. *Geophysical Research Letters,* 18**,** 195-198.

FITTON, J., SAUNDERS, A., NORRY, M., HARDARSON, B. & TAYLOR, R. 1997. Thermal and chemical structure of the Iceland plume. *Earth and Planetary Science Letters,* 153**,** 197-208.

FITTON, J. G. 1987. The Cameroon line, West Africa: a comparison between oceanic and continental alkaline volcanism. *Geological Society, London, Special Publications,* 30**,** 273-291.

FITTON, J. G. & DUNLOP, H. M. 1985. The Cameroon line, West Africa, and its bearing on the origin of oceanic and continental alkali basalt. *Earth and Planetary Science Letters,* 72**,** 23-38.

FITZSIMONS, I. 2000. A review of tectonic events in the East Antarctic Shield and their implications for Gondwana and earlier supercontinents. *Journal of African Earth Sciences,* 31**,** 3-23.

FRANCIS, P. W., THORPE, R. S. & AHMED, F. 1973. Setting and Significance of Tertiary-Recent Volcanism in the Darfur Province of Western Sudan. *Nature Physical Science,* 243**,** 30-32.

FRANZ, G., BREITKREUZ, C., COYLE, D. A., EL HUR, B., HEINRICH, W., PAULICK, H., PUDLO, D., SMITH, R. & STEINER, G. 1997. The alkaline Meidob volcanic field (Late Cenozoic, northwest Sudan). *Journal of African Earth Sciences,* 25**,** 263-291.

FRANZ, G., PUDLO, D., URLACHER, G., HAUSSMANN, U., BOVEN, A. & WEMMER, K. 1994. The Darfur Dome, western Sudan: the product of a subcontinental mantle plume. *Geologische Rundschau,* 83**,** 614-623.

FRANZ, G., STEINER, G., VOLKER, F., PUDLO, D. & HAMMERSCHMIDT, K. 1999. Plume related alkaline magmatism in central Africa—the Meidob Hills (W Sudan). *Chemical Geology,* 157**,** 27-47.

FUJIMAKI, H., TATSUMOTO, M. & AOKI, K. I. 1984. Partition coefficients of Hf, Zr, and REE between phenocrysts and groundmasses. *Journal of Geophysical Research: Solid Earth,* 89**,** B662-B672.

FURMAN, T., BRYCE, J., ROONEY, T., HANAN, B., YIRGU, G. & AYALEW, D. 2006. Heads and tails: 30 million years of the Afar plume. *Geological Society, London, Special Publications,* 259**,** 95-119.

FURMAN, T. & GRAHAM, D. 1999. Erosion of lithospheric mantle beneath the East African Rift system: geochemical evidence from the Kivu volcanic province. *Lithos,* 48**,** 237-262.

GASS, I. G. 1977. The evolution of the Pan African crystalline basement in NE Africa and Arabia. *Journal of the Geological Society,* 134**,** 129-138.

GEORGE, R., ROGERS, N. & KELLEY, S. 1998. Earliest magmatism in Ethiopia: Evidence for two mantle plumes in one flood basalt province. *Geology,* 26**,** 923-926.

GILFILLAN, S., GYÖRE, D., FLUDE, S., JOHNSON, G., BOND, C., HICKS, N., LISTER, R., JONES, D., KREMER, Y. & HASZELDINE, R. 2019. Noble gases confirm plume-related mantle degassing beneath Southern Africa. *Nature communications,* 10**,** 1-7.

HAASE, K. M., MÜHE, R. & STOFFERS, P. 2000. Magmatism during extension of the lithosphere: geochemical constraints from lavas of the Shaban Deep, northern Red Sea. *Chemical Geology,* 166**,** 225-239.

HENRY, B., LIÉGEOIS, J.-P., NOUAR, O., DERDER, M., BAYOU, B., BRUGUIER, O., OUABADI, A., BELHAI, D., AMENNA, M. & HEMMI, A. 2009. Repeated granitoid intrusions during the Neoproterozoic along the western boundary of the Saharan metacraton, Eastern Hoggar, Tuareg shield, Algeria: an AMS and U–Pb zircon age study. *Tectonophysics,* 474**,** 417-434.

HOFMANN, C., COURTILLOT, V., FERAUD, G., ROCHETTE, P., YIRGU, G., KETEFO, E. & PIK, R. 1997. Timing of the Ethiopian flood basalt event and implications for plume birth and global change. *Nature,* 389**,** 838.

HOSHIDE, T. & OBATA, M. 2014. Spinel inclusions in olivine and plagioclase crystals in a layered gabbro: a marker and a tracer for primary phenocrysts in a differentiating magma reservoir. *Contributions to Mineralogy and Petrology,* 168**,** 1049.

IRVINE, T. & BARAGAR, W. 1971. A guide to the chemical classification of the common volcanic rocks. *Canadian journal of earth sciences,* 8**,** 523-548.

IZZELDIN, A. 1987. Seismic, gravity and magnetic surveys in the central part of the Red Sea: their interpretation and implications for the structure and evolution of the Red Sea. *Tectonophysics,* 143**,** 269-306.

JANNEY, P., LE ROEX, A., CARLSON, R. & VILJOEN, K. 2002. A chemical and multi-isotope study of the Western Cape olivine melilitite province, South Africa: implications for the sources of kimberlites and the origin of the HIMU signature in Africa. *Journal of Petrology,* 43**,** 2339-2370.

JANOUŠEK, V., FARROW, C. & ERBAN, V. 2006. Interpretation of whole-rock geochemical data in igneous geochemistry: introducing Geochemical Data Toolkit (GCDkit). *Journal of Petrology,* 47**,** 1255-1259.

JOHNSON, P. R. & WOLDEHAIMANOT, B. 2003. Development of the Arabian-Nubian Shield: perspectives on accretion and deformation in the northern East African Orogen and the assembly of Gondwana. *Geological Society, London, Special Publications,* 206**,** 289-325.

KENEA, N., EBINGER, C. & REX, D. 2001. Late Oligocene volcanism and extension in the southern Red Sea Hills, Sudan. *Journal of the Geological Society,* 158**,** 285-294.

KERESZTURI, G. & NÉMETH, K. 2012. Monogenetic basaltic volcanoes: genetic classification, growth, geomorphology and degradation. *Updates in Volcanology-New Advances in Understanding Volcanic Systems.* InTech.

KRÖNER, A. 1985. Ophiolites and the evolution of tectonic boundaries in the late proterozoic Arabian—Nubian shield of northeast Africa and Arabia. *Precambrian Research,* 27**,** 277-300.

KRÖNER, A., STERN, R., DAWOUD, A. S., COMPSTON, W. & REISCHMANN, T. 1987. The Pan-African continental margin in northeastern Africa: evidence from a geochronological study of granulites at Sabaloka, Sudan. *Earth and Planetary Science Letters,* 85**,** 91-104.

KRÖNER, A. & STERN, R. J. 2005. AFRICA | Pan-African Orogeny. *In:* SELLEY, R. C., COCKS, L. R. M. & PLIMER, I. R. (eds.) *Encyclopedia of Geology.* Oxford: Elsevier.

KÜSTER, D. & LIÉGEOIS, J.-P. 2001. Sr, Nd isotopes and geochemistry of the Bayuda Desert high-grade metamorphic basement (Sudan): an early Pan-African oceanic convergent margin, not the edge of the East Saharan ghost craton? *Precambrian Research,* 109**,** 1-23.

KÜSTER, D., LIÉGEOIS, J.-P., MATUKOV, D., SERGEEV, S. & LUCASSEN, F. 2008. Zircon geochronology and Sr, Nd, Pb isotope geochemistry of granitoids from Bayuda Desert and Sabaloka (Sudan): evidence for a Bayudian event (920–900 Ma) preceding the Pan-African orogenic cycle (860–590 Ma) at the eastern boundary of the Saharan Metacraton. *Precambrian Research,* 164**,** 16-39.

LATOURRETTE, T., HERVIG, R. L. & HOLLOWAY, J. R. 1995. Trace element partitioning between amphibole, phlogopite, and basanite melt. *Earth and Planetary Science Letters,* 135**,** 13-30.

LE, W., ZENG, Z., KUSKY, T., ASIMOW, P., HE, C., LIU, Y., YANG, S. & XU, S. 2019. Geochemistry of middle-late Mesozoic mafic intrusions in the eastern North China Craton: New insights on lithospheric thinning and decratonization. *Gondwana Research,* 73.

LENHARDT, N., BORAH, S. B., LENHARDT, S. Z., BUMBY, A. J., IBINOOF, M. A. & SALIH, S. A. 2018. The monogenetic Bayuda Volcanic Field, Sudan – New insights into geology and volcanic morphology. *Journal of Volcanology and Geothermal Research,* 356**,** 211-224.

LI, C. & RIPLEY, E. M. 2010. The relative effects of composition and temperature on olivine-liquid Ni partitioning: Statistical deconvolution and implications for petrologic modeling. *Chemical Geology,* 275**,** 99-104.

LIÉGEOIS, J.-P., ABDELSALAM, M. G., ENNIH, N. & OUABADI, A. 2013. Metacraton: nature, genesis and behavior. *Gondwana Research,* 23**,** 220-237.

LIEGEOIS, J., BENHALLOU, A., AZZOUNI-SEKKAL, A., YAHIAOUI, R. & BONIN, B. 2005. The Hoggar swell and volcanism: reactivation of the Precambrian Tuareg shield during Alpine convergence and West African Cenozoic volcanism. *SPECIAL PAPERS-GEOLOGICAL SOCIETY OF AMERICA,* 388**,** 379.

LIGI, M., BONATTI, E., BOSWORTH, W., CAI, Y., CIPRIANI, A., PALMIOTTO, C., RONCA, S. & SEYLER, M. 2018. Birth of an ocean in the Red Sea: Oceanic-type basaltic melt intrusions precede continental rupture. *Gondwana Research,* 54**,** 150-160.

LUCASSEN, F., FRANZ, G., ROMER, R. L. & DULSKI, P. 2011. Late Mesozoic to Quaternary intraplate magmatism and its relation to the Neoproterozoic lithosphere in NE Africa—New data from lower-crustal and mantle xenoliths from the Bayuda volcanic field, Sudan. *In:* BECCALUVA, L., BIANCHINI, G. & WILSON, M. (eds.) *Volcanism and Evolution of the African Lithosphere.* Geological Society of America.

MARSH, J. S. 1987. Evolution of a strongly differentiated suite of phonolites from the Klinghardt Mountains, Namibia. *Lithos,* 20**,** 41-58.

MATTSSON, H. B. & TRIPOLI, B. A. 2011. Depositional characteristics and volcanic landforms in the Lake Natron–Engaruka monogenetic field, northern Tanzania. *Journal of Volcanology and Geothermal Research,* 203**,** 23-34.

MCCANTA, M. C., RUTHERFORD, M. J. & HAMMER, J. E. 2007. Pre-eruptive and syn-eruptive conditions in the Black Butte, California dacite: Insight into crystallization kinetics in a silicic magma system. *Journal of Volcanology and Geothermal Research,* 160**,** 263-284.

MEERT, J. G. & LIEBERMAN, B. S. 2008. The Neoproterozoic assembly of Gondwana and its relationship to the Ediacaran–Cambrian radiation. *Gondwana research,* 14**,** 5-21.

MOORE, A. & VERWOERD, W. 1985. The olivine melilitite-“kimberlite”-carbonatite suite of Namaqualand and Bushmanland, South Africa. *Transactions of the Geological Society of South Africa,* 88**,** 281-294.

MORIMOTO, N. 1988. Nomenclature of pyroxenes. *Mineralogy and Petrology,* 39**,** 55-76.

MOUFTI, M., MOGHAZI, A. & ALI, K. 2012. Geochemistry and Sr–Nd–Pb isotopic composition of the Harrat Al-Madinah Volcanic Field, Saudi Arabia. *Gondwana Research,* 21**,** 670-689.

MURCIA, H., BORRERO, C. & NÉMETH, K. 2019. Overview and plumbing system implications of monogenetic volcanism in the northernmost Andes' volcanic province. *Journal of Volcanology and Geothermal Research,* 383**,** 77-87.

MURCIA, H., NÉMETH, K., EL-MASRY, N. N., LINDSAY, J. M., MOUFTI, M. R. H., WAMEYO, P., CRONIN, S. J., SMITH, I. E. M. & KERESZTURI, G. 2015. The Al-Du’aythah volcanic cones, Al-Madinah City: implications for volcanic hazards in northern Harrat Rahat, Kingdom of Saudi Arabia. *Bulletin of Volcanology,* 77**,** 54.

MURCIA, H., NÉMETH, K., MOUFTI, M. R., LINDSAY, J. M., EL-MASRY, N., CRONIN, S. J., QADDAH, A. & SMITH, I. E. M. 2014. Late Holocene lava flow morphotypes of northern Harrat Rahat, Kingdom of Saudi Arabia: Implications for the description of continental lava fields. *Journal of Asian Earth Sciences,* 84**,** 131-145.

NAKAMURA, K. 1977. Volcanoes as possible indicators of tectonic stress orientation—principle and proposal. *Journal of Volcanology and Geothermal Research,* 2**,** 1-16.

NEAVE, D. A. & PUTIRKA, K. D. 2017. A new clinopyroxene-liquid barometer, and implications for magma storage pressures under Icelandic rift zones. *American Mineralogist,* 102**,** 777-794.

NÉMETH, K. 2010. Monogenetic volcanic fields: Origin, sedimentary record, and relationship with polygenetic volcanism. *What is a Volcano?,* 470**,** 43.

NÉMETH, K. & KERESZTURI, G. 2015. Monogenetic volcanism: personal views and discussion. *International Journal of Earth Sciences,* 104**,** 2131-2146.

NÉMETH, K., WHITE, J. D., REAY, A. & MARTIN, U. 2003. Compositional variation during monogenetic volcano growth and its implications for magma supply to continental volcanic fields. *Journal of the Geological Society,* 160**,** 523-530.

NGWA, C. N., LENHARDT, N., LE ROUX, P. & MBASSA, B. J. 2019. The Mount Cameroon southwest flank eruptions: Geochemical constraints on the subsurface magma plumbing system. *Journal of Volcanology and Geothermal Research,* 384**,** 179-188.

NICOLL, K. 2004. Recent environmental change and prehistoric human activity in Egypt and Northern Sudan. *Quaternary Science Reviews,* 23**,** 561-580.

NKOUATHIO, D. G., MÉNARD, J. J., WANDJI, P. & BARDINTZEFF, J. M. 2002. The Tombel graben (West Cameroon): a recent monogenetic volcanic field of the Cameroon Line. *Journal of African Earth Sciences,* 35**,** 285-300.

O'REILLY, S. Y., CHEN, D., GRIFFIN, W. & RYAN, C. 1997. Minor elements in olivine from spinel lherzolite xenoliths: implications for thermobarometry. *Mineralogical Magazine,* 61**,** 257-269.

PALME, H. & O'NEILL, H. S. C. 2003. Cosmochemical estimates of mantle composition. *Treatise on geochemistry,* 2**,** 568.

PAULICK, H. & FRANZ, G. 1997. The color of pumice: case study on a trachytic fall deposit, Meidob volcanic field, Sudan. *Bulletin of Volcanology,* 59**,** 171-185.

PAULISSEN, E. & VERMEERSCH, P. 1987. Earth, man and climate in the Egyptian Nile Valley during the Pleistocene.

PEARCE, J. & NORRY, M. 1979. *Petrogenetic implications of Ti, Zr, Y, and Nb variations in volcanic rocks*.

PHILIBERT, A., TIBBY, J. & WILLIAMS, M. 2010. A Pleistocene diatomite from the western piedmont of Jebel Marra volcano, Darfur, western Sudan, and its hydrological and climatic significance. *Quaternary International,* 216**,** 145-150.

PUTIRKA, K. 1999. Clinopyroxene+ liquid equilibria to 100 kbar and 2450 K. *Contributions to Mineralogy and Petrology,* 135**,** 151-163.

PUTIRKA, K., JOHNSON, M., KINZLER, R., LONGHI, J. & WALKER, D. 1996. Thermobarometry of mafic igneous rocks based on clinopyroxene-liquid equilibria, 0–30 kbar. *Contributions to Mineralogy and Petrology,* 123**,** 92-108.

PUTIRKA, K. D. 2005. Igneous thermometers and barometers based on plagioclase+ liquid equilibria: Tests of some existing models and new calibrations. *American Mineralogist,* 90**,** 336-346.

PUTIRKA, K. D. 2008. Thermometers and barometers for volcanic systems. *Reviews in mineralogy and geochemistry,* 69**,** 61-120.

PUTIRKA, K. D., MIKAELIAN, H., RYERSON, F. & SHAW, H. 2003. New clinopyroxene-liquid thermobarometers for mafic, evolved, and volatile-bearing lava compositions, with applications to lavas from Tibet and the Snake River Plain, Idaho. *American Mineralogist,* 88**,** 1542-1554.

RAY, A., HATUI, K., PAUL, D. K., SEN, G., BISWAS, S. & DAS, B. 2016. Mantle xenolith-xenocryst-bearing monogenetic alkali basaltic lava field from Kutch Basin, Gujarat, Western India: estimation of magma ascent rate. *Journal of Volcanology and Geothermal Research,* 312**,** 40-52.

RHODES, J., DUNGAN, M., BLANCHARD, D. & LONG, P. 1979. Magma mixing at mid-ocean ridges: evidence from basalts drilled near 22 N on the Mid-Atlantic Ridge. *Tectonophysics,* 55**,** 35-61.

ROEDER, P. & EMSLIE, R. 1970. Olivine-liquid equilibrium. *Contributions to mineralogy and petrology,* 29**,** 275-289.

ROGERS, N., MACDONALD, R., FITTON, J. G., GEORGE, R., SMITH, M. & BARREIRO, B. 2000. Two mantle plumes beneath the East African rift system: Sr, Nd and Pb isotope evidence from Kenya Rift basalts. *Earth and Planetary Science Letters,* 176**,** 387-400.

SALTERS, V. J. & LONGHI, J. 1999. Trace element partitioning during the initial stages of melting beneath mid-ocean ridges. *Earth and Planetary Science Letters,* 166**,** 15-30.

SATO, H. 1977. Nickel content of basaltic magmas: identification of primary magmas and a measure of the degree of olivine fractionation. *Lithos,* 10**,** 113-120.

SIMKIN, T. & SMITH, J. 1970. Minor-element distribution in olivine. *The Journal of Geology,* 78**,** 304-325.

SIMS, K. W., BLICHERT-TOFT, J., KYLE, P. R., PICHAT, S., GAUTHIER, P.-J., BLUSZTAJN, J., KELLY, P., BALL, L. & LAYNE, G. 2008. A Sr, Nd, Hf, and Pb isotope perspective on the genesis and long-term evolution of alkaline magmas from Erebus volcano, Antarctica. *Journal of Volcanology and Geothermal Research,* 177**,** 606-618.

SMITH, I. E. M., BLAKE, S., WILSON, C. J. N. & HOUGHTON, B. F. 2008. Deep-seated fractionation during the rise of a small-volume basalt magma batch: Crater Hill, Auckland, New Zealand. *Contributions to Mineralogy and Petrology,* 155**,** 511-527.

SMITH, I. E. M. & NÉMETH, K. 2017. Source to surface model of monogenetic volcanism: a critical review. *Geological Society, London, Special Publications,* 446**,** 1-28.

STERN, R., KRÖNER, A., BENDER, R., REISCHMANN, T. & DAWOUD, A. 1994. Precambrian basement around Wadi Halfa, Sudan: a new perspective on the evolution of the East Saharan Craton. *Geologische Rundschau,* 83**,** 564-577.

STERN, R. J. & JOHNSON, P. 2010. Continental lithosphere of the Arabian Plate: a geologic, petrologic, and geophysical synthesis. *Earth-Science Reviews,* 101**,** 29-67.

STOESER, D. B. & FROST, C. D. 2006. Nd, Pb, Sr, and O isotopic characterization of Saudi Arabian shield terranes. *Chemical Geology,* 226**,** 163-188.

STURM, R. 2002. PX-NOM—an interactive spreadsheet program for the computation of pyroxene analyses derived from the electron microprobe. *Computers & Geosciences,* 28**,** 473-483.

SULIMAN, A. & BAILO, E. T. 2000. Keraf Shear Zone, NE Sudan: Geodynamic characteristics of the Nile Craton-Nubian Shield boundary.

SUN, S.-S. & MCDONOUGH, W. F. 1989. Chemical and isotopic systematics of oceanic basalts: implications for mantle composition and processes. *Geological Society, London, Special Publications,* 42**,** 313-345.

TAKADA, A. 1994. The influence of regional stress and magmatic input on styles of monogenetic and polygenetic volcanism. *Journal of Geophysical Research: Solid Earth,* 99**,** 13563-13573.

THORPE, R. S. & SMITH, K. 1974. Distribution of Cenozoic volcanism in Africa. *Earth and Planetary Science Letters,* 22**,** 91-95.

TSUCHIYAMA, A. 1986. Experimental study of olivine-melt reaction and its petrological implications. *Journal of Volcanology and Geothermal Research,* 29**,** 245-264.

VAIL, J. 1985. Alkaline ring complexes in Sudan. *Journal of African Earth Sciences (1983),* 3**,** 51-59.

VERVOORT, J. D., PATCHETT, P. J., BLICHERT-TOFT, J. & ALBARÈDE, F. 1999. Relationships between Lu–Hf and Sm–Nd isotopic systems in the global sedimentary system. *Earth and Planetary Science Letters,* 168**,** 79-99.

VOLKER, F., MCCULLOCH, M. T. & ALTHERR, R. 1993. Submarine basalts from the Red Sea: new Pb, Sr, and Nd isotopic data. *Geophysical Research Letters,* 20**,** 927-930.

WALKER, G. P. 1993. Basaltic-volcano systems. *Geological Society, London, Special Publications,* 76**,** 3-38.

WALTER, M. J. 1998. Melting of garnet peridotite and the origin of komatiite and depleted lithosphere. *Journal of Petrology,* 39**,** 29-60.

WATANABE, S., WIDOM, E., UI, T., MIYAJI, N. & ROBERTS, A. 2006. The evolution of a chemically zoned magma chamber: The 1707 eruption of Fuji volcano, Japan. *Journal of volcanology and geothermal research,* 152**,** 1-19.

WATANABE, T., KOYAGUCHI, T. & SENO, T. 1999. Tectonic stress controls on ascent and emplacement of magmas. *Journal of Volcanology and Geothermal Research,* 91**,** 65-78.

WATERS, A. C. & FISHER, R. V. 1971. Base surges and their deposits: Capelinhos and Taal volcanoes. *Journal of Geophysical Research,* 76**,** 5596-5614.

WEAVER, B. L. 1991. The origin of ocean island basalt end-member compositions: trace element and isotopic constraints. *Earth and Planetary Science Letters,* 104**,** 381-397.

WOGELIUS, R. A. & WALTHER, J. V. 1992. Olivine dissolution kinetics at near-surface conditions. *Chemical Geology,* 97**,** 101-112.

ZHANG, L.-Y., PRELEVIĆ, D., LI, N., MERTZ-KRAUS, R. & BUHRE, S. 2016. Variation of olivine composition in the volcanic rocks in the Songliao basin, NE China: lithosphere control on the origin of the K-rich intraplate mafic lavas. *Lithos,* 262**,** 153-168.

ZHU, R., CHEN, L., WU, F. & LIU, J. 2011. Timing, scale and mechanism of the destruction of the North China Craton. *Science China Earth Sciences,* 54**,** 789-797.

ZHU, R., XU, Y., ZHU, G., ZHANG, H., XIA, Q. & ZHENG, T. 2012. Destruction of the North China craton. *Science China Earth Sciences,* 55**,** 1565-1587.

ZINDLER, A. & HART, S. 1986. Chemical geodynamics. *Annual review of earth and planetary sciences,* 14**,** 493-571.

8 Appendices

8.1 Appendix A: Major and trace element geochemical data of the lavas and scoria from the Bayuda Monogenetic Volcanic Field

Sample no	Latitude	Longitude	Volcano Nr.	Rock Type
B01	18°13'50.81"N	32°38'7.31"E	CC10	basanite
B02	18°13'50.85"N	32°38'7.34"E	CC10	basanite
B03	18°13'50.88"N	32°38'7.38"E	CC10	basanite
B04	18°14'55.10"N	32°38'22.50"E	CC10	basanite
B05	18°14'41.64"N	32°38'26.31"E	CC10	basanite
V01	18°14'27.85"N	32°38'29.81"E	CC10	basanite
V02	18°14'28.28"N	32°38'30.42"E	CC10	basanite
V03	18°14'28.31"N	32°38'30.46"E	CC10	basanite
B07	18°16'40.75"N	32°35'7.46"E	CC9	basanite
B08	18°19'19.23"N	32°34'33.73"E	DX1	basanite
B10	18°19'19.30"N	32°34'33.80"E	DX1	basanite
B09	18°20'15.25"N	32°37'34.92"E	DX2	basanite
B11	18°20'28.95"N	32°31'58.57"E	DX3	basanite
B12	18°22'5.02"N	32°34'24.03"E	CC44	basanite
B13	18°23'40.17"N	32°35'31.68"E	M3	basanite
B14	18°23'40.21"N	32°35'31.72"E	M3	basanite
10-1A	18°24'09.6'' N	32°30'59.8'' E	M7	basanite
10-1B	18°24'09.6'' N	32°30'59.8'' E	M7	basanite
B15	18°24'11.33"N	32°30'59.35"E	M7	basanite
B16	18°24'11.36"N	32°30'59.38"E	M7	basanite
B17	18°24'11.39"N	32°30'59.42"E	M7	basanite
B18	18°24'3.86"N	32°31'31.85"E	M6	basanite
B19	18°24'4.02"N	32°31'31.92"E	M6	basanite
B20	18°24'4.35"N	32°31'32.02"E	M6	basanite
B21	18°24'7.01"N	32°32'7.87"E	M5	basanite
B22	18°24'7.10"N	32°32'7.94"E	M5	basanite
B23	18°25'11.85"N	32°31'26.11"E	CC7	basanite
V04	18°25'10.45"N	32°31'28.70"E	CC7	basanite
B24	18°25'45.69"N	32°29'12.05"E	CC6	basanite
V05	18°25'48.35"N	32°29'9.07"E	CC6	basanite
B25	18°28'55.90"N	32°27'4.67"E	CC53	basanite
B26	18°28'55.97"N	32°27'4.73"E	CC53	basanite
V06	18°29'20.82"N	32°27'36.10"E	CC53	basanite
I-1	18°29'08.8'' N	32°28'40.7'' E	M8	basalt
I-4	18°29'08.8'' N	32°28'40.7'' E	M8	basalt
I-6	18°29'08.8'' N	32°28'40.7'' E	M8	basaltic andesite
V07	18°29'3.68"N	32°28'26.55"E	M8	basanite
V08	18°29'3.68"N	32°28'26.55"E	M8	basanite
II-1	N18°16'43.1''	E32°49'42.4''	CC48	basalt
II-2	N18°16'43.1''	E32°49'42.4''	CC48	basalt
II-3	N18°16'43.1''	E32°49'42.4''	CC48	basalt
II-4	N18°16'43.1''	E32°49'42.4''	CC48	trachy basalt
II-5	N18°16'43.1''	E32°49'42.4''	CC48	basalt
II-5(VA)	N18°16'43.1''	E32°49'42.4''	CC48	basalt
V-1	N18°18'57.6''	E32°47'56.6''	M11	trachy basalt

SiO_2	TiO_2	Al_2O_3	Fe_2O_3	MnO	MgO	CaO	Na_2O	K_2O	Cr_2O_3
42,99	2,34	15,13	11,76	0,20	9,58	10,27	3,99	1,53	0,03
43,73	2,24	15,20	11,39	0,21	9,27	9,82	3,32	1,40	0,03
42,88	2,40	14,84	12,00	0,21	10,07	10,51	3,80	1,46	0,03
43,13	2,37	14,97	11,86	0,20	10,09	10,36	3,92	1,50	0,04
41,49	2,46	14,19	12,89	0,21	12,19	10,57	3,16	1,17	0,04
42,58	2,52	15,08	12,47	0,20	9,94	10,54	3,56	1,47	0,04
42,44	2,53	15,21	12,44	0,20	10,03	10,67	3,74	1,19	0,03
42,23	2,38	14,54	12,19	0,21	10,69	10,44	3,16	1,26	0,04
42,97	2,16	14,3	11,04	0,206	10,79	11,12	4	1,48	0,0503
42,26	2,18	13,29	12,2	0,2	13,41	10,16	3,06	1,27	0,0802
43,49	1,82	13,41	11,26	0,199	14,18	8,71	3,72	1,13	0,0997
43,51	1,83	13,09	11,37	0,197	14,62	8,64	3,65	1,19	0,102
42,03	2,10	13,74	11,76	0,21	12,26	10,54	3,53	0,76	0,06
43,25	2,64	15,28	12,14	0,21	8,97	9,85	4,04	1,68	0,03
41,64	2,92	14,77	13,01	0,21	9,57	10,60	3,76	1,63	0,03
41,59	2,56	14,02	12,51	0,20	11,26	10,96	2,70	1,40	0,05
42,51	3,00	15,48	15,26	<0,01	9,68	9,11	3,43	1,27	0,02
42,52	2,97	15,95	14,65	0,01	8,41	9,43	3,61	1,39	0,02
43,73	2,69	15,14	12,78	0,21	9,26	9,39	3,28	1,54	0,03
41,41	2,16	13,46	11,84	0,19	13,58	10,76	3,63	0,79	0,06
41,79	2,22	13,60	12,13	0,20	13,46	10,41	3,45	0,78	0,06
41,79	2,64	14,30	12,90	0,21	11,48	9,52	3,03	1,31	0,04
41,54	2,58	13,98	12,66	0,21	11,33	9,88	2,80	1,50	0,04
42,25	2,70	14,26	13,18	0,21	11,32	9,59	2,81	1,33	0,04
42,95	2,53	14,66	12,60	0,21	11,47	9,52	3,25	1,31	0,04
43,06	2,54	14,41	12,52	0,20	11,54	9,63	3,30	1,23	0,04
40,78	2,11	12,62	11,29	0,19	14,92	11,42	3,49	1,23	0,08
40,85	2,11	12,76	11,15	0,19	14,83	11,28	3,54	1,32	0,08
45,83	1,84	15,18	10,72	0,20	10,43	8,34	4,31	1,67	0,04
46,69	1,78	15,70	10,57	0,20	9,62	7,70	4,53	1,74	0,03
42,23	2,90	14,85	13,57	0,21	9,73	9,87	3,12	1,48	0,02
41,69	2,80	14,82	13,24	0,20	9,86	9,89	2,95	1,45	0,03
42,09	2,86	15,20	13,39	0,21	9,30	9,93	3,70	1,51	0,02
49,14	2,36	15,13	11,98	0,00	7,80	7,76	2,70	1,38	0,02
47,20	2,44	14,64	12,08	<0,01	8,19	9,18	2,74	1,43	0,02
54,00	1,83	14,50	9,96	<0,01	6,18	5,86	1,30	1,85	0,02
43,56	2,61	15,36	12,02	0,20	10,09	9,91	3,33	1,40	0,03
43,85	2,53	15,29	11,83	0,20	9,83	9,80	3,42	1,50	0,04
45,18	1,90	14,61	11,24	<0,01	9,79	9,81	3,34	1,50	0,05
44,45	2,57	14,72	13,59	0,01	10,63	9,24	3,15	1,01	0,05
46,74	2,14	15,48	12,20	<0,01	7,78	7,97	3,47	1,43	0,04
47,06	2,20	15,38	12,28	<0,01	8,16	7,93	3,76	1,76	0,03
46,68	2,44	14,86	12,39	<0,01	9,72	8,01	2,09	1,44	0,03
48,18	2,31	15,92	10,70	<0,01	6,41	7,00	1,78	2,13	0,02
48,35	2,00	16,13	10,97	0,01	7,02	7,96	4,52	1,62	0,03

P_2O_5	NiO	V_2O_5	ZrO_2	TOTAL	Alkali	Mg#	CIA	LOI
0,66	0,02	0,05	0,08	**98,62**	5,52	61,74	48,93	0,13
0,68	0,02	0,04	0,09	**97,44**	4,72	61,72	51,11	1,65
0,69	0,02	0,05	0,08	**99,04**	5,26	62,44	48,48	0,04
0,68	0,02	0,05	0,08	**99,27**	5,42	62,76	48,68	*<0,01*
0,76	0,03	0,05	0,06	**99,28**	4,33	65,20	48,78	*<0,01*
0,74	0,02	0,05	0,08	**99,29**	5,03	61,23	49,20	*<0,01*
0,72	0,02	0,05	0,07	**99,34**	4,93	61,50	49,37	0,01
0,79	0,02	0,04	0,08	**98,07**	4,42	63,47	49,46	0,91
0,734	0,0202	0,0439	0,08	**98,99**	5,48	65,94	46,28	0,39408
0,691	0,0379	0,0399	0,0647	**98,94**	4,33	68,53	47,84	0,14828
0,638	0,0443	0,0374	0,0814	**98,82**	4,85	71,39	49,72	0,203
0,636	0,0449	0,0356	0,0811	**99,00**	4,84	71,81	49,27	0,18862
0,70	0,03	0,04	0,06	**97,83**	4,29	67,38	48,10	1,36
0,81	0,01	0,05	0,08	**99,05**	5,72	59,41	49,53	0,13
0,91	0,01	0,05	0,07	**99,18**	5,39	59,30	48,02	*<0,01*
0,96	0,02	0,05	0,07	**98,35**	4,10	64,07	48,21	1,00
0,66	<0,01	0,05	0,03	**100,49**	4,69	55,68	52,88	-0,44
0,73	<0,01	0,05	0,03	**99,79**	5,00	53,22	52,50	-0,30
0,82	0,01	0,04	0,08	**99,01**	4,82	58,94	51,58	0,34
0,68	0,03	0,05	0,05	**98,68**	4,42	69,44	47,00	0,74
0,70	0,03	0,05	0,06	**98,94**	4,23	68,73	48,16	0,25
0,82	0,03	0,05	0,07	**98,17**	4,34	63,81	50,78	0,98
0,81	0,03	0,04	0,07	**97,47**	4,30	63,94	49,64	1,92
0,83	0,02	0,04	0,07	**98,65**	4,14	62,98	50,95	0,51
0,70	0,02	0,05	0,07	**99,38**	4,56	64,33	51,01	*<0,01*
0,67	0,03	0,05	0,07	**99,28**	4,53	64,61	50,44	*<0,01*
0,87	0,04	0,05	0,06	**99,15**	4,72	72,36	43,88	0,19
0,86	0,05	0,04	0,06	**99,12**	4,86	72,49	44,15	0,13
0,57	0,03	0,03	0,10	**99,28**	5,98	65,84	51,46	*<0,01*
0,54	0,03	0,03	0,10	**99,27**	6,27	64,32	52,92	*<0,01*
0,75	0,01	0,05	0,07	**98,85**	4,60	58,69	50,65	0,38
0,72	0,01	0,05	0,07	**97,77**	4,40	59,60	50,91	1,59
0,78	0,01	0,05	0,07	**99,12**	5,21	57,91	50,10	*<0,01*
0,63	0,00	0,04	0,03	**99,00**	4,09	56,33	56,10	0,94
0,66	<0,01	0,04	0,04	**98,65**	4,16	57,31	52,32	1,08
0,44	<0,01	0,04	0,03	**96,01**	3,15	55,13	61,68	3,62
0,65	0,02	0,05	0,08	**99,30**	4,73	62,45	51,20	0,10
0,68	0,02	0,05	0,08	**99,11**	4,92	62,21	50,95	0,10
0,58	0,01	0,04	0,04	**98,10**	4,84	63,31	49,93	1,54
0,50	0,01	0,05	0,03	**100,00**	4,16	60,77	52,36	-0,19
0,65	<0,01	0,04	0,04	**97,97**	4,90	55,79	54,61	1,58
0,63	<0,01	0,04	0,04	**99,28**	5,52	56,84	53,34	0,67
0,55	<0,01	0,05	0,03	**98,28**	3,53	60,86	56,29	1,63
0,52	<0,01	0,04	0,03	**95,05**	3,91	54,28	59,34	4,44
0,43	<0,01	0,04	0,05	**99,13**	6,14	55,89	53,34	<0,01

Ga	Li	Sc	V	Cr	Co	Ni	Cu	Zn	Rb
22,197	9,144	25,651	273,982	268,931	97,62	121,54	39,579	99,634	35,457
22,374	8,307	25,919	236,533	256,314	86,304	133,44	66,666	96,084	17,816
22,117	8,038	27,643	283,942	278,92	91,672	135,753	42,343	98,752	34,947
22,366	7,595	28,087	285,135	288,162	93,408	138,531	41,981	109,873	36,158
20,652	7,883	29,231	295,811	329,548	90,234	205,404	42,012	100,213	24,24
24,631	10,595	43,449	317,483	259,250	93,151	127,192	61,472	119,020	48,162
24,621	10,587	45,516	332,078	260,152	105,940	122,456	64,013	106,788	48,568
24,430	11,088	45,830	303,187	318,707	89,469	168,403	61,645	109,330	46,087
23,666	9,21	26,966	289,014	389,722	99,023	175,589	47,378	109,451	39,523
20,45	7,3	27,056	279,371	521,089	97,197	281,346	47,547	101,592	27,06
20,78	10,565	22,571	225,343	602,714	93,955	363,092	37,496	104,067	26,338
20,336	8,184	22,488	230,515	616,598	96,55	377,862	37,536	104,804	28,699
21,687	7,994	25,828	277,809	449,364	87,916	266,906	66,369	108,304	11,583
22,625	8,02	25,994	275,263	285,43	77,703	109,49	48,958	104,814	36,733
21,883	5,823	29,331	322,093	240,599	92,609	87,89	80,841	98,758	34,338
20,559	6,719	26,464	263,627	376,753	86,444	156,783	65,221	90,503	29,072
20	5,446	25,22	267,4	184,5	82,1	109,7	63,75	109,2	26,96
19	6,191	23,96	254,1	175,9	86,03	90,71	62,8	109,3	28,67
20,277	7,86	24,78	237,439	260,623	91,999	109,356	67,939	98,552	30,586
19,804	4,971	23,572	247,592	407,803	91,957	268,392	66,92	97,77	11,023
19,851	8,646	23,448	251,939	424,058	86,319	267,177	94,977	100,425	10,146
19,069	6,445	24,114	233,128	252,551	81,631	193,016	49,739	96,169	25,712
19,489	6,625	24,107	232,82	264,532	91,763	194,105	53,301	88,976	27,488
19,049	4,159	24,376	242,724	264,172	86,307	188,715	53,821	89,699	26,962
19,5	6,464	24	241,052	293,002	97,774	197,301	82,502	91,14	25,626
19,178	5,037	24,5	243,162	283,442	92,685	193,911	72,809	91,06	25,585
20,813	7,142	25,304	248,699	502,437	88,408	313,684	62,883	99,202	29,272
24,665	10,833	44,901	315,297	565,912	98,441	332,049	76,834	108,483	51,371
21,478	8,145	18,716	178,463	274,155	81,557	209,937	53,063	97,748	42,261
26,004	14,952	30,073	218,595	271,691	76,704	210,246	47,149	113,697	70,398
20,046	3,701	24,258	246,243	194,2	82,759	94,468	48,033	95,946	25,656
19,605	5,521	24,149	244,566	207,278	81,205	100,371	72,031	95,188	26,618
24,610	11,180	42,746	334,528	265,159	91,435	97,349	57,522	110,141	44,906
19	9,309	24	196,9	205,1	64,39	104,4	55,76	108,5	44,72
19	9,947	24,77	210,3	221,2	71,45	111,1	55,47	109,3	39,99
19	13,09	20,01	177,5	163,8	49,92	89,37	53,14	103,4	63,81
24,148	11,993	46,850	327,000	271,947	88,337	122,282	60,356	105,648	49,202
24,544	11,917	45,023	320,047	279,212	94,439	120,868	57,416	103,626	53,696
18	7,157	21,61	215,9	369,5	97,72	193,4	68,22	107,5	36,96
18	5,495	25,98	260,9	387,8	92,34	208,4	69,85	116,2	22,97
21	8,572	20,73	199,8	299	69,99	140,9	52,04	112,8	38,94
21	11,58	20	200,4	257,5	85,7	129,2	51,4	115,9	40,29
18	7,955	25,23	216,3	226,1	84,01	136	61,82	99,09	31,66
24	8,546	18,14	182,3	202,6	59,6	110,4	50,83	107,8	39,59

Sr-avg	Y	Zr	Hf	Nb	Cs	Ba	La	Ce	Pr
839,649	24,52	264,764	5,302	97,358	0,393	455,481	48,204	97,629	10,515
849,886	25,248	273,507	5,507	95,841	0,157	492,061	48,846	98,686	10,517
818,394	24,486	248,107	5,08	92,103	0,362	470,576	45,822	93,338	10,054
825,769	24,504	250,144	5,132	93,403	0,383	453,898	46,306	93,71	10,136
723,441	23,366	197,533	4,161	71,507	0,217	344,78	36,632	78,674	8,782
1132,792	33,393	257,946	4,977	96,685	0,644	515,081	60,590	115,683	13,473
1090,877	33,251	252,952	4,833	93,864	0,639	494,791	57,860	112,829	13,002
1072,038	33,116	252,554	4,744	91,713	0,576	548,779	56,563	110,933	12,848
899,857	22,953	255,51	5,031	109,805	0,447	502,631	57,308	112,566	11,728
718,29	20,174	180,565	3,838	68,883	0,261	371,514	35,192	74,082	8,208
796,916	21,319	240,339	4,606	84,926	0,484	397,056	44,32	88,253	9,436
770,236	20,7	233,092	4,576	83,251	0,467	395,045	43,484	87,153	9,335
843,455	22,293	199,013	4,075	83,857	0,368	499,185	44,823	90,825	9,836
895,034	25,345	253,774	5,277	93,757	0,395	426,135	46,078	93,898	10,274
893,081	26,094	213,775	4,52	93,22	0,393	432,05	45,303	93,956	10,421
769,137	22,813	190,385	4,134	85,363	0,442	418,105	45,867	93,874	10,628
748,5	23,29	194,1	4,358	65,01		379,3	39,35	79,67	9,156
838,4	24,71	218,7	4,824	80,11		425,1	47,29	92,17	10,39
762,64	24,967	226,56	4,763	65,904	0,377	351,232	36,491	79,305	9,426
711,003	17,932	158,361	3,471	68,129	0,391	362,566	36,042	74,211	8,439
704,293	18,201	159,143	3,497	67,357	0,378	375,156	36,781	75,841	8,477
723,4	23,143	214,239	4,589	64,399	0,305	327,034	34,942	76,225	9,006
756,527	23,363	235,669	4,607	63,619	0,302	352,223	38,504	78,931	8,982
717,839	23,153	214,804	4,629	66,668	0,296	344,614	35,203	76,544	9,108
722,142	21,692	206,881	4,456	62,276	0,314	326,902	35,191	74,477	8,706
721,176	21,249	203,528	4,39	65,53	0,305	316,034	34,346	72,766	8,375
898,727	19,195	186,495	3,919	94,26	0,402	496,2	53,548	104,488	11,348
1216,576	27,641	214,876	3,990	113,896	0,708	586,829	71,939	137,751	14,967
810,266	21,357	292,387	5,844	82,878	0,476	436,922	48,227	96,989	10,556
1112,692	32,254	351,798	6,394	91,643	0,842	524,579	65,185	123,595	13,729
709,877	22,483	203,518	4,535	65,933	0,308	351,098	35,452	76,363	9,056
710,655	22,122	199,643	4,447	66,935	0,276	334,364	35,433	75,963	8,98
1090,093	34,803	255,510	4,965	81,600	0,360	433,661	52,720	109,411	12,832
654,9	24,99	191,9	4,234	56,96		411,2	42,21	86,14	9,49
676,3	25,59	230,8	4,4	59,46		421,7	43,03	87,81	9,611
468,6	21,33	147,6	3,458	41,05		454,5	37,4	79,66	8,419
1028,660	34,163	255,290	5,034	76,858	0,700	437,929	48,461	99,149	12,090
1037,493	35,076	257,430	5,069	79,254	0,740	436,892	48,413	99,982	12,039
861,8	21,92	284,3	5,123	104,5		558,4	66,05	120,9	12,61
712,2	22,2	202,5	4,328	64,71		350,5	40,48	81,08	8,721
774,5	26,27	304,3	5,467	80,87		460	56,69	110,7	12,24
779,6	25,63	291,3	4,089	81,84		496,7	58,19	112,4	12,48
599	21,93	180,8	6,127	53,74		379,4	33,34	69,07	7,982
838,6	22,91	344,8	6,127	86,16		480,2	61,87	115,1	12,14

Nd	Sm-avg	Eu-avg	Gd	Tb	Dy	Ho	Er	Tm	Yb
40,178	7,338	2,395	6,78	0,894	4,981	0,919	2,414	0,326	2,127
40,161	7,329	2,393	6,805	0,9	5,021	0,939	2,456	0,334	2,195
39,101	7,227	2,373	6,72	0,88	4,93	0,919	2,389	0,32	2,084
39,146	7,213	2,363	6,692	0,876	4,933	0,913	2,375	0,316	2,083
35,19	6,811	2,245	6,439	0,853	4,783	0,88	2,268	0,297	1,916
51,543	9,502	3,156	8,701	1,152	6,467	1,184	3,068	0,425	2,709
50,081	9,322	3,132	8,642	1,143	6,401	1,185	3,072	0,419	2,673
49,618	9,201	3,064	8,444	1,132	6,319	1,168	3,034	0,412	2,679
43,63	7,509	2,471	6,841	0,859	4,692	0,832	2,161	0,279	1,808
32,713	6,149	2,099	5,78	0,749	4,116	0,748	1,894	0,244	1,59
35,802	6,407	2,114	5,881	0,76	4,218	0,773	2,003	0,266	1,761
35,24	6,276	2,088	5,77	0,741	4,104	0,755	1,964	0,261	1,714
37,688	6,836	2,27	6,384	0,822	4,536	0,819	2,09	0,272	1,732
39,828	7,37	2,42	6,963	0,902	5,018	0,929	2,403	0,318	2,068
41,291	7,735	2,534	7,225	0,948	5,276	0,973	2,484	0,324	2,072
41,451	7,514	2,396	6,886	0,887	4,868	0,88	2,268	0,298	1,883
36,49	7,174	2,296	6,403	0,899	5,005	0,925	2,452	0,325	1,978
40,81	7,654	2,361	6,895	0,958	5,393	0,996	2,629	0,347	2,127
38,301	7,38	2,428	6,982	0,921	5,176	0,974	2,52	0,337	2,171
32,689	6,075	2,039	5,595	0,715	3,925	0,694	1,769	0,221	1,383
33,308	6,14	2,055	5,721	0,736	4,011	0,709	1,777	0,225	1,421
36,519	6,983	2,304	6,574	0,865	4,903	0,907	2,34	0,311	2,009
36,188	6,958	2,295	6,511	0,873	4,863	0,905	2,361	0,304	1,962
36,5	6,995	2,311	6,573	0,869	4,926	0,905	2,363	0,315	2,038
34,235	6,479	2,158	6,078	0,801	4,559	0,837	2,183	0,29	1,881
33,613	6,381	2,127	6,002	0,796	4,485	0,828	2,173	0,289	1,88
42,208	7,229	2,351	6,514	0,797	4,241	0,741	1,86	0,234	1,481
54,849	9,446	3,084	8,301	1,043	5,494	0,965	2,400	0,313	1,961
39,381	6,787	2,228	6,241	0,805	4,479	0,824	2,2	0,299	1,934
50,609	8,838	2,940	8,047	1,064	5,925	1,102	2,945	0,415	2,742
36,311	6,943	2,267	6,512	0,854	4,807	0,885	2,271	0,298	1,906
36,068	6,919	2,247	6,462	0,84	4,735	0,866	2,235	0,293	1,871
50,782	9,561	3,131	8,858	1,187	6,640	1,226	3,153	0,421	2,745
37,62	7,241	2,166	6,441	0,905	5,209	0,956	2,599	0,348	2,216
38,8	7,429	2,255	6,608	0,922	5,402	0,99	2,708	0,366	2,299
32,76	6,314	1,858	5,514	0,783	4,524	0,832	2,262	0,305	1,936
47,795	9,310	3,052	8,620	1,165	6,541	1,204	3,139	0,428	2,761
47,782	9,306	3,080	8,704	1,176	6,600	1,226	3,179	0,433	2,791
43,26	7,398	2,294	6,123	0,838	4,683	0,842	2,258	0,294	1,913
34,34	6,633	2,118	5,863	0,816	4,727	0,858	2,306	0,307	1,93
44,08	7,93	2,406	6,696	0,939	5,526	1	2,666	0,358	2,294
44,15	7,874	2,443	6,927	0,967	4,759	0,871	2,392	0,327	1,969
31,88	6,375	2,017	5,842	0,838	4,785	0,873	2,364	0,323	2,128
41,62	7,133	2,303	6,064	0,844	4,785	0,873	2,364	0,323	2,128

Lu	Ta	Pb-avg	Th	U
0,306	5,647	3,15	6,799	1,82
0,317	5,691	1,205	8,031	2,217
0,298	5,405	2,762	6,881	2,145
0,298	5,425	2,862	7,102	2,169
0,272	3,893	2,143	4,678	1,444
0,388	6,161	2,904	8,614	1,875
0,389	5,822	2,338	8,140	1,856
0,386	5,736	2,803	8,084	1,884
0,256	6,473	3,539	9,61	2,726
0,217	4,027	2,237	5,236	1,475
0,25	5,156	2,815	7,174	2,027
0,245	5,039	2,77	7,31	2,118
0,247	4,973	2,48	6,401	1,716
0,298	5,271	2,777	6,911	2,077
0,297	5,253	2,049	6,066	1,767
0,268	4,88	9,24	5,755	1,621
0,303	3,522	2,111	4,375	0,985
0,331	4,278	2,353	5,423	1,275
0,313	4,073	2,68	4,358	1,266
0,189	4,22	1,688	4,774	1,319
0,191	4,244	2,043	4,633	1,26
0,284	3,573	1,631	3,604	1,177
0,297	3,516	2,416	4,165	1,318
0,287	3,809	1,886	3,802	1,239
0,266	3,83	1,867	4,066	1,26
0,267	3,904	1,862	4,031	1,236
0,2	5,333	2,749	7,518	2,158
0,273	6,678	3,069	11,644	2,516
0,277	5,828	3,147	7,177	1,87
0,404	6,739	3,499	10,865	2,461
0,267	3,591	2,062	4,141	1,233
0,263	3,785	1,997	4,149	1,142
0,392	5,377	1,973	6,568	1,412
0,341	3,229	5,065	6,076	1,487
0,348	3,328	3,929	5,77	1,367
0,292	2,435	8,356	7,688	1,494
0,402	5,121	5,146	6,856	1,595
0,407	5,277	3,658	6,881	1,629
0,29	5,874	3,91	9,13	2,007
0,295	3,527	2,131	4,399	0,978
0,354	4,702	3,99	6,976	1,69
0,303	3,044	5,591	7,175	1,742
0,323	5,202	3,923	4,676	1,137
0,323	5,202	3,717	8,02	1,902

8.2 Appendix B: XRD data of the Bayuda Monogenetic Volcanic Field

XRD analysis of selected samples

Sample: 10-1A

Mineral	weight%
Augite	33,96
Forsterite	15,07
Magnetite	7,11
Nepheline	13,84
Plagioclase	30,02

Sample: 10-1B

Mineral	*weight%*
Augite	42,18
Forsterite	11,69
Magnetite	8,82
Nepheline	13,59
Plagioclase	23,72

Sample: II-1

Mineral	*weight%*
Augite	58,88
Enstatite	3,06
Forsterite	17,5
Hematite	0,93
Plagioclase	19,62

Sample: I-6

Mineral	*weight%*
Augite	23,4
Chlorite	7,13
Forsterite	4,54
Hematite	1,88
Muscovite	9,74
Plagioclase	32,33
Quartz	20,98

Sample: I-4

Mineral	*weight%*
Augite	36,59
Forsterite	11,96
Hematite	7,75
Muscovite	2,28
Plagioclase	35,71
Quartz	5,72

Sample: II-2

Mineral	*weight%*
Augite	37,07
Forsterite	17,4
Magnetite	6,5
Nepheline	12,45
Plagioclase	26,58

Sample: II-4

Mineral	*weight%*
Diopside	36,35
Forsterite	13,83
Hornblende	6,52
Plagioclase	41,35
Quartz	1,94

Sample: II-5

Mineral	*weight%*
Augite	39,45
Forsterite	20,8
Plagioclase	31,45
Quartz	8,3

8.3 Appendix C: Isotopic data of the Bayuda Monogenetic Volcanic field

Isotopic compositions of selected samples of the BMVF

Sample	Volcano Nr.	Latitiude	Longitude	$^{87}Sr/^{86}Sr \pm 2\sigma$	$^{143}Nd/^{144}Nd \pm 2\sigma$	ε_{Nd}	$^{176}Hf/^{177}Hf \pm 2\sigma$	ε_{Hf}	$^{206}Pb/^{204}Pb$	$^{207}Pb/^{204}Pb$	Pb$^{208}Pb/^{204}Pb$
BHVO2	NA	NA	NA	0.703487 (12)	0.512995 (13)	7.0	0.283099 (11)	11			
B07	CC9	18°16'40.75"N	32°35'7.46"E	0.703184 (7)	0.512898 (12)	5.1	0.283017 (8)	8.2			
B12	CC44	18°22'5.02"N	32°34'24.03"E	0.703010 (10)	0.512922 (10)	5.5	0.283018 (8)	8.2			
B18	M6	18°24'3.86"N	32°31'31.85"E	0.703132 (9)	0.512905 (12)	5.2	0.283025 (8)	8.5	19.895	15.653	39.678
V07	M8	18°29'3.68"N	32°28'26.55"E	0.703347 (9)	0.512869 (10)	4.5	0.283026 (9)	8.5	19.451	15.677	39.307
V04	CC7	18°25'11.85"N	32°31'26.11"E	0.703171 (9)	0.512889 (16)	4.9	0.283013 (8)	8.0			
B21	M5	18°24'7.01"N	32°32'7.87"E	0.703177 (11)	0.512939 (13)	5.9	0.283024 (8)	8.4	19.787	15.639	39.560
V05	CC6	18°25'45.69"N	32°29'12.05"E	0.703168 (6)	0.512900 (11)	5.1	0.283006 (8)	7.8			
B17	M7	18°24'11.39"N	32°30'59.42"E	0.703137 (12)	0.512919 (13)	5.5	0.283016 (8)	8.2	19.877	15.651	39.640
II-1	CC48	N18°16'43.1''	E32°49'42.4''	0.703152 (9)	0.512912 (13)	5.4	0.283017 (8)	8.2	19.862	15.650	39.625
V-1	M11	N18°18'57.6''	E32°47'56.6''	0.703250 (9)	0.512891 (13)	4.9	0.283006 (8)	7.8	19.882	15.644	39.639

8.4 Appendix D: Single mineral analysis

Point Analysis of the Minerals of the BMVF

Volcano	Sample	mineral	SiO2	TiO2	Al2O3	Cr2O3	FeO	MnO	MgO	NiO	CaO	Na2O	K2O	Total	X	Y	Z
M7	10-1A_mineral 1_core	olivine	35,89	0,06	0,06	0,01	18,79	0,25	40,58	0,09	0,39	0,02	0,03	96,17	-13287	30351	-82
M7	10-1A_mineral 1_rim	olivine	38,69	0,08	0,04	0,01	20,14	0,37	40,71	0,09	0,37	0	0	100,49	-13311	30331	-83
M7	10-1A_mineral 10_core	olivine	39,4	0,02	0,04	0,01	15,57	0,18	44,24	0,16	0,22	0	0,01	99,86	5624	23054	-9
M7	10-1A_mineral 10_rim	olivine	38,3	0,06	0,03	0,02	20,17	0,34	40,25	0,08	0,3	0	0	99,55	5595	22986	-9
M7	10-1A_mineral 11_fsp	plagioclase	49,19	0,21	29,79	0	0,8	0,02	0,02	0	14,34	3,21	0,15	97,74	5620	22897	-8
M7	10-1A_mineral 2_core	olivine	38,31	0,06	0,03	0	20,1	0,3	41,32	0,07	0,32	0	0	100,52	-14064	30957	-90
M7	10-1A_mineral 2_rim	pyroxene	43,94	0,18	11,95	0	12,46	0,31	16,43	0	4,74	2,43	0,91	93,34	-14133	31013	-90
M7	10-1A_mineral 3_core	olivine	38,31	0,04	0,05	0,01	19,43	0,28	41,4	0,09	0,25	0	0,01	99,87	-13937	30137	-86
M7	10-1A_mineral 3_rim	olivine	38,19	0,04	0,03	0	22,59	0,47	38,85	0,06	0,38	0	0,01	100,62	-13963	30063	-84
M7	10-1A_mineral 4_core	olivine	38,61	0,03	0,04	0	18,49	0,22	42,61	0,08	0,23	0	0	100,32	-13927	29213	-79
M7	10-1A_mineral 4_rim	olivine	37,86	0,05	0,05	0,02	21,83	0,4	41,3	0,09	0,24	0	0,01	101,85	-13929	29120	-76
M7	10-1A_mineral 5_core	olivine	38,53	0,03	0,05	0,01	19,21	0,27	41,59	0,09	0,21	0	0	99,99	-13137	28171	-70
M7	10-1A_mineral 5_rim	olivine	37,31	0,07	0,03	0	25,55	0,57	35,9	0,03	0,42	0	0	99,89	-13140	28249	-69
M7	10-1A_mineral 6_core	olivine	39,65	0,01	0,07	0,03	14,73	0,2	44,8	0,19	0,21	0,01	0,01	99,91	-14100	28003	-69
M7	10-1A_mineral 6_rim	olivine	37,9	0,05	0,05	0	22,98	0,41	38,47	0,08	0,24	0	0,01	100,18	-14399	27808	-70
M7	10-1A_mineral 7_core	olivine	0,02	0,04	0,03	16,9	0,22	42,96	0,11	0,23	0,23	0	0,02	99,39	15444	24031	-7
M7	10-1A_mineral 7_rim	olivine	37,38	0,06	0,03	0	24,64	0,59	36,74	0,05	0,41	0	0,02	99,91	15458	23914	-7
M7	10-1A_mineral 8_core	olivine	38,42	0,04	0,05	0	19,52	0,28	41,11	0,08	0,21	0	0,01	99,74	16445	24017	-7
M7	10-1A_mineral 8_core_grey patch		0,7	1,57	49,15	2,46	29,06	0,17	14,86	0,13	0,05	0	0	98,16	16403	24083	-6
M7	10-1A_mineral 8_rim	olivine	38,18	0,04	0,04	0,01	20,97	0,36	39,72	0,06	0,34	0	0,02	99,74	16395	23972	-6
M7	10-1A_mineral 9_core	olivine	38,44	0,04	0,04	0	18,88	0,25	41,29	0,07	0,28	0	0,01	99,3	7964	19415	15
M7	10-1A_mineral 9_rim	olivine	36,22	0,13	0,04	0	29,06	0,81	32,87	0,03	0,45	0	0,03	99,64	7920	19372	15
M7	10-1B_mineral1_core	pyroxene	48,05	1,55	6,58	0,02	10,76	0,23	10,69	0,01	20,15	1,48	0	99,52	-12664	-26193	-216
M7	10-1B_mineral1_rim	pyroxene	46,16	2,12	9,25	0,06	7,21	0,11	12,45	0,02	21,2	0,86	0,02	99,45	-11697	-25901	-213
M7	10-1B_mineral1_rim2	pyroxene	41,2	5,18	10,79	0,03	8,41	0,12	10,17	0	22,6	0,53	0,02	99,04	-11170	-26602	-212
M7	10-1B_mineral10_core	olivine	39,97	0,02	0,08	0,03	14,08	0,19	45,21	0,16	0,24	0,01	0,01	100,02	-18196	-29665	-251
M7	10-1B_mineral10_rim	olivine	39,3	0,04	0,04	0	18,85	0,3	41,13	0,1	0,29	0	0	100,06	-18040	-29677	-249
M7	10-1B_mineral2_core	olivine	39,09	0,04	0,05	0,01	18,94	0,3	41,04	0,13	0,26	0,02	0,01	99,89	-12829	-31120	-229
M7	10-1B_mineral2_rim	olivine	37,32	0,14	0,08	0,01	27,31	0,67	33,64	0,01	0,59	0,01	0,01	99,78	-12932	-31068	-228
M7	10-1B_mineral3_core	pyroxene	46,58	2,17	8,19	0,01	8,71	0,16	10,43	0,01	21,92	1,16	0,01	99,36	-13445	-33158	-235
M7	10-1B_mineral3_rim	pyroxene	46,55	2,23	7,89	0,44	6,57	0,1	12,56	0,01	22,26	0,65	0,01	99,29	-13396	-33172	-235
M7	10-1B_mineral4_L1	olivine	40,17	0,01	0,06	0,02	14,57	0,21	44,75	0,16	0,22	0	0,01	100,2	-13928	-33514	-238
M7	10-1B_mineral4_L2	olivine	40	0,08	0,08	0,04	15,17	0,18	44,33	0,23	0,23	0	0,01	100,22	-13904	-33509	-238
M7	10-1B_mineral4_L3	olivine	39,39	0,04	0,04	0,02	18,9	0,27	41,44	0,13	0,25	0,01	0,01	100,5	-13845	-33508	-238
M7	10-1B_mineral4_L4	olivine	39,36	0,03	0,04	0,02	18,66	0,28	41,74	0,08	0,3	0	0,01	100,52	-13828	-33525	-238
M7	10-1B_mineral4_L5	olivine	39,22	0,03	0,04	0	19,65	0,31	40,93	0,08	0,39	0	0,02	100,69	-13811	-33525	-236
M7	10-1B_mineral5_core	olivine	39,88	0,01	0,06	0,02	15,7	0,22	43,91	0,14	0,25	0	0,01	100,2	7377	-23270	-133
M7	10-1B_mineral5_rim	olivine	39,27	0,07	0,05	0,01	19,35	0,31	41,11	0,09	0,35	0	0,01	100,62	7298	-23427	-137
M7	10-1B_mineral6_core	olivine	40,1	0,03	0,06	0,02	15,09	0,21	44,61	0,14	0,23	0	0,01	100,5	7250	-21474	-131
M7	10-1B_mineral6_rim	olivine	39,32	0,03	0,05	0,01	18,89	0,3	40,96	0,1	0,3	0	0	99,97	7369	-21459	-131
M7	10-1B_mineral7_core	olivine	40,33	0,02	0,07	0,04	14,22	0,17	45,49	0,17	0,24	0,02	0	100,77	4768	-25519	-150
M7	10-1B_mineral7_rim	olivine	39,48	0,04	0,04	0,02	18,76	0,31	41,49	0,1	0,3	0	0	100,52	4563	-25520	-150
M7	10-1B_mineral8_core	olivine	40,62	0,02	0,07	0,07	12,21	0,15	46,51	0,27	0,22	0,03	0,02	100,19	-4722	-35477	-209
M7	10-1B_mineral8_rim	olivine	39,39	0,04	0,05	0,03	18,66	0,29	41,28	0,12	0,28	0	0,01	100,15	-5128	-35671	-211
M7	10-1B_mineral9_core	pyroxene	48,57	1,92	5,18	0,12	6,86	0,13	13,76	0,01	22,81	0,4	0,02	99,79	1759	-35202	-190
M7	10-1B_mineral9_rim	pyroxene	41,04	5,2	10,89	0,03	8,57	0,12	10,13	0,02	22,64	0,54	0,01	99,19	1800	-35188	-190
DX1	B10_1_centre	olivine	39,59	0,04	0,04	0,02	17,01	0,27	42,63	0,16	0,29	0,01	0	100,06	10501	30530	-100
DX1	B10_1_rim	olivine	39,41	0,02	0,04	0	17,38	0,29	42,83	0,17	0,26	0	0,01	100,4	7366	21545	-91
DX1	B10_2_centre	olivine	40,13	0	0,07	0,06	12,56	0,16	46,63	0,28	0,22	0,01	0,01	100,14	10968	31336	-103
DX1	B10_2_inclusion1		0,15	0,73	35,4	26,44	19,45	0,14	16,66	0,23	0,01	0	0	99,23	10581	31277	-104
DX1	B10_2_rim	olivine	39,27	0,03	0,02	0,01	16,67	0,29	42,4	0,15	0,28	0	0,01	99,14	10501	30530	-91
DX1	B10_3_centre	olivine	40,29	0,01	0,07	0,05	11,76	0,16	47,46	0,23	0,25	0,01	0	100,29	7584	23446	-94
DX1	B10_3_inclusion1	spinel	0,17	0,75	40,89	21,26	18,01	0,12	17,33	0,22	0,01	0	0	98,77	7717	23298	-94
DX1	B10_3_inclusion2		0,18	0,71	43,41	18,66	17,58	0,12	18,06	0,25	0,01	0	0,01	98,99	7630	23203	-92
DX1	B10_3_rim	olivine	39,78	0,02	0,05	0,03	15,82	0,25	43,96	0,15	0,27	0	0,01	100,34	7527	23904	-92
DX1	B10_4_needle1		36,14	10,35	10,86	0	23,45	0,66	6,23	0	0,07	0,72	8,42	96,9	-4864	31742	-70
DX1	B10_4_needle2		64,17	0,14	19,62	0	0,34	0	0,04	0	0,51	3,7	9,89	98,4	-4937	31726	-71
DX1	B10_5_centre	olivine	40,66	0,02	0,08	0,04	11,66	0,16	47,59	0,22	0,23	0	0,01	100,68	-7132	32621	-63
DX1	B10_5_rim	olivine	39,7	0,02	0,03	0,04	15,74	0,27	44,71	0,2	0,25	0	0	100,96	-7114	32977	-67
DX1	B10_6_centre		0,13	0,83	34,1	28,82	18,31	0,16	16,73	0,22	0	0	0	99,3	-6833	32352	-63
DX1	B10_6_rim		0,07	13,46	7,05	6,98	62,71	0,72	3,4	0,03	0,19	0	0	94,59	-6840	32251	-66
DX1	B10_7_centre1	olivine	40,84	0,01	0,06	0,07	11,4	0,15	47,55	0,24	0,23	0,01	0	100,56	-6662	31447	-63
DX1	B10_7_centre2	olivine	40,7	0	0,09	0,06	11,62	0,17	47,69	0,28	0,22	0,01	0,01	100,84	-6503	31478	-65
DX1	B10_7_centre3	olivine	40,66	0,01	0,05	0,07	11,42	0,17	47,78	0,29	0,26	0	0,01	100,73	-6331	31511	-65
DX1	B10_7_rim1	olivine	39,61	0,03	0,05	0,03	15,74	0,26	44,43	0,17	0,29	0	0	100,6	-6235	31562	-68
DX1	B10_7_rim2	olivine	37,26	0,15	0,21	0,01	26,26	0,73	34,19	0,04	1,46	0	0,02	100,34	-6197	31527	-70
DX1	B10_8_core1	olivine	39,22	0	0,06	0,04	12,5	0,16	46,78	0,29	0,21	0	0	99,28	-3189	33093	-82
DX1	B10_8_core2	olivine	37,25	0,02	0,05	0,06	11,65	0,17	46,8	0,26	0,25	0,01	0,01	96,52	-4181	33154	-89
DX1	B10_8_rim	olivine	37,24	0,03	0,02	0	24,81	0,66	36,94	0,07	0,43	0	0	100,19	-4444	33198	-79
CC44	B12_min1_core	olivine	38,88	0,05	0,04	0	20,24	0,34	40,47	0,06	0,38	0	0	100,46	13421	23109	-32
CC44	B12_min1_rim	pyroxene (poor total)	51,47	0,66	23,77	0,01	2,77	0,05	1,22	0	9,9	4,57	1,33	95,75	13403	23119	-34
CC44	B12_min10_core1	olivine	39,28	0,06	0,06	0	19,07	0,21	41,51	0	0,25	0	0,01	100,46	1314	20029	-17
CC44	B12_min10_core2	olivine	39,72	0,03	0,05	0,03	16,28	0,28	43,38	0,13	0,27	0	0,01	100,18	1353	20119	-18
CC44	B12_min10_rim	pyroxene	45,59	3,2	6,58	0,01	8,58	0,17	12,25	0	22,09	0,42	0,04	98,94	1399	20128	-19
CC44	B12_min2_core	olivine	39,82	0,04	0,06	0,03	16,06	0,21	43,63	0,13	0,23	0,03	0	100,24	6752	29928	-91
CC44	B12_min2_rim	olivine	37,94	0,06	0,05	0	23,57	0,43	38,1	0,03	0,48	0	0,01	100,65	6825	29937	-92
CC44	B12_min3_core	olivine	39,8	0,03	0,04	0,02	16,58	0,28	43,42	0,11	0,28	0	0	100,57	7004	30824	-96
CC44	B12_min3_rim	olivine	38,82	0,11	0,63	0,1	20,39	0,34	38,79	0,09	0,45	0,15	0,07	99,94	7035	30854	-95
CC44	B12_min4_core	olivine	39,6	0,04	0,05	0,03	16,6	0,27	43,5	0,17	0,3	0	0	100,56	6685	31063	-94

CC44	B12_min4_rim1	olivne	38,78	0,04	0,07	0,02	17,05	0,26	42,54	0,11	0,31	0	0	99,18	6718	31041	-96
CC44	B12_min4_rim2	olivine	39,44	0,04	0,05	0,03	16,75	0,24	42,77	0,12	0,27	0	0,01	99,7	6702	31016	-94
CC44	B12_min5_core	olivine	39,77	0,02	0,06	0,03	16,2	0,2	43,89	0,12	0,24	0	0,01	100,54	5947	34710	-120
CC44	B12_min5_rim	pyroxene	41,57	4,78	10,31	0,01	8,61	0,14	10,42	0	22,35	0,59	0	98,78	6089	34692	-122
CC44	B12_min6_core	olivine	39,29	0,03	0,04	0,03	18,95	0,3	40,71	0,08	0,33	0	0	99,77	6007	34383	-117
CC44	B12_min6_rim	pyroxene	48,27	1,17	19,74	0,01	5,38	0,12	0,9	0	10,21	5,23	3,46	94,48	6027	34416	-118
CC44	B12_min7_core	olivine	39,07	0,03	0,05	0,01	19,25	0,3	40,98	0,09	0,35	0	0,01	100,13	6475	34134	-116
CC44	B12_min7_rim	pyroxene	54,48	1,11	23,18	0	3,15	0,07	0,27	0	6,86	6,43	2,29	97,84	6501	34163	-115
CC44	B12_min8_core	olivine	39,54	0,06	0,05	0,01	16,88	0,25	43,08	0,14	0,3	0	0	100,32	6265	33928	-116
CC44	B12_min8_rim	olivine	38,89	0,07	0,03	0	20,23	0,35	40,24	0,06	0,41	0	0	100,28	6264	33880	-115
CC44	B12_min9_core	olivine	39,56	0,02	0,03	0,02	17,23	0,25	42,68	0,12	0,32	0	0	100,24	6671	31692	-98
CC44	B12_min9_rim	olivine	38,81	0,04	0,04	0,02	19,23	0,32	40,64	0,08	0,37	0	0,01	99,55	6695	31660	-99
CC44	B12_neph?	Qtz	98,9	0,01	0	0,01	0	0	0	0	0,01	0,01	0,01	98,96	-1715	19228	-15
CC44	B12_sym_core		53,31	0,05	2,59	0,04	18,03	0,3	25,55	0,02	0,33	0	0	100,23	-10046	19195	-34
CC44	B12_sym_innerzone		54,07	0,34	1,08	0,14	8,31	0,26	19,46	0	15,87	0,45	0,01	100	-10308	19180	-35
CC44	B12_sym_outerzone1		39,43	0,02	0,02	0,02	17,45	0,28	42,77	0,09	0,31	0	0,01	100,39	-10377	19510	-39
CC44	B12_sym_outerzone2		32,4	0,1	16,84	0	0,38	0	0,3	0,02	8,06	0,17	6,35	64,62	-10387	19488	-39
M5	B22_mineral 1_core	pyroxene	49,38	1	6,92	0,02	7,39	0,08	12,04	0,01	21,24	1,45	0,01	99,53	9612	-24746	-135
M5	B22_mineral 1_rim	pyroxene	41,06	4,88	11,06	0,05	8,21	0,12	10,31	0,01	22,73	0,47	0,01	98,9	10023	-25015	-135
M5	B22_mineral 10_core	pyroxene	45,65	2,52	8,45	0,25	6,96	0,08	12,22	0,02	22,57	0,54	0,01	99,27	-7233	-22198	-177
M5	B22_mineral 10_rim	plagioclase	50,05	0,14	30,58	0	0,62	0,01	0,09	0	14,44	3,11	0,22	99,24	-6908	-21841	-175
M5	B22_mineral 11	plagioclase	50,33	0,18	30,27	0,01	0,75	0	0,12	0,01	14,22	3,32	0,25	99,46	-7211	-21457	-176
M5	B22_mineral 12	plagioclase	49,38	0,14	30,86	0,02	0,55	0	0,09	0,01	14,84	3	0,22	99,1	4676	-35122	-189
M5	B22_mineral 13	plagioclase	50,38	0,18	30,44	0	0,73	0	0,11	0,01	14,18	3,42	0,25	99,7	15906	-27053	-127
M5	B22_mineral 14	olivine	34,96	0,02	0,46	0,01	32,08	0,71	24,92	0,06	0,66	0	0,04	93,92	12396	29631	-47
M5	B22_mineral 2_core	olivine	39,87	0	0,06	0,02	15,94	0,22	43,76	0,18	0,23	0	0,01	100,29	7419	-24271	-141
M5	B22_mineral 2_rim	olivine	39,34	0,03	0,03	0,02	19,22	0,31	41,07	0,09	0,34	0	0	100,45	7466	-24149	-139
M5	B22_mineral 3_core	olivine	40,26	0	0,07	0,04	14,16	0,2	45,41	0,2	0,23	0,01	0	100,58	-9777	-28942	-208
M5	B22_mineral 3_rim	pyroxene	46,39	0,6	15,21	0	16,77	0,44	15,84	0,01	3,69	1,87	2,82	103,65	-9847	-29007	-207
M5	B22_mineral 3_rim2	pyroxene	38,38	0,09	0,15	0	24,53	0,52	36,86	0,06	0,53	0	0,03	101,16	-9844	-29001	-203
M5	B22_mineral 4_core	olivine	40,29	0,02	0,06	0,02	14,06	0,2	45,05	0,17	0,26	0	0	100,14	-11807	-31382	-219
M5	B22_mineral 4_rim	olivne	39,06	0,04	0,04	0,02	19,89	0,34	40,52	0,11	0,39	0	0	100,41	-11721	-31312	-219
M5	B22_mineral 5_core	olivine	40,23	0,02	0,07	0,02	14,63	0,21	44,72	0,21	0,24	0,01	0	100,38	-14357	-29971	-224
M5	B22_mineral 5_rim	olivine	37,6	0,14	0,17	0	27,8	0,63	33,53	0,01	0,62	0,06	0,02	100,58	-14442	-30083	-224
M5	B22_mineral 6_core	olivine	39,75	0,02	0,04	0,02	17,5	0,26	41,88	0,14	0,23	0	0	99,85	-14984	-29337	-225
M5	B22_mineral 6_rim	olivine	39,14	0,03	0,04	0,01	21,16	0,35	39,15	0,09	0,37	0	0,01	100,35	-14895	-29402	-224
M5	B22_mineral 7_core	olivine	39,5	0,04	0,04	0,03	17,93	0,28	42,3	0,11	0,27	0	0	100,51	-8731	-25556	-193
M5	B22_mineral 7_rim	olivine	39,08	0,06	0,03	0	23,05	0,45	36,83	0,07	0,48	0	0	100,05	-8874	-25615	-195
M5	B22_mineral 8_core	olivine	39,17	0,05	0,06	0,01	19,98	0,3	40,54	0,1	0,24	0,01	0	100,46	-7207	-22863	-178
M5	B22_mineral 8_rim	pyroxene?	52,55	0,73	21,46	0,01	4,96	0,15	1,77	0,01	1,8	5,18	1,41	90,03	-7207	-22902	-179
M5	B22_mineral 8_rim	olivne	39,84	0,05	0,07	0,02	17,97	0,27	41,66	0,11	0,23	0	0	100,22	-7455	-23162	-181
M5	B22_mineral 9_core	olivine	39,08	0,06	0,04	0	20,13	0,34	39,9	0,1	0,4	0	0,01	100,05	-7428	-23172	-182
M5	B22_mineral 9_rim	pyroxene	49,39	1,19	7,7	0,01	6,74	0,04	11,87	0,01	20,89	1,88	0	99,73	-7080	-22064	-177
CC53	B25_mineral 1_core	olivine	40,36	0	0,15	0,08	12,76	0,17	46,46	0,26	0,22	0,01	0	100,47	-277	-23826	-174
CC53	B25_mineral 1_rim	olivine	39,47	0,04	0,04	0	19,26	0,29	40,71	0,08	0,34	0	0	100,23	-19	-23392	-171
CC53	B25_mineral 10_core	olivine	38,99	0,03	0,04	0	19,11	0,26	41,33	0,08	0,22	0	0	100,06	-3973	-33963	-204
CC53	B25_mineral 10_rim	olivine	38,7	0,16	0,07	0,01	21,61	0,44	38,48	0,03	0,69	0	0,02	100,2	-3839	-33993	-203
CC53	B25_mineral 11_core	olivine	40	0,01	0,06	0,04	12,38	0,17	46,68	0,26	0,23	0	0	99,83	342	-20130	-166
CC53	B25_mineral 11_rim	olivine	39,31	0,04	0,04	0	19,61	0,3	40,47	0,1	0,35	0	0	100,24	-336	-20524	-164
CC53	B25_mineral 12	plagioclase	42,8	4,46	9,48	0,01	8,29	0,11	10,78	0,01	22,89	0,47	0,06	99,37	-3928	-34863	-204
CC53	B25_mineral 13	plagioclase	43,26	3,97	8,58	0,01	9,84	0,16	10,63	0	22,03	0,49	0,02	98,99	-4091	-34847	-204
CC53	B25_mineral 2_core_sp?	plagioclase	48,25	2,55	21,93	0,14	3,97	0,06	3,3	0,03	14,07	2,14	0,54	96,97	110	-24080	-166
CC53	B25_mineral 2_rim_magnetite		0,14	0,88	35,34	24,47	25,42	0,31	12,66	0,14	0,03	0	0,01	99,41	131	-24069	-171
CC53	B25_mineral 3_dark material		16,5	1,43	40,91	2,33	21,58	0,27	11,11	0,04	3,32	2,66	0,34	100,49	-14450	-31442	-243
CC53	B25_mineral 3_grey core		0,09	1,29	52,66	2,58	26,28	0,28	15,44	0,09	0	0	0	98,71	-14292	-31352	-245
CC53	B25_mineral 3_white rim		1,62	8,27	14,61	2,26	63,81	0,58	5,53	0,04	0,13	0,8	0,06	97,71	-14376	-31350	-243
CC53	B25_mineral 4_core	pyroxene	45,7	2,56	10,76	0,02	7,77	0,14	12,57	0	18,34	1,28	0,01	99,16	-13601	-17677	-216
CC53	B25_mineral 4_rim	pyroxene	43,18	3,76	9,66	0,08	7,81	0,1	11,25	0,01	22,61	0,47	0,01	98,95	-14192	-17280	-220
CC53	B25_mineral 5_core	olivine	38,68	0,05	0,04	0	19,4	0,31	41,34	0,1	0,34	0	0	100,28	-9747	-18799	-202
CC53	B25_mineral 5_rim	pyroxene	38,97	6,38	12,02	0	8,99	0,1	9,31	0	22,5	0,49	0,03	98,8	-9697	-18887	-201
CC53	B25_mineral 6_core	olivine	39,63	0,02	0,04	0,03	16,24	0,24	43,33	0,13	0,23	0	0	99,88	-9435	-18696	-202
CC53	B25_mineral 6_rim	olivine	39,59	0,09	0,05	0,01	19,9	0,33	38,95	0,06	0,44	0	0	99,43	-9304	-18736	-195
CC53	B25_mineral 7_core	olivine	39,81	0,02	0,06	0,01	16,01	0,19	43,26	0,11	0,23	0	0	99,7	-10344	-19400	-204
CC53	B25_mineral 7_rim	olivine	39,98	0,03	0,05	0	18,75	0,26	40,19	0,06	0,3	0	0	99,62	-10602	-19169	-205
CC53	B25_mineral 8_core	quartz	99,78	0	0,01	0	0,04	0,02	0	0,02	0,02	0	0	99,88	-11032	-19218	-204
CC53	B25_mineral 8_rim	pyroxene	50,95	1,71	3,3	0,02	8,07	0,2	12,62	0	21,45	0,57	0,53	99,42	-10998	-19165	-209
CC53	B25_mineral 9_core	olivine	39,12	0,04	0,04	0,01	19,38	0,27	41,04	0,1	0,22	0	0	100,2	-6633	-33056	-213
CC53	B25_mineral 9_rim	olivine	39,3	0,09	0,27	0,01	21,11	0,6	38,66	0,04	0,41	0	0,04	100,54	-6756	-33113	-212
CC48	II-2_mineral1	feldspar?	61,95	0,02	22,7	0	0,17	0	0,01	0	4,83	7,85	0,87	98,4	-11247	-33362	-209
CC48	II-2_mineral10_core	olivine	40,01	0	0,06	0,04	12,54	0,18	46,44	0,26	0,24	0,01	0,01	99,79	-13487	-24789	-205
CC48	II-2_mineral10_rim	olivine	38,64	0,05	0,04	0,02	19,53	0,32	41,1	0,1	0,28	0	0,01	100,09	-13434	-24881	-204
CC48	II-2_mineral11_core	olivine	40,16	0,01	0,06	0,04	12,71	0,16	46,34	0,25	0,23	0	0	99,97	-13742	-23773	-204
CC48	II-2_mineral11_core	olivine	38,88	0,05	0,22	0,05	18,85	0,31	41,05	0,12	0,33	0	0,01	99,86	-14017	-23197	-204
CC48	II-2_mineral11_rim	olivine	38,81	0,04	0,15	0,02	18,88	0,29	41,25	0,1	0,34	0	0,01	99,9	-14017	-23197	-204
CC48	II-2_mineral12_core	olivine	40,87	0,02	0,12	0,06	11,94	0,16	46,74	0,34	0,21	0,02	0,01	100,48	1688	-28402	-139
CC48	II-2_mineral12_rim	olivine	38,68	0,04	0,03	0	18,98	0,31	41,55	0,11	0,36	0,01	0	100,09	1370	-28401	-143
CC48	II-2_mineral2_core	olivine	40,79	0,02	0,05	0,05	11,65	0,18	46,98	0,27	0,21	0	0	100,23	-14071	-27755	-211
CC48	II-2_mineral2_rim	olivine	39,13	0,03	0,04	0	18,76	0,32	41,22	0,1	0,37	0	0,01	99,98	-13921	-27687	-211
CC48	II-2_mineral3_core	olivine	40,38	0	0,08	0,06	12,23	0,17	46,72	0,31	0,24	0,02	0,01	100,22	-14706	-27265	-217
CC48	II-2_mineral3_rim	olivine	39,09	0,04	0,04	0,03	19,2	0,31	41,1	0,1	0,33	0,01	0	100,25	-14853	-27024	-217

CC48	II-2_mineral4_dark grey	pyroxene	52,77	0,34	3,78	0,01	9,09	0,09	12,43	0	20,51	1,51	0,01	100,54	6186	-29977	-132
CC48	II-2_mineral4_light grey	pyroxene	51,88	0,06	1,41	0	23,42	0,23	21,92	0	0,5	0,03	0,01	99,47	6012	-30192	-138
CC48	II-2_mineral5_core	pyroxene	45,82	1,95	8,69	0	13,39	0,34	7,15	0	19,85	2,17	0	99,35	-1524	-23483	-141
CC48	II-2_mineral5_rim1	pyroxene	45,93	2,06	10,01	0,24	6,6	0,13	13,03	0,02	20,43	0,89	0,01	99,36	-904	-23512	-139
CC48	II-2_mineral5_rim2	pyroxene	46,83	2,42	5,92	0,11	7,25	0,13	13,29	0,04	23,01	0,34	0,01	99,35	-864	-23504	-139
CC48	II-2_mineral6_core	olivine	40,07	0	0,05	0,06	11,54	0,14	47,21	0,31	0,21	0	0,01	99,59	9287	-17270	-90
CC48	II-2_mineral6_rim	olivine	39,03	0,04	0,04	0,01	18,82	0,29	41,81	0,11	0,29	0	0,01	100,46	9144	-17275	-90
CC48	II-2_mineral7_core	olivine	40,38	0,02	0,07	0,08	11,73	0,17	46,99	0,28	0,23	0,02	0,01	99,97	-14030	-31398	-219
CC48	II-2_mineral7_rim	olivine	38,78	0,04	0,05	0,03	19,44	0,31	41,37	0,08	0,27	0	0	100,36	-14251	-31484	-224
CC48	II-2_mineral8_core	olivine	40,54	0,01	0,07	0,05	11,89	0,17	46,91	0,26	0,23	0	0	100,14	-14686	-32007	-224
CC48	II-2_mineral8_rim	olivine	38,8	0,03	0,06	0,01	18,32	0,27	41,1	0,12	0,23	0	0,01	98,95	-14717	-31945	-224
CC48	II-2_mineral9_core	pyroxene	49,63	1,13	6,89	0,06	6,48	0,04	12,05	0,01	20,95	1,85	0,01	99,11	-13968	-25865	-208
CC48	II-2_mineral9_rim	pyroxene	45,09	3,21	7,16	0,04	8,5	0,17	12,13	0,03	22,2	0,43	0,02	98,98	-13732	-25784	-207
CC10	V01_mineral1_core	pyroxene	45,93	1,63	6,33	0	16,05	0,45	6,69	0,02	21,46	1,44	0,01	100,01	-8226	19295	-37
CC11	V01_mineral1_dark intergrowth1	pyroxene	49,06	0,95	13,8	0,01	9,91	0,28	3,61	0	15,79	2,49	0,32	96,23	-8811	19100	-36
CC12	V01_mineral1_dark intergrowth2		29,73	0,2	19,68	0	0,36	0,04	0,27	0	8,12	0,09	5,61	64,1	-8328	19220	-34
CC13	V01_mineral1_half	pyroxene	45,4	1,44	4,65	0,01	17,51	0,69	6,38	0	21,81	0,82	0,02	98,73	-8661	19145	-35
CC14	V01_mineral1_rim	pyroxene	45,51	1,44	8,48	0,01	15,55	0,5	6,42	0	19,73	1,78	0,01	99,43	-8909	19185	-36
CC15	V01_mineral10_core	olivine	40,13	0,03	0,06	0,05	12,86	0,19	46,82	0,21	0,3	0	0	100,65	10335	30300	-55
CC16	V01_mineral10_inclusion	spinel	0,11	0,75	40,51	17,43	23,7	0,18	15,08	0,19	0,03	0	0,01	97,99	10290	30257	-55
CC17	V01_mineral10_rim	olivine	39,17	0,03	0,05	0	21,13	0,47	39,49	0,08	0,38	0	0,01	100,81	10270	30298	-55
CC18	V01_mineral2_core	pyroxene	49,18	1,5	7,83	0,04	6,12	0,05	12,17	0	21,13	1,73	0	99,76	-651	23737	-38
CC19	V01_mineral2_rim	pyroxene	44,6	3,59	8,08	0	7,84	0,15	11,49	0	23,06	0,56	0,01	99,37	-530	23833	-38
CC20	V01_mineral3_L1	pyroxene	45,97	2,34	8,39	0	7,2	0,1	13,07	0,02	21,39	0,73	0	99,23	1510	34095	-73
CC21	V01_mineral3_L10	pyroxene	46,93	2,09	8,12	0,02	6,97	0,11	13,32	0,02	21,61	0,74	0	99,93	1927	33965	-69
CC22	V01_mineral3_L11	pyroxene	45,52	2,28	9,91	0,18	6,44	0,11	12,58	0,03	21,83	0,74	0,01	99,64	1947	33958	-69
CC23	V01_mineral3_L12	pyroxene	45,63	2,25	9,9	0,17	6,43	0,08	12,62	0,01	21,76	0,75	0	99,59	1951	33948	-69
CC24	V01_mineral3_L13	pyroxene	43,96	3	10,29	0,13	7,33	0,12	11,63	0,01	21,91	0,78	0,01	99,18	1955	33941	-69
CC25	V01_mineral3_L14	pyroxene	42,53	3,94	10,8	0,01	7,78	0,11	10,81	0	22,48	0,63	0,01	99,11	1955	33939	-69
CC26	V01_mineral3_L15	pyroxene	42,62	4,32	9,81	0,01	8,25	0,18	10,56	0	22,64	0,65	0,05	99,07	1962	33935	-69
CC27	V01_mineral3_L16	pyroxene	43,94	3,85	8,74	0,02	8,16	0,18	10,95	0	22,66	0,67	0,08	99,26	1965	33934	-71
CC28	V01_mineral3_L2	pyroxene	45,98	2,21	7,8	0	7,15	0,12	13,64	0,02	21,4	0,8	0	99,13	1548	34078	-73
CC29	V01_mineral3_L3	pyroxene	46,66	2,35	8,34	0,01	7,35	0,11	12,98	0	21,04	0,77	0,01	99,62	1624	34074	-73
CC30	V01_mineral3_L4	pyroxene	46,38	2,27	8,49	0	7,18	0,13	13,1	0,01	21,08	0,86	0,01	99,51	1700	34073	-71
CC31	V01_mineral3_L5	pyroxene	45,48	2,28	8,72	0	7,38	0,11	12,7	0,02	21,26	0,85	0,01	98,81	1747	34071	-75
CC32	V01_mineral3_L6	pyroxene	46,73	2,02	7,51	0,02	6,92	0,12	13,63	0,01	21,36	0,74	0,01	99,07	1799	34059	-74
CC33	V01_mineral3_L7	pyroxene	46,09	2,24	8,39	0	7,02	0,09	13,2	0	21,47	0,75	0,01	99,27	1862	34067	-74
CC34	V01_mineral3_L8	pyroxene	46,78	2,17	8,43	0,01	7,22	0,12	13,22	0	20,9	0,79	0	99,65	1895	34023	-70
CC35	V01_mineral3_L9	pyroxene	45,24	2,62	8,43	0	7,73	0,13	12,67	0	21,55	0,69	0,01	99,08	1908	33996	-69
CC36	V01_mineral4_L1	pyroxene	46,07	1,69	7,41	0,02	11,37	0,23	9,61	0,04	20,77	1,63	0	98,84	109	32728	-70
CC37	V01_mineral4_L2	pyroxene	46,43	1,73	7,42	0,01	11,26	0,26	9,44	0,01	20,87	1,52	0,01	98,94	175	32728	-67
CC38	V01_mineral4_L3	pyroxene	46,46	1,74	7,47	0	11,5	0,25	9,42	0,01	20,85	1,61	0	99,29	233	32735	-67
CC39	V01_mineral4_L4	pyroxene	44,99	2,05	8,89	0,01	9,71	0,18	10,43	0,01	21,48	1,05	0	98,83	250	32742	-67
CC40	V01_mineral4_L5	pyroxene	45,54	2,24	9,2	0,24	6,54	0,1	12,59	0,02	22,36	0,66	0	99,49	278	32742	-67
CC41	V01_mineral4_L6	pyroxene	43,74	2,81	9,92	0,1	7,27	0,12	12,06	0,01	21,72	0,86	0,01	98,61	306	32742	-68
CC42	V01_mineral4_L7	pyroxene	39,54	4,76	10,94	0,01	8,11	0,11	10,99	0	22,96	0,59	0,02	98,05	313	32744	-68
CC43	V01_mineral5_core	olivine	39,27	0	0,05	0,03	12,35	0,17	47,23	0,22	0,31	0	0,01	99,64	7803	21791	-29
CC44	V01_mineral5_rim	olivine	38,21	0,09	3,82	0	32,51	1,11	24,65	0,01	1,04	0,03	0,4	101,88	7732	21869	-24
CC45	V01_mineral6_core	olivine	40,07	0,01	0,07	0,02	12,61	0,18	46,76	0,21	0,33	0	0	100,26	946	18579	-16
CC46	V01_mineral6_rim	olivine	38,39	0,05	0,03	0	21,71	0,61	38,38	0,05	0,44	0	0,01	99,67	1007	18605	-16
CC47	V01_mineral7_core	olivine	39,79	0,02	0,05	0,05	13,42	0,19	45,92	0,2	0,28	0,02	0,01	99,94	10451	27980	-47
CC48	V01_mineral7_rim	olivine	37,94	0,22	2,18	0	21,77	0,66	32,29	0,02	3,04	0,33	0,29	98,75	10464	28033	-47
CC49	V01_mineral8_core	pyroxene	48,67	0,97	6,78	0,97	4,39	0,09	14,94	0	22,14	0,67	0	99,61	11322	28278	-50
CC50	V01_mineral8_rim	pyroxene	43,87	3,74	8,7	0	7,72	0,14	11,09	0	23,06	0,57	0,02	98,92	11322	28266	-50
CC51	V01_mineral9_core	pyroxene	43,12	4,16	10,61	0,02	6,41	0,08	12,2	0,01	21,86	0,71	0	99,19	11070	28477	-50
CC52	V01_mineral9_rim	pyroxene	40,4	5,05	11,38	0,01	8,13	0,11	10,03	0	22,84	0,54	0,02	98,49	11110	28502	-50
M11	V-1_mineral 1_core	olivine	39,3	0,01	0,06	0	18,4	0,25	42,13	0,06	0,2	0	0	100,41	13645	32680	-78
M11	V-1_mineral 1_rim	pyroxene	46,93	2,12	6,16	0,34	7,01	0,15	13,1	0	22,73	0,46	0	99,02	13905	31413	-69
M11	V-1_mineral 10_core	olivine	39,13	0,03	0,04	0,02	19,55	0,34	41,17	0,16	0,22	0	0	100,67	-10015	29738	-82
M11	V-1_mineral 10_rim	olivine	36,47	0,04	0,03	0	31,97	0,77	30,46	0,05	0,46	0	0,01	100,26	-10056	29634	-82
M11	V-1_mineral 11	plagioclase	52,03	0,12	29,1	0	0,61	0,01	0,04	0,01	12,42	4,36	0,27	98,98	-10117	29988	-85
M11	V-1_mineral 12	plagioclase	51,43	0,12	29,52	0,01	0,61	0,02	0,05	0,01	13,03	3,97	0,25	99,02	-5510	22605	-15
M11	V-1_mineral 13	plagioclase	52,37	0,14	29,02	0	0,53	0,01	0,04	0	12,35	4,36	0,28	99,1	11114	22858	6
M11	V-1_mineral 14	plagioclase	53,51	0,14	27,85	0	0,45	0	0,05	0	11,23	5,02	0,32	98,58	11521	30792	-62
M11	V-1_mineral 2_core	olivine	40,3	0	0,06	0,05	12,52	0,18	46,74	0,21	0,24	0	0	100,3	12730	29652	-53
M11	V-1_mineral 2_rim	olivine	36	0,03	0,86	0	29,39	0,6	26,28	0,07	0,58	0	0,06	93,88	12383	29638	-53
M11	V-1_mineral 2_rim2	olivine	35,65	0,05	0,28	0	34,49	0,86	27,43	0,04	0,58	0	0,02	99,41	-9597	29264	-75
M11	V-1_mineral 3_core	olivine	39,37	0,03	0,03	0,02	18,74	0,34	41,63	0,14	0,25	0	0,01	100,56	-10504	28636	-77
M11	V-1_mineral 3_rim	olivine	36,41	0,06	0,14	0	32,79	0,76	26,49	0,07	0,58	0,02	0,05	97,37	-10433	28610	-77
M11	V-1_mineral 4_core	olivine	38,96	0,03	0,03	0,02	19,76	0,35	40,76	0,15	0,22	0	0	100,28	-9549	29270	-80
M11	V-1_mineral 4_rim	olivine	42,05	0,14	12,68	0,01	18,86	0,34	12,91	0,04	1,26	0,95	6,62	95,85	-9605	29261	-80
M11	V-1_mineral 4_rim2	olivine	30,55	0,06	1,39	0	37,35	0,98	19,91	0,06	0,83	0	0,05	91,18	14329	25281	-6
M11	V-1_mineral 5_core	olivine	40,19	0,04	0,06	0,04	13,13	0,2	46,33	0,26	0,27	0	0	100,52	14323	25622	-17
M11	V-1_mineral 5_rim1	olivine	39,37	0,03	0,03	0	18,34	0,31	42,28	0,17	0,2	0	0,01	100,75	14364	25304	-14
M11	V-1_mineral 5_rim2	olivne	34,87	0,05	0,22	0	35,98	0,93	24,85	0,03	0,57	0	0,04	97,53	14321	25281	-13
M11	V-1_mineral 5_rim2	olivine	34,89	0,05	0,18	0,01	34,32	0,85	24,08	0,06	0,71	0	0,03	95,18	7507	24980	-15
M11	V-1_mineral 6_core	olivine	38,77	0,01	0,04	0,04	20,99	0,37	39,9	0,16	0,24	0	0	100,52	13549	26463	-24
M11	V-1_mineral 6_rim	olivine	34,04	0,05	0,91	0	44,68	1,37	19,1	0,01	0,36	0,08	0,5	101,1	13599	26414	-23
M11	V-1_mineral 7_core	olivine	40,25	0	0,05	0,05	14,36	0,2	45,42	0,22	0,24	0	0,01	100,8	7605	25074	-17
M11	V-1_mineral 7_rim	olivine	34,13	0,06	0,13	0,01	34,69	0,88	24,01	0,04	0,69	0	0,03	94,66	7506	24977	-15
M11	V-1_mineral 7_rim2	olivine	38,46	0,11	0,05	0,01	22,83	0,41	38,56	0,07	0,43	0	0,01	100,95	-7203	-22898	-176
M11	V-1_mineral 8_core	olivine	40,66	0	0,04	0,05	12,4	0,16	46,96	0,3	0,28	0	0	100,84	5717	24882	-18
M11	V-1_mineral 8_rim	olivine	37,45	0	0,02	0	28,55	0,58	33,54	0,08	0,28	0	0,01	100,52	5630	24617	-14
M11	V-1_mineral 9_core	olivine	40,47	0,01	0,06	0,04	12,48	0,15	47,02	0,28	0,25	0,03	0,01	100,79	3181	24805	-20
M11	V-1_mineral 9_rim	olivine	35,44	0,05	0,35	0,01	31,27	0,7	25,15	0,09	0,7	0	0,03	93,79	3418	24900	-21

8.5 Appendix E: Backscatter Electron Images of the olivine types found in the Bayuda Monogenetic Volcanic Field

Sample: Mineral Number	Backscatter Electron Images
10-1B_mineral8_core	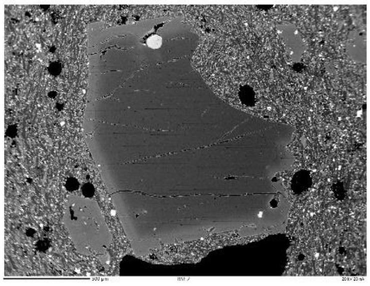
B10_2_centre	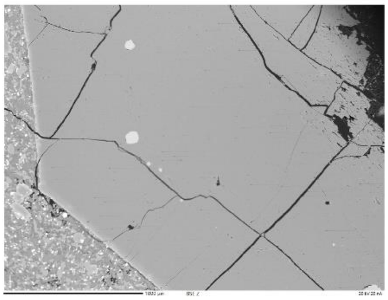
B10_3_centre	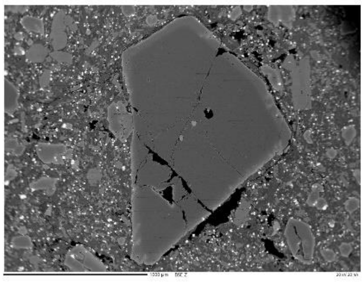
B10_5_centre	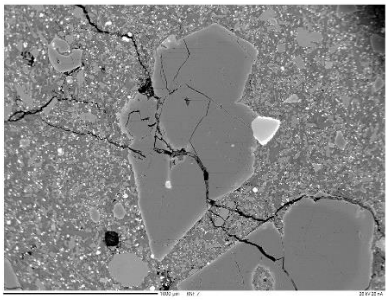
B10_7_centre1	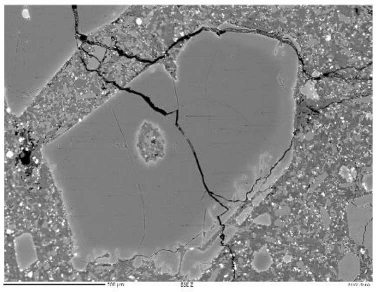

Sample: Mineral Number	Backscatter Electron Images
B10_8_core2	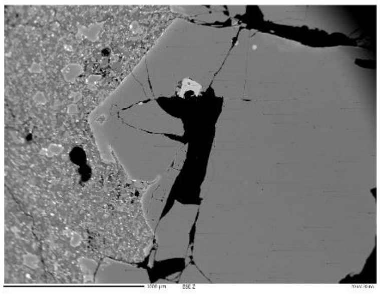
B25_mineral 1_core	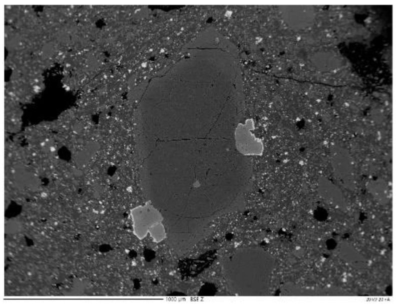
B25_mineral 11_core	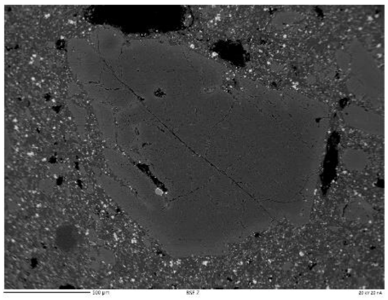
II-2_mineral2_core	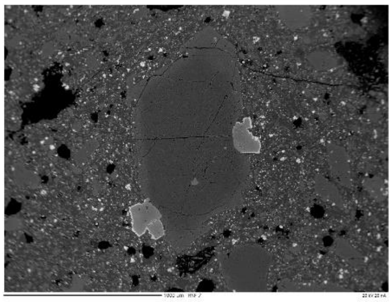

II-2_mineral3_core	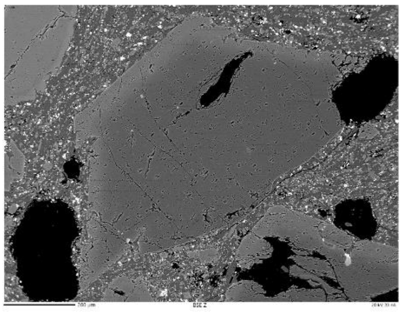
II-2_mineral6_core	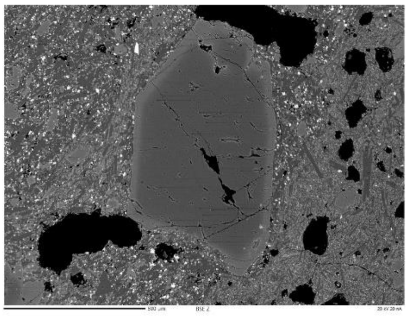
II-2_mineral7_core	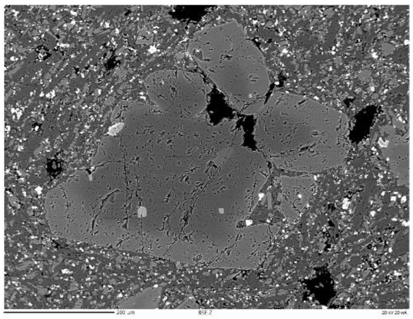
II-2_mineral8_core	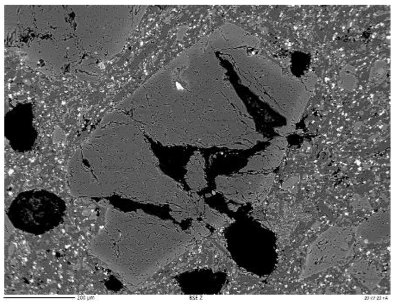
II-2_mineral 10_core	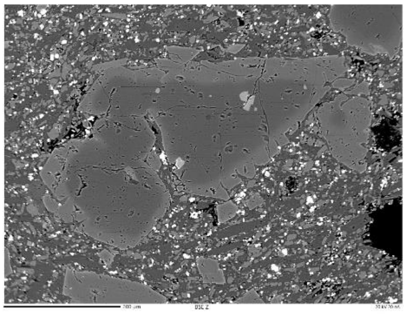

II-2_mineral11_core	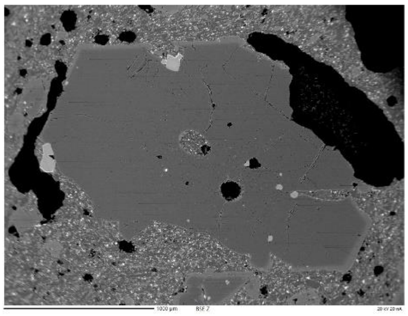
II-2_mineral12_core	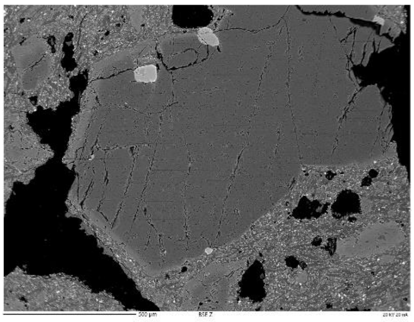
V-1_mineral 5_core	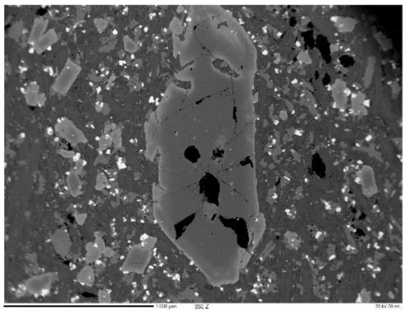
V-1_mineral 8_core	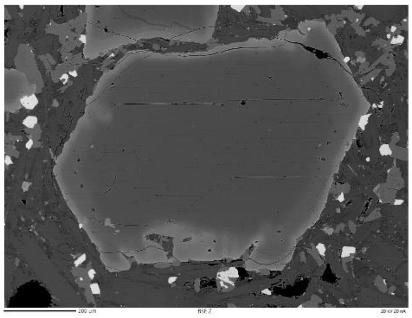
V-1_mineral 9_core	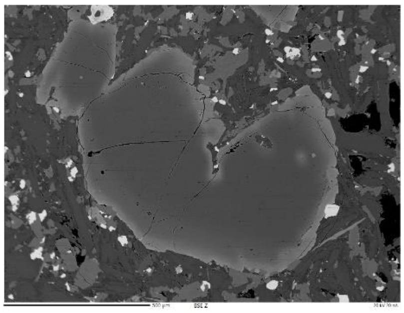

Type 2 Olivines

Sample: Mineral Number	Backscatter Electron Images
10-1A_mineral 6_core	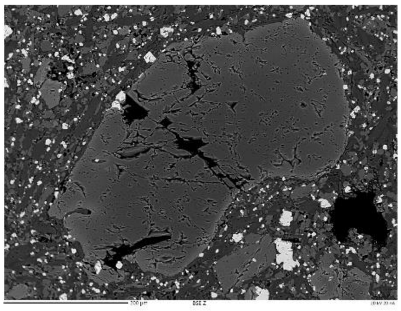
10-1A_mineral 7_core	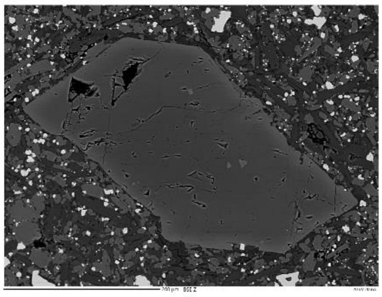
10-1A_mineral 10_core	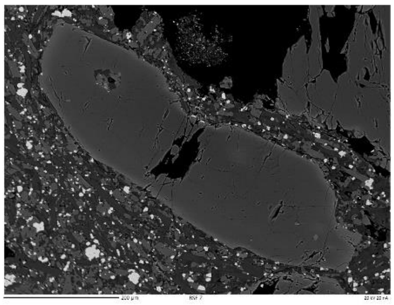
10-1B_mineral10_core	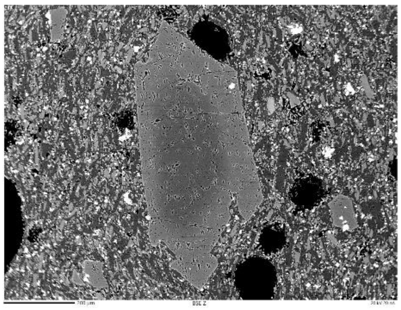
10-1B_mineral2_core	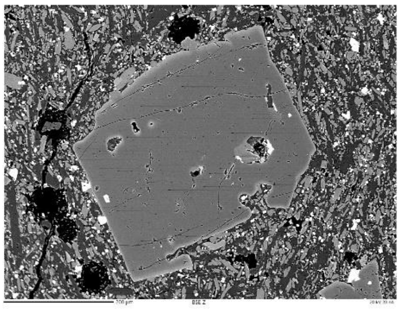

Sample: Mineral Number	Backscatter Electron Images
10-1B_mineral4_L1_core	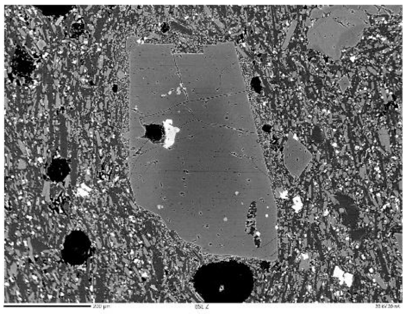
10-1B_mineral5_core	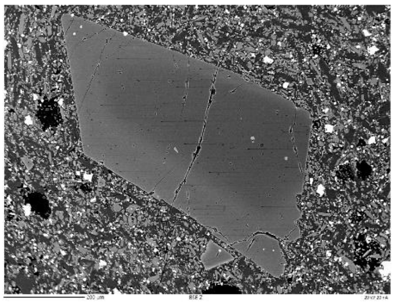
10-1B_mineral6_core	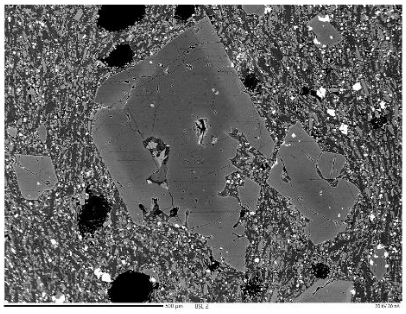
10-1B_mineral7_core	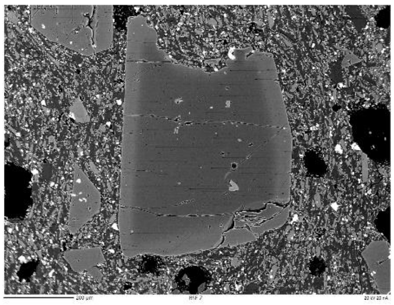
B10_1_centre	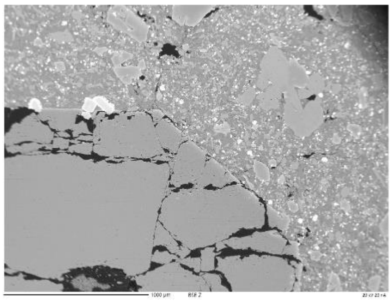

Sample: Mineral Number	Backscatter Electron Images
B12_min10_core2	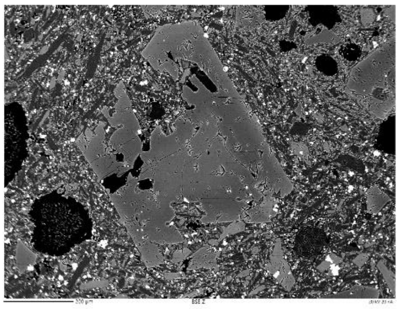
B12_min2_core	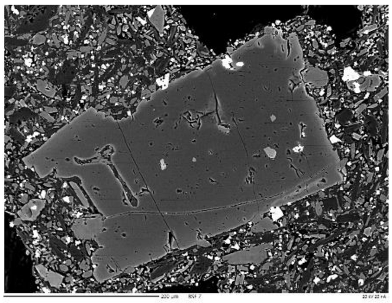
B12_min3_core	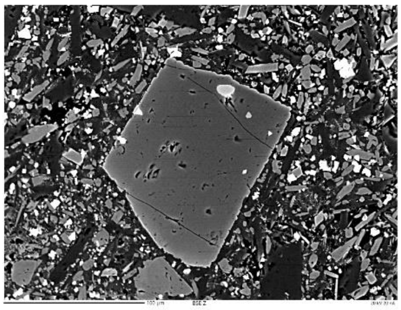
B12_min4_core	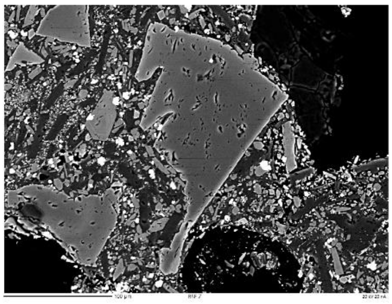
B12_min5_core	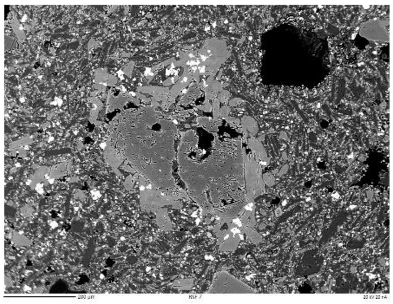

Sample: Mineral Number	Backscatter Electron Images
B12_min8_core	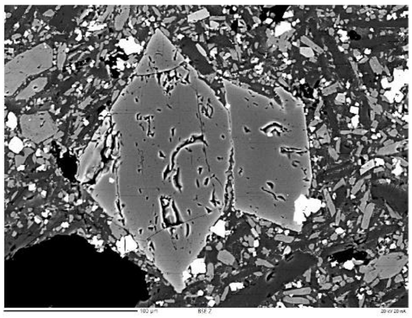
B12_mineral9_core	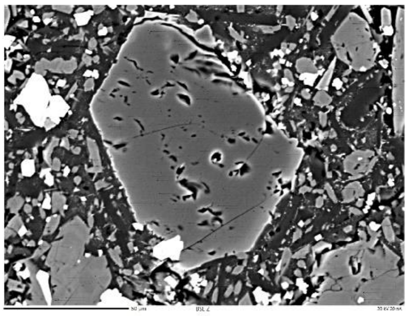
B22_mineral 2_core	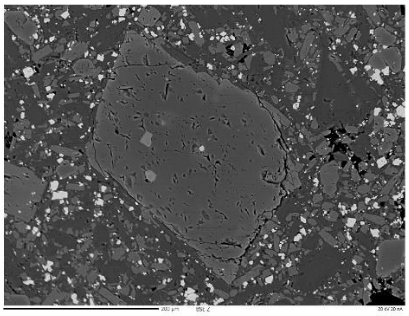
B22_mineral 3_core	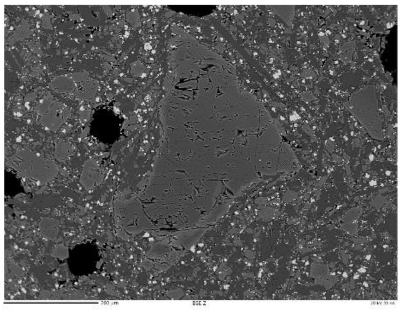
B22_mineral 4_core	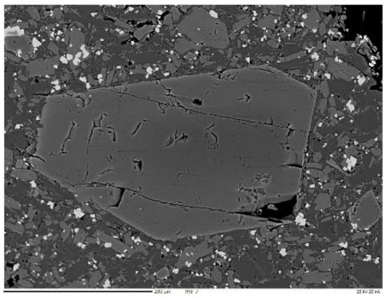

Sample: Mineral Number	Backscatter Electron Images
B22_mineral 5_core	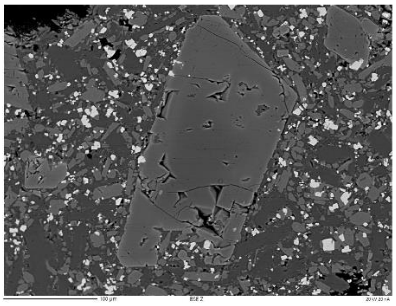
B22_mineral 6_core	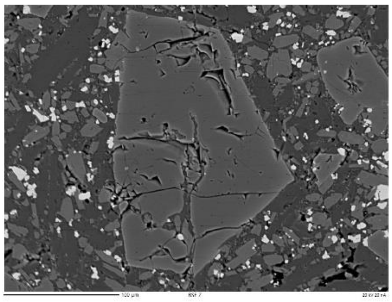
B22_mineral 7_core	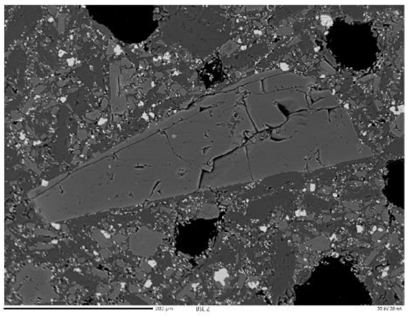
B25_mineral 6_core	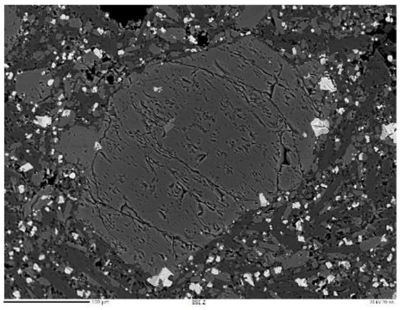
B25_mineral 7_core	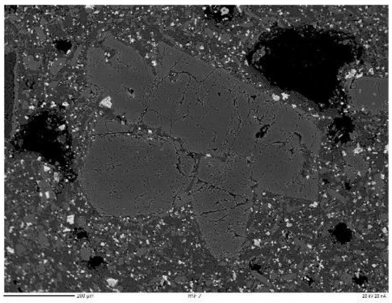

Sample: Mineral Number	Backscatter Electron Images
V01_mineral10_core	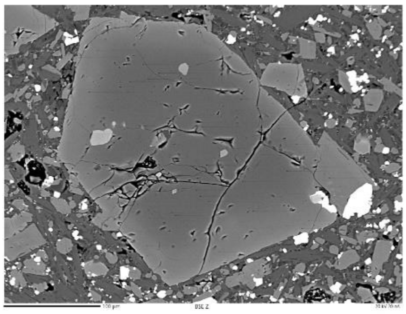
V01_mineral5_core	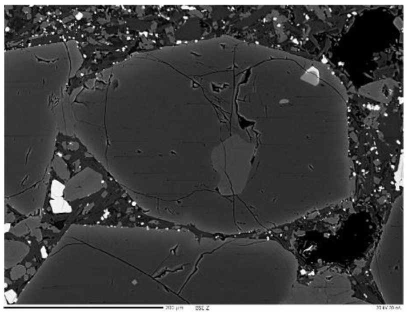
V01_mineral6_core	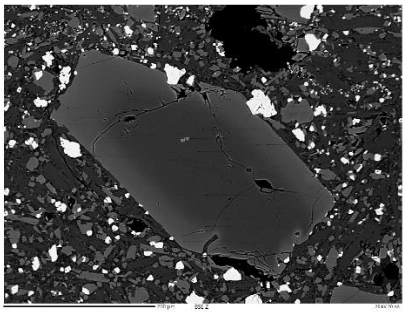
V01_mineral7_core	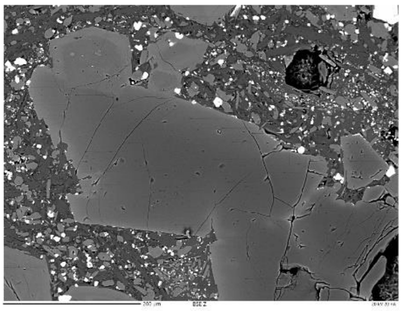
V-1_mineral 2_core	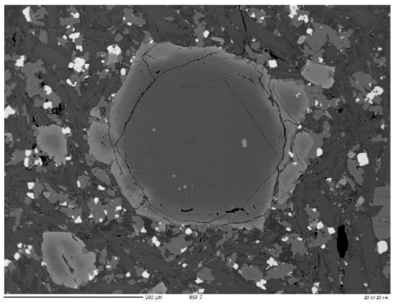

V-1_mineral 3_core	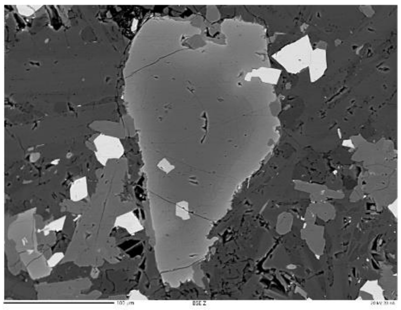
V-1_mineral 4_core	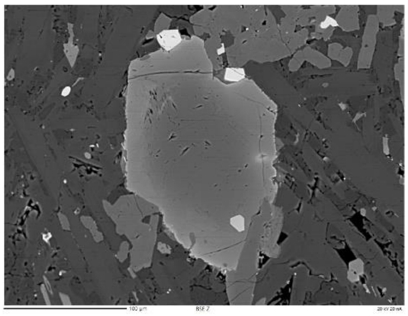
V-1_mineral 6_core	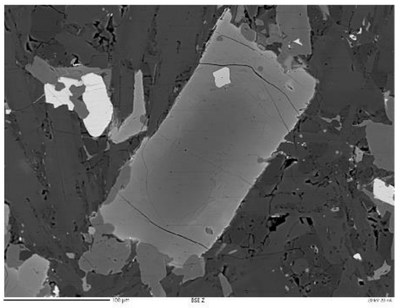
V-1_mineral 7_core	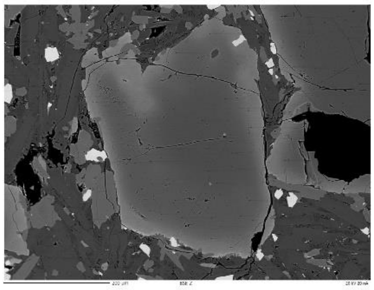
V-1_mineral 10_core	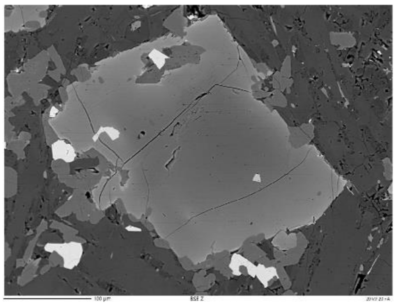

Type 3 olivines

Sample: Mineral Number	Backscatter Electron Images
10-1A_mineral 1_core	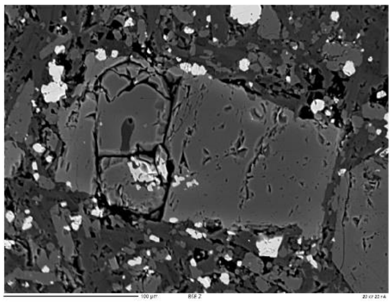
10-1A_mineral 2_core	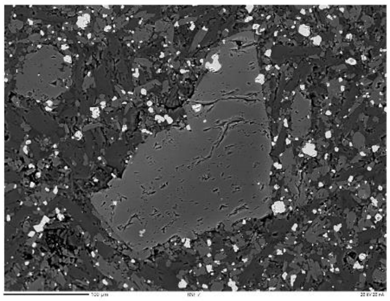
10-1A_mineral 3_core	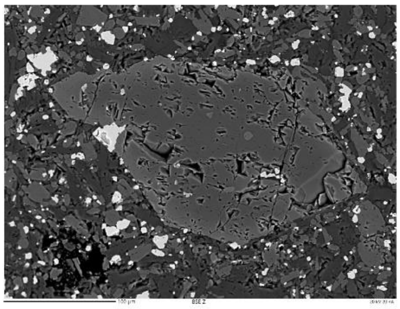
10-1A_mineral 4_core	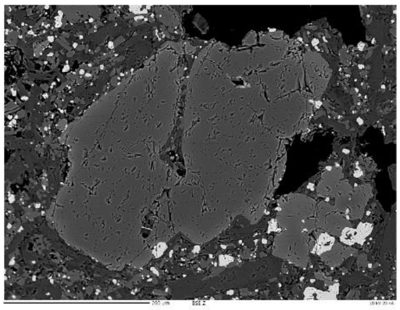
10-1A_mineral 5_core	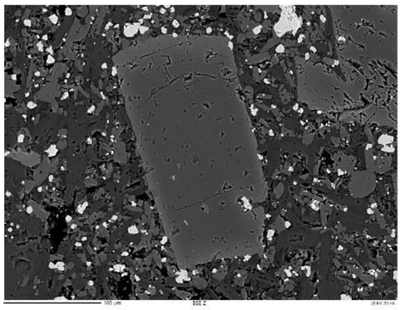

Sample: Mineral Number	Backscatter Electron Images
10-1A_mineral 8_core	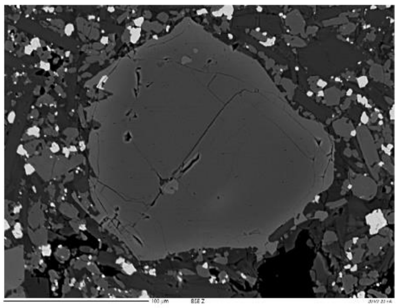
10-1A_mineral 9_core	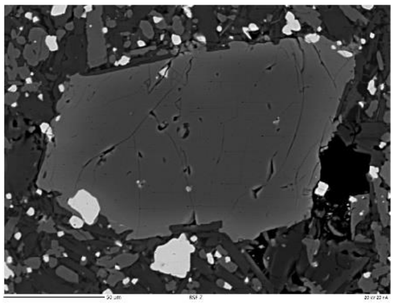
B12_min1_core	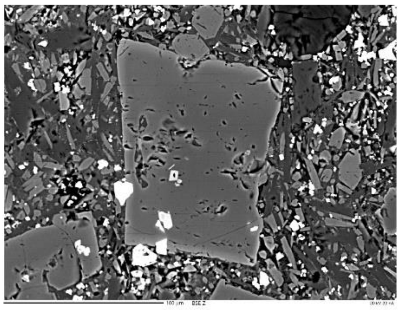
B12_min6_core	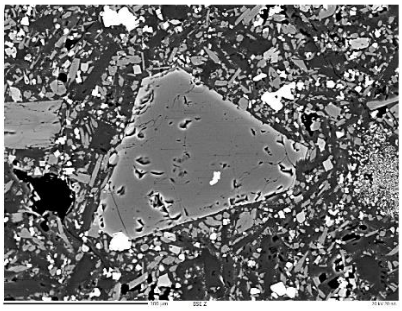
B12_min7_core	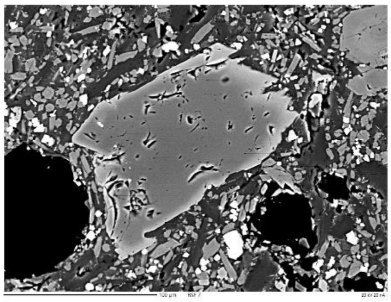

Sample: Mineral Number	Backscatter Electron Images
B22_mineral 8_core	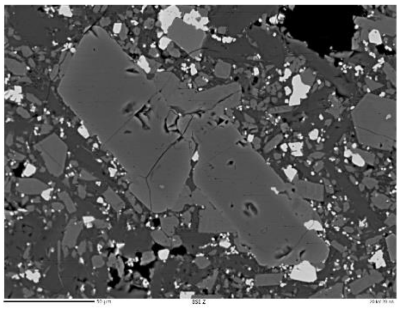
B22_mineral 9_core	Not applicable
B25_mineral 10_core	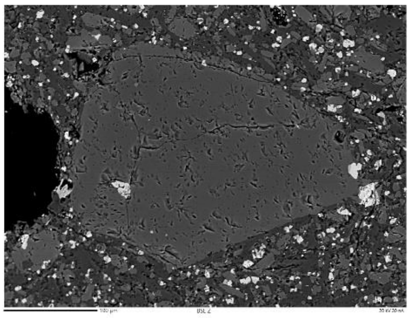
B25_mineral 5_core	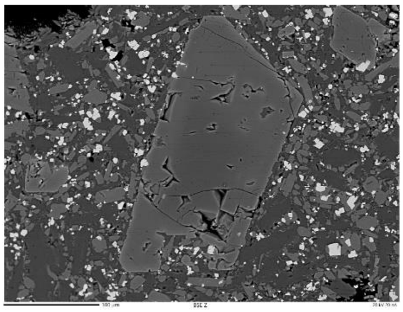
B25_mineral 9_core	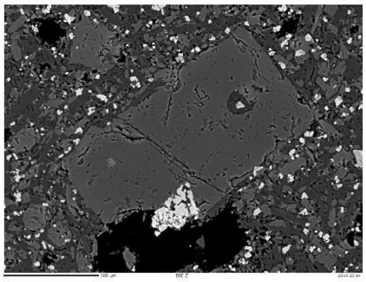

V-1_mineral 1_core